Synthesis and Coordination Chemistry of Phenanthridine-Containing Monoanionic *N*^*N*$^-$^*N* Pincer Motifs

By

Pavan Mandapati

A Thesis submitted to the Faculty of Graduate Studies in partial fulfilment of the requirements of the degree of

Doctor of Philosophy

Department of Chemistry
University of Manitoba
Winnipeg, MB, Canada

Abstract:

This thesis involves a series of projects that explore the synthesis of phenanthridine-containing monoanionic *N^N-^N* 'pincer' motifs as ancillary ligands which can stabilize group 10 transition metals (Ni, Pd and Pt). Phenanthridines are 14π electron annulated tricyclic aromatic *N*-heterocycles with extended π-conjugation. Phenanthridines have been reported in the context of chemical synthesis, material synthesis, and catalysis, and show interesting photophysical and luminescence properties which find applications in bio-imaging techniques as fluorescent markers. Compared to its congener quinoline, however, phenanthridines have been rather underexplored in coordination chemistry. This thesis demonstrates how functionalized phenanthridines can be easily accessed in one-pot syntheses via palladium catalyzed Suzuki C-C coupling followed by condensation at high temperatures. With a route to functionalized phenanthridines with electron donating groups (Me, *t*Bu) and electron withdrawing groups (CF_3) in hand, they were incorporated into 'pincer' ligand frameworks using Buchwald-Hartwig C-N coupling, to isolate a series of phenanthridinyl/quinolinyl containing symmetric and asymmetric monoanionic *N^N-^N* proligands (**L1-L16**).

My subsequent work then focused on examining the effects of systematic benzannulation in pincer-type ligands, through studies of the electronic, material and catalytic properties compared to quinoline in the presence of transition metals. To study these properties, a series of square-planar metal complexes of Group 10 metals (Ni, Pd and Pt) were synthesized containing both phenanthridines and quinolines. Platinum(II) complexes of phenanthridinyl/quinolinyl containing symmetric and asymmetric monoanionic *N^N-^N* ligands are photo-emissive in nature. These emissive complexes with electron donating groups (Me, *t*Bu) and electron withdrawing groups (CF_3) provided a

platform to study the effect of site selective benzannulation and ring substituent effects on highest occupied molecular orbitals (HOMO) and lowest unoccupied molecular orbitals (LUMO) and their impact on absorption and emission properties. The results from these studies will be discussed in the following chapters. Although these complexes exhibit interesting photophysical properties, the complexes are relatively less soluble when compared to metal complexes of bis(quinolinyl)amine, in common organic solvents due to strong π-π stacking interactions, which hindered the opportunity to explore reactivity of the complexes. To overcome the issue of solubility, a new ligand design approach was made to synthesize proligands with solubilizing NMe_2 groups that help break the planarity of their coordination complexes. Divalent nickel and palladium chloride complexes were synthesized with these proligands, the complexes were soluble in common organic solvents. Moreover, phenanthridine-containing nickel(II) chloride complexes of these more soluble ligands were found to be active catalyst for alkylation of azoles.

Acknowledgements:

To achieve one of the greatest milestones of my career, I have started the long journey from a warm southern part of India to one of the coldest places in the world to pursue my graduate research thesis as a graduate student at University of Manitoba, Winnipeg in January 2014. After six years, I am glad to submit my thesis and move further ahead to achieve future endeavors. During my research career I have come across many ups and downs, hardships, learned many life lessons and I now feel very proud to complete my studies smoothly beating all the odds. There are many people who have supported me all the way along, without which I would not have completed my thesis.

Firstly, I would like to sincerely thank my principal investigator and supervisor Prof. David Herbert for providing me an opportunity to work in his research group. He was available for me for my entire time I have spent in Winnipeg. I was carefully nurtured under his immense care, kindness and support, and always extended his friendly support towards me with a lot of patience and respect. From the beginning he was more like a friendly colleague with great knowledge in chemistry and wisdom, always makes everyone happy with a smile on a face and constantly encouraged them to reach their successful career heights. He is a great teacher with excellent skills and knowledge and always ready to transfer them to students and colleagues. He made me forget my family miles away with his care, emotional support and love, especially during pandemic.

I would like to thank and extend my deepest gratitude to my committee members Prof. Mario Bieringer, Prof. Jamie Ritch and Prof. Wen Zhong for their strong support during my entire graduate studies, while I was sick and unhealthy, and during the pandemic. They have continuously encouraged me to improve and become a better scientist with their positive feedback during my annual progress meetings. I also thank the late Prof.

Philip Hultin, Prof. Mario Bieringer, Prof. Peter Budzelaar and Prof. David Herbert for providing excellent graduate level courses which helped me to understand chemistry in depth with reasoning and pushed boundaries of knowledge. Collaboration with Prof. Rebecca Davis and Prof. Gareth Williams (University of Durham) for DFT studies and luminescent studies respectively provided great insights and better understanding of my research projects.

A great team always produces a great student, and I take the opportunity to thank all my team players Dr. Paul Gray, Dr. Rajarshi Mondal, Jason Braun, Issiah Lozada, Dion Nemez, Bladeep Sidhu, Robert Ortiz, Gabrielle Wilson and all undergraduates who were part of Herbert research family tree. They have been great friends, colleagues, we collaborated with each other to improve the knowledge and understanding of my projects and we have spent a lot time discussing memorable immature chemistry. Working for Prof. Horace Luong as a teaching assistant helped me to improve my teaching skills to students. I sincerely appreciate for all the help I have received from other teaching and non-teaching staff members, lab technicians of chemistry department Dr. Marat, Dr. Davidson and Mark Cooper (geology department) who helped me with NMR experiments and X-ray data respectively.

A teacher plays an important role for motivating students to pursue their dreams by providing knowledge and guidance. I deeply extend my gratitude to my gurus Dr. D. Bala Karuna Kumar at Andhra Loyola College (Vijayawada, India) and Prof. Anil J. Elias at IIT Delhi (New Delhi, India) who nurtured me with great care towards chemistry. My research career in chemistry was completely motivated and inspired by them, have I not met them

during my undergraduate studies and graduate studies respectively I would have not reached this far to pursue chemistry.

My thesis is dedicated to my father Mandapati Showry (late) and mother Mandapati Mariamma for giving life to me and I sure they are proud of me. I sincerely thank and extend my deep love and gratitude to all my siblings and family members who are taking care of my mother during my absence, their emotional support and love towards me during the crucial times is priceless. I cannot imagine myself to spend time in Winnipeg without my siblings around me and family members for almost six years, I am sure they will understand and forgive me for not taking up family responsibilities when needed. I am grateful to have awesome friends and roommates like Dr. Gurpreet Kaur, Dr. Vinod Kumar Paidi, Reddy, Lakshmipathi Chinnappa (Lucky), Suraksh, Kannan, Dr. Ethender, Dr. Varathan, Pushparaju, Ajay, Gurmeet Singh, Krishna, Amir, Wenhao Mo, Monika, Amit, Arun, Kiran, Navriti, Shane, Troy, Laura and all my childhood friends who have provided the warmth and love which I missed from my family, I cannot imagine life in Winnipeg without them.

I whole heartedly thank you all who made my graduate studies possible and helped me navigating the odds smoothly.

- Pavan Mandapati

Table of Contents:

List of Figures:

List of schemes:

List of Tables:

List of Abbreviations:

1,5-COD: 1,5-cyclooctadiene

BINAP: 2,2′-bis(diphenylphosphino)-1,1′-binaphthyl

CCD: charge coupled device

CV: cyclic voltammetry

DPV: differential pulse voltammetry

DME: 1,2-dimethoxyethane

DPPF: (1,1'-diphenylphosphino)ferrocene

DNA : deoxyribonucleic acid

RNA: ribonucleic acid

DFT : density functional theory

dpybH : 1,3-di(2-pyridyl)benzene

E_s : singlet state energies

EtAc : ethyl acetate

FWHM : fullwidth half maximun

MO: molecular orbital(s)

HOMO: highest occupied molecular orbital

LUMO: lowest unoccupied molecular orbital

NaO*t*Bu : sodium *tert*-butoxide

NaO*t*Pen : sodium *tert*-pentoxide

OLED : organic light emitting diode

PCM : polarizable continuum model

TD-DFT : time-dependent density functional theory

TGA: thermogravimetric analysis

UV: ultraviolet

TADF: thermally activated delayed fluorescence

MLCT: metal to ligand charge transfer

LLCT: ligand to ligand charge transfer

BOPA: bis(oxazolinylphenyl)amine

BOX: bis(oxazoline)

BOXMI: bis(oxazolinylmethylidene)isoindoline

BPI: bis(2-pyridylimino)isoindole

BQA: bis(8-quinolinyl)amine

Cbzbox: bis-oxazoline carbazole

DIPEA: diisopropylethylamine

DMS: dimethylsilane

NHK: Nozaki–Hiyama–Kishi

pyBOX: pyridine bis(oxazoline)

PyrrMeBOX: 2,5-bis(2-oxazolinylmethyl)pyrrole

TADF: thermally activated delayed fluorescence

DCM: dichloromethane

MeOH: methanol

THF: tetrahydrofuran

NMR: nuclear magnetic resonance

XRD: X-ray diffraction

Chapter 1: Introduction

1.1. Brief Introduction to the History of Organometallic Chemistry:

The elements of the periodic table can be classified as main-group elements (consisting of *s*- and *p*-block), transition elements (consisting of the *d*-block) or rare-earths (consisting of the *f* -block), according to the main orbital occupied by valence electrons in the ground-state of each element. Main-group organometallic compounds, containing a main group metal-carbon bond (e.g., *n*BuLi) find significant use in organic synthesis but cannot be easily regenerated and so have to be used in stoichiometric amounts for a given chemical reaction. Moreover, these compounds do not have vacant orbitals to accommodate incoming nucleophiles/electrophiles to participate in a catalytic reaction, and so reactions typically involve the organic fragment acting as a nucleophile, without further participation of the metal. They are also extremely corrosive and difficult to handle due to their moisture and air sensitivity. On the other hand, transition metal elements have energetically accessible *d* orbitals which can participate in reactions of transition metal organometallics, opening up new reaction pathways. Complexes of these elements have accordingly proven to be excellent catalysts for organic syntheses. Studies of organometallic compounds can also enable understanding of mechanistic aspects of a chemical reaction, in particular via the isolation of reaction intermediates. Unlike main-group reagents, these transition metal complexes are relatively easy to handle, and so can be used as precatalysts on industrial scale for mass production of organic compounds and essential polymers for clothing and plastic. In general, replacing main-group reagents with transition metal catalysts is therefore not only good economically, but also environmentally friendly to avoid bulk chemical waste generated over an industry scale chemical synthesis and organic

transformations.[1] Some important developments and events in the history of organometallic chemistry are given below.[7]

Year	Major Discoveries
1760	Discovery of 'Cadet's fuming liquid known as "*cacodyl*"; the first main-group organometallic compound tetramethyldiarsine $As_2(CH_3)_4$.[2,3] This discovery led the chemists to debate whether or not arsenic can be categorized as a metal that is bound to carbon.[4]
1827	Discovery of Zeise's salt ($K[PtCl_3(C_2H_4)].H_2O$), the first transition metal organometallic olefin (π) compound isolated by W. C. Zeise.[5]
1849	Edward Franklin made the first main-group organometallic compounds ethylzinc iodide (EtZnI) diethylzinc (Et_2Zn), a pyrophoric liquid isolated in an attempt to make ethyl radicals from the reaction of granulated zinc and ethyliodide in a sealed tube.[6] Franklin also coined the term 'organometallic'.[7]
1890	Ludwig Mond made $Ni(CO)_4$, the first binary metal carbonyl; it is used for the refining of Nickel.[8]
1900	Discovery and applications of Grignard reagents (RMgX); they have more versatile applications than organozinc reagents.[9]
1912	Victor Grignard and Paul Sabatier received Nobel Prize for the Grignard reagent and Sabatier's method of hydrogenation using metal powders.
1917	Synthesis of first alkyl lithium compounds by William Schlenk, later found a wide range of applications when compared to Grignard's reagents.

1938 Otto Roelen discovered hydroformylation (the Oxo process), the first use of an organometallic compound in homogeneous catalysis.[10]

1951 Synthesis of a first sandwich compound ferrocene; the structure was proposed by Wilkinson, Fischer and Woodward.[11] Later bis(benzene)chromium was prepared by E. O. Fischer and W. Hafner.[12]

1955 K. Zieglar and G. Natta developed olefin polymerization.[13]

1961 Discovery of Vaska's complex which reversibly binds oxygen {*trans* $IrCl(CO)(PPh_3)_2$}.

1963 Nobel prize of K. Zeigler and G. Natta

1964 E. O. Fischer synthesized first metal carbene complex.[14] Later he prepared first metal carbyne complex.[15]

1965 Discovery and applications of Wilkinson's catalyst [$(PPh_3)_3RhCl$] for the hydrogenation of alkenes.[16]

1968 William Knowles discovered asymmetric catalysis, and thereby the synthesis of complexes containing chiral ligands.[18]

1972 Richard F. Heck and T. Mizoraki discovered the palladium catalyzed C-C coupling with vinylic hydrogen atoms with aryl halides.[24]

1973 E. O. Fischer and G. Wilkinson shared Nobel prize for their work on metal sandwich compounds.

1979 Suzuki and Miyaura reported palladium catalyzed C-C coupling with aryl boronic acids and aryl halides.[25]

1980 Discovery of zirconocene based catalysts for iso and syndiotactic polypropylene.[19]

1990 Richard Schrock discovered a molybdenum-based catalyst for olefin metathesis.[20]

1991 Discovery of first fullerene based organometallic compound.[17]

1995 Robert Grubbs synthesised ruthenium-based olefin metathesis catalyst.[21]

2001 W. S. Knowles, K. B. Sharpless and R. Noyori share the Nobel Prize in Chemistry for asymmetric hydrogenation.

2005 Y. Chauvin, Robert H. Grubbs and R. R. Schrock received Nobel Prize in Chemistry for olefin metathesis.

2005 Phillip Power synthesized first stable metal-metal quintuple bonds.[23]

2010 Richard F. Heck, E. Negishi and A. Suzuki receive the Nobel Prize in Chemistry for palladium catalyzed C-C coupling reactions.

1.2. Ligand Design - Pincer Ligands and Their Compounds:

1.2.1. Ligands:

Many significant advances have taken place in the last couple decades in field of homogenous catalysis,[26] water oxidation chemistry,[27,28] bond activation chemistry,[29] C-N cross coupling reactions,[30] organic synthesis and pharmaceutical industry,[31] supramolecular chemistry,[32] OLEDs[33] and many other fields in organometallic chemistry, of which ligand design plays an important role. To orient discussion of designing ligands, an overview of the topic is first provided here. The fundamentals of metal-ligand bonding and the concept of coordination chemistry originates with Alfred Werner, who studied the chemistry and characterization of CoL_6 complexes (popular octahedral cobalt ammonia complexes), where he debunked the theory of linear amines bound to cobalt metal center proposed by Jørgensen, thereby synthesizing *cis*-$[Co(NH_3)_4Cl_2]^+$ (purple color) and *trans*-

$[Co(NH_3)_4Cl_2]^+$ (green color) in an ingenious route without the benefit of modern spectroscopic or crystallographic techniques. [1] Any atom/molecule which has the ability to bind to a metal centre either by donating a single electron or pair of electrons forming a coordinate bond can be termed as a 'ligand'. Based on the number of donor atoms present on the ligand that can bind to a metal centre, ligands can be classified as monodentate (one donor atom) or multidentate (e.g., bidentate, two donor atoms; tridentate, via three donor atoms - which also include variations popularly known as 'pincer' ligands) tetradentate (four donor atoms), hexadentate (six donor atoms) and so on. Many of these types commonly appear in organometallic coordination chemistry. In general, ligands are mostly Lewis basic and can be neutral or negatively charged, however, positively charged (H^+) or Lewis acidic ligands (boranes) can also form complexes with Lewis basic metals. Neutral ligands (known as L-type) form bonds datively by donating a pair of electrons. Examples of L-type ligands include phosphines (e.g., PPh_3, PMe_3), amines (NH_3), carbon monoxide (CO), and also π-donors, such as alkenes. Negatively charged ligands (known as X-type) form covalent bonds with metal centres. Examples include halides (e.g., Cl^-, Br^-), hydrides (H^-), and alkoxides (OR^-). Lewis acids (known as Z-type) are such as BF_3, H^+, electron deficient metal centres etc., often accept electrons from electron rich metal centres, L-type or Lewis bases to form covalent bonds.

Ligands can play an important role in the course of a reaction of a metal-ligand complex. They may associate or dissociate to control the coordination number and available coordination sites at a metal or participate along with the reactant in a given transformation. In the latter case, they are known as 'actor' ligands. Similarly, there are ligands which bind to the metal centres but do not participate directly in chemical transformations of

substrates, instead stabilizing the metal in the process. These are known as 'spectator' ligands and are often used to influence the electronics and control the steric environment around the metal centre. Phosphines commonly used as spectator ligands as they help increase the stability and solubility of metal complexes, and provide some control over the sterics and electronics as well.[1,7]

In general, most of ligands in transition metal complexes maintain a spectator role, with reactions of substrates taking place at the metal centre. Spectator ligands can be fine-tuned with specific and unique properties that can both control sterics and electronics, helping researchers to improve the performance of homogenous catalysts by adjusting these parameters. In comparison, actor ligands that serve as the site of oxidation/reduction and also participate directly in electron transfer are also known. These kinds of actor ligands are referred to as 'redox non-innocent', and there are four strategies to use them in catalysis (Figure 1.1).

The four strategies can be distinguished as follows. Strategy I: Oxidation/reduction of the ligand can increase the Lewis acidity of the metal, which strongly influences the substrate affinity as well as the energy profile of subsequent follow-up reactions. Strategy II: To avoid uncommon oxidation states at the metal centre during the course of a reaction, ligands can be designed to use as "electron reservoirs" meaning they can be used to store any excessive electron density and also participate in elementary steps by helping adjust for any electronic deficiency at the metal during catalysis. Strategy III: The ligand can cooperate with the metal in substrate activation directly, for example, in 1,2-addition reactions across metal-ligand bonds. Strategy IV: The last strategy has the substrate itself acting as a redox non-innocent ligand, leading to radical-type chemistry activated by

substrate binding to the metal. In other words, redox non-innocent ligands can either participate in the catalytic cycle through approach (A) accepting/releasing electrons (strategies I and II) or by approach (B) forming/breaking chemical bonds of the substrate (strategies III and IV) as shown in Figure 1.1.[34]

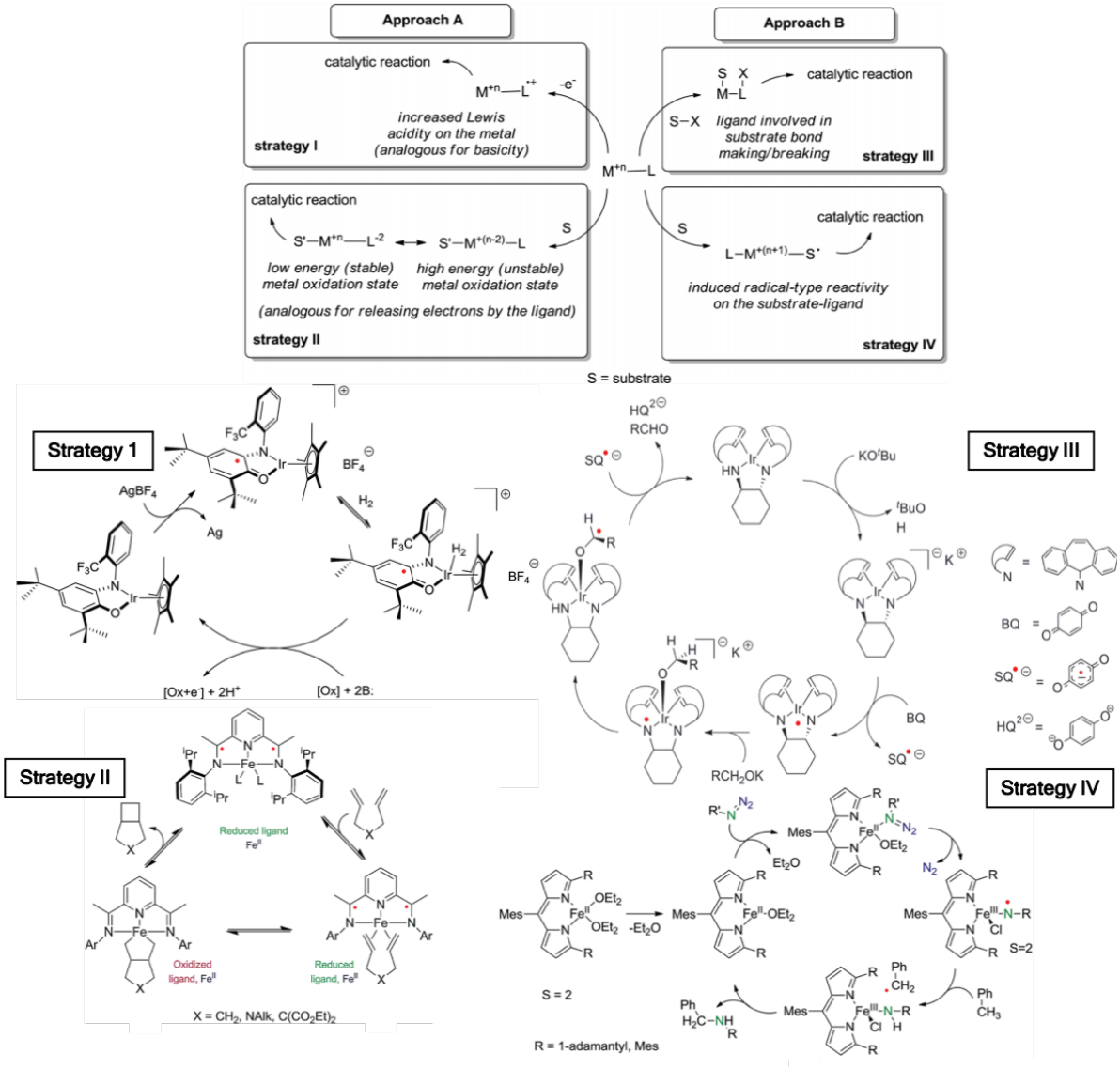

Figure 1.1. Four main strategies of using redox non-innocent ligands in catalysis. Graphic adapted from reference.[34]

Strategy I: Tuning electronic properties of the ligand can have a strong influence on the reactivity and catalytic behavior of the complex, can be achieved by introducing electron withdrawing groups and electron donating substituents on the ligand framework. But, very often this process involves laborious multistep ligand synthesis and repeating synthetic protocols. However, using redox non-innocent ligands involving oxidation and reduction of ligands can influence the Lewis acidic properties of the metal centre. In the example shown in Figure 1.1, an iridium complex is oxidized by silver tetrafluoroborate to form a cationic complex that contains a one-electron oxidized ligand-radical. This makes the iridium metal centre a stronger Lewis acid. Dihydrogen reacts with the cationic iridium complex to produce an adduct, which undergoes deprotonation by non-coordinating base 2,6-(*t*-Bu)$_2$C$_5$H$_3$N (2,6-di-*t*Bu-pyridine; TBP) to complete the catalytic cycle and reform the neutral iridium complex.

Strategy II: Noble metals (*e.g.*, Pd, Pt, Rh, Ir, etc.,) typically undergo 2e$^-$ oxidation or reduction steps in catalytic cycles to promote crucial oxidative addition and reductive elimination reactions. In comparison, abundant first row transition metals such as Fe, Ni can more easily engage in 1e$^-$ oxidation or reduction steps. Redox non-innocent ligands as electron-reservoir can play an important role to mimic reactivity of noble metals. In the example shown in Figure 1.1, Chirik and co-workers made significant progress in the application of this theory in [2+2]-cycloaddition reactions catalyzed by Fe^{II} complexes containing 2,6-diiminepyridines as electron-reservoir.[34]

Strategy III: In the above-mentioned strategies (I and II), redox non-innocent ligands were involved either by playing a “spectator” role by tuning electronic properties of the

metal or by acting as an electron reservoir; in both cases, the reactions that occur are metal-based. In other cases, however, "actor" behavior of redox non-innocent ligands was shown to play a much more prominent role in bond activation processes involving radical-type mechanisms. In the example shown in Figure 1.1, a bio-inspired iridium complex engages in cooperative substrate activation with both the metal and the radical-type redox-active ligand assisting in the catalytic oxidation to of an alcohol to an aldehyde.

Strategy IV: This strategy involves the direct use of redox non-innocent properties of a substrate itself, which effectively leads to substrate-centered radical species that often have a completely different reactivity and selectivity compared to analogous closed-shell intermediates. In the example shown in Figure 1.1, a non-heme Fe^{II} complex (S = 2) catalyzes the insertion of nitrenes into benzylic C−H bonds by stabilizing a nitrogen-containing substrate with radical character by coordination to the transition metal.[34]

1.2.2. Pincer Ligands – Ligand Design:

Chelating ligands form more stable complexes than monodentate ligands due to entropy considerations. Accordingly, they are harder to completely displace from the central metal atom. For example, when $[M(NH_3)_6]^{n+}$ is treated with three molecules of ethylenediamine ($H_2N\text{-}CH_2\text{-}CH_2\text{-}NH_2$; commonly referred as 'en'), the more stable complex $[M(en)_3]^{n+}$ will form, releasing six ammonia (NH_3) molecules. As the total number of particles increases from four to seven, this reaction is entropically favored which increases the equilibrium constant 10^5 times. Ethylenediaminetetracetic acid (EDTA) is used as a food preservative as it binds to free metal ions and prevent aerial oxidation.

A type of chelating ligand that has gained in popularity in recent decades is the so-called 'pincer' ligand. The term 'pincer' is derived from the Dutch word *tang* which is equivalent to wrench or spanner in English, and was first used in 1989 by van Koten to refer to a specific class of chelating, meridionally binding, tridentate ligands.[35] The term 'pincer ligand' has since come to emphasize the way in which ligands are tightly bound to the metal centre, with a central anionic carbon and two flanking donor arms binding strongly in a tridentate fashion. The first examples of pincer ligands (e.g., 1,3-bis[(di-*tert*-butylphosphino)methyl]- benzene $[PCP]^-$) were reported in the literature in 1976 by Bernard L. Shaw[36] and Gerard van Koten[37] in 1978 (Scheme 1.1). The nomenclature for these types of ligands is given by the donor atoms that are bound to the metal centre. For example, in the above case the three donor atoms are neutral phosphorous (L-type), anionic carbon (X-type) and neutral phosphorous (L-type), in short represented as $[PCP]^-$ pincer bound to the metal centre (Z-type). The most favorable ring size around the metal is five, although six membered rings are often observed.

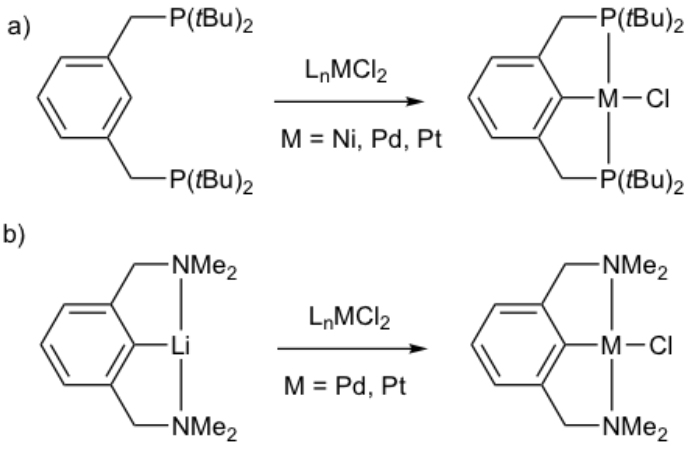

Scheme 1.1. Synthesis of a) Shaw's first metallo-PCP pincer ligand[36] and b) van Koten's metallo-NCN pincer ligand[37]

Pincer-like tridentate scaffolds typically bind with a meridional geometry to a metal centre with a central strong σ metal-ligand bond usually responsible for the unique stability of the resulting metal complexes. For comparison, non-pincer tripodal systems tend to prefer facial coordination. In general, a pincer ligand could have an aryl or alkyl backbone bound to a metal centre as shown in Figure 1.2. One of the main advantages to the 'pincer ligand' idea is that the ligand design is modular in nature, and the selection of each part can be used to tune the electronic and steric properties of the complex while maintaining a specific coordination geometry. For example, in a complex containing a 2,6-substituted aromatic ring, the steric hindrance around the metal can be controlled by introducing bulkier R groups and/or linker arms (Y) in order to directly affect the size of the bite angle, with minimum electronic impact. Alternatively, the electronics of the aromatic ring can be controlled via modification of Z in the *para* position with electron donating groups (EDGs -Me, *t*Bu) or electron withdrawing groups (EWGs $-CF_3$, NO_2). The central atom X (typically C or N) can furthermore be used to control the electronic properties of a pincer complex through its *trans* influence. Lastly, by employing chiral LR_n groups, chiral metal complexes can be synthesized for potential use in asymmetric catalysis.

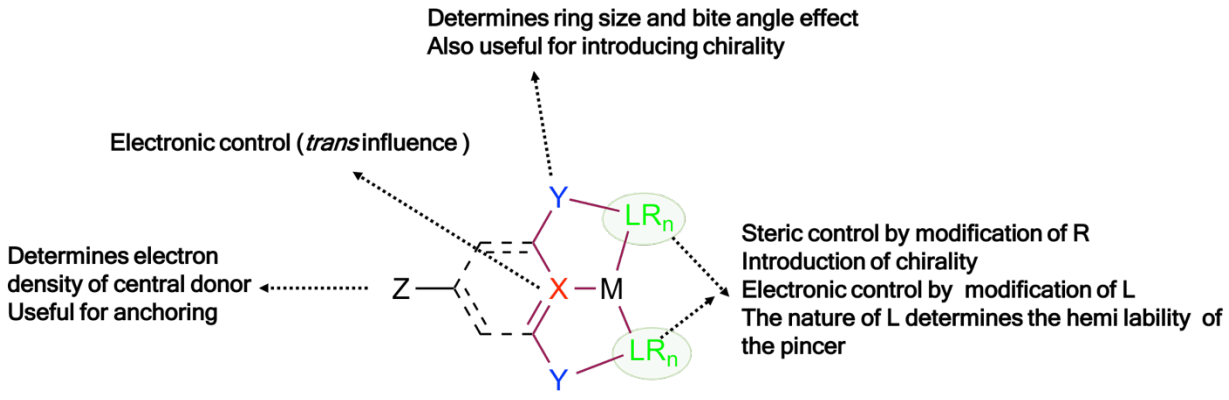

Figure 1.2. The general representation of a 'pincer' ligand bound to the metal centre.[38]

In addition to the nature of the donor atoms (e.g., PCP), pincer ligands can be classified according to (a) their symmetry (palindromic and non-palindromic, Figure 1.3); and (b) the neutral or ionic nature of donor atoms (L-type, anionic X-type or Z-type). Both neutral and monoanionic pincers appear in popularly known ligand frameworks, with highly charged trianionic palindromic pincers used to stabilize high-valent metals. Recently non-palindromic pincers (e.g., NNP, PCN etc.,) have gathered more interest as they present advantages for fine-tuning electronic and steric properties for specific applications. Incorporation of monoanionic pincer ligand via a central aryl (C_5H_3) unit as the central unit of the pincer (as in the PCP or NCN examples shown in Scheme 1.1) can be accomplished via cyclometallation. Intramolecular activation of the central C-H bond is easier compared to intermolecular activation of an aryl CH in general, due to the presence of flanking donor arms. Alternatively, pyridinyl units (C_5H_3N) represent another common neutral central donor.

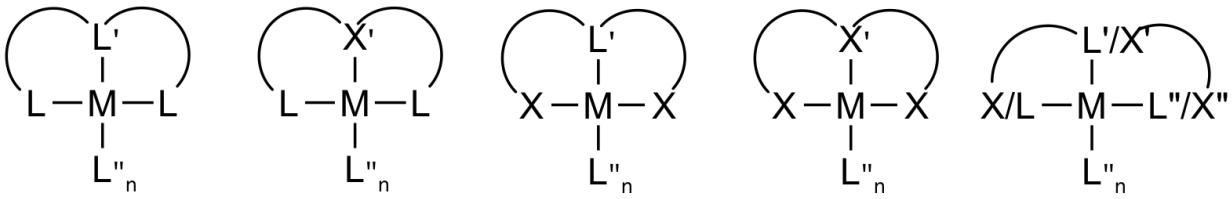

L = flanking neutral donor = PR_2,NR_2, OR, SR, C(from NHC)
L'R_2 = central neutral donor = pyridine, PR_3, NR_3, C (from NHC)
X = flanking anionic donor = O, NR, C (from phenyl)
X' = central anionic donor = C (from phenyl), SiR, N (imide), etc.,

Figure 1.3. Classification of pincer ligands based on symmetry and ionic nature.[38]

The multidentate, rigid nature of the pincer ligand means these typically form robust complexes that can withstand high temperatures and avoid decomposition, leading to high turnover numbers (TONs) in catalytic reactions. As noted, the geometrical and electronic properties can be adjusted through chemical modification of the ligand backbone and/or donor arms thus tuning the reactivity of the metal centres. In general, these complexes tend to have C_{2v} symmetry, but disturbing this symmetry yields numerous potential ligands that can provide additional parameters for tuning stereoselectivity in catalytic reactions. For example, chirality can be introduced onto the ligand arms with potential applications in the field of asymmetric catalysis. Alternatively, introducing labile donor atoms on the ligand framework can provide a vacant coordination site at the metal centre, while maintaining compound stability through the two remaining ligating moieties.[39,40,41] All told, the versatile coordination chemistry of pincers has attracted scientists from different fields with application in C-H, C-C bond activation, small molecule activation, C-C, C-N coupling reactions, alkane hydrogenation and dehydrogenation reactions,[42] understanding mechanisms,[43] optoelectronics, polymer,[44] and pharmaceutical industry applications and many more. Figure 1.4 reflects the works of scientists like Michael Fryzuk,[45] David Milstein,[46] Robert Morris,[47] Oleg Ozerov,[48] Maurice Brookhart,[42] Alan Goldman,[49] Xile Hu,[50] Karl Kirchner,[51] and many others who have extensively contributed and developed pincers for earlier mentioned applications.[26,52]

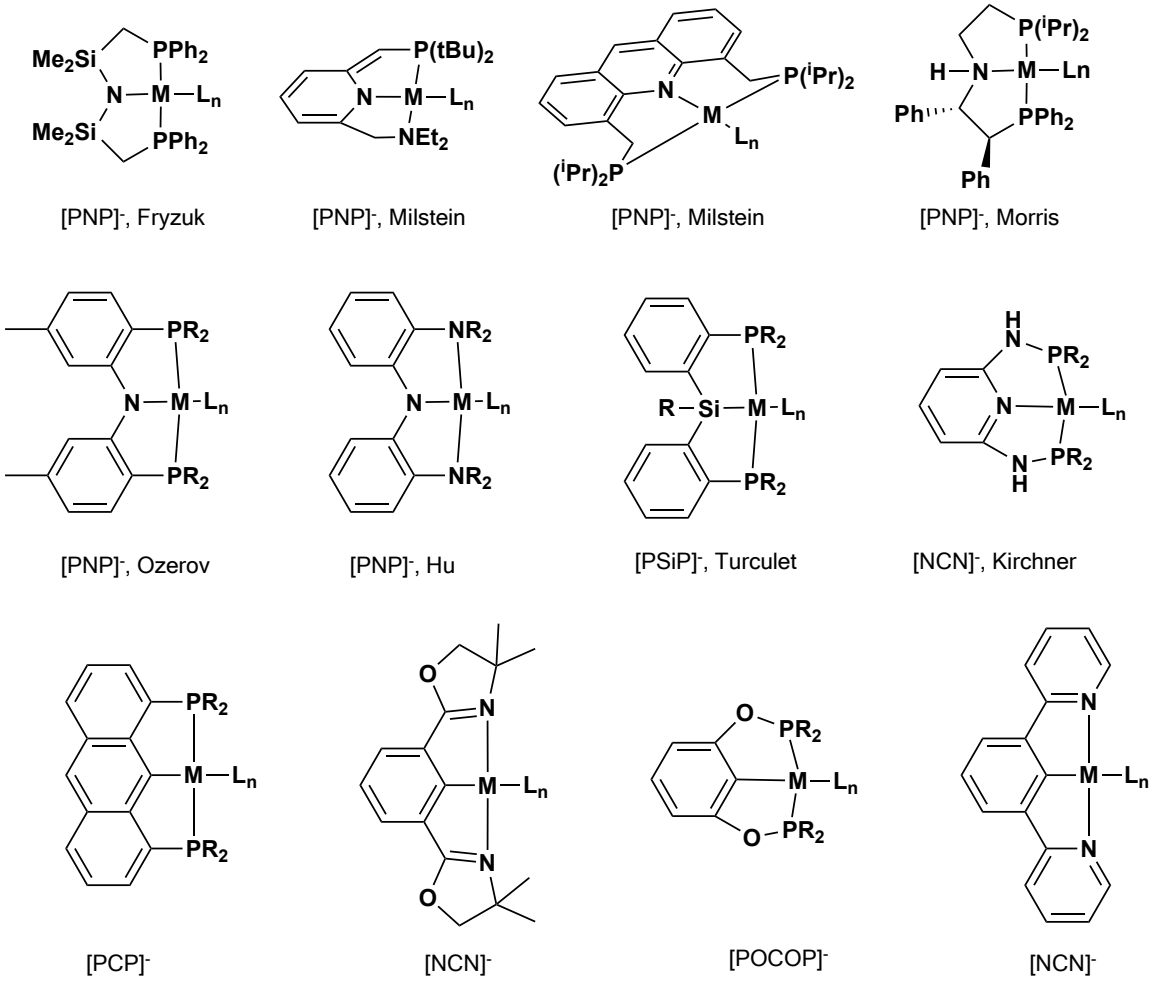

Figure 1.4. Examples of popular 'pincer' complexes in organometallic chemistry and organic synthesis.

1.3. Anionic *N^N^-N* Pincer Ligands – Applications in Catalysis:

As part of my PhD thesis, I have focused on the design, construction and evaluation of monoanionic symmetric/asymmetric *N^N^-N* tridentate 'pincer' type ligand motifs and their coordination complexes of Group 10 metals in catalysis and optoelectronic applications. The most common types of palindromic/non-palindromic ligand frameworks

that either contain pyridine or *N*-heterocycles, alkyl or aryl arms containing nitrogen donor atoms are shown in Figure 1.5. In this work, the pincer ligands under investigation comprise a central anionic (X-type) *N*-donor atom that is bound covalently to the metal centre (Z-type) and two neutral (L-type) *N*-donor atoms or *N*-heterocyclic units. The use of such *N*^*N*^-*N* tridentate 'pincer' type ligand frameworks began in the early 1990s, and since then many modifications of the ligand design have been reported, introducing innocent/non-innocent donor arms.

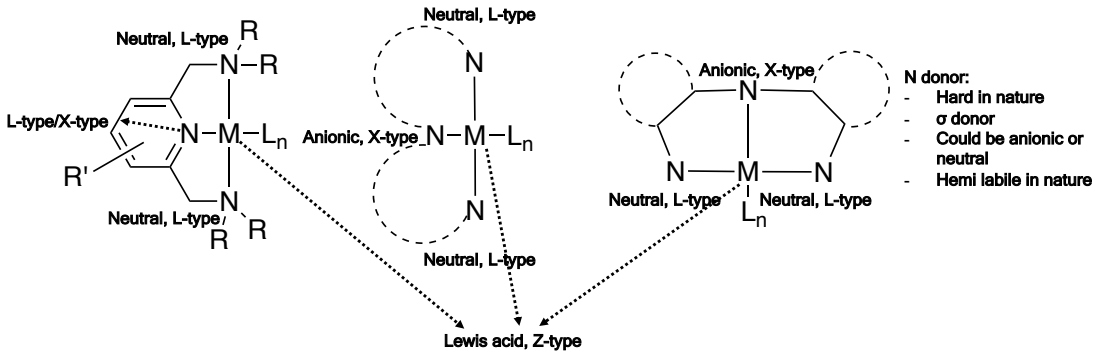

Figure 1.5. Ligand frameworks showing *N*^*N*^-*N* tridentate 'pincer' motifs.

Shown in Figure 1.6 are a few examples of *N*^*N*^-*N* tridentate pincer ligands. *N*-donor atoms are considered 'hard' Lewis bases in nature, preferring to bind hard metals and so when bound to softer transition metals, can exhibit hemilability to open an extra vacant site during the process of a catalytic cycle. Unlike phosphorus donor arms, sp^2-N centres are not as prone to oxidation. The above-mentioned ligand frameworks have been found to be very useful in the field of organometallic and coordination chemistry,[53,54] as active catalysts for C-C coupling reactions hydrosilylation of alkenes,[50] olefin polymerization,[55,56,57] in asymmetric catalysis like enantioselective aziridations and

alkylations, reduction of aldehydes to chiral alcohols,[41] for their luminescence properties, and in many other applications.[33,58]

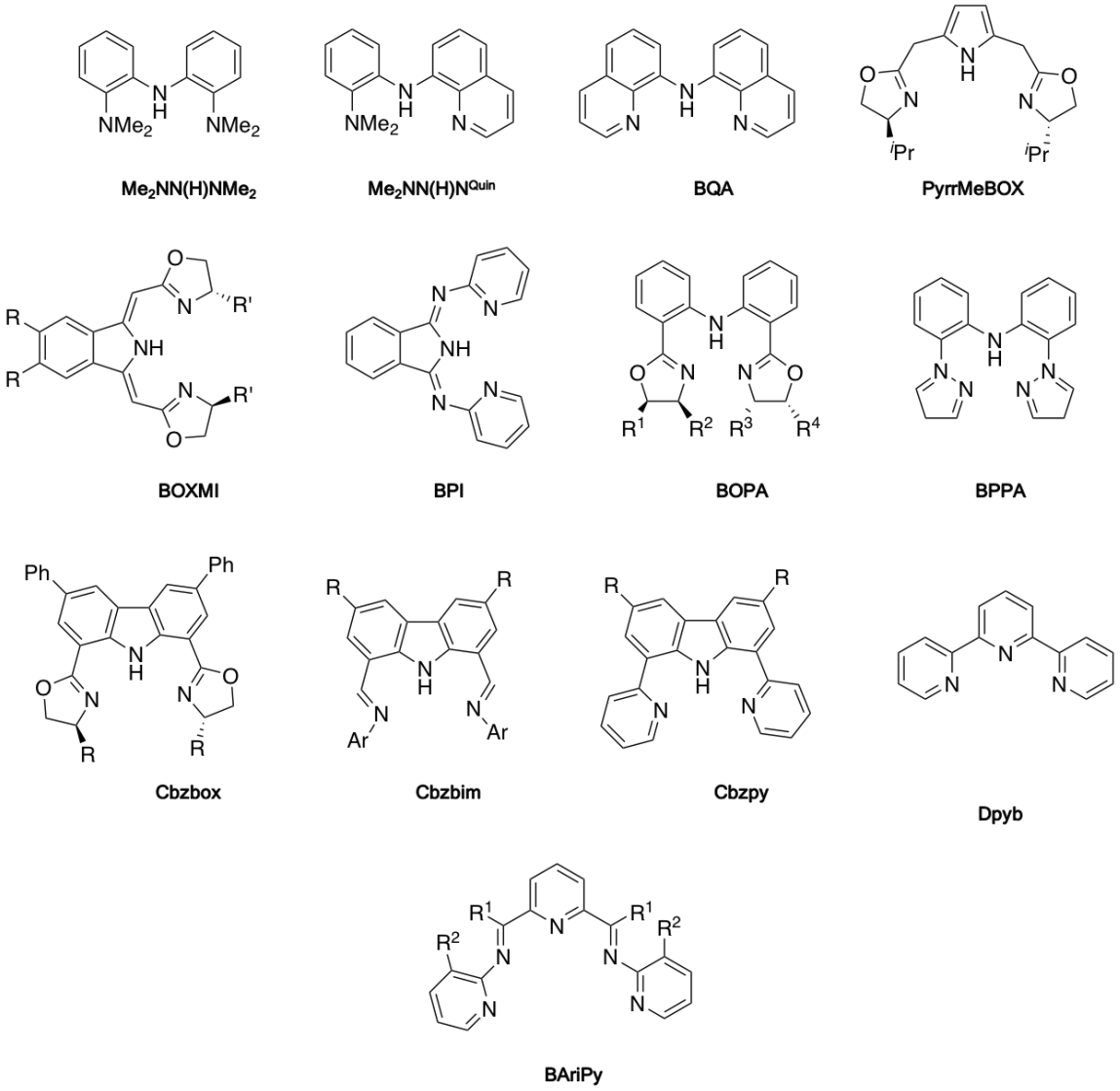

Figure 1.6. Selected examples of monoanionic *N^N^N* tridentate pincer ligands

van Koten and coworkers isolated nitrogen (N_2) bridged ruthenium complexes such as [{$RuCl_2(\eta^3$-NN′N)}$_2(\mu$-N_2)] (**1**).[59] When treated with alkene at room temperature, ruthenium-alkenes such as *mer*,*trans*-[$RuCl_2(\eta^3$-NN′N)(η^2-RCH_2=CH_2)] (**2**) can be isolated, as shown in Scheme 1.2.[60] Such N_2-bridged complexes have the potential to act

as catalysts in the synthesis of piperidines and piperizines via the (cyclo)alkylation of aromatic imines and alcohols.[61]

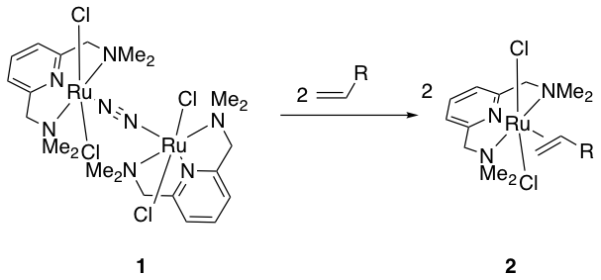

Scheme 1.2. Reaction of N_2-bridged ruthenium complex **1** with alkene.

The carbazolyl/bis(imine) (**Cbzbim**) *N^N^N* pincer ligand shown in Figure 1.6 plays an important role in enabling isolation of aqua complexes of palladium and platinum [(*N^N^N*)M(OH_2)]OTf (**4**) through the reaction of (*N^N^N*)MOTf (**3**) (M = Pd, Pt) complex with water. In these reactions, the pincer supports and stabilizes the Group 10 metal centre, which has an incoming water displace a weakly coordinating triflate (OTf^-; trifluoromethane sulfonate) ion from the metal centre as shown in Scheme 1.3. This reactivity was not observed in the same reaction with an analogous (*P^N^P*)MOTf complex, highlighting the importance of the ligand.[62] In the case of palladium, the triflato complex **3** can be regenerated by either applying vacuum or molecular sieves; this reversibility was not observed with platinum.[63]

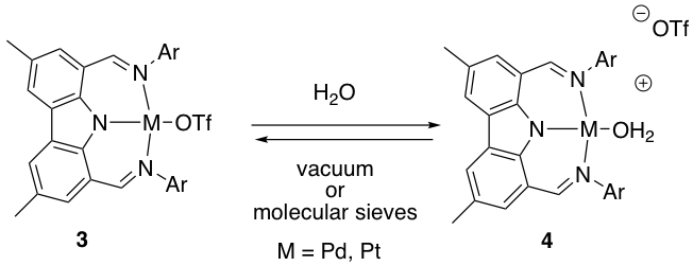

Scheme. 1.3. Reaction of (NNN)MOTf (**3**), M = Pd, Pt complex with water

Xile Hu and co-workers have designed the synthesis of "N_2N" type pincer ligands (e.g., ^{Me}**NN(H)N**^{Me}; Figure 1.6) and extensively studied the coordination chemistry and reactivity of their late transition metal complexes. The nickel (II) complex of this N_2N ligand, known as 'nickamine', has proven to be an excellent catalyst design for various C-C coupling reactions, especially those involving challenging non-activated electrophiles prone to *β*-hydride elimination. Some coupling reactions involving sp^3-sp^3, sp^3-sp^2, sp^3-sp, and the hydrosilylation of alkenes mediated by nickamine[50] are shown in Scheme 1.4.

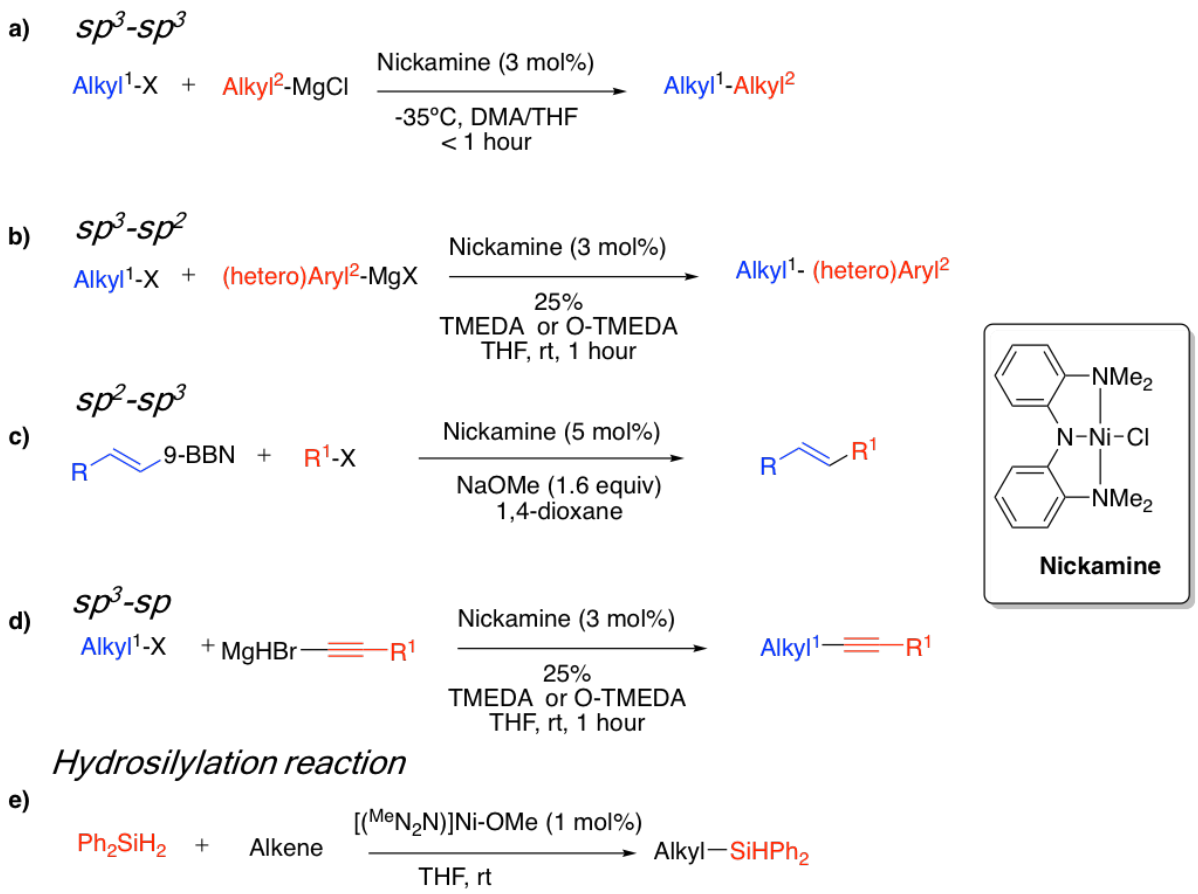

Scheme 1.4. Various coupling reactions mediated by the 'nickamine' catalyst.

Asymmetric C-C coupling reactions are important for synthesizing various compounds relevant to natural product synthesis and pharmaceutical industry applications.

One such reaction is the chromium-catalyzed Nozaki-Hiyama-Kishi (NHK) reaction. This involves the addition of allyl, propargyl or allenyl nucleophiles to aldehyde substrates. For these reactions, *N^N^N* pincer type ligands like Cbzbox, BOPA, BOXMI (as shown in Figure 1.6) are found to be very promising with >95% yields when used along with chromium chloride in the NHK reactions of allylic halides with aldehydes as shown in Scheme 1.5.

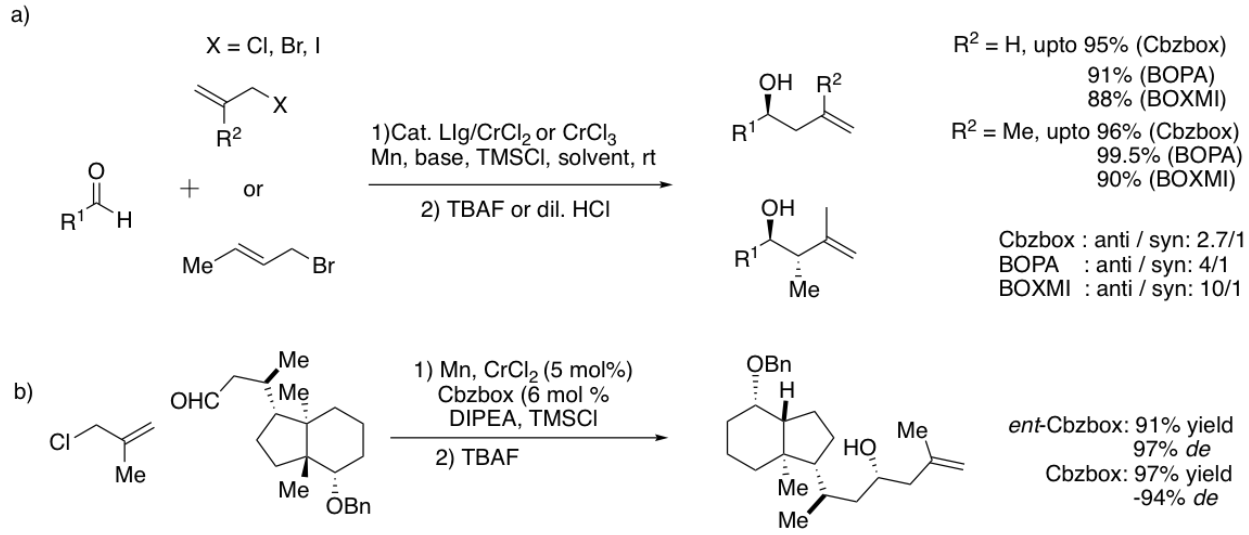

Scheme 1.5. a) Cr-NNN pincers catalyzed asymmetric NHK reactions. b) Synthesis of calcitriol lactone (natural product) using chiral NNN pincer ligands.[41]

Another notable application of Ni pincer complexes is the hydrosilylation of alkenes using less volatile alkoxyhydrosilanes in place of more commonly used gaseous alkylhydrosilanes such as Me_2SiH_2, $MeSiH_3$, and SiH_4. These latter compounds are flammable and tough to handle during the reactions to synthesize alkyl silanes. Xile Hu and his co-workers found out that Ni(II)amido(bisoxazoline)Cl (BOPA as shown in Figure 1.6) efficient catalyzes the hydrosilylation of alkenes with alkoxy hydroxysilanes in the presence catalytic amount of base producing alkyl silanes rather than alkoxysilanes

(Scheme 1.6). Further mechanistic investigations suggested hydrosilylation first occurs, followed by base-catalyzed disproportionation of two alkoxysilanes to give a dihydrosilane, and then conventional hydrosilylation with this dihydrosilane.[64, 50]

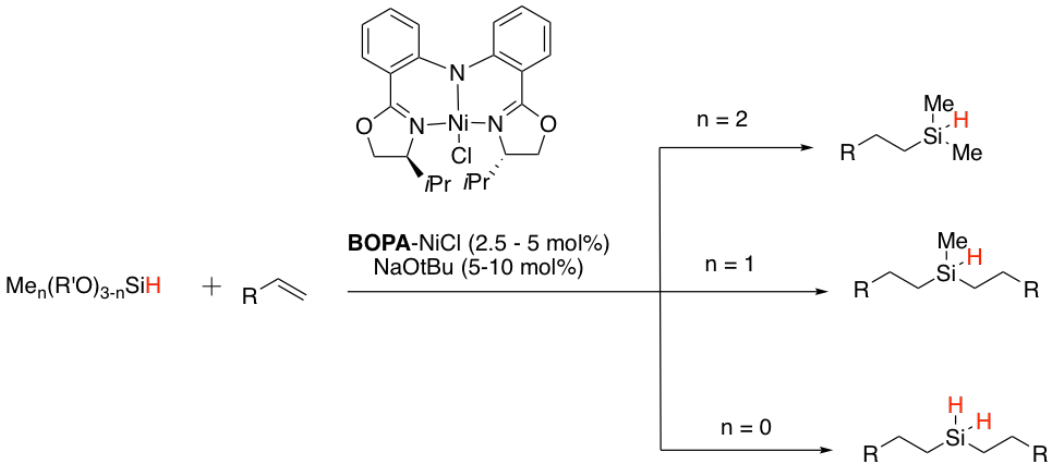

Scheme 1.6. Synthesis of alkyl hydrosilanes via hydrosilylation of alkenes with alkoxy hydrosilanes.[50]

There are many interesting applications of different *N^N^-N* pincer type ligands in catalysis for hydrosilylation of ketones,[65] hydrogenation/ hydrohydrazidation of aliphatic terminal alkynes,[66] N-N bond cleavage reactions,[67] carbon dioxide reduction[68] and so many others. As the area monoanionic *N^N^-N* pincer type ligands has broad scope and yet to be explored further, my research was focused on designing, construction of new pincer ligand motifs bearing phenanthridine as part of the ligand.

1.4. Phenanthridine – Relevance and Applications:

1.4.1. Phenanthridine:

Phenanthridine is a 14π electron aromatic *N*-heterocycle, annulated tricyclic species with extended π-conjugation. It has a broad range of applications in various fields of chemistry,[69,70] including industrial applications.[71] Phenanthridine is a structural isomer of acridine, and analogous to phenanthrene but with a C=N ('imine') bond at position 5 (Figure 1.7). The compound is white in color and sparingly soluble in water. It can be crystallized from ethanol as needles.[72] Phenanthridine is thermally stable (melting point: 106 °C, boiling point 349 °C) with a p*K*a of 4.47 for its conjugate acid. Rademacher and his co-workers reported the first solid-state structure of phenanthridine (Figure 1.7). As expected from its Lewis structure, it is co-planar with a mean deviation at C=N of only 0.002 Å from the mean plane. As the compound is a extended π-conjugated system, it could possibly exhibit π-π stacking interactions making it sparingly soluble in organic solvents.[72] Another interesting feature of phenanthridine is its different properties compared to pyridine, quinoline, and acridine. For example, the C=N subunit has emphasized 'imine' character. The imine proton (*H*C=N) appears far downfield around 9.27 ppm in the ^{1}H NMR spectra. In comparison, in pyridine this same signal resonates at 8.6 ppm. As a result, the C=N (imine) bond of phenanthridine can be easily reduced to a C-N single bond, forming dihydrophenanthridine. This reaction is reversible and so dihydrophenanthridine/phenanthridine can be rearomatized/dearomatized under the right conditions.[74] Compared with phenanthrene and acridine (C_{2v}), phenanthridine has a lower symmetry (*Cs*) and shows efficient fluorescence in solution. DFT studies on free phenanthridine suggests the energy gap between HOMO and LUMO to be 2.98 eV. The

HOMO is distributed across the phenanthridine ring while the LUMO is localized on the C=N (imine) bond, making it a Lewis acidic site with the rest of the ring a π-donor.[75]

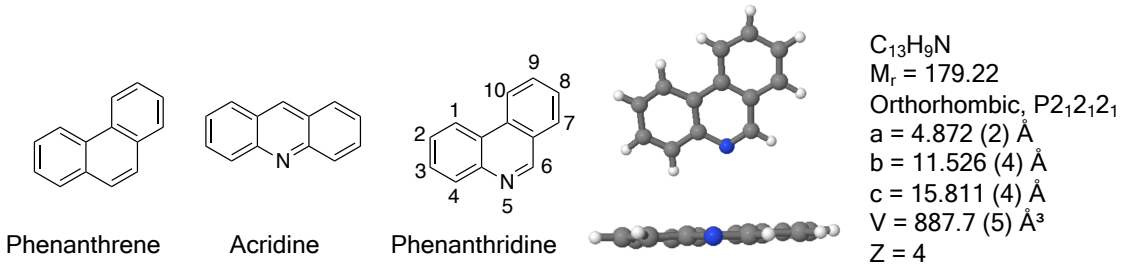

Figure 1.7. Crystal structure of phenanthridine.

Phenanthridine was first synthesized through pyrolysis of benzylidene-aniline, a condensation product of benzaldehyde and aniline, at bright red heat in 1889 by Pictet and Ankersmit.[76] Later many groups came up with different approaches to isolate phenanthridines in good yields. For example, Gronowtiz made phenanthridine by the reaction of 2-bromoacetanilide and 2-formylphenyboronic acid in the presence of $Pd(PPh_3)_4$, the reaction undergoes C-C Suzuki coupling followed by intermolecular amination followed by elimination of acetic acid in the presence of HCl to give the corresponding product with 89% yield as shown in Scheme 1.7.[77]

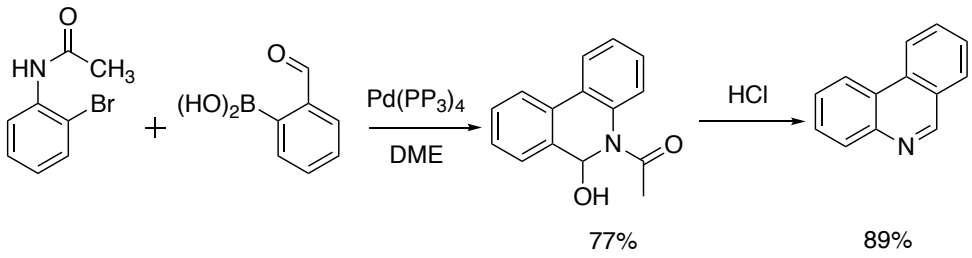

Scheme 1.7. Synthesis of phenanthridine in a two-step process.

Following the discovery of the trypanocidal activity of phenanthridines, synthesis of non-functional and functionalized phenanthridines became the focus of a number of research groups. These efforts involve synthetic routes including Suzuki coupling followed by condensation,[78] cobalt-catalyzed radical cyclization of isocyanides,[79] Grignard-based procedures, radical aromatic cyclization pathways,[80] metal free conditions[81] and many other organic reactions. A selection of synthetic routes to functionalized phenanthridines is shown in Scheme 1.8.[82-85]

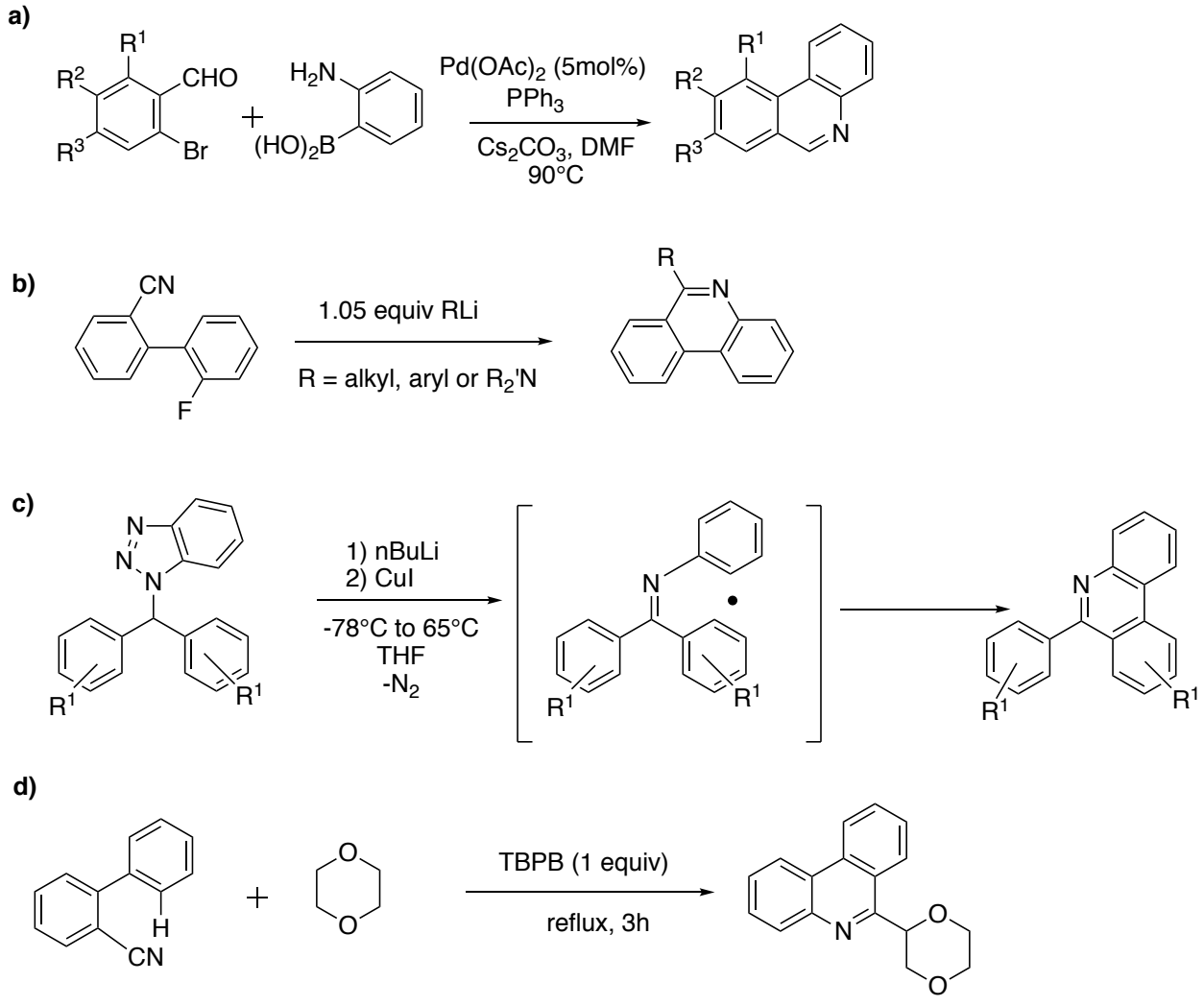

Scheme 1.8. Various synthetic routes to functionalized phenanthridines.

As discussed briefly above phenanthridine has unique properties due to its low symmetry (C_s) when compared to pyridine, quinoline, and acridine. When corresponding bond lengths are compared to one another as shown in Figure 1.8, phenanthridine has significantly shorter C-N bond length (1.29 Å) compared to in other *N*-heterocycles, which is close to an isolated imine bond.

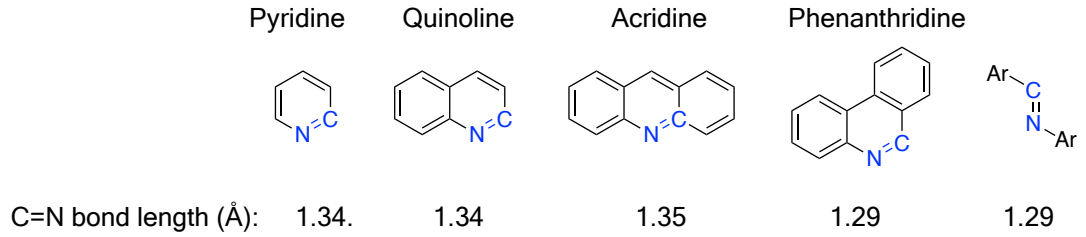

Figure 1.8. Bond lengths of C=N (imine) subunit for various N-heterocycles.[75]

Similarly, when the LUMO energy is calculated upon systematic π-extension moving from pyridine to phenanthridine, we can observe a significant energy difference as shown in Figure 1.9, which makes phenanthridine unique and interesting as a potential ligand arm to incorporate into monoanionic *N^N^-N* pincer ligand frameworks to explore further properties when bound to a metal centre.

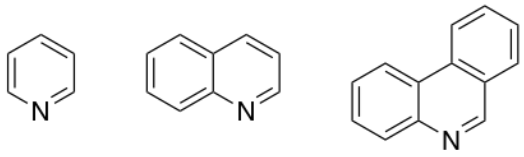

LUMO Energy	Pyridine	Quinoline	Phenanthridine
eV	0.14	-0.47	-0.60

Figure 1.9. Effect of systematic π-extension on LUMO energy.[86]

1.4.2. Applications of Phenanthridine:

Aromatic benzannulated π-extended functionalized/non-functionalized phenanthridines and phenanthridine derivatives have found a wide range of applications in various areas. In 1938, an article published by Walls[87] reported the outstanding trypanocidal activity of phenanthridinium compounds which caught the attention of scientists and prompted further exploration into phenanthridine derivatives. One such derivative is 3,8-diamino-5-ethyl-6-phenylphenanthridinium, now known as ethidium bromide (EB). EB and its close analogue propidium iodide exhibit red fluorescence in hydrophobic environments. Both have been used as the gold-standard DNA- and RNA fluorescent markers. Their planar structures and aromatic surface area make them perfect intercalators studying for DNA and RNA, also play an important role in aromatic and electrostatic interactions with polynucleotides as shown in Figure 1.10 and Scheme 1.9. Apart from fluorescent marker ability, ethidium bromide also exhibits interesting anti-parasitic activity, along with anti-tumor activity both *in vivo* and *in vitro*.[82, 89] Lastly, it might be noted that examples of naturally occurring alkaloids containing benzo-fused phenanthridines are also known, such as fagaronine, nitidine, chelerythrine, and sanguinarine which all show a variety of pharmacological applications.[88] In brief, phenanthridine and its derivatives have diverse applications in bioimaging,[90] sensors,[91] and as ligand in catalysis,[92] and in photo-emissive materials.[93]

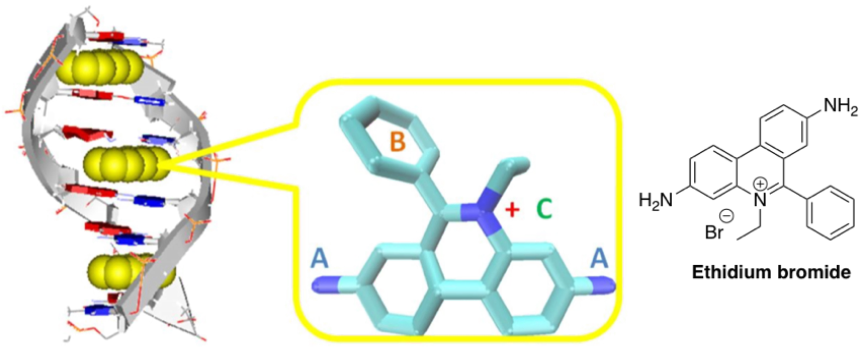

Figure 1.10. Schematic presentation of intercalative binding mode of ethidium bromide. Graphic adapted from reference.[82]

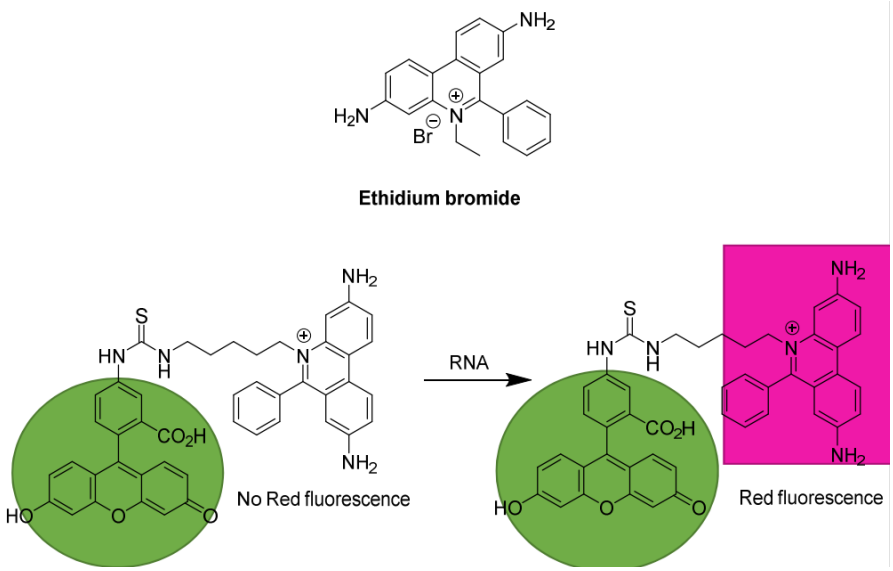

Scheme 1.9. Application of ethidium bromide for cell imaging in RNA.[89]

Some other applications of phenanthridines include phenanthridine moieties tetherered to metal complexes as molecular probes for physiologically differentiation between adenosine triphosphate (ATP), adenosine diphosphate (ADP) and adenosine monophosphate (AMP). These systems are used to investigate enzymatic mechanisms.[94] For example, Tb-DOTAm-Phen contains a macrocyclic polyaminocarboxylate terbium

complex conjugated to phenanthridine. This molecule can serve as molecular probe to distinguish three adenosine nucleotides (ATP, ADP, AMP; Scheme 1.10).

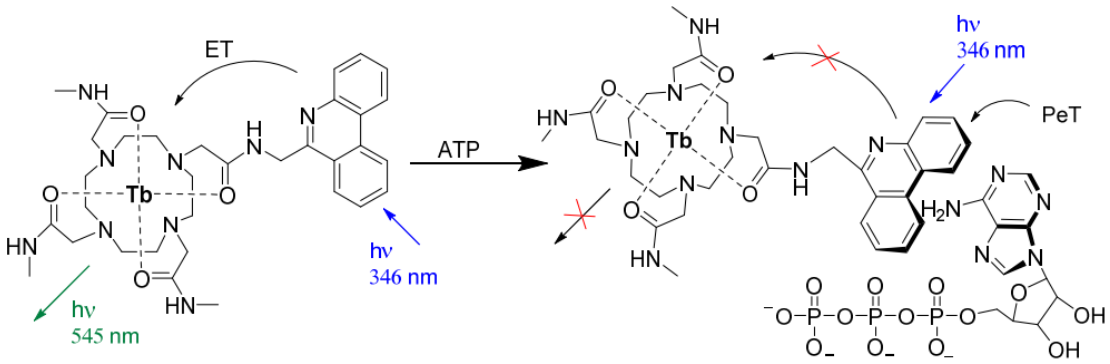

Scheme 1.10. Tb-DOTAm-Phen metal complex in action as ATP sensor.[94]

Platinum(II) metal complexes have been known to be excellent anti-cancer agents for almost 40 years, among which cisplatin [*cis*-($Pt(NH_3)_2Cl_2$] is the most popular for the treatment of testicular cancer patients.[95] When one ammonia (NH_3) ligand in cisplatin is replaced with a pyridine, pyriplatin was synthesized, which improved the efficacy and discarded the side effects from cisplatin. Similarily, phenanthriplatin was synthesized by replacing one ammonia molecule with phenanthridine (Figure 1.11). Phenanthriplatin is a monofunctional DNA-binding anticancer drug that binds DNA at single site inducing less distortion to the double helix.[96] It is chiral in nature,[97] and exhibits significantly high antitumor activity compared to cisplatin and pyriplatin, cellular uptake of phenanthriplatin is much higher due to hydrophobic nature from phenanthridine.

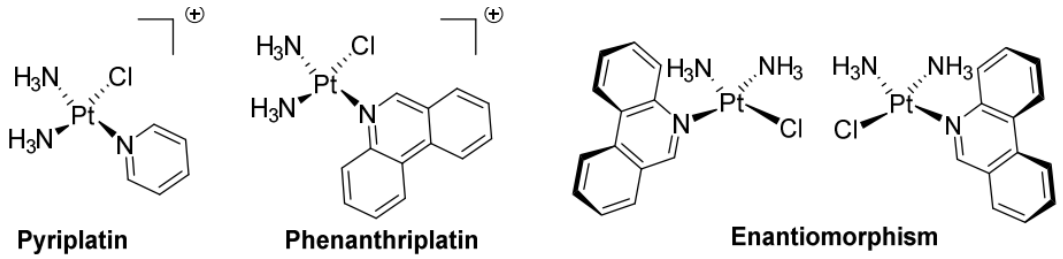

Figure 1.11. Popular platinum (II) metal complexes known anti-cancer agents.

Phenanthridine, as mentioned above, is luminescent in nature, which can lead to a great deal of applications when bound to metals. The resulting photo-emissive materials have potential uses in organometallic light-emitting devices (OLEDs). For example, Yang and co-workers have designed and synthesized two 6-phenanthridine-based heteroleptic iridium complexes $(TP\text{-}BQ)_2Ir(acac)$ and $(TPA\text{-}BQ)_2Ir(acac)$, both of which are deep-red emitters. By introducing phenanthridines, π-conjugation of the ligand is extended which causes emissions to shift to the deep red region [656 nm for $(TP\text{-}BQ)_2Ir(acac)$ and 665 nm for $(TPA\text{-}BQ)_2Ir(acac)$] (Figure 1.12).[98] Similarly, gold(III) complexes bearing phenanthridine also exhibit luminescent properties.[99]

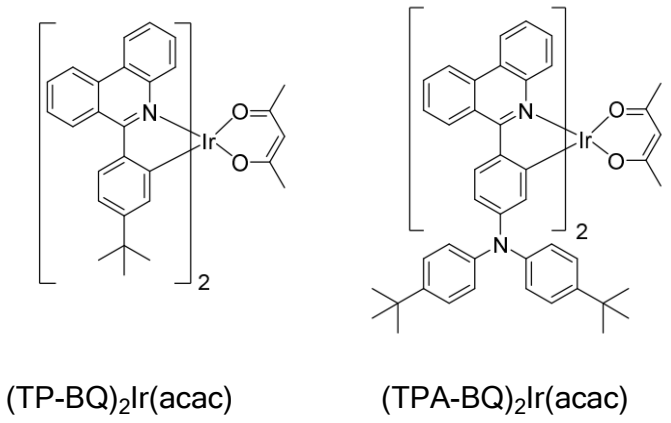

Figure 1.12. Cyclometalated iridium(III) complexes, deep red emmiters.

Phenanthridines were introduced to the tridentate *N^N^N* tridentate ligand framework by Meztler-Nolte and co-workers[100] to harness luminescent properties in bioimaging applications. The pincer *N^N^N* ligand system has two phenanthridinyl units tethered to an amide resulting a neutral *N^N^N* pincer (bis-phenanthridinyl)amine (bpm). A novel $Re^{I}(CO)_3$(R-bpm) metal complex was synthesized via reaction of $[Re(CO)_3(H_2O)_3]Br$ and the bpm ligand using a microwave. The resulting complexes were used for fluorescence imaging to study live cancer cells, and also a potential anti-cancer drug as shown in Scheme 1.11.[100, 101]

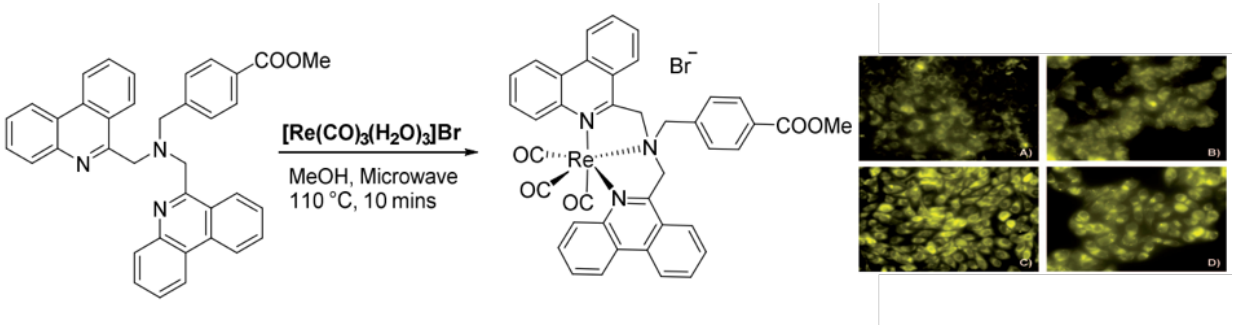

Scheme 1.11. Microwave assisted synthesis of a novel Re(I) metal complex, and fluorescence images of live cancer cells after 24 h incubation with metal complexes. Graphic adapted from reference.[100]

Naturally occurring coenzymes reduced nicotinamide adenine dinucleotide (NADH) and nicotinamide adenine dinucleotide phosphate (NAD(P)H) play important roles in reduction-oxidation (redox) metabolism in which they act as natural hydride shuttles during the metabolism. Compounds that mimic NADH/NAD(P)H are accordingly

of great interest for applications in asymmetric hydrogenation or reduction reactions involving a hydride transfer. They are highly enantioselective for 1,2-hydride shifts, commercially available, and can be easily regenerated using H_2. Phenanthridine is an example of a commercially available molecule that mimics NADH/NAD(P)H model. Zhou and co-workers have used commercially phenanthridines for asymmetric hydrogenation of benzoxazinones, benzoxazines, quinoxalines, and quinolines in the presence of Ru(II) metal complex in high yields and enantiomeric excess as shown in Scheme 1.12.[92] Recently, Beller and co-workers have used phenanthridine for biomimetic reduction of α-keto/α-imino esters in the presence of a earth abundant cheap commercially available iron catalyst.[102]

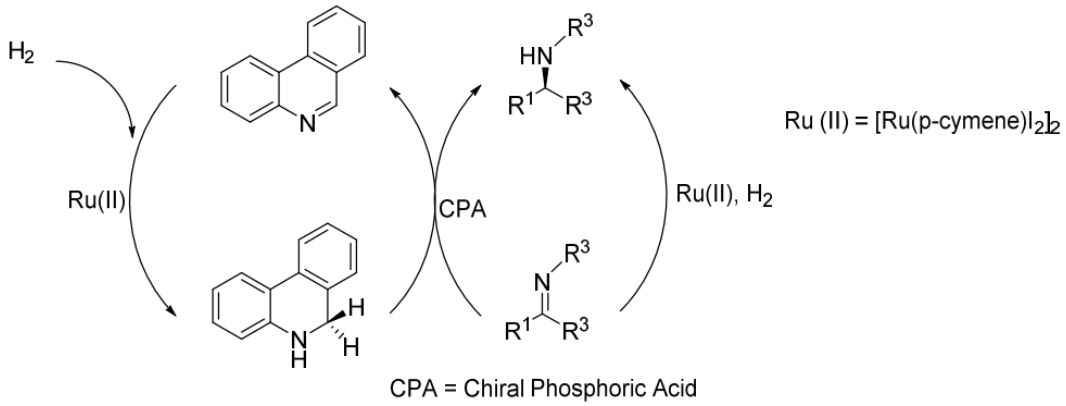

Scheme 1.12. A general catalytic cycle involving biomimetic reduction of imines using phenanthridine.

To summarize, phenanthridines have a broad scope of applications which harness its diverse reactivity and properties in materials science, anti-cancer drugs, photo emissive materials and catalysis and many more areas. So far, in the literature, however, only a few

research groups have focused on exploring phenanthridine as a ligand, making this area of research unique to pursue. Incorporating phenanthridines into *N^N^N* pincer would help explore further avenues of applications, for sustainable and green chemistry.

1.4.3. Herbert Group's Phenanthridine Research:

In late 2013, the Herbert research group began studying the incorporation of phenanthridine units into neutral bidentate *P^N*, monoanionic bidentate *N(H)^N*, monoanionic tridentate *N^N(H)^N* and monoanionic tridentate *N^N(H)^O* ligand motifs. This was done starting with the synthesis of functionalized phenanthridines as ligand precursors in a one-pot synthetic procedure. Outside of this work, and beyond what I described in the previous pages, not much research has otherwise been conducted into the applications of phenanthridine in coordination chemistry. Accordingly, I therefore take the opportunity to briefly discuss some of the results obtained by my colleagues based on phenanthridine to put my work as presented in this thesis into proper context.

As discussed earlier, phenanthridine is a commercially available molecule that mimics NADH/NAD(P)H model to reversibly generate dihydrophenanthridine in the presence of H_2 and metal centre. Our group was able to successfully synthesize dihydrophenanthridine from phenanthridine under metal-free electrochemical conditions, that occurs selectively at glassy carbon electrodes over longer timescales of potentiostatic electrolysis. The electrochemically generated dihyrophenanthridine is used for transfer hydrogenation of benzoxazines,[74] as shown in Scheme 1.13.

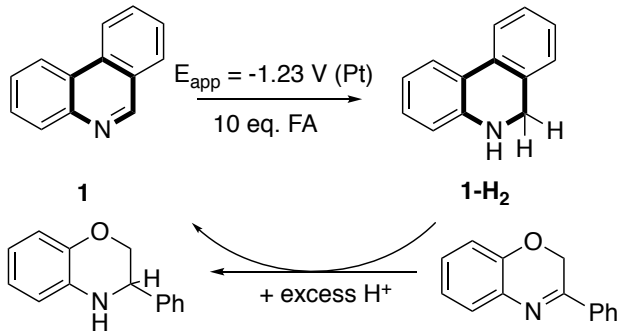

Scheme 1.13. Transfer hydrogenation of benzoxazines using electrochemically generated **1-H_2**

Our group has also reported the construction, synthesis and coordination of chemistry of (4-diphenylphosphino)phenanthridine (*P^N*) with late transitional metals like Ni(II), Cu(I) and Zn(II). To access the proligand, a synthetic route to 4-bromophananthridine was established by Pd-catalyzed C-C coupling between 2-formlyphenylboronic acid and 2,6-dibromoaniline followed by condensation at elevated temperatures is key. The ligand constitutes a neutral bidentate *P^N* that contains heterobifunctional hard/soft Lewis base, that contains both phosphine and phenanthridine donor units. The extended benzo-fused ligands when bound to Cu(I) and Zn(II) emit at 431nm and 382 nm respectively (Scheme 1.14).[103] The solid-state structure of Cu(1) complex has two [(Ph_2PNPhen)CuBr] units and is stabilized by dimerization into a butterfly-shaped [Cu_2Br_2] core.

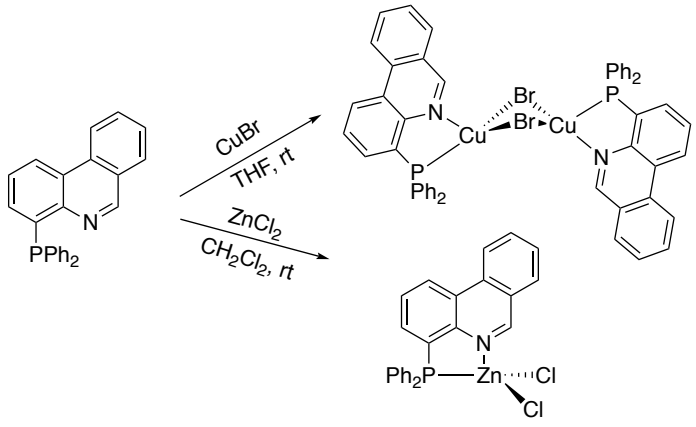

Scheme 1.14. Synthesis of emissive Cu(I) and Zn(II) metal complexes.

Similarly, phenanthridine-based bidentate (*N(H)^N*) ligands were designed to synthesize Zn(II) complexes. Examples of homoleptic Zn(II) amides were constructed using benzannulated 4-amidophenanthridine ligands as shown in Scheme 1.15.[104] The aminophenanthridine precursors were synthesized following procedures described earlier,[105] followed by Buchwald-Hartwig C-N coupling reactions at high temperatures to give proligands **L1** (4-(*N*-phenylamine)-2-tert-butylphenanthridine) and **L2** (2,6-dimethyl-4-(*N*-phenylamine)phenanthridine). Cyclic voltammetry studies show quasi-reversible oxidations on the electrochemical scale, both ligands (**L1**, **L2**) and zinc(II) (**1-Zn**, **2-Zn**) complexes exhibit ligand-to-ligand charge transfer (LLCT), an assignment supported by DFT and TD-DFT studies. Ligand **L1** and its complex **1-Zn** are both emissive, while **L2** and **2-Zn** complex are non-emissive, ascribed to methyl substitution at the C_6=N position of the phenanthridine.[104]

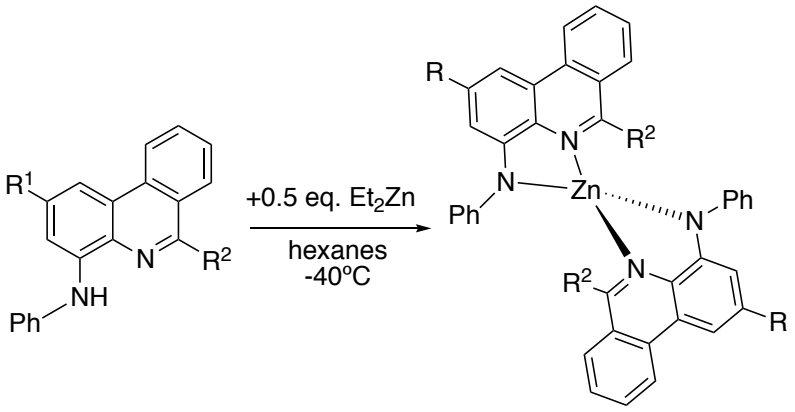

L1 R^1 = Me, R^2 = H
L2 R^1 = *t*Bu, R^2 = Me

1-Zn R^1 = Me, R^2 = H
2-Zn R^1 = *t*Bu, R^2 = Me

Scheme 1.15. synthesis of bidentate ($^{P}N(H)\text{^}N^{Ph}$) ligands and their corresponding Zn(II) complexes.[104]

As noted above, platinum(II) complexes like cisplatin and phenanthriplatin are established and promising anticancer drugs, respectively. We have reported the synthesis and coordination complexes of chelating *N^N(H)^O* tridentate ligand coordinated to platinum (Scheme 1.16). Complexes **1** and **2** show a superior *in vitro* therapeutic index compared with phenanthriplatin and cisplatin.[106]

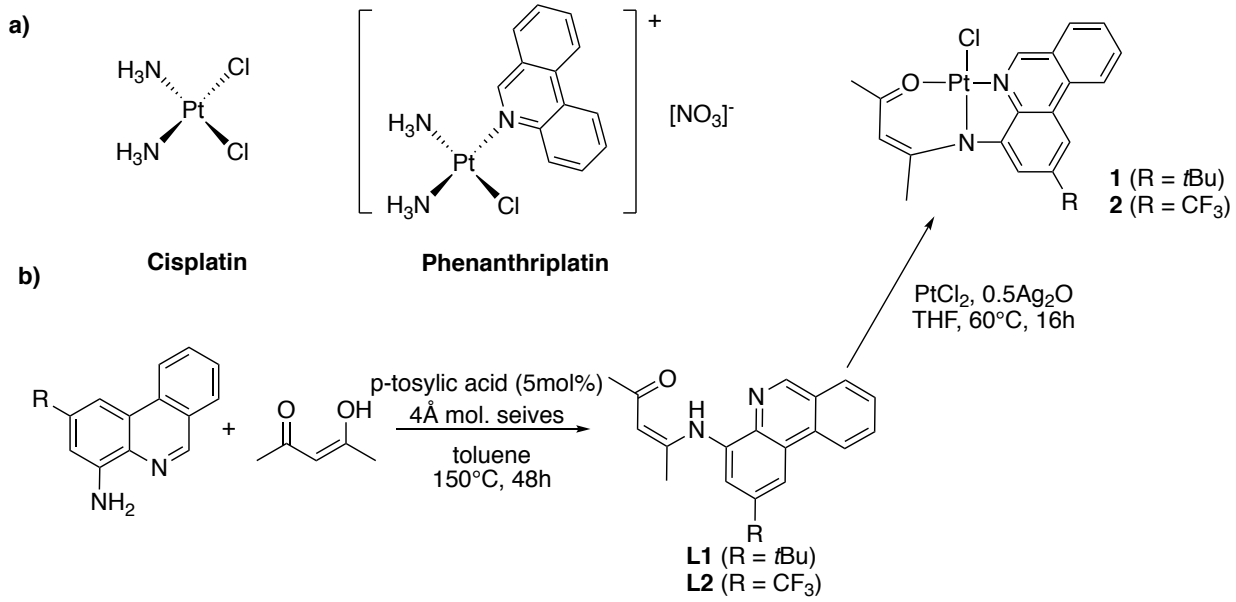

Scheme 1.16. a) structures of cisplatin, phenanthriplatin and phenanthridine based chelating *N^N(H)^O* ligand bound to Pt. b) synthesis of phenanthridine based *N^N(H)^O* proligands (**L1**, **L2**) and their platinum complexes **1-2**.[106]

Our group has also reported the use of phenanthridine containing *N^N(H)^N* pincers to synthesize pseudo-octahedral iron(II) coordination complexes with panchromatic absorption and long-lived CT excited states into nanosecond regime.[107] Other reported works from our group include synthesis of halide bridged dimeric Cu(I) complexes of the form $[(P\text{^}N)\text{-}Cu]_2(\mu\text{-}X)_2$ (X = Cl, Br, I) as shown partly in Scheme 1.14, with benzannulated bidentate pyridine/phosphine (*P^N*) ligands containing quinoline/phenanthridine. The reported complexes are phosphorescent in the solid-state. This report studies the effect of systematic π-extension on emission.[108] Isolated $(P\text{^}N)_2Cu(I)$ cations were also prepared with counter anions. We discovered a synergistic effect of counterion choice and ligand design that impacts the solid-state emission at room termperature.[109] Another interesting article was published on heteroleptic ruthenium

hydrido chloride complex synthesized bases on phenanthridine containing *P^N*, and its application as catalyst for synthesizing *N*-heterocycles like pyridines, quinolines, and pyrimidines via acceptorless dehydrogenative coupling.[110]

1.5. Description of Thesis and Acknowledgements:

As a PhD graduate student, my research was focused on designing phenanthridine-based, *N^N(H)^N* type proligands with both symmetric and asymmetric character, along with exploring the possibility of installing both electron donating groups (EDG) and electron withdrawing groups (EWG) at the donor arms. To synthesize proligands as shown in Scheme 1.1, first I have successfully managed to synthesize functionalized phenanthridines which are key ligand precursors. With these functionalized phenanthridines in hand, I have synthesized a broad range of ligands based on phenanthridines and quinolines as shown in Figure 1.13. In the forthcoming chapters, I would like to disclose and discuss the synthesis, coordination chemistry, and characterization of all the compounds using both solution and solid-state spectroscopic techniques, and their applications in photo-emissive materials and as effective catalysts for C-C of azoles and alkyl halides.

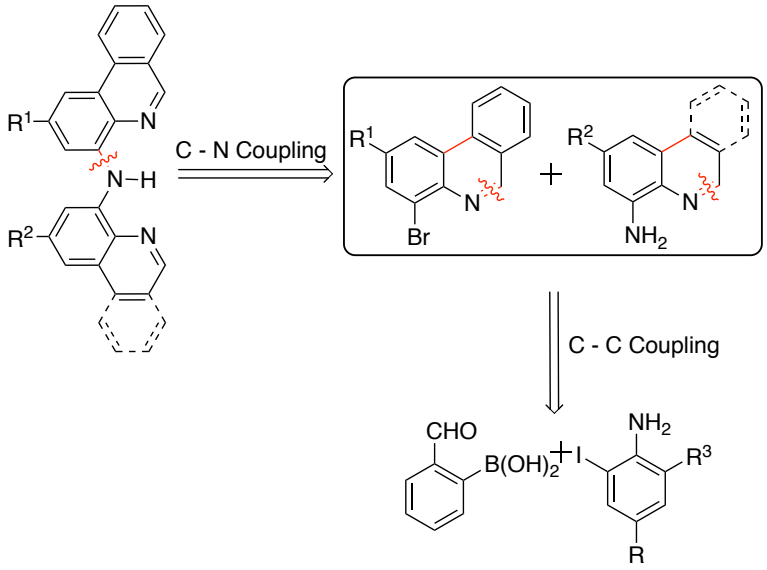

Scheme 1.17. A retrosynthetic approach to synthesize desired pincer ligand motifs.

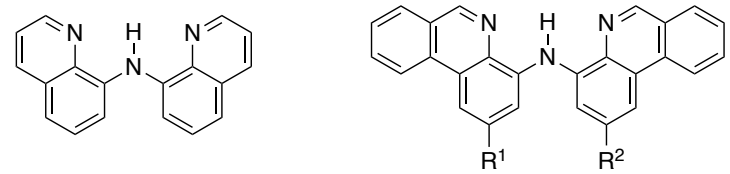

L1 (R^1 = H,R^2 = H)

L10 (R^1 = *t*Bu, R^2 = *t*Bu)
L11 (R^1 = CF_3, R^2 = CF_3)
L12 (R^1 = CF_3, R^2 = *t*Bu)

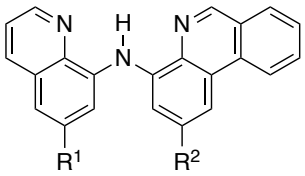

L2 (R^1 = H, R^2 = CH_3)
L4 (R^1 = H, R^2 = *t*Bu)
L7 (R^1 = H, R^2 = CF_3)
L8 (R^1 = CH_3, R^2 = *t*Bu)
L9 (R^1 = CH_3, R^2 = CF_3)

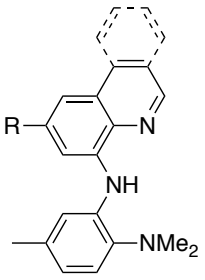

L13 (R = Me)
L14 (R = Me)
L15 (R = *t*Bu)
L16 (R = CF_3)

Figure 1.13. Series of ligands discussed in my PhD thesis.

1.5.1: Acknowledgements:

Chapter 1:

The introduction chapter was inspired from many research materials including books by R. H. Crabtree '*The Organometallic Chemistry of the Transition Metals, Seventh edition.; John Wiley & Sons, Inc.: Hoboken, NJ,* **2019** and B. D. Gupta, Anil J. Elias, *Basic Organometallic Chemistry*: *Concepts Syntheses and Applications,* Second edition.; Universities Press, **2013**. Apart from many research articles, the works of my colleagues Dr. Rajarshi Mondal and his PhD thesis, Jason D. Braun, Patrick K. Giesbrecht, Issiah B. Lozada and Dion Nemez were also consulted.

Chapter 2:

A form of this chapter was published as "Phenanthridine-Containing Pincer-like Amido Complexes of Nickel, Palladium, and Platinum" Mandapati, P.; Giesbrecht, P. K.; Davis, R. L.; Herbert, D. E. *Inorg. Chem.* **2017**, *56*, 3674–3685. I, Pavan Mandapati, have synthesized and characterized all the ligands and metal complexes reported in this chapter. Patrick K. Giesbrecht ran cyclic voltammetry experiments, while DFT calculations were done by Prof. Rebecca L. Davis. All the crystal structures were solved by Dr. David. E. Herbert. I am thankful to Dr. Mazdak Khajehpour for access to a UV-Visible spectrometer. The initial draft was written by myself, and later modified to publishing standard in collaboration with my supervisor, Dr. David. E. Herbert.

Chapter 3 and Chapter 4:

These chapters were assembled from work published in two different publications "Luminescent Platinum(II) Complexes of *N^N-^N* Amido Ligands with Benzannulated N-Heterocyclic Donor Arms: Quinolines Offer Unexpectedly Deeper Red Phosphorescence

than Phenanthridines" Mandapati, P.; Braun, J. D.; Killeen, C.; Davis, R. L.; Williams, G. A. J.; Herbert, D. E. *Inorg. Chem.* **2019**, *58*, 14808-14817; and "Deep-Red Luminescence from Platinum(II) Complexes of *N^N-^N*-Amido Ligands with Benzannulated N-Heterocyclic Donor Arms" Mandapati, P.; Braun, J. D.; Lozada, B. L; Williams, G. A. J.; Herbert, D. E. *Inorg. Chem.* **2020**, *59*, 12504–12517. I, Pavan Mandapati, synthesized and characterized all the ligands and metal complexes reported in this chapter. X-ray crystal structures were solved by Jason D. Braun and Dr. David E. Herbert, and elemental analysis was collected by Jason D. Braun. Charles Killeen, Prof. Rebecca L. Davis and Issiah B. Lozada performed DFT calculations. For photophysical experiments and analysis, we have collaborated with Prof. Gareth J. A. Williams at the University of Durham, UK. The initial draft of this chapter (in the form of both manuscripts) was written by myself, and later modified to publishing standard in collaboration with Jason D. Braun, Issiah B. Lozada and my supervisor, Dr. David. E. Herbert.

Chapter 5:

Parts of the chapter were published as "Catalytic C−H Bond Alkylation of Azoles with Alkyl Halides Mediated by Nickel(II) Complexes of Phenanthridine-Based N^N-^N Pincer Ligands" Mandapati, P.; Braun, J. D.; Sidhu, B. K.; Wilson, G.; Herbert, D. E. *Organometallics* **2020**, *39*, 1989-1997. I, Pavan Mandapati, synthesized and characterized all the ligands and metal complexes. Elemental analysis for all the published metal complexes, and all the X-ray quality crystal structures with publication standards were solved by Jason D. Braun and Dr. David. E. Herbert. I have collaborated with Baldeep K. Sidhu to separate and isolate pure coupled products from the catalysis reaction using my

Ni(II) complexes, using column chromatography techniques. I also have collaborated with Gabrielle Wilson during her summer project to stabilize the reaction condition for the catalysis reactions and GC methods. I am thankful to Dr. Mazdak Khajehpour for access to a UV-Visible spectrometer. Initial draft was written by myself, and later modified to publishing standard in collaboration with Jason D. Braun and my supervisor, Dr. David. E. Herbert.

1.6. References:

1. Crabtree, R. H. The Organometallic Chemistry of the Transition Metals, Seventh edition.; John Wiley & Sons, Inc.: Hoboken, NJ, **2019**.
2. Cadet de Gassicourt, L-C., *Math. Phys.* **1760**, *3*, 623.
3. Baeyer, A., *Ann. Chem. Pharm.* **1858**, *107*, 257–293.
4. Werner, H. *Landmarks in Organo-Transition Metal Chemistry: A Personal View*; Springer, 2009.
5. Zeise, W. C. *Ann. Phys. Chem.* **1827**, *9*, 632.
6. Sayferth, D. *Organometallics*, **2001**, *20*, 2940.
7. Gupta, B. D.; Elias, A. J. *Basic Organometallic Chemistry*: *Concepts Syntheses and Applicatons,* Second edition.; Universities Press, **2013**.
8. Hermann, W. A. *J. Organometal. Chem.,* **1990**, *383*, 21.
9. Rheinboldt, H. *J. Chem. Educ.,* **1950**, *27*, 476.
10. Cornils, B.; Herrmann, W. A.; Rasch, M.; *Angew. Chem. Ind. Ed.,* **1994**, *33*, 2144.
11. Wilkinson, G.; Rosenblum, M.; Whiting, M. C.; Woodward, R. B. *J. Am. Chem. Soc.,* **1952**, *74*, 2125.
12. Seyferth, D. *Organometallics*, **2002**, *21*, 2800.
13. Ziegler, K.; Natta, G.; Rosset, R. *Nature*, **1963**, *3344*, 503.
14. Fischer, E. O.; Massboel, A. *Angew. Chem.,* **1964**, *76*, 645.
15. Fischer, E. O.; Kries, G.; Kreiter, E. G.; Muller, J.; Huttner, G.; Lorenz, H. *Angew. Chem., Int. Ed.,* **1973**, *12*, 564.
16. Osborn, J. A.; Jardine, F. H.; Young, J. F. Wilkinson, G. *J. Chem. Soc.,* **1966**, 1711.

17. Hawkins, J. M.; Meyer, A.; Lewis, T. A.; Loven, S.; Hollander, F. J. *Science*, **1991**, *252*, 312.

18. Knowles, W. S.; Sabecky, M. J. *Chem. Comm.,* **1968**, 1445.

19. Sinn, H.; Kaminsky, W.; Voller, H. J.; Woldt, R. *Angew. Chem.,* **1980**, *92*, 396.

20. Schrock, R. R.; Murdzek, J. S.; Bazan G. C.; Robbins, J.; DiMare, M.; O'Regan, M. *J. Am. Chem. Soc.,* **1990**, *112*, 3875.

21. Schwab, P.; France, M. B.; Ziller, J. W.; Grubs, R. H. *Angew. Chem. Int. Ed.,* **1995**, *34*, 2039.

22. Goldman, A. S.; Roy, A. H.; Huang, Z.; Ahuja, R.; Schinski, W.; Brookhart, M. *Science*, **2006**, *312*, 258.

23. Nguyen, T.; Sutton, A. D.; Brynda, M.; Fettinger, I. C.; Long, G. J.; Power, P. P. *Science*, **2005**, *310*, 844.

24. Dieck, H. A.; Heck, R. F. *J. Org. Chem.,* **1975**, *40*, 1083.

25. Miyaura, N.; Yamada, K.; Suzuki, A. *Terahedron Lett.,* **1979**, *36*, 3437.

26. Valdes, H.; Garcia-Eleno, M. A.; Canseco-Gonzalez, D.; Morales-Morales, D. *ChemCatChem*, **2018**, *10*, 3136.

27. Matheu, R.; Ertem, M. Z.; Gimbert-Suriñach, C.; Sala, X.; Llobet, A. *Chem. Rev.,* **2019**, *119*, 3453.

28. Blakemore, J. D.; Crabtree, R. H.; Brudvig, G. W. *Chem. Rev.,* **2015**, *115*, 12974.

29. Chidambaram, G.; Milstein, D. *Chem. Rev.,* **2014**, *114*, 12024.

30. Ruiz-Castillo, P.; Buchwald, S. L. *Chem. Rev.,* **2016**, *116*, 12564.

31. Bolm, C. *Org. Lett.,* **2012**, *14*, 2925.

32. Ogoshi, T.; Yamagishi, T.; Nakamoto, Y. *Chem. Rev.,* **2016**, *116*, 7937.

33. Williams, J. A. G.; Develay, S.; Rochester, D. l.; Murphy, L. *Coord. Chem. Rev.,* **2008**, *252*, 2596.

34. Lyaskovskyy, V.; de Bruin, B. *ACS Catal.* **2012**, *2*, 270.

35. van Koten, G. *Pure Appl. Chem.,* **1989**, *61*, 1681.

36. Moulton, C. J.; Shaw, B. L. J. *Chem. Soc., Dalton Trans.* **1976**, 1020.

37. van Koten. G.; Timmer, K.; Noltes, J. G.; Spek, A. L. *J. Chem. Soc. Chem. Commun.* **1978**, 250.

38. Peris, E.; Crabtree, R. H. *Chem. Soc. Rev.,* **2018**, *47*, 1959.

39. Morales-Morales, D. *Rev. Soc. Quím. Méx.* **2004**, *48*, 338-346.

40. Spasyuk, D.; Smith, S.; Gusev, D. G. *Angew. Chem., Int. Ed.* **2012**, *51*, 2772.

41. van Koten, G.; Gossage, R. A. The Privileged Pincer-Metal platform: Coordination Chemistry & Applications; Springer, **2016**.

42. Choi, J.; MacArthur, A. H. R., Brookhart, M.; Goldman, A. S. *Chem. Rev.,* **2011**, *111*, 1761.

43. Morris, S. A.; Gusev, D. G. *Angew. Chem., Int. Ed.* **2017**, *56*, 6228.

44. Wang, Z.; Solan, G. A.; Zhang, Z.; Sun, W-H. *Coord. Chem. Rev.* **2018**, *363*, 92.

45. Fryzuk, M. D.; MacNeil, P. A. *J. Am. Chem. Soc.,* **1981**, *103*, 3592.

46. Gunanathan, C. Milstein, D. *Acc. Chem. Res.* **2011**, *44*, 588.

47. Seo, C. S. G.; Tannoux, T. Smith, S. A. M.; Lough, A. J.; Morris, R. H. *J. Org. Chem.,* **2019**, *84*, 12040.

48. Ozerov, O. V.; guo, C.; Papkov, V. A.; Foxman, B. M. *J. Am. Chem. Soc.,* **2004**, *126*, 4792.

49. Kumar, A.; Bhatti, T. A. Goldman, A. S. *Chem. Rev.,* **2017**, *117*, 12357.

50. Shi, R. Zhang, Z.; Hu, X. *Acc. Chem. Res.* **2019**, *52*, 1471.

51. Benito-Garragorri, D.; Kirchner, K. *Acc. Chem. Res.* **2008**, *41*, 201.

52. Dupont, J.; Consorti, C. S.; Spencer, J. *Chem. Rev.,* **2005**, *105*, 2527.

53. Peters, J. C.; Harkins, S. B.; Brown, S. D.; Day, M. W. *Inorg. Chem.,* **2001**, *40*, 5083.

54. Betley, T. A.; Qian, B. A.; Peters, J. C. *Inorg. Chem.,* **2008**, *47*, 11570.

55. Kwon, S. J.; Baek, J. W.; Lee, H. J.; Kim, T. J.; Ryu, J. Y.; Lee, J.; Shin, E. J.; Lee, K. S.; Lee, B. Y. *Molecules*, **2019**, *24*, 1676.

56. Gong, D.; Liu, W.; Chen, T.; Chen, Z-R.; Huang, K-W. *J. Mol. Catal. A: Chem.* **2014**, *395*, 100.

57. Wang, Z.; Solan, G. A.; Zhang, W.; Sun, W-H. *Coord. Chem. Rev.* **2018**, *363*, 92.

58. Puttock, E. V.; Walden, M. T.; Williams, J. A. G. *Coord. Chem. Rev.* **2018**, *367*, 127.

59. Abbenhuis, R. A. T. M.; del Rio, I.; Bergshoef, M. M.; Boersma, J.; Veldman, N.; Spek, A. L.; van Koten, G. *Inorg. Chem.* **1998**, *37*, 1749.

60. Abbenhuis, R. A. T. M.; Boersma, J.; van Koten, G. *J. Org. Chem.* **1998**, *63*, 4282.

61. del Rio, I.; Gossage, R. A.; Hannu, M. S.; Lutz, M.; Spek, A. L.; van Koten, G. *Organometallics*, **1999**, *18*, 1097.

62. Hollas, A. M.; Weixing Gu, W.; Bhuvanesh, N.; Ozerov, O. V. *Inorg. Chem.* **2001**, *50*, 3673.

63. DeMott, J. C.; Dekarske, J. R.; McCulloch, B. J.; Ozerov, O. V. *Inorg. Chem. Front.,* **2015**, *2*, 912.

64. Buslov, I.; Keller, S. C.; Hu, X. *Org. Lett.* **2016**, *18*, 1928.

65. Bleith, T.; Wadepohl, H.; Gade, L. H. *J. Am. Chem. Soc.* **2015**, *137*, 2456.

66. Chen, J.; Shen, X.; Lu, Z. *J. Am. Chem. Soc.* **2020**, *142*, 14455.

67. Milsmann, C.; Semproni, S. P.; Chirik, P. J. *J. Am. Chem. Soc.* **2014**, *136*, 12099.

68. Zeng, G.; Maeda, S.; Taketsugu, T.; Sakaki, S. *J. Am. Chem. Soc.* **2016**, *138*, 13481.

69. Umir, L.-M. *Beilstein J. Org. Chem.* **2014**, *10*, 2930.

70. Keller, P. A. Phenanthridines. *ChemInform*, **2005**, 36.

71. Keller, P. A. *Sci. Synth.:Oxidation of Phenanthridines* **2005**, *15*, 1094.

72. Brett, W. A.; Rademacher, P.; Boese, R. Redetermination of the structure of phenanthridine. *Acta Crystallogr., Sect. C: Cryst. Struct. Commun.* **1993**, *C49*, 1564–1566.

73. Pictet, A.; Ankersmit, H. *J. Ber.* **1989**, *22*, 3393.

74. Giesbrecht, P. K.; Nemez, D. B.; Herbert, D. E. *Chem. Commun.* **2018**, *54*, 338.

75. Benmachiche, A.; Zendaoui, S.-M.; Bouaoud, S.-E.; Zouchoune, B. *Int. J. Quantum. Chem.* **2013***, 113,* 985.

76. Theobald, R. S.; Schofield, K. *Chem. Rev.* **1950**, *46*, 170.

77. Yang, Y.; Hörnfeldt, A-B.; Gronowitz, S. *J. Heterocyclic. Chem.,* **1989**, *26*, 865.

78. Dhara, S.; Ghosh, M.; Ray, J. K. *Synlett*, **2013**, *24*, 2263.

79. Liu, X.; Wu, C.; Jing Zhang, J.; Shi, Y.; Zhang, S.; Geng, Y.; Tung, C-H.; Wang, W. *Org. Chem. Front.,* **2018**, *5*, 2997.

80. Sha, W.; Yu, J-T.; Jiang, Y.; Yang, H.; Cheng, J. *Chem. Commun.,* **2014**, *50*, 9179.

81. Cao, J-J.; Zhu, T-H.; Wang, S-Y.; Gu, Z-Y.; Wang, X.; Ji, S-J. *Chem. Commun.,* **2014**, *50*, 6439.

82. Tumir, L-M, Stojkovic, M. R.; Piatanida, I. *Beilstein J. Org. Chem.* **2014**, *10*, 2930.

83. Bao, X.; Yao, W.; Zhu, Q.; Xu, Y. *Eur. J. Org. Chem.* **2014**, 7443.

84. Chen, Y.; Li, F.; Bo, Z. *Macromolecules*, **2010**, *43*, 1349.

85. Pearson, R.; Zhang, S.; He, G.; Edwards, N.; Chen, G. *Beilstein J. Org. Chem.* **2013**, *9*, 891.

86. *Handbook of Heterocyclic Chemistry*, 3rd ed.; Katritzky, A. R., Series Ed.; Elsevier: Amsterdam, **2010**.

87. Browning, C. H.; Morgan, G. T.; Robb, J. V. M.; Walls, L. P. *J. Pathol. Bacteriol.* **1938**, *46*, 203.

88. Clement, B.; Weide, M.; Wolschendorf, U.; Kock, I. *Angew. Chem. Int. Ed.* **2005**, *44*, 635.

89. Stevens, N.; O'Connor, N.; Vishwasrao, H.; Samaroo, D.; Kandel, E. R.; Akins, D. L.; Drain, C. M.; Turro, N. J. *J. Am. Chem. Soc.* **2008**, *130*, 7182.

90. Raszeja, L.; Maghnouj, A.; Hahn, S.; Metzler-Nolte, Nils. *ChemBioChem*, **2011**, *12*, 371.

91. Bakić, M. T.; Jadreško, D.; Hrenar, T.; Horvat, G.; Požar, J.; Galić, N.; Sokol, V.; Tomaš, R.; Alihodžić, S.; Žinić, M.; et al. *RSC Adv.* **2015**, *5*, 23900.

92. Chen, Q.-A.; Gao, K.; Duan, Y.; Ye, Z.-S.; Shi, L.; Yang, Y.; Zhou, Y.-Gui. *J. Am. Chem. Soc.* **2012**, *134*, 2442.

93. Mondal, R.; Lozada, I. B.; Davis, R. L.; Williams, J. A. G.; Herbert, D. E. *J. Mater. Chem. C.* **2019**, *7*, 3772.

94. Weitz, E. A.; Chang, J. Y.; Rosenfield, A. H.; Pierre, V. C. *J. Am. Chem. Soc.* **2012**, *134*, 16099.

95. Johnstone, T. C.; Suntharalingam, K.; Lippard, S. J. *Chem. Rev.* **2016**, *116*, 3436.

96. Park, G. Y.; Wilson, J. J.; Song, Y.; Lippard, S. J. *Proc. Natl. Acad. Sci.* **2012**, *109*, 11987.

97. Johnstone, T. C.; Lippard, S. J. *J. Am. Chem. Soc.* **2014**, *136*, 2126.

98. Jiang, B.; Gu, Y.; Qin, J.; Ning, X.; Gong, S.; Xie, G.; Yang, Chuluo. *J. Mater. Chem. C* **2016**, *4*, 3492.

99. Alizadeh, R.; Hafezeffati, S.; Amani, V.; Khavasi, H. R.; Harms, K. *Monatsh Chem.* **2015**, *146*, 581.

100. Raszeja, L.; Maghnouj, A.; Hahn, S.; Metzler-Nolte, N. *ChemBioChem* **2011**, *12*, 371, 101.

101. König, M.; Siegmund, D.; Raszeja, L. J.; Prokop, A.; Metzler-Nolte, N. *Med. Chem. Commun.* **2018**, 173.

102. Lu, L.-Q.; Li, Y.; Junge, K.; Beller, Matthias. *Angew. Chem. Int. Ed.* **2013**, 52, 8382.

103. Mondal, R.; Giesbrecht, P. K.; Herbert, D. E. *Polyhedron* **2016**, *108*, 156.

104. Lozada, I. B.; Murray, T.; Herbert, D. E. *Polyhedron* **2019**, *161*, 261.

105. Mandapati, P.; Giesbrecht, P. K.; Davis, R. L.; Herbert, D. E. *Inorg. Chem.* **2017**, *56*, 3674.

106. Lozada I. B.; Huang, B.; Stilgenbauer, M.; Beach, T.; Qiu, Z.; Zheng, Y.; Herbert, D. E. *Dalton Trans.,* **2020**, *49*, 6557.

107. Braun, J. D.; Lozada, I. B.; Kolodziej, C.; Burda, C.; Newman, K. M. E.; van Lierop, J.; Davis, R. L.; Herbert, D. E. *Nature Chem.* **2019**, *11*, 1144.

108. Mondal, R.; Lozada, I. B.; Davis, R. L.; Williams, J. A. G.; Herbert, D. E. *Inorg. Chem.* **2018**, *57*, 4966.

109. Mondal, R.; Lozada, I. B.; Davis, R. L.; Williams, J. A. G.; Herbert, D. E. *J. Mater. Chem. C.* **2019**, *7*, 3772.

110. Mondal, R.; Herbert. D. E. *Organometallics* **2020**, *39*, 1310.

Chapter 2: Phenanthridine-Containing Pincer-like N^N⁻^N Amido Complexes of Nickel, Palladium and Platinum

2.1. Abstract:

Proligands based on *bis*(8-quinolinyl)amine (**L1**) were prepared containing one (**L2**) and two (**L3**) benzo-fused *N*-heterocyclic phenanthridinyl (3,4-benzoquinolinyl) units. Taken as a series, **L1**-**L3** provides a ligand template for exploring systematic π-extension in the context of tridentate pincer-like amido complexes of Group 10 metals (**L1-MCl**, **L2-MCl** and **L3-MCl**; **M** = Ni, Pd, Pt). Inclusion of phenanthridinyl units was enabled by development of a cross-coupling/condensation route to 6-unsubstituted, 4-substituted phenanthridines (**4-Br**, **4-NO$_2$**, **4-NH$_2$**) suitable for elaboration into the target ligand frameworks. Complexes **L1-MCl**, **L2-MCl** and **L3-MCl** are redox-active; electrochemistry and UV-Vis absorption spectroscopy were used to investigate the impact of π-extension on the electronic properties of the metal complexes. Unlike what is typically observed for benzannulated ligand-metal complexes, extending the π-system in metal complexes **L1-MCl** to **L2-MCl** to **L3-MCl** led to only a moderate red shift in the relative HOMO-LUMO gap as estimated by electrochemistry, and similarly subtle changes to the onset of the lowest energy absorption observed by UV-Vis spectroscopy. TD-DFT revealed that benzannulation significantly impacts the atomic contributions to the LUMO and LUMO+1 orbitals, altering the orbital contributions to the lowest energy transition but leaving the energy of this transition essentially unchanged.

2.2. Introduction:

Extending the π-system of conjugated ligands is widely used to tune electronic transitions in transition metal[1] and main-group[2] complexes without significantly altering the parent ligand framework. This can provide important flexibility in the design of new emissive molecules and photosensitizers, as photophysical properties can be adjusted without wholesale changes to the core molecular shape. Furthermore, as exemplified by a published series of (BPI)PtCl (BPI = *bis*(2-pyridylimino)isoindolate) complexes, red or blue shifts are both possible with increasing π-extension. The direction of the shift was rationalized by establishing how the site of benzannulation impacts the energies of the frontier orbitals (HOMO/LUMO).[1d]

In this context, tridentate pincer-type ligands containing benzannulated aromatic *N*-heterocycles offer the potential to form robust complexes bearing an electronically accessible extended π-system.[3] The benzannulated aromatic *N*-heterocycle phenanthridine (3,4-benzoquinoline) is much less well-known as a ligand than its more symmetric isomer acridine (2,3-benzoquinoline),[4] the readily cyclometallated benzo[h]quinoline (7,8-benzoquinoline)[5] and quinoline itself (2,3-benzopyridine). This is despite phenanthridine's utility in fluorescent DNA intercalators such as ethidium bromide[6] and related emissive organic materials,[7] in platin drug candidates (phenathriplatin: *cis*-$[Pt(NH_3)_2$(phenanthridine)Cl$]NO_3$),[8] and as a co-catalyst in hydrogenation reactions.[9] To our knowledge, only a handful of multi-dentate ligands that bring phenanthridinyl units into the coordination sphere of metals are known. Emissive *tris*(4-phenanthridinolato)lithium and aluminum complexes have been used in electroluminescent devices.[10] (*R*) and (*S*)-6-(2'-diphenylphosphino-l'-naphthyl)phenanthridines were applied

as atropisomeric ligands in Pd-catalyzed allylic alkylations.[11] *Fac*-binding, tridentate *bis*(phenanthridinylmethyl)amines bound to Re(I) carbonyls have been used for live-cell fluorescence imaging.[12] Chelate-assisted C-H activation of substituted 6-arylphenanthridines has been used to generate luminescent C,N-cyclometalated phenanthridine-containing platinum(II)[13] and deep-red emitting iridium(III) complexes.[14] We have reported the preparation of (4-diphenylphosphino)phenanthridine analogs of (8-diphenylphosphino)quinolines that can be used to form luminescent Cu and Zn coordination compounds.[15]

In this work, a synthetic route to tridentate phenanthridine-containing ligand frameworks based on *bis*(8-quinolinyl)amine (**L1**; Figure 1).[16] Once deprotonated, these compounds (**L2**, **L3**) are capable of binding as monoanionic $\{NNN\}^-$ amido ligands,[17] and therefore present an opportunity to investigate the coordination chemistry of phenanthridine-containing 'pincer-type' ligands with divalent Group 10 metal ions. The resultant complexes allowed to evaluate the impact of sequential quinoline-to-phenanthridine π-extension on their electronic properties, which we reasoned would be substantial given that benzannulation site-dependent red shifts of 10 nm and blue shifts of nearly 50 nm of the lowest energy absorption were observed in related series of π-extended ligand-metal complexes.[1d] Contrary to our initial hypothesis, while significant shifts are observed in the absorption spectra of **L1**, **L2** and **L3**, the impact of π-system extension proved to be much more subtle in the Group 10 metal complexes **L1-MCl**, **L2-MCl**, **L3-MCl** (M = Ni, Pd, Pt).

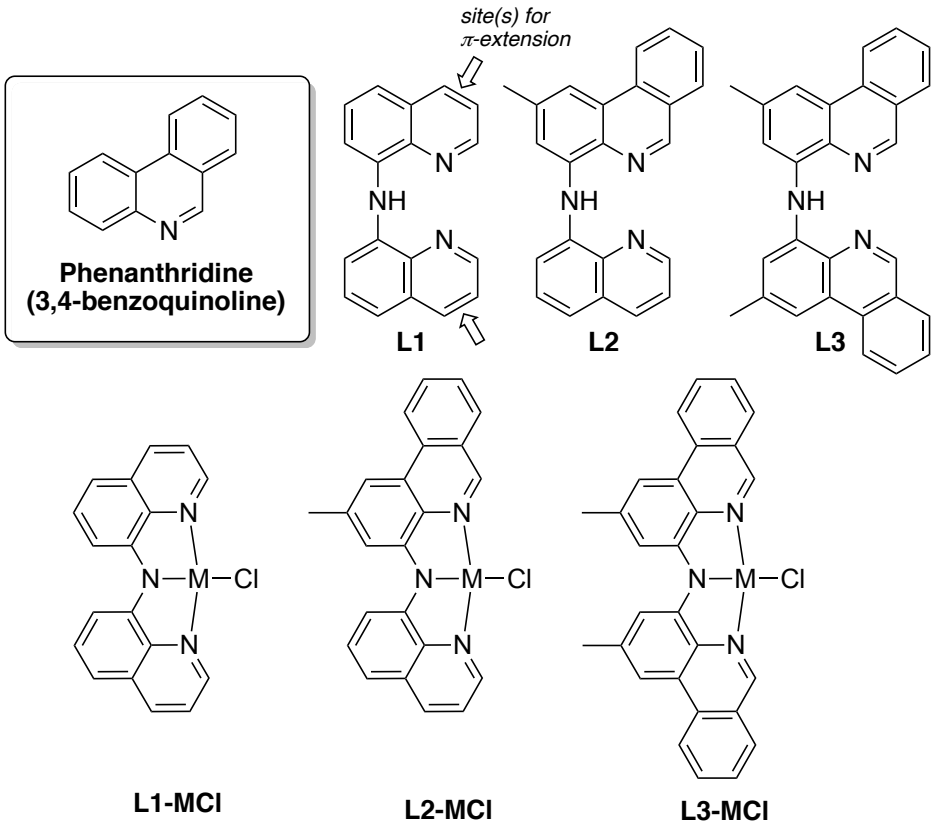

Figure 2.1. Proligands *bis*(8-quinolinyl)amine (**L1**), (4-methylphenanthridinyl)(8-quinolinyl)amine (**L2**), *bis*(4-methylphenanthridinyl)amine (**L3**), and Group 10 metal complexes (**L1-MCl**, **L2-MCl** and **L3-MCl**; M = Ni, Pd, Pt) discussed in this work.

2.3. Results and Discussion:

Bis(8-quinolinyl)amine (**L1**) provides two equivalent conceptual sites for π-extension to phenanthridinyl analogs as shown in Figure 2.1. Having adapted Peters' cross-coupling methodology[16c] for the synthesis of **L2**-**L3** and so first established a general preparative route to 4-substituted halo- and aminophenanthridines by combining C-C and C-N bond formation in a one-pot, Pd-catalyzed cross-coupling/condensation of substituted anilines with 2-formylphenylboronic acid as shown in Scheme 2.1 and Table 2.1.[18] Phenanthridines lacking substituents in the 6-position are less common than 6-subsituted analogs, due to

the electrophilic reactivity of the carbon at this position.[19] Using *para*-substituted 2-bromo-6-iodo-4-methylaniline, achieved higher isolated yields (> 90 %) of 4-bromo-2-methylphenanthridine (**1-Br**) compared with the analogous preparation of 4-bromophenanthridine from 2,6-dibromoaniline (isolated yields ~ 35 %),[15] as the iodoarene can be easily prepared and is more active in cross-coupling. Direct coupling of 2-formylphenyl boronic acid with 1,2-diamino-6-iodo-toluene gave only moderate conversions (~ 60 % by NMR) to **1-NH$_2$**, likely due to coordination of the aminophenanthridine to Pd as shown in Table 3. However, 2-methyl-4-nitrophenanthridine (**1-NO$_2$**) was readily obtained from 2-bromo-6-nitro-4-methylaniline as shown in Table 2.2, and reduction of **1-NO$_2$** with Zn/NH_2-NH_2 and formic acid allowed isolation of **1-NH$_2$** in 85% yield is shown in Scheme 2.2. With the 4-substituted phenanthridines in hand, forcing conditions as shown in Table 4 and Table 5 [150 °C, 72 h; 5 mol % $Pd(OAc)_2$, (1,1'-diphenylphosphino)ferrocene (dppf); sodium-*tert*-pentoxide] gave high isolated yields (> 90 %) of both the asymmetric (4-methylphenanthridinyl)(8-quinolinyl)amine (**L2**) and the symmetric *bis*(4-methylphenanthridinyl)amine (**L3)** is shown in Scheme 2.3.

Table 2.1. Optimization of Cross-Coupling/Condensation Conditions – Synthesis of **1-Br**

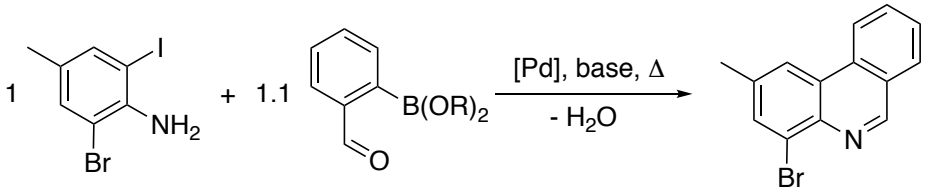

1-Br

R	[Pd]	mol%	solvent	t (h)	T (°C)	base	Conversion[c]
catechol	$Pd(PPh_3)_4$	10	DMF	8	100	K_3PO_4	20
catechol	$Pd(PPh_3)_4$	10	DMF	24	100	K_3PO_4	50
catechol	$Pd(OAc)_2$	10	DMF	24	100	K_3PO_4	0
catechol	$Pd(PPh_3)_4$	8	DMF	24	22	K_3PO_4	0
H	$Pd(PPh_3)_4$	10	DMF	24	100	K_3PO_4	70
H	$Pd(PPh_3)_4$	30	DME[b]	8	100	$NaHCO_3$	70
H	$Pd(PPh_3)_4$	30	DME[b]	24	100	$NaHCO_3$	70
H	$Pd(PPh_3)_4$	20	DME[b]	24	100	$NaHCO_3$	65
H[a]	$Pd(PPh_3)_4$	30	DME[b]	8	110	$NaHCO_3$	90
H[a]	$Pd(PPh_3)_4$	5	DME[b]	5	110	$NaHCO_3$	90
H	$Pd(PPh_3)_4$	5	DME[b]	5	110	Na_2CO_3	>95
H	**$Pd(PPh_3)_4$**	**3**	DME[b]	**5**	**130**	**Na_2CO_3**	**>95**
H	$Pd(PPh_3)_4$	2	DME[b]	5	130	Na_2CO_3	90
H	$Pd(PPh_3)_4$	1	DME[b]	24	130	K_2CO_3	5

[a] 1:1 stoichiometry; [b] DME = 1,2-dimethoxyethane; reflux continued an additional 2-3 h following addition of 2N HCl; [c] determined by comparing integrals for products to starting materials remaining, observed by ^{1}H NMR

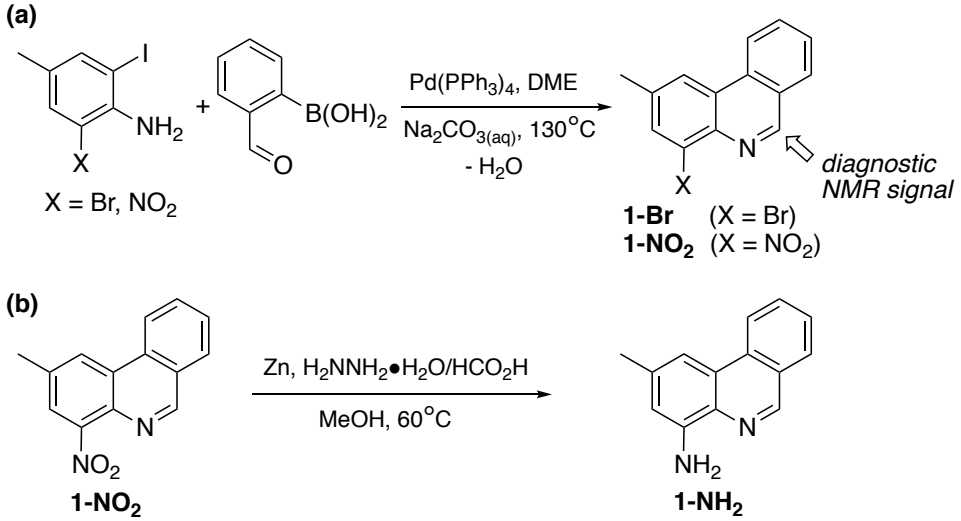

Scheme 2.1. (a) One-pot Pd-catalyzed coupling/condensation route to 4-substituted phenanthridines (**1-Br/1-NO_2**); (b) reduction of **1-NO_2** to **1-NH_2**.

Table 2.2. Optimization of Cross-Coupling/Condensation Route to **1-NO_2**

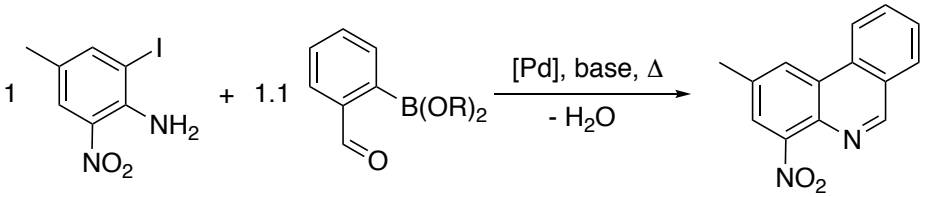

1-NO_2

R	[Pd]	mol %	solvent	t (h)	T (°C)	base	Conversion[c]
catechol	$Pd(PPh_3)_4$	10	DMF	8	100	K_3PO_4	0
H	$Pd(PPh_3)_4$	2	DMF	24	100	NaO*t*Bu	0
H[a]	$Pd(PPh_3)_4$	5	DME[b]	8	100	$NaHCO_3$	95
H[a]	$Pd(PPh_3)_4$	5	DME[b]	8	100	Na_2CO_3	96
H	$Pd(PPh_3)_4$	1	DME[b]	24	100	$NaHCO_3$	70
H	**$Pd(PPh_3)_4$**	**2**	DME[b]	**8**	**130**	**Na_2CO_3**	**100**

[a] 1:1 stoichiometry

[b] DME = 1,2-dimethoxyethane; reflux continued an additional 2-3 h following addition of 2N HCl

[c] determined by comparing integrals for products to starting materials remaining, observed by ^{1}H NMR

Table 2.3. Conditions Attempted in Synthesis of **1-NH_2**

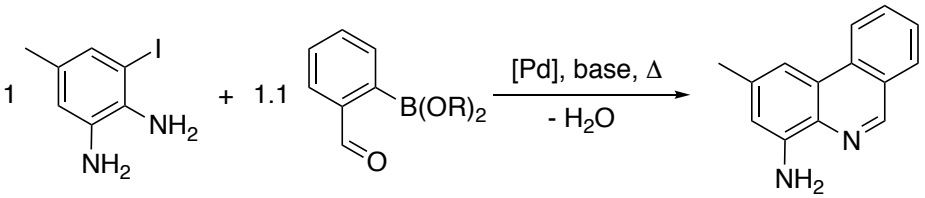

1-NH_2

R	[Pd]	mol %	solvent	t (h)	T (°C)	base	Conversion[c]
catechol	$Pd(PPh_3)_4$	10	DMF	8	100	K_3PO_4	-
H[a]	$Pd(PPh_3)_4$	5	DME[b]	24	100	$NaHCO_3$	22
H[a]	$Pd(PPh_3)_4$	5	DME[b]	24	100	Na_2CO_3	50
H	$Pd(PPh_3)_4$	5	DMF	24	100	$NaHCO_3$	30
H	$Pd(PPh_3)_4$	1	DME[b]	24	100	K_2CO_3	60

[a] 1:1 stoichiometry

[b] DME = 1,2-dimethoxyethane; reflux continued an additional 2-3 h following addition of 2N HCl

[c] determined by comparing integrals for products to starting materials remaining, observed by ^{1}H NMR

Table 2.4. Optimization of Cross-Coupling Route to **L2**

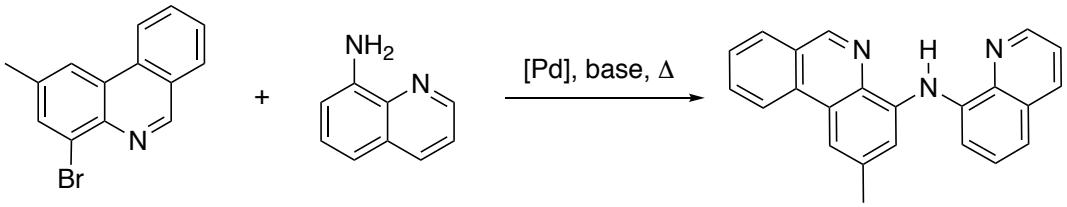

1-Br **AQ** **L2**

1-Br:AQ	[Pd]	mol %	ligand	t (h)	T (°C)	base	Conversion[a]
1 : 1.22	$Pd(OAc)_2$	20	BINAP	24	120	NaO*t*Pent	16
1 : 1.22	$Pd(OAc)_2$	10	BINAP	24	120	NaO*t*Pent	26
1 : 1.22	$Pd(OAc)_2$	5	dppf	72	130	NaO*t*Pent	80
1 : 1.03	$Pd_2(dba)_3$	2	BINAP	72	120	NaO*t*Bu	46
1 : 1.03	$Pd_2(dba)_3$	2	BINAP	72	120	NaO*t*Pent	32
1 : 1.03	$Pd_2(dba)_3$	2	dppf	72	120	NaO*t*Bu	42
1 : 1.03	$Pd_2(dba)_3$	3	dppf	72	120	NaO*t*Bu	56
1 : 1.03	$Pd(OAc)_2$	5	dppf	72	130	NaO*t*Pent	74
1 : 1.03	$Pd(OAc)_2$	5	dppf	72	130	NaO*t*Bu	67
1 : 1.03	$Pd(OAc)_2$	5	BINAP	72	130	NaO*t*Pent	16
1 : 1.22	$Pd(OAc)_2$	5	dppf	96	130	NaO*t*Pent	78
1 : 1.03	**$Pd(OAc)_2$**	**5**	**dppf**	**72**	**150**	**NaO*t*Pent**	**99**
1 : 1.03	$Pd_2(dba)_3$	2	BINAP	72	130	NaO*t*Bu	45

[a] determined by comparing integrals for products to starting materials remaining, observed by ^{1}H NMR

BINAP = *rac*-BINAP, (±)-2,2'-bis(diphenylphosphino)-1,1'-binaphthalene; dppf = (1,1'-diphenylphosphino)ferrocene

Table 2.5. Optimization of Cross-Coupling Route to **L3**

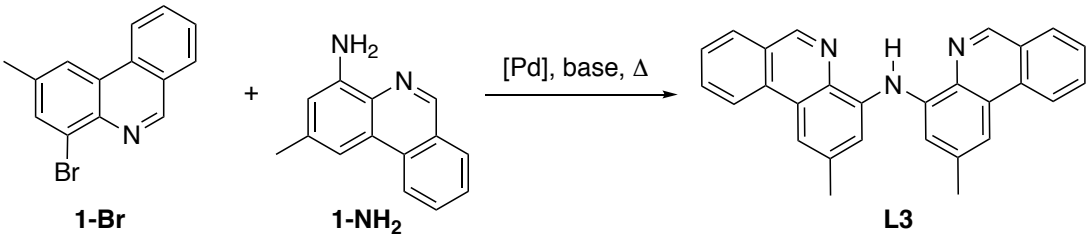

1-Br **1-NH_2** **L3**

1-Br:1-NH_2	[Pd]	mol %	ligand	t (h)	T (°C)	base	Conversion[a]
1 : 1.03	$Pd(OAc)_2$	5	dppf	96h	140	NaO*t*Pent	51
1 : 1.03	$Pd(OAc)_2$	5	dppf	72h	150	NaO*t*Pent	95
1 : 1.03	**$Pd(OAc)_2$**	**5**	**dppf**	**72h**	**155**	**NaO*t*Pent**	**100**

[a] determined by comparing integrals for products to starting materials remaining, observed by ^{1}H NMR

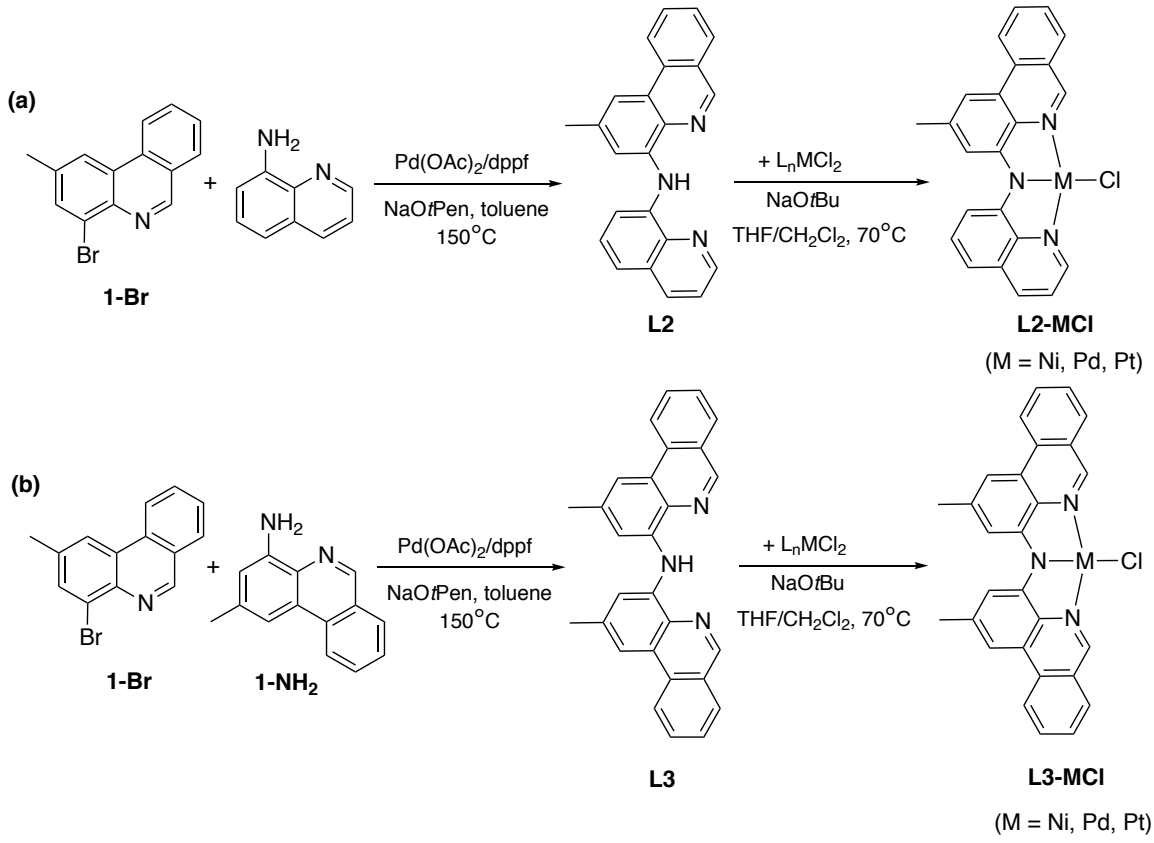

Scheme 2.2. (a) synthesis of π-extended pincer-type proligand **L2** and metal complexes **L2-MCl**; (b) synthesis of **L3** and metal complexes **L3-MCl** (L_nMCl_2 = $NiCl_2(H_2O)_6$, (1,5-COD)$PdCl_2$ or (1,5-COD)$PtCl_2$).

Both **L2** and **L3** show spectroscopic features diagnostic of phenanthridine groups as shown in Table 6. The downfield shift of the ^1H and ^{13}C NMR resonances attributed to the [C-H] unit in the 6-position adjacent to the nitrogen in the phenanthridinyl ring system is consistent with a dominant 'imine-bridged, biphenyl' resonance contributor, which maximizes the number of aromatic subunits in accordance with Clar's postulate.[20] Accordingly, the solid-state X-ray structures of **L2** and **L3** show one short C=N distance in each phenanthridine unit [**L2**: N(1)-C(1) 1.298(2); **L3**: N(1)-C(1) 1.305(4), N(3)-C(15) 1.307(3) Å; Figure 2.2].

Table 2.5. Selected solution NMR data (diagnostic [CH] resonances) for **L1-L3**

	L1	**L2**	**L3**
$\delta(^1H)$ C_6-*H* /ppm	8.97	9.27	9.29
$\delta(^{13}C)$ *C*$_6$-H/ ppm	148.1	150.1	150.1

Table 2.6. Selected solution NMR data (diagnostic [CH] resonances) for and **L1-MCl/L2-MCl/L3-MCl** (from reference[16c] and this work).

	L1-NiCl	**L1-PdCl**	**L1-PtCl**	**L2-NiCl**	**L2-PdCl**	**L2-PtCl**	**L3-NiCl**	**L3-PdCl**	**L3-PtCl**
$\delta(^1H)$ C_6-*H* /ppm	8.66	8.95	9.14	9.05	9.27	9.49	9.10	9.38	9.58
$\delta(^{13}C)$ *C*$_6$-H/ ppm	150.6	149.5	148.8	154.1	151.8	151.1	154.0	151.8	151.0

No significant changes to the pseudo C_{2v} symmetric ^{1}H NMR spectrum of **L3** in CD_2Cl_2 were observed on cooling from 25 °C to -90 °C, implying that there is no significant barrier to the compound adopting a planar configuration, though in the solid-state **L3** adopts a non-planar structure (dihedral angle between the two phenanthridinyl units = 31.1°). In comparison, the dihedral angle between phenanthridinyl and quinolinyl units observed in the solid-state structure of **L2** is considerably smaller (3.4°) as shown in Figure 2.2.

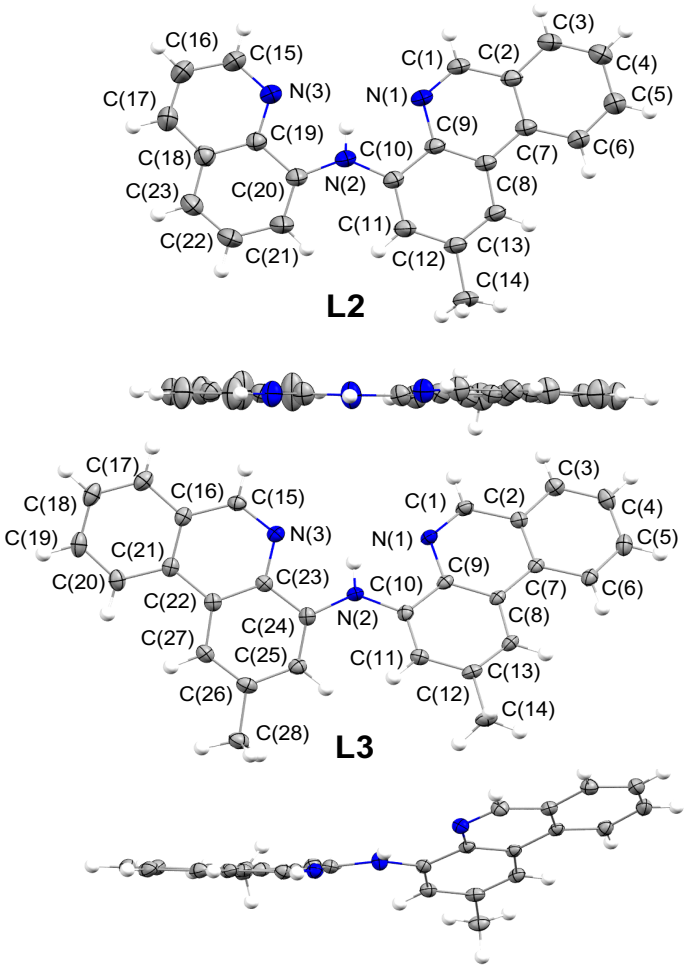

Figure 2.2. ORTEPs[21] of **L2** and **L3**, with thermal ellipsoids shown at 30% (**L2**) and 50% (**L3**) probability levels. For each structure, two views are shown. Selected bond distances (Å) for **L2**: C(1)-N(1) 1.298(2), C(9)-N(1) 1.3811(17), C(9)-C(8) 1.4068(19), C(8)-C(7) 1.4444(19), C(2)-C(1) 1.426(2), C(2)-C(7) 1.4127(18), C(15)-N(3) 1.319(2); and **L3**: C(1)-N(1) 1.305(4), C(9)-N(1) 1.382(3), C(1)-C(2) 1.432(4), C(2)-C(7) 1.410(3), C(7)-C(8) 1.448(4), C(8)-C(9) 1.410(3), C(15)-N(3) 1.307(3), C(23)-N(3) 1.385(3), C(15)-C(16) 1.428(4), C(16)-C(21) 1.413(4), C(21)-C(22) 1.447(3), C(22)-C(23) 1.412(3).

L2 and **L3** bear two sp^2-hybridized, hard N donors and, on deprotonation, a diarylamido Lewis basic site. **L1** has a similar donor set and as might be expected from this rigid donor core, binds to

Group 8,[22] Group 9,[16d] divalent Group 10,[16c] Cu(II)[16b] and Zn(II)[16d] ions in a planar, meridional fashion. Facial binding, however, was also shown to be possible in an octahedral Pt(IV) complex.[23] **L2** and **L3** provide an opportunity to assess the impact of benzannulation on the donor strength of the *N*-heterocyclic arms. The donor ability of pyridine toward the Lewis acid BCl_3 is in between that of quinoline and acridine,[24] consistent with the order of their pK_a's (quinoline < pyridine < acridine). Phenanthridine has a similar pK_a to acridine (5.58), implying a similar 'donor strength' toward H^+. With larger Lewis acids, phenanthridine (3,4-benzoquinoline) should be less sterically encumbered than acridine (2,3-benzoquinoline), due to the asymmetry of benzannulation. To compare the coordination chemistry of our phenanthridine-containing ligands **L2** and **L3** with that of **L1**, we targeted halide complexes of the Group 10 triad, as the analogous complexes of **L1** (**L1-MCl**) are known.[16c]

Divalent nickel, palladium and platinum complexes of **L1-L3** were prepared in 65-89 % yields from reaction with the appropriate metal chloride salt in the presence of a base (NaO*t*Bu) in hot THF or CH_2Cl_2. Benzannulation decreases solubility, which was found to be generally poor in organic solvents for all complexes despite introduction of methyl groups to the *N*-heterocyclic arms in **L2** and **L3**, with metal complexes of **L2**-**L3** precipitating from solution over the course of the reaction. Coordination of the proligands was followed by the shift of the diagnostic NMR spectroscopic resonances of the [CH] unit in the 6-position of the phenanthridinyl arms of **L2** and **L3** is shown in Table 2.6. Coordination of **L2** in **L2-NiCl** results in shifts of the signals for the [C_6-H] unit to 9.05 (^{1}H, $CDCl_3$) and 154.1 ppm ($^{13}C\{^1H\}$), with the equivalent resonances in **L2-PtCl** observed at 9.49 and 151.1 ppm. In comparison, the same signals in **L2-PdCl** are only slightly different from those of the free amine (9.27 ppm and 151.8 ppm; *cf.* **L1-NiCl**: ^{1}H 8.66, $^{13}C\{^1H\}$ 150.6 ppm; **L1-PdCl**: ^{1}H 8.95, $^{13}C\{^1H\}$ 149.5 ppm; **L1-PtCl**: ^{1}H 9.14, $^{13}C\{^1H\}$ 148.8 ppm).[16c] For

L3-MCl, the same trend is observed, with increasing deshielding of the diagnostic ^{1}H NMR resonance going down the group; the C_6-*H* proton signal resonates at 9.10 (**L3-NiCl**), 9.38 (**L3-PdCl**) and 9.58 ppm (**L3-PtCl**). No exchange is seen with free ligand in solution. The diagnostic spectroscopic signatures confirm stable complexation.

Slow diffusion of diethyl ether into chloroform solutions of **L2-MCl** or **L3-MCl** (M = Ni, Pd, Pt) afforded single-crystals suitable for X-ray diffraction. In each case, high quality single-crystals with long-range order were obtained as a $CHCl_3$-solvate. The metal complexes of **L2** (**L2-MCl**) and **L3** (**L3-MCl**) are isostructural with previously reported structures of **L1-NiCl**, **L1-PdCl** and **L1-PtCl** as shown in Figure 2.3.[16c] In each structure, the three nitrogen donor atoms of the ligands are coplanar with the coordinated metal atom, with M-Cl distances increasing with the size of the divalent metal ion Table 2.7. The trans influence of the amido N donor in **L1** was previously suggested to be minimal, as the amido N was found to bind selectively *trans*-disposed to strong trans influence alkyls/hydrides when a cis disposition was possible.[22] Direct comparison of trans influence of the amido N in **L2-MCl**/**L3-MCl** to **L1-MCl** through solid-state M-Cl bond distances is complicated by the presence of close-contacts between $CHCl_3$ and the chloride ligand in the crystal lattice of **L2-MCl** and **L3-MCl**. Complexes of the two phenanthridine-containing ligands (**L2-MCl**, **L3-MCl**) show statistically indistinguishable M-Cl bond distances, consistent with similar trans influences of the amido N in **L2** and **L3**.

The trans influence of phenanthridine as a ligand can be thought of as similar to that of pyridine; statistically indistinguishable Pt-N bond distances were reported trans to the *N*-heterocyclic donor in *cis*-$[Pt(NH_3)_2(phenanthridine)Cl][OSO_2CF_3]$ and *cis*-$[Pt(NH_3)_2(pyridine)Cl][OSO_2CF_3]$.[25] In all **L2-MCl** complexes, the phenanthridinyl N(1)-M distances are shorter than the quinolinyl N(3)-M distance trans to them, and also shorter than the corresponding phenanthridinyl N(3)-M bond

distance in **L3-MCl** (which is trans to a phenanthridinyl donor); however, the values are not distinguishable outside of the 3σ statistical limit as shown in Table 2.7. The comparable bond distances suggest similar donor strengths for the phenanthridinyl and quinolinyl arms as well; however, they may also be a consequence of the rigid tridentate ligand scaffold.

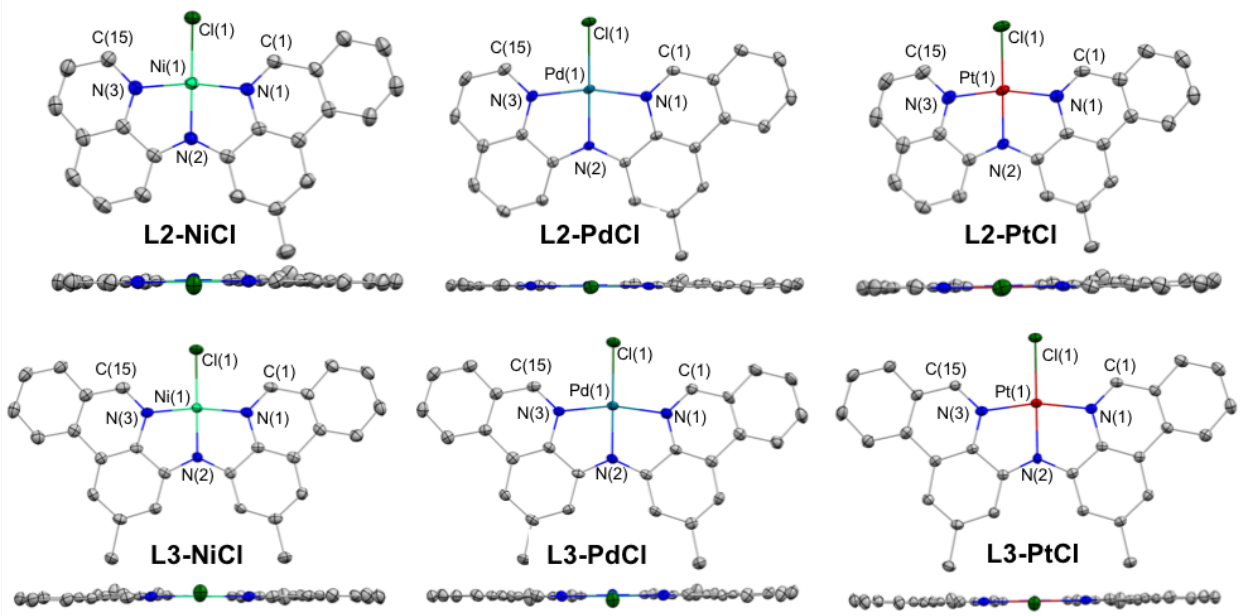

Figure 2.3. ORTEPs[21] with thermal ellipsoids shown at 50% (**L2-PdCl, L3-NiCl, L3-PdCl**) and 30% (**L2-NiCl**) probability levels, and hydrogens omitted for clarity. For each structure, a top view perpendicular to the metal square plane and a bottom view along the Cl–M–N(2) axis are shown.

Selected bond angles (°) for **L2-NiCl**: N(1)-Ni(1)-N(3) 169.31(12), Cl(1)-Ni(1)-N(2) 178.67(10), N(1)-Ni(1)-N(2) 84.72(12), N(3)-Ni(1)-N(2) 84.60(13), N(1)-Ni(1)-Cl(1) 95.33(9), N(3)-Ni(1)-Cl(1) 95.34(10). **L2-PdCl**: N(1)-Pd(1)-N(3) 165.94(8), Cl(1)-Pd(1)-N(2) 179.66(6), N(1)-Pd(1)-N(2) 83.05(8), N(3)-Pd(1)-N(2) 82.89(8), N(1)-Pd(1)-Cl(1) 97.28(6), N(3)-Pd(1)-Cl(1) 96.78(6). **L2-PtCl**: N(1)-Pt(1)-N(3) 166.16(9), Cl(1)-Pt(1)-N(2) 179.20(7), N(1)-Pt(1)-N(2) 83.29(9), N(3)-Pt(1)-N(2) 82.88(9), N(1)-Pt(1)-Cl(1) 97.24(7), N(3)-Pt(1)-Cl(1) 96.60(7). **L3-NiCl**: N(1)-Ni(1)-N(3) 169.48(9), Cl(1)-Ni(1)-N(2) 176.71(7), N(1)-Ni(1)-N(2) 84.84(9), N(3)-Ni(1)-N(2) 84.68(9),

N(1)-Ni(1)-Cl(1) 95.20(6), N(3)-Ni(1)-Cl(1) 95.31(7). **L3-PdCl**: N(1)-Pd(1)-N(3) 166.04(12), Cl(1)-Pd(1)-N(2) 177.52(9), N(1)-Pd(1)-N(2) 82.89(13), N(3)-Pd(1)-N(2) 83.17(12), N(1)-Pd(1)-Cl(1) 97.22(9), N(3)-Pd(1)-Cl(1) 96.74(9). **L3-PtCl**: N(1)-Pt(1)-N(3) 166.12(7), Cl(1)-Pt(1)-N(2) 178.56(6), N(1)-Pt(1)-N(2) 83.16(8), N(3)-Pt(1)-N(2) 82.98(8), N(1)-Pt(1)-Cl(1) 96.84(6), N(3)-Pt(1)-Cl(1) 97.04(6).

Table 2.7. Selected bond distances for **L1-MCl** (from reference[16c]) and **L2-MCl/L3-MCl** (this work).

Distance (Å)	M-N(1)[a]	M-N(3)[b]	M-N(2)	M-Cl(1)[c]	N(1)-C(1)	N(3)-C(15)[d]
L1-NiCl	1.8973(16)	1.8973(16)	1.8586(14)	2.1779(5)	1.323(2)	1.326(2)
L2-NiCl	1.899(3)	1.906(3)	1.858(3)	2.2067(11)	1.316(4)	1.331(5)
L3-NiCl	1.900(2)	1.900(2)	1.858(2)	2.2080(7)	1.312(3)	1.311(3)
L1-PdCl	2.0114(19)	2.0017(19)	1.962(2)	2.3298(7)	1.331(3)	1.329(3)
L2-PdCl	1.997(2)	2.001(2)	1.9620(19)	2.3406(6)	1.301(3)	1.331(3)
L3-PdCl	2.001(3)	2.001(3)	1.959(3)	2.3387(10)	1.308(5)	1.301(5)
L1-PtCl	1.994(3)	1.999(3)	1.966(3)	2.3175(11)	1.338(5)	1.318(5)
L2-PtCl	1.993(2)	1.999(2)	1.969(2)	2.3427(7)	1.302(4)	1.331(3)
L3-PtCl	1.995(2)	1.991(2)	1.9779(18)	2.3449(6)	1.312(3)	1.315(3)

[a] Quinolinyl-N in **L1-MCl**; phenanthridinyl-N in **L2-MCl/L3-MCl**; [b] Quinolinyl-N in **L1-MCl/L2-MCl**; phenanthridinyl-N in **L3-MCl**; [c] Cl(1) shows close contact to $CHCl_3$ in lattice of **L2-MCl/L3-MCl**; [d] Labeled C(10) in reference[16c]

2.4.1. UV-Visible Absorption Spectroscopy:

The electronic absorption spectra of proligands **L1-L3** and metal complexes **L1-MCl**, **L2-MCl**, and **L3-MCl** were measured in both CH_2Cl_2 and *N*,*N*-dimethylformamide. The absorption observed for **L1-MCl/L2-MCl/L3-MCl** obeys Beers' Law only over a limited low concentration

range (< $5x10^{-5}$ M), suggesting ground-state aggregation may occur at higher concentrations. The UV-Vis absorption spectra of **L1**, **L2** and **L3** are marked by a broad peak at low energy, whose maximum shifts to shorter wavelength (**L1**: 400 nm; **L2**: 392 nm; **L3**: 382 nm; Figure 5a) with increasing conjugation. However, this low energy peak also broadens, and the onset of absorption is observed at higher wavelengths (i.e., λ_{onset} **L3** > **L2** > **L1**). For comparison, the first absorption band maximum of phenanthridine itself is found at 343 nm (hexanes, π-π*), shifting slightly to 346 nm in methanol,[26] while the analogous peak for quinoline is at 311 nm (ethanol).[27] Consistent with the deep red color of all nine metal complexes, spectra collected for **L1-MCl**, **L2-MCl** and **L3-MCl** contained a broad absorption with a maximum at ~ 500 nm as shown in Figures 2.4 (b-d) and Table 2.8. The significant red shift of the lowest energy peak for **L1-L3** upon coordination to a metal is consistent with metal participation in the transition (i.e., M-π* metal-to-ligand charge transfer (MLCT) character) in addition to ligand-centreed π-π* character.[16d, 22] The large extinction coefficients support the contribution of charge transfer to this transition.

In contrast to the free amines, there is no significant shift in the maximum of this broad absorption band when changing from **L1** to **L2** to **L3** for any of the three series of metal complexes. This was surprising, given we intuitively expected extending ligand conjugation to have some impact on the frontier orbital energies. Modest broadening of the low energy absorption can be seen for **L1-NiCl/L2-NiCl/L3-NiCl** and **L1-PdCl/L2-PdCl/L3-PdCl**, with the full width at half max (FWHM) increasing on average by 7 nm, and up to 17 nm when the FWHM for the broad absorption of **1-Pd** is compared with **3-Pd**. As with **L1**-**L3**, the onset of absorption is observed at higher wavelengths as well (i.e., λ_{onset} **L3-MCl** > **L2-MCl** > **L1-MCl**; M = Ni, Pd). The low energy absorptions for **L1-PtCl/L2-PtCl/L3-PtCl** are essentially unchanged by the alterations to the ligand structure. The major difference to the absorption spectrum for each of the three series

of metal complexes is the appearance of up to four additional peaks at higher energy (300-430 nm), that grow in intensity when comparing complexes of **L2** and **L3**, and therefore result from the phenanthridinyl arms.

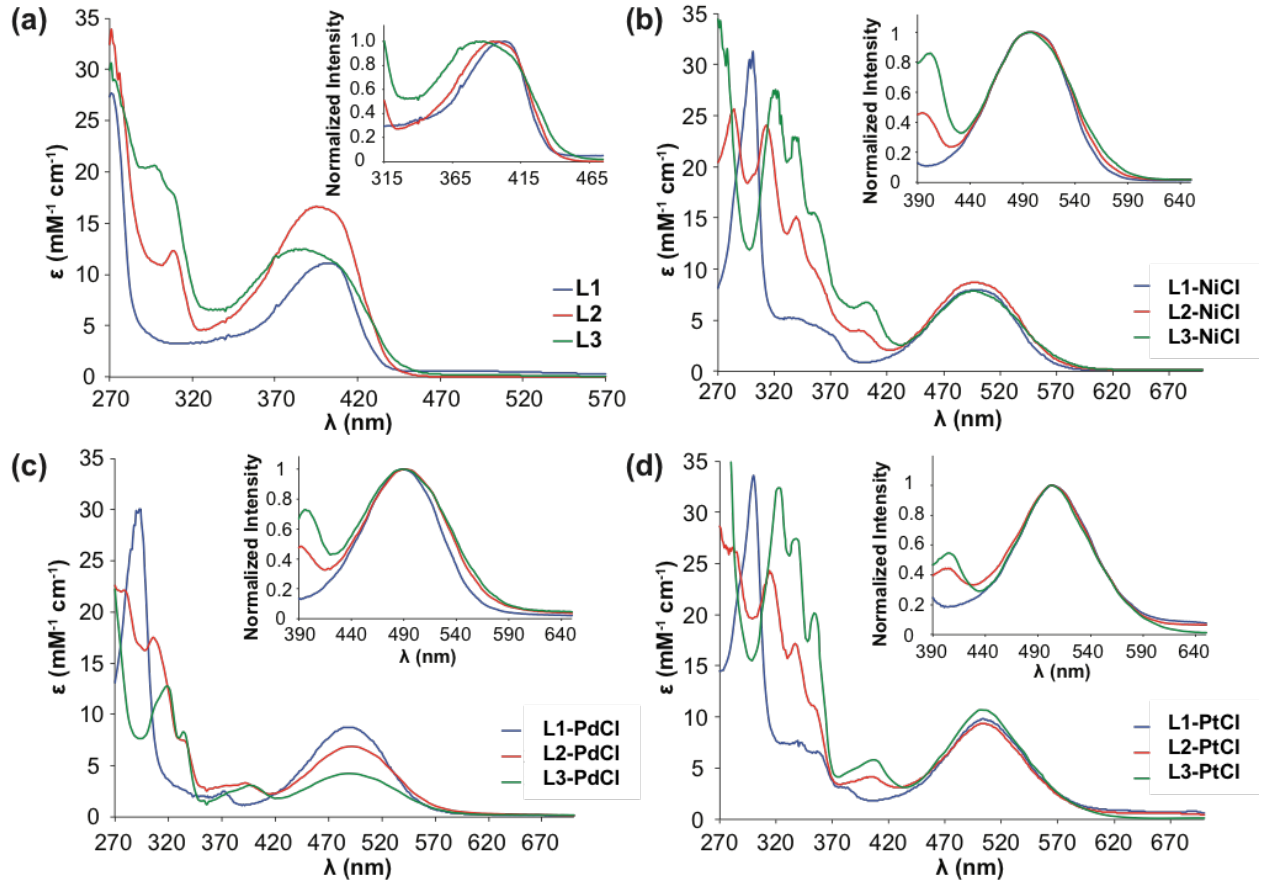

Figure 2.4. UV-Vis absorption spectra (CH_2Cl_2, 22 °C) for (a) **L1-L3**, (b) **L1-NiCl/L2-NiCl/L3-NiCl**, (c) **L1-PdCl/L2-PdCl/L3-PdCl**, (d) **L1-PtCl/L2-PtCl/L3-PtCl**.

2.4.2. Electrochemistry of L1-MCl, L2-MCl and L3-MCl:

The invariant position of the maximum of the lowest energy absorption band observed for each set of metal complexes led us to expect that the optical HOMO-LUMO gap is mostly unaffected by increasing conjugation from **L1-MCl** to **L2-MCl** to **L3-MCl**, apart from a slight red shift indicated by the shift in the long wavelength edge of the absorption spectra. Electrochemistry has

been used to evaluate trends in the relative energies of the frontier orbitals within series of similar compounds.[28]

In collaboration with Patrick. K. Giesbrecht, the electrochemical properties of **L1-MCl**, **L2-MCl**, and **L3-MCl** were examined in solution using cyclic voltammetry (CV) and differential pulse voltammetry (DPV) as shown in Figure 2.5 and Table 2.8. All complexes show irreversible reduction waves at ~ -2 V (vs $Fc^{0/+}$; Fc = ferrocene) with no return wave apparent at any of the tested scan rates (50-800 $mV \cdot s^{-1}$). The low solubility of the compounds results in the appearance of a pre-peak feature observed in the cathodic scans not observed at faster scan rates, attributed to adsorption of dissolved complex onto the electrode surface.[29] This is particularly pronounced for the Pt complexes (the maximum solution concentration achieved with **L3-PtCl** was 0.72 mM). Comparing these reductive events for **L1-MCl/L2-MCl/L3-MCl** (M = Ni, Pd), a slight anodic shift is observed with extended conjugation (**L1-MCl→L2-MCl→L3-MCl**). This trend is in keeping with the conventional expectation that a larger π-system would stabilize the negative charge to a greater extent, however we are cautious in over-interpreting this observation due to the issues with low complex solubility. In contrast, a slight cathodic shift is observed for the Pt series, with $E_{peak,cathodic}$ (**L3-PtCl**) < $E_{peak,cathodic}$ (**L2-PtCl**) < $E_{peak,cathodic}$ (**L1-PtCl**).

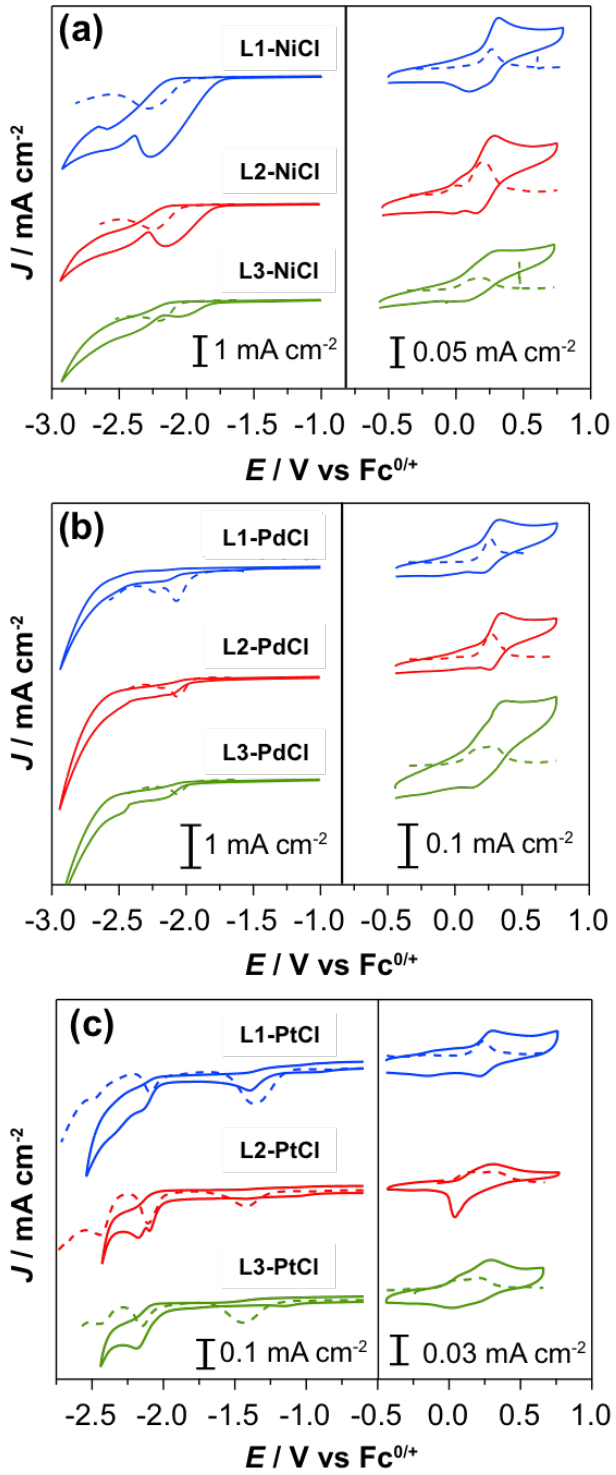

Figure 2.5. Cyclic voltammograms (—) and corresponding differential pulse voltammograms (---) of **L1-MCl**, **L2-MCl**, and **L3-MCl** (1.5 mg/15 mL) in CH_2Cl_2 with 0.1 M $[nBu_4N][PF_6]$ as the supporting electrolyte; (a) M = Ni, (b) M = Pd, (c) M = Pt. CV scan rates were 100 mV/s. Data in the high and low potential regions were collected in separate scans.

Quasi-reversible, broad oxidation events were also observed for all nine complexes at ~ 0.2 V vs $Fc^{0/+}$. The addition of a second fused ring in **L3-MCl** leads to the appearance of a second broad feature at less anodic potentials. While we cannot rule out whether this feature is due to aggregate formation, no visible deposition was observed on the electrodes following these scans; so far we have been unable to isolate a soluble chemically oxidized cationic species. In comparison, Pt complexes of π-extended derivatives of 1,3-*bis*(2-pyridiylimino)pyrrole/pyrrolate/isoindolate exhibited reversible reductions and irreversible oxidations.[1d] The reduction and oxidation events, respectively, observed for all nine Group 10 metal complexes of **L1-L3** are within a relatively narrow potential window. This is consistent with largely ligand-based redox events influenced by coordination to a metal;[30] the redox chemistry of organic *N*-heterocycle fused phenanthridines has been reported in a similar range (0.38-1.5 V vs $Fc^{0/+}$).[31] Taking the difference between the first observed oxidation event and the reduction peak observed by DPV ($\Delta E_{ox1\text{-}red}$), the relative HOMO-LUMO gap for the series of complexes can be estimated. The irreversibility of the peaks and presence of an absorption pre-feature makes it problematic to precisely quantify the HOMO-LUMO separation using redox data, but the relative trend for all three metals is that $\Delta E_{ox\text{-}1red}$ decreases with increasing conjugation (**L1-MCl→L2-MCl→L3-MCl**).[32]

Table 2.8. Electrochemical potentials and UV-Vis absorption parameters for complexes (**L1-L3)MCl** (M = Ni, Pd, Pt**)**.

	$E_{peak, red}$[a]/V	$E_{peak, ox}$ [a]/V	ΔE_{ox1-ed}[b]/V	λ[c]/nm (ε/$M^{-1}cm^{-1}10^{-3}$)	FWHM λ_{max}/nm[d]
L1-NiCl	-2.28	0.26	2.54	301 (31.2), 337 (5.2), 371 (sh), 499 (8.0)	86
L2-NiCl	-2.25	0.20	2.45	284 (25.6), 313 (24.1), 339 (15.1), 356 (sh), 395 (4.0), 498 (8.7)	89
L3-NiCl	-2.20	0.16[e]	2.36[e]	319 (27.4), 336 (22.9), 354 (15.5), 402 (6.7), 496 (7.8)	91
L1-PdCl	-2.08	0.26	2.34	291 (29.8), 372 (2.5), 489 (8.8)	87
L2-PdCl	-2.06	0.27	2.33	278 (22.1), 306 (17.5), 338 (sh), 392 (3.3), 492 (6.9)	98
L3-PdCl	-2.05	0.18, 0.30	2.23	308 (sh), 318 (12.8), 334 (8.3), 398 (3.1), 489 (4.2)	104
L1-PtCl	-2.09, -1.37[f]	0.25	2.34	300 (33.6), 339 (7.7), 356 (6.6), 383 (3.1), 503 (9.8)	87
L2-PtCl	-2.10, -1.40[f]	0.15, 0.31	2.25	314(24.3), 337 (17.2), 353 (sh), 405 (4.2), 503 (9.4)	91
L3-PtCl	-2.15, -1.45[f]	0.05, 0.20	2.20	322 (32.4), 336 (27.4), 354 (20.1), 406 (5.6), 503 (10.7)	88

[a] Measured for CH_2Cl_2 solutions with 0.1 M [nBu$_4$N][PF_6] as the supporting electrolyte, via DPV with potentials reported referenced to the $Fc^{0/+}$ redox couple.

[b] $\Delta E_p = E^{ox}{}_{1/2}-E^{red}$

[c] Ambient temperature, CH_2Cl_2

[d] Maximum of broad peak observed at lowest energy in spectrum in CH_2Cl_2

[e] Value represents middle of two unresolved peaks.

[f] Surface-based deposition observable only at slow scan rates and/or DPV.

2.4.3. Electronic Structure Calculations:

We, in collaboration with Prof. Rebecca L. Davis, carried out density functional theory (DFT) calculations, incorporating a polarizable continuum model (DFT-PCM) to model solvent effects, and time-dependent DFT-PCM (TDDFT-PCM) calculations to probe the impact of benzannulation on the electronic structure of **L1-MCl/L2-MCl/L3-MCl**, and explain the experimental UV−Vis absorption spectra. As the trends for the Ni and Pd systems were found to be similar, only the Ni complexes are presented. The Pt complexes were not analyzed for this work. All structures were optimized with (SMD-M06/6-31+G(d,p)) and optimized geometries are in good agreement with the experimental X-ray crystallography data (see Supporting Information for details).[33]

The trends in calculated energies shown in Table 4 correspond well with those observed in the experimental electrochemistry. The calculated HOMO energy levels increase with extended conjugation of the ligand (**L1-MCl→L2-MCl→L3-MCl**), consistent with the observed cathodic shift in oxidation potential. The observed trend in the onset of reduction potentials is not reproduced; however, as noted above, the irreversibility of the cathodic electrochemical events and presence of absorption pre-features complicate precise analysis of the peak positions.

Using the optimized structures, vertical excitation energies were determined using TDDFT. The lowest energy vertical transitions for solution (SMD) calculations are in good qualitative agreement with the experimental absorption trends as shown in Table 2.8. Consistent with the observed experimental spectra, the increase in conjugation in the ligands has little effect on the position of the low energy absorption of the metal complexes. However, benzannulation does impact the nature of the absorption, as can be seen through analysis of atomic contributions to the computed molecular orbitals.

Our calculations on the complex with the smallest π-system (**L1-NiCl**) predict that the HOMO→LUMO transition defines the lowest energy excitation at 494 nm (98% calculated contribution). The HOMO of this complex consists largely of contributions from the π system of the C_6-benzo rings and amido lone pair, with small contributions from the d- and p-orbitals of the nickel and chloride respectively, and the C-N π bond of the quinolinyl rings as shown in Figure 2.6. The LUMO of this system has a small contribution from the Ni but is otherwise largely delocalized across the π system of the ligand.

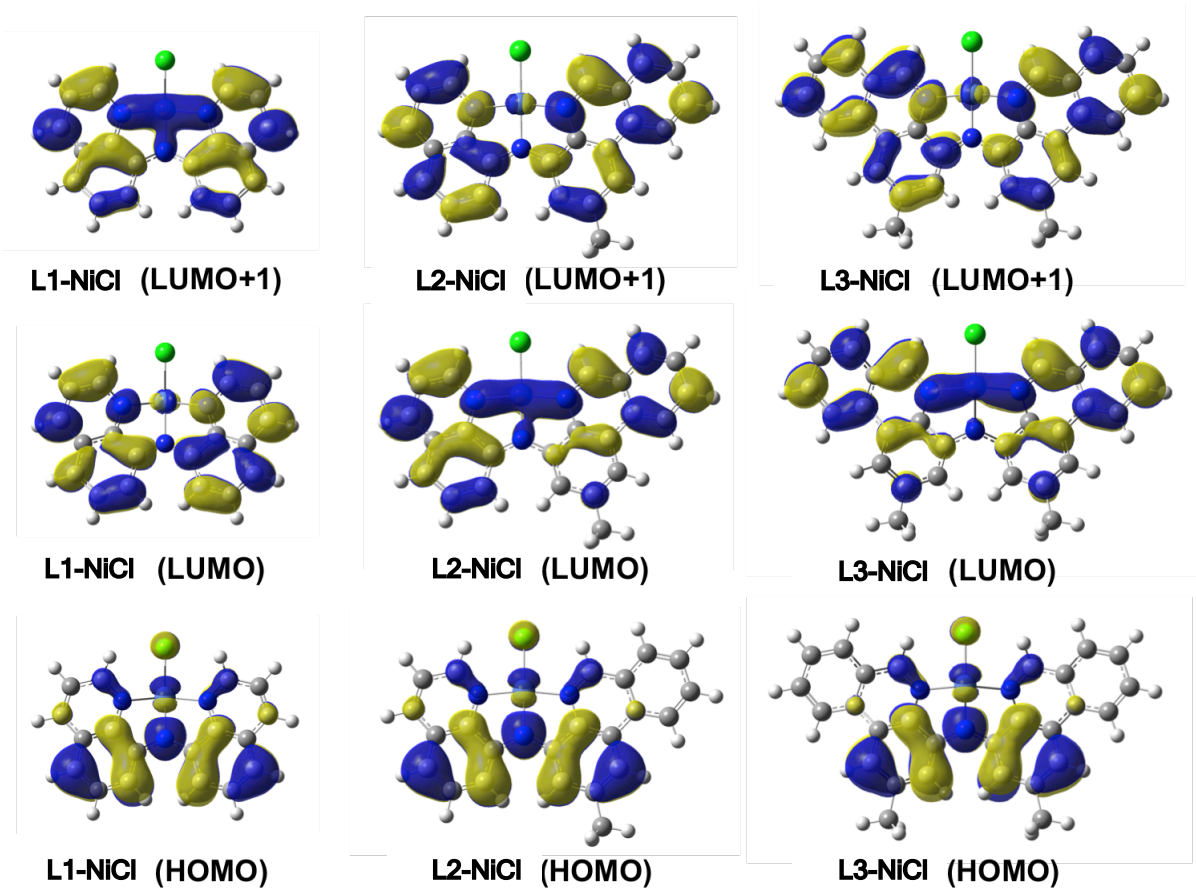

Figure 2.6. Orbital diagrams of the HOMO, LUMO and LUMO+1 for **L1-NiCl**, **L2-NiCl**, and **L3-NiCl**

The extended π system of **L2-NiCl** produces two low energy excitations at 491 nm and 484 nm with nearly equal oscillator strengths (Table 4). The excitation at 491 nm is dominated by the HOMO→LUMO transition (58% calculated contribution) but contains significant HOMO→LUMO+1 character (41% calculated contribution). The excitation at 484 nm is dominated by the HOMO→LUMO+1 transition (57%) but contains significant HOMO→LUMO character (41%). The HOMO of this system is similar to that of **L1-NiCl** in that it consists largely of contributions from the π system of the benzo moieties, the central amido lone pair and, to a smaller extent, the C=N π-bond. The LUMO of **L2-NiCl** consists of contributions from both ligand arms and Ni. Qualitatively, the structure of the LUMO+1 in the calculated structure of **L2-NiCl** more closely resembles the orbital configuration of the LUMO of **L1-NiCl** and is delocalized across the π system of the ligand as shown in Figure 2.6. Further expansion of the π system of the ligand in **L3-NiCl** produces an excitation at 490 nm that is defined by the HOMO→LUMO+1 transition (97%). The orbital contributions of the HOMO, LUMO and LUMO+1 of the **L3-NiCl** complex closely resemble those of the **L2-NiCl** complex, with the LUMO/LUMO+1 character inverted compared to **L1-NiCl** as shown in Figure 2.6. The main impact of benzannulation in the series **L1-NiCl→L2-NiCl→L3-NiCl** therefore appears to be to cause the energy of the LUMO of **L1-NiCl** to rise, while at the same time lowering the energy of the LUMO+1 (which becomes the LUMO of **L2-NiCl** and **L3-NiCl**). The orbital contributions to the HOMO, in comparison, remain largely unchanged from **L1-NiCl→L2-NiCl→L3-NiCl**, while the energy of this orbital is calculated to rise slightly, in keeping with conventional expectations of extended conjugation and consistent with the trends in the experimental anodic electrochemistry. Interestingly, in both pseudo-C_{2v} symmetric complexes (**L1-NiCl** and **L3-NiCl**), only one low energy transition has

significant calculated oscillator strength and the atomic contributions to the orbitals involved in this transition are very similar. In the C_s symmetric **L2-NiCl**, both the HOMO→LUMO and HOMO→LUMO+1 transitions contribute to the low energy absorptions.

This is qualitatively consistent with Gordon and Thompson's model[1d] for understanding shifts in frontier orbital energies following benzannulation: there is minimal HOMO density at the site of benzannulation in **L1-NiCl** by a conceptual *cis*-1,3-butadiene fragment. No orbital mixing or significant change to the HOMO energy/character would therefore be expected. In contrast, there is a bisecting nodal plane in the LUMO of **L1-NiCl** at the site of benzannulation. There is therefore a symmetry match with the HOMO of a *cis*-1,3-butadiene fragment (a_2, C_{2v} point group), which can therefore act as an effective electron-donating group to the LUMO of **L1-NiCl**, leading to its destabilization.

Table 2.9. TDDFT Vertical Excitation Energies and HOMO, LUMO, and LUMO+1 energies for complexes **L1-NiCl/L2-NiCl/L3-NiCl**.

	HOMO (eV)	LUMO (eV)	LUMO+1 (eV)	λ_{calc} (nm)	Assignment	Oscillator Strength	Coefficient	% Contribution
L1-NiCl	-5.35	-1.90	-1.85	494.34	HOMO→LUMO	0.3698	0.70142	98.4
				483.13	HOMO→LUMO+1	0.0078	0.70319	98.9
L2-NiCl	-5.32	-1.88	-1.84	490.66	HOMO→LUMO	0.2131	0.53712	57.7
					HOMO→LUMO+1		0.45206	40.9
				483.83	HOMO→LUMO	0.1722	-0.45215	40.9
					HOMO→LUMO+1		0.53581	57.4
L3-NiCl	-5.28	-1.90	-1.79	496.51	HOMO→LUMO	0.0221	0.70183	98.5
				485.04	HOMO→LUMO+1	0.3536	0.69707	97.2

In a relevant literature example, similarly extending ligand conjugation for a series of annulated *meso*-tetraphenylmetalloporphyrins was found not to significantly impact the energy of the HOMO and LUMO with respect to the parent porphyrin, but did lead to significant destabilization of the HOMO-1.[34] In this case, destabilization of the HOMO-1 led to this orbital rising above the parent

HOMO in energy (and become the new HOMO in the benzannulated complexes), thus leading to a red shift in the absorption and emission spectra. A similar effect occurs in the series **L1-NiCl→L2-NiCl→L3-NiCl**, where the orbitals comprising the LUMO and LUMO+1 in the parent complex (**L1-NiCl**) formally change positions upon benzannulation (**L2-NiCl/L3-NiCl**). In our series, however, the slight rise in the energy of the HOMO upon benzannulation is matched by a similar rise in the energy of the LUMO+1. The shift in the character of the lowest energy transition from HOMO→LUMO (**L1-NiCl**) to HOMO→LUMO/HOMO→LUMO+1 to strictly HOMO→LUMO+1 (**L3-NiCl**) then results in similar energies for these transitions calculated by theory and observed experimentally.

2.4.4. Synthesis of $^{t\mathrm{Bu,Phen}}$N^N^N$^{\mathrm{Quin,H}}$ (L4):

From the above experiments it is evident systematic benzannulation the solubility of the metal complexes decreases in organic solvents as **L1-MCl** > **L2-M-Cl** > **L3-MCl** (M = Ni, Pd, Pt), with symmetric amido bis(phenathridinyl) complexes being poor. To study the reactivity of these metal complexes, solubility in organic solvents is necessary. One way to increase the solubility is by introducing bulky *tert*-butyl group onto the phenanthridinyl ring, which should theoretically break the strong π-π stacking interactions between the complexes in solution. Having the previous knowledge of synthesizing 2-methyl substituted phenanthridines, 2-*tert*-butyl-4-aminophenanthridine (**2-NH$_2$**) was synthesized [9.10ppm (^{1}H, $CDCl_3$); 150.9 ppm (^{13}C, $CDCl_3$)] as shown in Scheme 2.4 (a-b) and was isolated as a pale green compound in high yields. Asymmetric proligand (4-*tert*-butylphenanthridinyl)(8-quinolinyl)amine **L4** is synthesized using C-N coupling between 2-*tert*-butyl-4-aminophenanthridine and 8-bromoquinoline as shown in Scheme 2.4c [150 °C, 72 h; 5 mol % $Pd(OAc)_2$, (1,1'-diphenylphosphino)ferrocene (dppf); sodium-*tert*-pentoxide] gave high isolated yields (> 92 %).

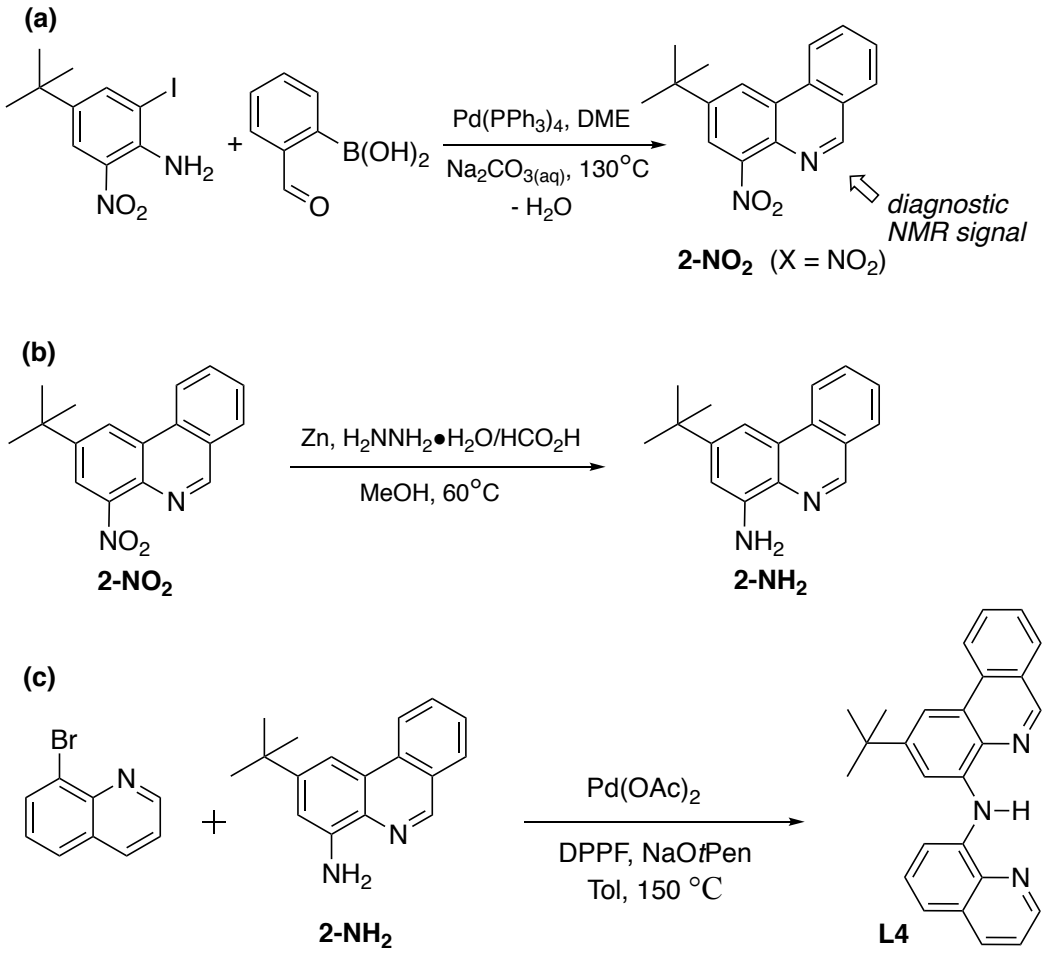

Scheme 2.3. (a) One-pot Pd-catalyzed coupling/condensation route to 4-substituted phenanthridines (**2-NO₂**); (b) reduction of **2-NO₂** to **2-NH₂**; (c) synthesis of π-extended pincer-type proligand **L4**.

Proligand **L4** shows spectroscopic features diagnostic of phenanthridine, the downfield shift of the ^{1}H and ^{13}C NMR resonances attributed to the [C-H] unit in the 6-position adjacent to the nitrogen in the phenanthridinyl ring system at 9.10 ppm (^{1}H, $CDCl_3$) and 150.5 ppm (^{13}C, $CDCl_3$) as observed for ligands **L1-L3**. Also, the ^{1}H NMR resonance for [N-H] appears far downfield at 11.58 ppm (^{1}H, $CDCl_3$). Having the proligand **L4** synthesized in good yields, have targeted the synthesis of divalent nickel and palladium complexes using $NiCl_2.6H_2O$ and $Pd(COD)Cl_2$/$Pd(OAc)_2$ with NaO*t*Bu as base in refluxing dichloromethane or THF. Metal

complexes **L4-NiCl**, **L4-PdCl** and **L4-PdOAc** were isolated as deep red colored compounds in high yields (74 – 87%) as shown in Scheme 2.5. The disappearance of the far downfield [N-H] proton of **L4** in the ^{1}H NMR spectrum and the significant shift of diagnostic [C_6-H] proton confirmed the synthesis of the corresponding complexes as shown in Table 2.10. Although, even after introducing a *tert*-butyl group into the ligand framework the solubility of the metal complexes improved but not significantly in organic solvents.

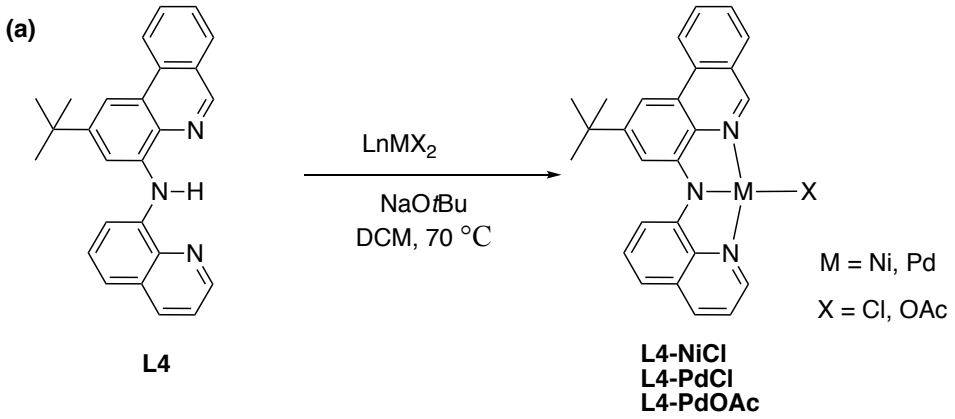

Scheme 2.4. (a) synthesis of metal complexes **L4-MX** (L_nMCl_2 = $NiCl_2(H_2O)_6$, (1,5-COD)$PdCl_2$ or $Pd(OAc)_2$.

Table 2.10. Selected solution ^{1}H NMR data (diagnostic [CH] resonances) for and **L4**, **L4-NiCl**, **L4-PdCl** and **L4-PdOAc**.

	L4	**L4-NiCl**	**L4-PdCl**	**L4-PdOAc**
δ(^{1}H) C_6-*H* /ppm	9.10	9.12	9.37	8.63

Attempts were made to reduce the **L4-MCl** complexes to their corresponding metal hydrides using a broad range of reducing agents like trimethylsilane, $NaBH_4$, NaH and $LiAlH_4$ in DCM and THF but were not fruitful. Often, have observed either insoluble material or demetalated complex after the analysis. Similar attempts to synthesize metal triflates using AgOTf/TMS-OTf were not

successful, gave insoluble red precipitates. These compounds were only soluble on coordinating solvents like THF, DMSO and acetonitrile, which is not interesting for further reactivity studies.

2.5. Conclusion:

A synthetic methodology has been established allowing the preparation of a series of tridentate proligands templated on *bis*(8-quinolinyl)amine (**L1**), bearing one (**L2**) or two phenanthridinyl (**L3**) units. Compounds **L2**-**L3** bind as tridentate, *mer*-bound pincer-like amido ligands to divalent group 10 metal ions (Ni, Pd and Pt). In contrast to the differences observed in the low energy absorption transitions of **L1**-**L3**, the maxima observed for the lowest energy absorptions of **L1-MCl** to **L2-MCl** to **L3-MCl** (M = Ni, Pd, Pt) do not shift appreciably, though the onset of absorption edges to higher wavelengths, consistent with the trend of slight red shift in the HOMO-LUMO gap estimated from electrochemistry. DFT calculations reveal that, more so than simply impacting the frontier orbital energies, benzannulation strongly affects the atomic contributions to the LUMO and LUMO+1, with the orbital character of these MOs in **L2-MCl** and **L3-MCl** switched compared with **L1-MCl**. In addition, while the lowest energy absorption in the *bis*(quinolinyl) **L1-MCl** is dominated by the HOMO→LUMO excitation, the analogous absorption in the *bis*(phenanthridinyl) **L3-MCl** is dominated by the HOMO→LUMO+1 excitation; the mixed quinolinyl/phenanthridinyl **L2-MCl** has both HOMO→LUMO and HOMO→LUMO+1 character. This suggests that complexes of ligands **L1**-**L3** with heavier metals such as **L1-PtCl**, **L2-PtCl** and **L3-PtCl** may present interesting trends in their emission spectra, where a straightforward correlation with the extent of π-conjugation may not exist and the orbital structure of the frontier orbitals may influence other parameters such as radiative rate constants and zero-field splittings. Investigations to this extent are currently underway in our labs.

2.6. Experimental Section:

Unless otherwise specified, all air sensitive manipulations were carried out either in a N_2 filled glove box or using standard Schlenk techniques under Ar. 2-Formylphenylboronic acid (AK Scientific), *N*-iodosuccinimide (AK Scientific), *N*-bromosuccinimide (Alpha Aesar), $Pd(PPh_3)_4$ (Sigma Aldrich), $Pd(OAc)_2$ (Sigma Aldrich), (1,1'-diphenylphosphino)ferrocene (dppf, Sigma Aldrich), Na_2CO_3 (Alpha Aesar), trifluoroacetic acid (Sigma Aldrich), sodium *tert*-pentoxide (NaO*t*Pen, Sigma Aldrich), sodium *tert*-butoxide (NaO*t*Bu, Sigma Aldrich), zinc (Alpha Aesar), hydrazine hydrate (Sigma Aldrich), formic acid (Alpha Aesar), and $NiCl_2 \cdot 6H_2O$ (Alpha Aesar) were purchased and used without any further purification. 2-bromo-4-methylaniline,[35] Pd(1,5-cyclooctadiene)Cl_2,[36] Pt(1,5-cyclooctadiene)Cl_2, **L1**, **L1-NiCl**, **L1-PdCl** and **L1-PtCl**[16c] were synthesized according to published procedures. Organic solvents were dried and distilled using appropriate drying agents prior to use. Distilled water was degassed prior to use. 1- and 2D NMR spectra were recorded on Bruker Avance 300 MHz or Bruker Avance-III 500 MHz spectrometers. ^1H and $^{13}C\{^1H\}$ NMR spectra were referenced to residual solvent peaks.[37] Elemental analyses were performed by Microanalytical Service Ltd., Delta, BC (Canada).

For electrochemical analysis, 1-2 mg of each compound was dissolved in 15 mL of CH_2Cl_2 containing 0.1 M (nBu$_4$N)PF_6, and purged with Ar for 20 minutes before analysis. All electrochemical experiments were conducted under inert (Ar) atmosphere using a CHI 760c bipotentiostat, a freshly polished (0.03 μm alumina paste) 3 mm diameter glassy carbon working electrode (BASi), a Ag/Ag^+ quasi-non-aqueous reference electrode separated by a Vycor tip, and a Pt wire counter electrode. Cyclic voltammetric (CV) experiments were conducted using scan rates of 50-800 mV/s. Differential Pulse Voltammetry (DPV) experiments were conducted using a 5 mV increment, 50 mV amplitude, 0.1 s pulse width, 0.0167 s sample width, and 0.5 s pulse

period. Upon completion of all CV and DPV analyses, ferrocene (Fc) was added to the solution as an internal standard, with all potentials reported versus the $Fc^{0/+}$ redox couple.[38]

Preparation of 2-bromo-6-iodo-*p*-toluidine: Trifluoroacetic acid (30 mol %, 1.23 mL) was added to a stirred acetonitrile solution (300 mL) of 2-bromo-4-methylaniline (10.1 g, 53.7 mmol) at 0 °C, followed by addition of *N*-iodosuccinimide (12.7 g, 56.4 mmol) in small portions over 1.5 h. The mixture was stirred for 0.5h at this temperature, after which the ice bath was removed and stirring continued for 2 h. The solvent was then removed *in vacuo*, the residue taken up in CH_2Cl_2, and washed with brine (3 x 100 mL). The organic layer was dried over Na_2SO_4, and volatiles removed to leave a gray solid, which was used without further purification. Isolated yield = 16.0 g (95 %). The ^1H NMR spectrum was consistent with that previously reported.[39]

Preparation of 2-iodo-6-nitro-*p*-toluidine: An identical procedure to the synthesis of 2-bromo-6-iodo-*p*-toluidine was employed, using 2-nitro-*p*-toluidine (5.01 g, 32.9 mmol) and *N*-iodosuccinimide (12.7 g, 34.5 mmol). Isolated yield of orange solid = 7.60 g (96 %). The ^1H NMR spectrum was consistent with previously reported values.[40]

Preparation of 4-bromo-2-methylphenanthridine (1-Br): A 500 mL teflon-stoppered flask was charged with $Pd(PPh_3)_4$ (0.87 g, 0.75 mmol), and 50 mL of 1,2-dimethoxyethane (DME). After stirring briefly to mix, 2-bromo-6-iodo-*p*-toluidine (7.80 g, 25.0 mmol), 2-formylphenylboronic acid (4.16 g, 27.8 mmol) and an additional 70 mL of DME were added, followed by Na_2CO_3 (8.0 g, 76 mmol) dissolved in 100 mL of degassed water. The flask was then sealed and the mixture stirred vigorously for 6 h in an oil bath (130 °C). The flask was then allowed to cool, charged with 80 mL of 2M HCl, and refluxed for additional 2 h. The reaction mixture was cooled, neutralized with NaOH, and pumped to dryness. The residue was then taken up in CH_2Cl_2 (100 mL) and washed with brine (3 x 100 mL). The organic layer was separated, dried over Na_2SO_4

and volatiles removed to leave yellow-brown solid. Column chromatography on basic alumina gave a pale yellow solid (R_f = 0.41; 1:5 EtOAc/hexane). Isolated yield = 6.3 g (91 %). ^{1}H NMR ($CDCl_3$, 500 MHz, 22 ºC): δ 9.29 (s, 1H, C_6-H), 8.52 (d, 1H, J_{HH} = 8.3 Hz, C_{10}-H), 8.26 (s, 1H, C_3-H), 8.03 (d, 1H, J_{HH} = 7.9 Hz, C_7-H), 7.90-7.77 (overlapped m, 2H, C_1-H, C_9-H), 7.70 (app t, 1H, J_{HH} = 7.5 Hz, C_8-H), 2.57 ppm (s, 3H, CH_3). ^{13}C{^{1}H} NMR ($CDCl_3$, 300 MHz, 22 °C): δ 153.5 (C_6), 144.3 (C_{Ar}), 142.8 (C_{Ar}), 140.0 (C_{Ar}), 137.8 (C_{Ar}), 134.1 (C_1), 132.1 (C_{Ar}), 131. 3 (C_9), 129.0 (C_7), 128.1 (C_8), 126.6 (C_{Ar}), 125.6 (C_{Ar}), 125.4 (C_{Ar}), 122.1 (C_{10}), 121.7 (C_3), 21.7 ppm (CH_3).

Preparation of 2-methyl-4-nitrophenanthridine (1-NO_2): An identical procedure to the synthesis of 4-bromo-2-methylphenanthridine was employed, using $Pd(PPh_3)_4$ (0.42 g, 0.36 mmol), 2-iodo-6-nitro-*p*-toluidine (5.02 g, 18.0 mmol), and 2-formylphenylboronic acid (3.01 g, 20.0 mmol). Following column chromatography (R_f = 0.25; 1:5 EtOAc/hexane), isolated yield of yellow-brown solid = 4.0 g (93 %). ^{1}H NMR ($CDCl_3$, 300 MHz, 22 °C): δ 9.34 (s, 1H, C_6-H), 8.61 (d, 1H, J_{HH} = 8.3 Hz, C_{10}-H), 8.54 (s, 1H, C_3-H), 8.11 (d, 1H, J_{HH} = 7.9 Hz, C_7-H), 7.99-7.89 (m, 1H, C_9-H), 7.88-7.71 (overlapped m, 2H; C_1-H, C_8-H), 2.69 ppm (s, 3H, CH_3). ^{13}C{^{1}H} NMR ($CDCl_3$, 300 MHz, 22 °C): δ 155.1 (C_6), 149.3 (C_{Ar}), 136.8 (C_{Ar}), 134.3 (C_{Ar}), 132.0 (C_8), 131.3 (C_{Ar}), 129.3 (C_7), 128.9 (C_9), 126.7 (C_{Ar}), 125.6 (C_{Ar}), 125.5 (C_3), 123.8 (C_1), 122.2 (C_{10}), 21.9 ppm (CH_3).

Preparation of 4-amino-2-methylphenanthridine (1-NH_2): To a stirred solution of **4-NO_2** (5.02 g, 21.0 mmol) in methanol (100 mL), Zn dust (2.75 g, 42.0 mmol), and hydrazinium monoformate solution (54 mL; prepared by slowly neutralizing equal molar amounts of hydrazine hydrate (50 mL) with 85% formic acid (4 mL) in an ice-water bath) were added, and stirred vigorously at 60 °C. The resulting green suspension was cooled and filtered using celite. The filtrate was pumped dry, the residue dissolved in CH_2Cl_2 (100 mL), and washed with brine (3 x 60

mL). The organic layer was dried over Na_2SO_4, filtered, and the volatiles removed to leave a green-brown solid, which was purified using column chromatography (basic alumina, R_f = 0.25; 1:5 EtOAc/hexane). Isolated yield = 3.74 g (86 %). ^{1}H NMR ($CDCl_3$, 300 MHz, 22 °C): δ 9.07 (s, 1H, C_6-H), 8.52 (d, 1H, J_{HH} = 8.3 Hz, C_{10}-H), 7.97 (d, 1H, J_{HH} = 7.9 Hz, C_7-H), 7.86-7.74 (m, 1H, C_9-H), 7.69-7.61 (overlapped m, 2H; C_1-H, C_8-H), 6.85 (s, 1H, C_3-H), 4.96 (br s, 2H, N-H), 2.51 ppm (s, 3H, CH_3). ^{13}C{^{1}H} NMR ($CDCl_3$, 300 MHz, 22 °C): δ 149.4 (C_6), 144.5 (C_{Ar}), 137.8 (C_{Ar}), 132.6 (C_{Ar}), 132.0 (C_{Ar}), 130.4 (C_{Ar}), 128.6 (C_{Ar}), 127.1 (C_{Ar}), 126.8 (C_{Ar}), 124.6 (C_{Ar}), 122.4 (C_{Ar}), 113.1 (C_{Ar}), 110.9 (C_3), 22.4 ppm (CH_3).

4-nitro-2-*tert*-butylphenanthridine (2-NO_2): A 500 mL Teflon-stoppered flask was charged with $Pd(PPh_3)_4$ (1.03 g, 0.89 mmol), and 50 mL of DME. After stirring briefly to mix, 2-iodo-6-nitro-4-*tert*-butylaniline (5.73 g, 17.91 mmol), 2-formylphenylboronic acid (2.96 g, 19.70 mmol) and an additional 70 mL of DME were added, followed by Na_2CO_3 (5.69 g, 53.73 mmol) dissolved in 100 mL of degassed water. The flask was then sealed and the mixture stirred vigorously for 6 h in an oil bath (130 °C). The flask was then allowed to cool, charged with 130 mL of 2M HCl, and refluxed for additional 2 h. The reaction mixture was cooled, neutralized with NaOH, and pumped to dryness. The residue was then taken up in dichloromethane (100 mL) and washed with brine (3 x 100 mL). The organic layer was separated, dried over Na_2SO_4 and volatiles removed. Column chromatography on silica gave a pale yellow solid (R_f = 0.42; 20% EtOAc/hexane). Isolated yield = 5.54 g (96 %). ^{1}H NMR ($CDCl_3$, 500 MHz, 22 °C): δ 9.48 (s, 1H; $C_{Ar}H$), 9.01 (d, 1H, J_{HH} = 1.7 Hz; $C_{Ar}H$), 8.67 (d, 1H, J_{HH} = 8.3 Hz; $C_{Ar}H$), 8.25-8.13 (m, 2H; $C_{Ar}H$), 8.05 (ddd, 1H, J_{HH} = 8.4, 7.1, 1.4 Hz; $C_{Ar}H$), 7.87 (ddd, 1H, J_{HH} = 8.0, 7.1, 1.0 Hz; $C_{Ar}H$). ^{13}C{^{1}H} NMR ($CDCl_3$, 125 MHz, 22 °C): δ 158.0 (C_{Ar}), 149.8 (C_{Ar}), 137.5 (C_{Ar}), 133.1 (C_{Ar}), 131.2 (C_{Ar}), 130.0 (C_{Ar}), 128.4 (q,

C_{Ar}), 126.9 (C_{Ar}), 126.0 (C_{Ar}), 124.4 (C_{Ar}), 123.2 (C_{Ar}), 122.3 (C_{Ar}), 118.7 (C_{Ar}). $^{19}F\{^{1}H\}$ NMR ($CDCl_3$, 470 MHz, 22 °C): δ -62.03 ppm.

4-amino-2-*tert*-butylphenanthridine (2-NH$_2$): To a stirred solution of 4-nitro-2-*tert*-butylphenanthridine (4.5 g, 16.1 mmol) in methanol (100 mL), Zn dust (2.1 g, 32.2 mmol), and hydrazinium monoformate solution (54 mL; prepared by slowly neutralizing equal molar amounts of hydrazine hydrate (50 mL) with 85% formic acid (4 mL) in an ice-water bath) were added, and stirred vigorously at 60 °C. The resulting green suspension was cooled and filtered using celite. The filtrate was pumped dry, the residue dissolved in dichloromethane (100 mL), and washed with brine (3 x 60 mL). The organic layer was separated, dried over Na_2SO_4 and dried to leave a green-brown solid, which was purified using column chromatography (silica, R_f = 0.29; 20% EtOAc/hexane). Isolated yield = 3.74 g (86 %). ^{1}H NMR ($CDCl_3$, 300 MHz, 25 °C): δ 9.10 (s, 1H, $C_{Ar}H$), 8.61 (dd, 1H, J_{HH} = 8.5, 1.1 Hz; $C_{Ar}H$), 8.00 (dd, 1H, J_{HH} = 7.9, 1.5 Hz; $C_{Ar}H$), 7.93 (d, 1H, J_{HH} = 1.9, $C_{Ar}H$), 7.81 (app td, 1H, J_{HH} = 8.4, 7.0, 1.4 Hz; $C_{Ar}H$), 7.65 (app td, 1H, J_{HH} = 8.0, 7.0, 1.1 Hz; $C_{Ar}H$), 7.14 (d, 1H, J_{HH} = 1.9 Hz; $C_{Ar}H$), 5.01 (s, 2H, NH_2), 1.48 ppm (s, 9H, *t*Bu-*H*). $^{13}C\{^{1}H\}$ NMR ($CDCl_3$, 75 MHz, 22 °C): δ 150.9 (C_{Ar}), 149.8 (C_{Ar}), 144.3 (C_{Ar}), 133.1 (C_{Ar}), 132.1 (C_{Ar}), 130.5 (C_{Ar}), 128.7 (C_{Ar}), 127.1 (C_{Ar}), 126.9 (C_{Ar}), 124.2 (C_{Ar}), 122.4 (C_{Ar}), 110.1 (C_{Ar}), 107.1 (C_{Ar}), 35.3 ((CCH$_3$)$_3$), 31.6 ppm (CH$_3$).

Synthesis of ^{Me,Phen}NN(H)N^{Quin,H} (4-methyl-phenanthridinyl)(8-quinolinyl)amine (L2): A 500 mL Teflon-stoppered flask was charged with $Pd(OAc)_2$ (0.25 g, 1.10 mmol), 1,2-diphenylphosphinoferrocene (dppf; 0.96 g, 1.76 mmol), and toluene (30 mL). After stirring briefly, **4-Br** (6.01 g, 22.0 mmol), 8-aminoquinoline (3.33 g, 23 mmol) and an additional 120 mL of toluene were added, followed by sodium *tert*-pentoxide (NaO*t*Pen; 3.60 g, 33.0 mmol) and the mixture stirred vigorously for 72 h in an oil bath (150 °C). After cooling the flask and removing

the volatiles, the residue was taken up in CH_2Cl_2 (120 mL), and the resulting suspension filtered over celite and dried to leave a red solid, which was purified using column chromatography (basic alumina; 1:5 EtOAc/hexane; $R_f = 0.5$). Isolated yield = 6.8 g (93 %). ^{1}H NMR ($CDCl_3$, 500 MHz, 22 °C): δ 10.69 (br s, 1H, N-H), 9.27 (s, 1H, C_6-H), 8.99 (dd, 1H, J_{HH} = 4.1, 1.7 Hz; $^{Quin}C_{Ar}$-H), 8.57 (d, 1H, J_{HH} = 8.3 Hz; $^{Phen}C_{Ar}$-H), 8.14 (dd, 1H, J_{HH} = 8.2, 1.6 Hz; $^{Quin}C_{Ar}$-H), 8.04 (d, 1H, J_{HH} = 7.7 Hz; $^{Phen}C_{Ar}$-H), 7.94 (d, 1H, J_{HH} = 7.6 Hz; $^{Quin}C_{Ar}$-H), 7.86 (s, 1H, $^{Phen}C_{Ar}$-H), 7.85 (s, 1H, $^{Phen}C_{Ar}$-H), 7.83-7.77 (m, 1H, $^{Phen}C_{Ar}$-H), 7.67 (app t, 1H, J_{HH} = 7.7 Hz; $^{Phen}C_{Ar}$-H), 7.54 (app t, 1H, J_{HH} = 7.9 Hz, $^{Quin}C_{Ar}$-H), 7.45 (dd, 1H, J_{HH} = 8.2, 4.2 Hz; $^{Quin}C_{Ar}$-H), 7.32 (d, 1H, J_{HH} = 8.1 Hz, $^{Quin}C_{Ar}$-H), 2.65 ppm (s, 3H, CH_3). $^{13}C\{^1H\}$ NMR ($CDCl_3$, 500 MHz, 22 °C): δ 150.1 ($^{Phen}C_{Ar}H$), 148.1 ($^{Quin}C_{Ar}H$), 140.2 (C_{Ar}), 139.4 (C_{Ar}), 139.2 (C_{Ar}), 137.5 (C_{Ar}), 136.2 ($^{Quin}C_{Ar}H$), 133.8 (C_{Ar}), 132.6 (C_{Ar}), 130.6 ($^{Phen}C_{Ar}H$), 129.1 (C_{Ar}), 128.7 ($^{Phen}C_{Ar}H$), 127.3 ($^{Quin}C_{Ar}H$), 127.2 ($^{Phen}C_{Ar}H$), 126.4 (C_{Ar}), 124.8 (C_{Ar}), 122.4 ($^{Phen}C_{Ar}H$), 121.7 ($^{Quin}C_{Ar}H$), 117.7 ($^{Quin}C_{Ar}H$), 112.8 ($^{Phen}C_{Ar}H$), 112.6 ($^{Phen}C_{Ar}H$), 109.8 ($^{Quin}C_{Ar}H$), 22.9 ppm (CH_3). UV-Vis (DMF): λ (ε) 267 (45 400), 308 (14 700), 392 nm (17 650 $M^{-1}cm^{-1}$).

Synthesis of ^{Me,Phen}NN(H)N^{Phen,Me} *bis*(4-methylphenanthridinyl)amine (L3): A 500 mL Teflon-stoppered flask was charged with $Pd(OAc)_2$ (0.25 g, 1.10 mmol), dppf (0.96 g, 1.76 mmol), and 30 mL of toluene and stirred briefly. Next, **4-Br** (6.02 g, 22.1 mmol), **4-NH$_2$** (5.01 g, 24.0 mmol) and an additional 120 mL of toluene were added, followed by NaO*t*Pen (3.60 g, 32.6 mmol). The flask was then sealed and the mixture stirred vigorously for 72 h in an oil bath (150 °C) then dried *in vacuo*. Isolation and work up was as for **L2** ($R_f = 0.5$; 1:5 EtOAc/hexane). Isolated yield = 7.9 g (90 %). ^{1}H NMR ($CDCl_3$, 300 MHz, 22 °C): δ 10.63 (br s, 1H, N-H), 9.29 (s, 2H, C_6-H), 8.61 (d, 2H, J_{HH} = 8.3 Hz, C_{10}-H), 8.08 (app d, 2H, J_{HH} = 8.0 Hz, C_7-H), 7.90-7.80 (overlapped m, 6H; C_1-H, C_3-H, C_9-H), 7.73-7.67 (app t, 2H, J_{HH} = 7.5 Hz, C_8-H), 2.67 ppm (s, 6H, CH_3).

$^{13}C\{^{1}H\}$ NMR ($CDCl_3$, 300 MHz, 22 °C): δ 150.1 ($^{Phen}C_{Ar}H$), 139.7 ($^{Phen}C_{Ar}$), 137.6 ($^{Phen}C_{Ar}$), 133.9 ($^{Phen}C_{Ar}$), 132.7 ($^{Phen}C_{Ar}$), 130.7 ($^{Phen}C_{Ar}H$), 128.8 ($^{Phen}C_{Ar}H$), 127.3 ($^{Phen}C_{Ar}H$), 127.0 ($^{Phen}C_{Ar}$), 124.9 ($^{Phen}C_{Ar}$), 122.5 ($^{Phen}C_{Ar}H$), 112.7 ($^{Phen}C_{Ar}H$), 112.5 ($^{Phen}C_{Ar}H$), 23.0 ppm (CH_3). UV-Vis (DMF): λ (ε) 266 (44 800), 297 (24 500), 307 (shoulder), 382 nm (17 050 $M^{-1}cm^{-1}$).

Synthesis of ^{tBu,Phen}NN(H)N^{Quin,H} (4-*tert*-butyl-phenanthridinyl)(8-quinolinyl)amine (L4): A 500 mL Teflon-stoppered flask was charged with $Pd_2(dba)_3$ (0.26 g, 0.30 mmol), BINAP (0.42 g, 0.70 mmol) and toluene (30 mL). After stirring for 5 minutes, 8-bromoquinoline (2.0 g, 10.1 mmol), 4-amino-2-*tert*-butylphenanthridine (2.5 g, 10.1 mmol), and an additional 20 mL of toluene were added, followed by sodium *tert*-butoxide (NaO^{t}Bu; 1.4 g, 15.1 mmol). The reaction mixture was stirred and subject to reflux in an oil bath at 150 °C for 72 h. After cooling the flask, the volatiles were removed, and the residue was taken up in dichloromethane. The suspension was then filtered over a silica plug and the solvent was removed to leave a brown solid. Isolated yield = 3.8 g (> 99 %). ^{1}H NMR (C_6D_6, 500 MHz, 25 °C): δ 11.58 (s, 1H, N-H), 9.10 (s, 1H, $C_{Ar}H$), 8.73 (dd, 1H, J_{HH} = 4.3, 1.6 Hz, $C_{Ar}H$), 8.40 (d, 1H, J_{HH} = 8.3 Hz, $C_{Ar}H$), 8.32 (s, 1H, $C_{Ar}H$), 8.12-8.05 (m, 2H, C_{11}-H, $C_{Ar}H$), 7.59 (dd, 1H, J_{HH} = 8.2, 1.6 Hz, $C_{Ar}H$), 7.44 (d, 1H, J_{HH} = 7.9 Hz, $C_{Ar}H$), 7.39 (m, 2H, C_4-H, $C_{Ar}H$), 7.20 (t, 1H, J_{HH} = 7.4 Hz, $C_{Ar}H$), 7.06 (d, 1H, J_{HH} = 8.2 Hz, $C_{Ar}H$), 6.83 (dd, 1H, J_{HH} = 8.2, 4.1 Hz, $C_{Ar}H$), 1.46 ppm (s, 9H, *t*Bu). $^{13}C\{^{1}H\}$ NMR ($CDCl_3$, 125 MHz, 25 °C): δ 150.5 (C_{Ar}), 150.5 (C_{Ar}), 148.0 (C_{Ar}), 140.8 (C_{Ar}), 140.2 (C_{Ar}),140.0 (C_{Ar}), 135.9 (C_{Ar}), 134.6 (C_{Ar}), 133.3 (C_{Ar}), 130.5 (C_{Ar}), 129.5 (C_{Ar}), 129.0 (C_{Ar}), 127.5 (C_{Ar}), 127.3 (C_{Ar}), 127.1 (C_{Ar}), 124.7 (C_{Ar}), 122.4 (C_{Ar}), 121.8 (C_{Ar}), 117.6 (C_{Ar}), 110.3 (C_{Ar}), 109.3 (C_{Ar}), 108.9 (C_{Ar}), 35.6 ((CCH$_3$)$_3$), 31.7 ppm (CH$_3$).

Synthesis of (^{Me,Phen}NNN^{Quin,H})NiCl (L2-NiCl): NiCl•6H_2O (0.14 g, 0.6 mmol) and NaO*t*Bu (60 mg, 0.63 mmol) were added as solids to a solution of **L2** (0.2 g, 0.6 mmol) in CH_2Cl_2 (10 mL) and the mixture stirred vigorously at 50 °C for 12 h. The resulting red suspension was allowed to cool and the volatiles removed *in vacuo*. The residue was then washed with diethyl ether (3 x 10 mL) and ethanol (3 x 10 mL). While the solubility of **L2-NiCl** is poor in general, it was observed to be highest in $CHCl_3$ compared with other common organic solvents. Isolated yield = 0.209 g (81 %). ^{1}H NMR ($CDCl_3$, 300 MHz, 22 °C): δ 9.05 (s, 1H, C_{Ar}-H), 8.71 (d, 1H, J_{HH} = 4.8 Hz, C_{Ar}-H), 8.43 (d, 1H, J_{HH} = 8.3 Hz, C_{Ar}-H), 8.13 (d, 1H, J_{HH} = 8.2 Hz, C_{Ar}-H), 7.97 (d, J_{HH} = 1H, 7.9 Hz, C_{Ar}-H), 7.85 (t, 1H, J_{HH} = 7.6 Hz, C_{Ar}-H), 7.64 (t, 1H, J_{HH} = 7.5 Hz, C_{Ar}-H), 7.55 (d, 1H, J_{HH} = 7.9 Hz, C_{Ar}-H), 7.50-7.32 (overlapped m, 3H, C_{Ar}-H), 7.29 (t, 1H, J_{HH} = 5.4 Hz, C_{Ar}-H), 6.93 (d, 1H, J_{HH} = 8.0 Hz), 2.58 ppm (s, 3H, CH_3). ^{13}C{^{1}H} NMR ($CDCl_3$, 500 MHz, 22 °C): 154.1 (C_{Ar}H), 150.5 (C_{Ar}H), 148.4 (C_{Ar}), 148.3 (C_{Ar}), 147.7 (C_{Ar}), 140.8 (C_{Ar}), 139.9 (C_{Ar}H), 138.6 (C_{Ar}H), 133.0 (C_{Ar}), 132.6 (C_{Ar}H), 130.0 (C_{Ar}H), 129.8 (C_{Ar}), 129.5 (C_{Ar}H), 127.8 (C_{Ar}H), 126.3 (C_{Ar}), 125.5 (C_{Ar}), 122.4 (C_{Ar}H), 121.1 (C_{Ar}H), 22.8 ppm (CH_3). UV-Vis (DMF): λ (ε) 282 (25 750), 311 (21 800), 337 (13 200), 360 (sh), 400 (sh), 485 nm (8 400 $M^{-1}cm^{-1}$). Anal. Calcd for $C_{23}H_{16}N_3NiCl$: C, 64.46; H, 3.76. Found: C, 64.30; H, 3.99.

Synthesis of (^{Me,Phen}NNN^{Quin,H})PdCl (L2-PdCl): To a stirred solution of **L2** (0.22 g, 0.66 mmol) in 10 mL of THF, Pd(COD)Cl_2 (0.17 g, 0.60 mmol), and NaO*t*Bu (0.060 g, 0.63 mmol) were added, and the mixture stirred vigorously at 70 °C for 12 h. The resulting red suspension was allowed to cool, and the volatiles removed *in vacuo*. The residue was then washed with diethyl ether (3 x 10 mL) and ethanol (3 x 10 mL). Solubility is similar to **L2-NiCl**. Isolated yield = 0.228 g (83 %). ^{1}H NMR ($CDCl_3$, 500 MHz, 22 °C): δ 9.27 (s, 1H, C_{Ar}-H), 8.96 (br s, 1H, C_{Ar}-H), 8.43 (d, 1H, J_{HH} = 8.6 Hz, C_{Ar}-H), 8.17 (d, 1H, J_{HH} = 8.0 Hz, C_{Ar}-H), 8.00 (d, 1H, J_{HH} = 7.9 Hz, C_{Ar}-

H), 7.86 (app t, 1H, J_{HH} = 7.3 Hz, C_{Ar}-H), 7.67 (app t, 1H, J_{HH} = 7.0 Hz, C_{Ar}-H), 7.54 (s, 1H, C_{Ar}-H), 7.48-7.43 (overlapped m, 2H, C_{Ar}-H), 7.40-7.31 (m, 1H, C_{Ar}-H), 7.0 (br s, 1H, C_{Ar}-H), 2.60 ppm (s, 3H, CH_3). $^{13}C\{^1H\}$ NMR ($CDCl_3$, 500 MHz, 22 °C): δ 151.8 ($C_{Ar}H$), 149.9 (C_{Ar}), 149.8 (C_{Ar}), 148.9 ($C_{Ar}H$), 148.3 (C_{Ar}), 141.4 (C_{Ar}), 140.1 ($C_{Ar}H$), 138.7 ($C_{Ar}H$), 132.8 (C_{Ar}), 132.7 ($C_{Ar}H$), 131.3 (C_{Ar}), 129.9 ($C_{Ar}H$), 129.6 ($C_{Ar}H$), 128.1 ($C_{Ar}H$), 126.9 (C_{Ar}), 126.2 ($C_{Ar}H$), 122.6 ($C_{Ar}H$), 121.2 ($C_{Ar}H$), 114.8 ($C_{Ar}H$), 114.2 (C_{Ar}), 112.5 (C_{Ar}), 110.7 (C_{Ar}), 22.8 ppm (CH_3). UV-Vis (DMF): λ (ε) 266 (30 000), 277 (28 850), 307 (22 050), 336 (sh), 392 (4 250), 489 nm (9 950 $M^{-1}cm^{-1}$). Anal. Calcd for $C_{23}H_{16}N_3PdCl$: C, 58.00; H, 3.39. Found: C, 57.54; H, 3.37.

Synthesis of (^{Me,Phen}NNN^{Quin,H})PtCl (L2-PtCl): To a stirred solution of compound **L2** (0.20 g, 0.60 mmol) in 10 mL of THF, Pt(COD)Cl_2 (0.22g, 0.60 mmol), and NaO*t*Bu (0.06 g, 0.63 mmol) were added, and the mixture stirred vigorously at 70 °C for 12 h. The resulting red suspension was allowed to cool, and the volatiles removed *in vacuo*. The residue was then was washed with diethyl ether (3 x 10 mL) and acetonitrile (3 x 10 mL). Solubility is similar to **L2-NiCl** and **L2-PdCl**. Isolated yield = 0.239 g (71 %). ^1H NMR ($CDCl_3$, 500 MHz, 22 °C): δ 9.49 (s, 1H, C_{Ar}-H), 9.17 (d, 1H, J_{HH} = 4.7 Hz, C_{Ar}-H), 8.40 (d, 1H, J_{HH} = 8.2 Hz, C_{Ar}-H), 8.22 (d, 1H, J_{HH} = 8.1 Hz, C_{Ar}-H), 8.02 (d, 1H, J_{HH} = 7.8 Hz, C_{Ar}-H), 7.86 (app t, 1H, J_{HH} = 7.5 Hz, C_{Ar}-H), 7.67-7.65 (overlapped m, 2H, C_{Ar}-H), 7.53 (s, 1H, C_{Ar}-H), 7.47-7.40 (overlapped m, 2H, C_{Ar}-H), 7.36 (dd, 1H, J_{HH} = 7.9, 4.9 Hz; C_{Ar}-H), 6.97 (d, 1H, J_{HH} = 7.7 C_{Ar}-H), 2.60 ppm (s, 3H, CH_3). $^{13}C\{^1H\}$ NMR ($CDCl_3$, 500 MHz, 22 °C): δ 151.1 ($C_{Ar}H$), 149.3 (C_{Ar}), 149.2 (C_{Ar}), 148.7 (C_{Ar}), 148.3 ($C_{Ar}H$), 142.2 (C_{Ar}), 140.0 ($C_{Ar}H$), 138.8 ($C_{Ar}H$), 132.9 ($C_{Ar}H$), 132.7 ($C_{Ar}H$), 131.5 (C_{Ar}), 129.9 ($C_{Ar}H$), 129.4 ($C_{Ar}H$), 128.2 ($C_{Ar}H$), 127.0 (C_{Ar}), 126.2 (C_{Ar}), 122.6 ($C_{Ar}H$), 121.2 ($C_{Ar}H$), 115.4 ($C_{Ar}H$), 114.7 (C_{Ar}), 113.5 (C_{Ar}), 111.1 ($C_{Ar}H$), 22.8 (CH_3) ppm. Anal. Calcd for $C_{23}H_{16}N_3PtCl$: C, 48.90; H, 2.85. Found: C: 48.64; H: 2.87.

Synthesis of (^{Me,Phen}NNN^{Phen,Me})NiCl (L3-NiCl): To a stirred solution of **L3** (0.20 g, 0.50 mmol) in CH_2Cl_2 (10 mL), $NiCl_2$•$6H_2O$ (0.12 g, 0.50 mmol) and NaO*t*Bu (0.052 g, 0.53 mmol) were added, and then stirred vigorously at 50 °C for 12 h. The resulting red suspension was allowed to cool, and the volatiles removed *in vacuo*. The red residue was then washed with diethyl ether (3 x 10 mL) and ethanol (3 x 10 mL). Isolated yield = 0.221 g (89 %). ^{1}H NMR ($CDCl_3$, 500 MHz, 22 °C): δ 9.10 (s, 2H, C_{Ar}-H), 8.43 (d, 2H, J_{HH} = 8.3 Hz, C_{Ar}-H), 8.00 (d, 2H, J_{HH} = 8.1 Hz, C_{Ar}-H), 7.92-7.81 (m, 2H, C_{Ar}-H), 7.65 (app t, 2H, J_{HH} = 7.5 Hz, C_{Ar}-H), 7.48 (s, 2H, C_{Ar}-H), 7.36 (s, 2H, C_{Ar}-H), 2.60 ppm (s, 6H, CH_3). ^{13}C{^{1}H} NMR ($CDCl_3$, 500 MHz, 22 °C): δ 154.0 (C_{Ar}H), 139.9 (C_{Ar}H), 133.0 (C_{Ar}), 132.6 (C_{Ar}H), 130.0 (C_{Ar}H), 127.8 (C_{Ar}H), 126.3 (C_{Ar}), 125.6 (C_{Ar}H), 122.4 (C_{Ar}H), 116.24 (C_{Ar}), 113.3 (C_{Ar}), 109.2 (C_{Ar}H), 107.1 (C_{Ar}H), 23.0 ppm (CH_3). UV-Vis (DMF): λ (ε) 265 (22 300), 274 (sh), 319 (13 600), 339 (11 250), 358 (7 500), 398 (sh), 498 nm (4 100 $M^{-1}cm^{-1}$). Anal. Calcd for $C_{28}H_{20}N_3NiCl$: C, 68.27; H, 4.09. Found: C, 68.28; H, 4.11.

Synthesis of (^{Me,Phen}NNN^{Phen,Me})PdCl (L3-PdCl): To a stirred solution of **L3** (0.22 g, 0.55 mmol) in THF (10 mL), Pd(COD)Cl_2 (0.14 g, 0.50 mmol), and NaO*t*Bu (0.050 g, 0.53 mmol) were added, and the mixture stirred vigorously at 70 °C for 12 h. The resulting red suspension was allowed to cool, and the volatiles removed in *vacuo*. The red residue was then washed with diethyl ether (3 x 10 mL) and ethanol (3 x 10 mL). Isolated yield = 0.211 g (78%). ^{1}H NMR ($CDCl_3$, 500 MHz, 22 °C): δ 9.38 (s, 2H, C_{Ar}-H), 8.50 (d, 2H, J_{HH} = 8.3 Hz, C_{Ar}-H), 8.08 (d, 2H, J_{HH} = 7.9 Hz, C_{Ar}-H), 7.94-7.87 (m, 2H, C_{Ar}-H), 7.72 (app t, 2H, J_{HH} = 7.4 Hz, C_{Ar}-H), 7.67 (s, 2H, C_{Ar}-H), 7.53 (s, 2H, C_{Ar}-H), 2.66 ppm (s, 6H, CH_3). ^{13}C{^{1}H} NMR ($CDCl_3$, 500 MHz, 22 °C): δ 151.8 (C_{Ar}H), 132.8 (C_{Ar}H), 130.0 (C_{Ar}H), 128.2 (C_{Ar}H), 122.7 (C_{Ar}H), 22.9 ppm (CH_3). The poor solubility of **L3-PdCl** precluded assignment of all peaks in the ^{13}C{^{1}H} NMR spectrum. UV-Vis (DMF): λ (ε)

266 (31 350), 318(16 200), 335 (10 550), 397 (3 800), 496 nm (5 350 $M^{-1}cm^{-1}$). Anal. Calcd for $C_{28}H_{20}N_3PdCl•(CHCl_3)$: C, 52.80; H, 3.21. Found: C, 52.72; H, 3.01.

Synthesis of (^{Me,Phen}NNN^{Phen,Me})PtCl (L3-PtCl): To a stirred solution of compound **L3** (0.22 g, 0.55 mmol) in THF (10 mL), Pt(COD)Cl_2 (0.14 g, 0.5 mmol), and NaO*t*Bu (0.050 g, 0.53 mmol) were added, and the mixture stirred vigorously at 70 ºC for 12 h. The resulting red suspension was allowed to cool, and the volatiles removed in *vacuo*. The red residue was washed with diethyl ether (3 x 10 mL) and acetonitrile (3 x 10 mL). Solubility of the **L3-PtCl** was generally poor in all organic solvents. Isolated yield = 0.226 g (65 %). ^{1}H NMR ($CDCl_3$, 300 MHz, 22 °C): δ 9.58 (s, 2H, C_{Ar}-H), 8.45 (d, 2H, J_{HH} = 8.3 Hz, C_{Ar}-H), 8.07 (d, 2H, J_{HH} =7.9 Hz, C_{Ar}-H), 7.93-7.86 (m, 2H, C_{Ar}-H), 7.77-7.60 (overlapped m, 4H, C_{Ar}-H), 7.47 (s, 2H, C_{Ar}-H), 2.65 ppm (s, 6H, CH_3). $^{13}C\{^1H\}$ NMR ($CDCl_3$, 500 MHz, 22 °C): δ 151.0 ($C_{Ar}H$), 140.0 ($C_{Ar}H$), 132.7 ($C_{Ar}H$), 129.9 ($C_{Ar}H$), 128.3 ($C_{Ar}H$), 126.2 ($C_{Ar}H$), 122.7 ($C_{Ar}H$), 22.9 ppm (CH_3). Six aromatic carbon signals could not be assigned in the ^{13}C NMR spectrum due poor solubility. Anal. Calcd for $C_{28}H_{20}N_3PtCl$: C, 53.47; H, 3.20. Found: C, 52.83; H, 3.31.

Synthesis of (^{tBu,Phen}NNN^{Quin,H})NiCl (L4-NiCl): NiCl•6H_2O (0.14 g, 0.53 mmol) and NaO*t*Bu (60 mg, 0.55 mmol) were added as solids to a solution of **L4** (0.2 g, 0.53 mmol) in CH_2Cl_2 (10 mL) and the mixture stirred vigorously at 50 °C for 12 h. The resulting red suspension was allowed to cool and the volatiles removed *in vacuo*. The residue was then washed with diethyl ether (3 x 10 mL) and ethanol (3 x 10 mL). While the solubility of **L2-NiCl** is poor in general, it was observed **L4-NiCl** to be highest in $CHCl_3$ compared with other common organic solvents. Isolated yield = 0.183 g (74 %). ^{1}H NMR ($CDCl_3$, 300 MHz, 22 °C): δ 9.12 (s, 1H, C_{Ar}-H), 8.75 (d, 1H, C_{Ar}-H), 8.55 (d, 1H, C_{Ar}-H), 8.16 (d, 1H, C_{Ar}-H), 8.02 (d, 1H, C_{Ar}-H), 7.91 (t, 1H, C_{Ar}-H), 7.77-7.62 (m,

3H, C_{Ar}-H), 7.55 (d, 1H, C_{Ar}-H), 7.51-7.41 (overlapped m, 2H, C_{Ar}-H), 7.29 (t, 1H, J_{HH} = 5.4 Hz, C_{Ar}-H), 6.97 (d, 1H, C_{Ar}-H), 1.53 ppm (s, 9H, $C(CH_3)_3$).

Synthesis of (^{tBu,Phen}NNN^{Quin,H})PdCl (L4-PdCl): To a stirred solution of **L4** (0.20 g, 0.53 mmol) in 10 mL of THF, Pd(COD)Cl_2 (0.15 g, 0.53 mmol), and NaO*t*Bu (0.060 g, 0.55 mmol) were added, and the mixture stirred vigorously at 70 °C for 12 h. The resulting red suspension was allowed to cool, and the volatiles removed *in vacuo*. The residue was then washed with diethyl ether (3 x 10 mL) and ethanol (3 x 10 mL). Solubility is similar to **L4-NiCl**. Isolated yield = 0.228 g (83 %). ^{1}H NMR ($CDCl_3$, 500 MHz, 22 °C): δ 9.37 (s, 1H, C_{Ar}-H), 9.04 (d, 1H, C_{Ar}-H), 8.61 (d, 1H, C_{Ar}-H), 8.24 (d, 1H, C_{Ar}-H), 8.10 (d, 1H, C_{Ar}-H), 7.99-7.88 (m, 2H, C_{Ar}-H), 7.83 (s, 1H, C_{Ar}-H), 7.79-7.69 (m, 2H, C_{Ar}-H), 7.54 (t, 1H, C_{Ar}-H), 7.46-7.38 (overlapped m, 1H, C_{Ar}-H), 7.10 (d, 1H, C_{Ar}-H), and 1.57 ppm (s, 9H, $C(CH_3)_3$).

Synthesis of (^{tBu,Phen}NNN^{Quin,H})PdCl (L4-PdOAc): To a stirred solution of **L4** (0.20 g, 0.53 mmol) in 10 mL of THF, Pd(OAc)$_2$ (0.17 g, 0.60 mmol was added, and the mixture stirred vigorously at 70 °C for 12 h. The resulting red suspension was allowed to cool, and the volatiles removed *in vacuo*. The residue was then washed with diethyl ether (3 x 10 mL) and ethanol (3 x 10 mL). Solubility is similar to **L4-NiCl**. Isolated yield = 0.228 g (86 %). ^{1}H NMR ($CDCl_3$, 500 MHz, 22 °C): δ 8.63 (s, 1H, C_{Ar}-H), 8.55 (d, 1H, C_{Ar}-H), 8.29 (d, 1H, C_{Ar}-H), 8.19 (d, 1H, C_{Ar}-H), 8.00 (d, 1H, C_{Ar}-H), 7.89 (t, 1H, C_{Ar}-H), 7.81 (s, 1H, C_{Ar}-H), 7.75 (s, 1H, C_{Ar}-H), 7.71-7.60 (m, 1H, C_{Ar}-H), 7.47 (t, 1H, C_{Ar}-H), 7.40-7.33 (overlapped m, 1H, C_{Ar}-H), 7.02 (d, 1H, C_{Ar}-H), 2.33 (s, 3H, O-CH_3) and 1.53 ppm (s, 9H, $C(CH_3)_3$).

2.6.1. Computational Details:

All calculations were carried out using the Gaussian 09 program package.[41] Initial geometries were taken from X-ray crystallographic data and were optimized with M06/6-31+G(d,p) method.

Vibrational frequencies were computed at the same level to identify structures as energy minimum or transition state structures and to evaluate zero-point vibrational energies (ZPVE) and thermal energies at 298 K. Solvation effects (CH_2Cl_2) were modeled using the SMD approach. SMD-TDDFT calculations were conducted using M06/6-31+G(d,p) with solvent equilibration. The first 50 states were considered in all SMD-TDDFT calculations to cover UV and visible range of the spectrum.

2.7. References:

1. (a) Roznyatovskiy, V. V.; Lee, C.-H.; Sessler, J. L. *Chem. Soc. Rev.* **2013,** *42*, 1921; (b) Flamigni, L.; Encinas, S.; Barigelletti, F.; MacDonnell, F. M.; Kim, K.-J.; Puntoriero, F.; Campagna, S. *Chem. Commun.* **2000**, 1185; (c) Hayashi, K.; Nakatani, M.; Hayashi, A.; Takano, M.; Okazaki, M.; Toyota, K.; Yoshifuji, M.; Ozawa, F. *Organometallics* **2008,** *27*, 1970; (d) Hanson, K.; Roskop, L.; Djurovich, P. I.; Zahariev, F.; Gordon, M. S.; Thompson, M. E. *J. Am. Chem. Soc.* **2010,** *132*, 16247; (e) Hussain, M.; El-Shafei, A.; Islam, A.; Han, L. *Phys. Chem. Chem. Phys.* **2013,** *15*, 8401; (f) Li, Z.; Sun, W. *Dalton Trans.* **2013,** *42*, 14021; (g) He, M.; Ji, Z.; Huang, Z.; Wu, Y. *J. Phys. Chem. C* **2014,** *118*, 16518; (h) Li, Z.; Cui, P.; Wang, C.; Kilina, S.; Sun, W. *J. Phys. Chem. C* **2014,** *118*, 28764; (i) Ozawa, H.; Fukushima, K.; Urayama, A.; Arakawa, H. *Inorg. Chem.* **2015,** *54*, 8887; (j) Kuramochi, Y.; Ishitani, O. *Inorg. Chem.* **2016**, *55*, 5702; (k) Fuertes, S.; Chueca, A. J.; Peralvarez, M.; Borja, P.; Torrell, M.; Carreras, J.; Sicilia, V. *ACS Appl. Mater. Interfaces* **2016,** *8*, 16160.

2. (a) Kappaun, S.; Rentenberger, S.; Pogantsch, A.; Zojer, E.; Mereiter, K.; Trimmel, G.; Saf, R.; Moeller, K. C.; Stelzer, F.; Slugovc, C. *Chem. Mater.* **2006,** *18*, 3539; (b) Kiprof, P.; Carlson, J. C.; Anderson, D. R.; Nemykin, V. N. *Dalton Trans.* **2013,** *42*, 15120; (c) Barbon, S. M.; Staroverov, V. N.; Gilroy, J. B. *J. Org. Chem.* **2015,** *80*, 5226; (d) Yamazawa, S.; Nakashima, M.; Suda, Y.; Nishiyabu, R.; Kubo, Y. *J. Org. Chem.* **2016,** *81*, 1310.

3. Chelucci, G.; Thummel, R. P. *Chem. Rev.* **2002,** *102*, 3129.

4. Gunanathan, C.; Gnanaprakasam, B.; Iron, M. A.; Shimon, L. J. W.; Milstein, D. *J. Am. Chem. Soc.* **2010,** *132*, 14763.

5. Neufeldt, S. R.; Sanford, M. S. *Acc. Chem. Res.* **2012,** *45*, 936.

6. Krichevsky, O.; Bonnet, G. *Rep. Prog. Phys.* **2002,** *65*, 251.

7. Tumir, L.-M.; Stojkovic, M. R.; Piantanida, I. *Beilstein J. Org. Chem.* **2014,** *10*, 2930, 25 pp.

8. Park, G. Y.; Wilson, J. J.; Song, Y.; Lippard, S. J. *Proc. Natl. Acad. Sci.* **2012,** *109*, 11987.

9. (a) Lu, L.-Q.; Li, Y.; Junge, K.; Beller, M. *Angew. Chem., Int. Ed.* **2013,** *52*, 8382; (b) Chen, Q.-A.; Gao, K.; Duan, Y.; Ye, Z.-S.; Shi, L.; Yang, Y.; Zhou, Y.-G. *J. Am. Chem. Soc.* **2012,** *134*, 2442.

10. (a) Kido, J.; Endo, J. *Chem. Lett.* **1997**, 593; (b) Fukase, A.; Kido, J. *Jpn. J. Appl. Phys., Part 2* **2002,** *41*, L334.

11. Valk, J.-M.; Claridge, T. D. W.; Brown, J. M.; Hibbs, D.; Hursthouse, M. B. *Tetrahedron: Asymm.* **1995,** *6*, 2597.

12. Raszeja, L.; Maghnouj, A.; Hahn, S.; Metzler-Nolte, N. *ChemBioChem* **2011,** *12*, 371.

13. Sicilia, V.; Fuertes, S.; Martin, A.; Palacios, A. *Organometallics* **2013,** *32*, 4092.

14. Jiang, B.; Gu, Y.; Qin, J.; Ning, X.; Gong, S.; Xie, G.; Yang, C. *J. Mater. Chem. C* **2016,** *4*, 3492.

15. Mondal, R.; Giesbrecht, P. K.; Herbert, D. E. *Polyhedron* **2016,** *108*, 156.

16. (a) Jensen, K. A.; Nielsen, P. H. *Acta Chem. Scand.* **1964,** *18*, 1-10; (b) Puzas, J. P.; Nakon, R.; Petersen, J. L. *Inorg. Chem.* **1986,** *25*, 3837; (c) Peters, J. C.; Harkins, S. B.; Brown, S. D.; Day, M. W. *Inorg. Chem.* **2001,** *40*, 5083; (d) Maiti, D.; Paul, H.; Chanda, N.; Chakraborty, S.; Mondal, B.; Puranik, V. G.; Lahiri, G. K. *Polyhedron* **2004,** *23*, 831.

17. (a) Chase, P. A.; van Koten, G., Nitrogen-Based Pincers: A Versatile Platform for Organometallic Chemistry. In *The Chemistry of Pincer Compounds*, Jensen, C. M., Ed. Elsevier Science B.V.: Amsterdam, 2007; pp 181-233; (b) Gade, L. H.; Melen, R. L., New Chemistry with Anionic NNN Pincer Ligands. In *The Privileged Pincer-Metal Platform: Coordination Chemistry & Applications*, van Koten, G.; Gossage, R. A., Eds. Springer International Publishing: New York, 2016; Vol. 54, pp 179.

18. Ruiz-Castillo, P.; Buchwald, S. L. *Chem. Rev.* **2016,** *116*, 12564.

19. Tummatorn, J.; Krajangsri, S.; Norseeda, K.; Thongsornkleeb, C.; Ruchirawat, S*Org. Biomol. Chem.* **2014,** *12*, 5077.

20. Maksić, Z. B.; Barić, D.; Müller, T. *J. Phys. Chem. A* **2006,** *110*, 10135.

21. Macrae, C. F.; Edgington, P. R.; McCabe, P.; Pidcock, E.; Shields, G. P.; Taylor, R.; Towler, M.; van de Streek, J. *J. Appl. Cryst.* **2006,** *39*, 453.

22. Betley, T. A.; Qian, B. A.; Peters, J. C. *Inorg. Chem.* **2008,** *47*, 11570.

23. Harkins, S. B.; Peters, J. C. *Inorg. Chem.* **2006,** *45*, 4316.

24. Testa, A. C. *Spectrochim. Acta, Part A* **1999,** *55A*, 299.

25. Johnstone, T. C.; Lippard, S. J. *J. Am. Chem. Soc.* **2014,** *136*, 2126.

26. Norek, M.; Dresner, J.; Prochorow, J. *Acta Phys. Pol., A* **2003,** *104*, 425.

27. Sutherland, D.; Compton, C. *J. Org. Chem.* **1952,** *17*, 1257.

28. (a) Slattery, D. K.; Linkous, C. A.; Gruhn, N. E.; Baum, J. C. *Dyes Pigm.* **2001,** *49*, 21; (b) D'Andrade, B. W.; Datta, S.; Forrest, S. R.; Djurovich, P.; Polikarpov, E.; Thompson, M. E. *Org. Electron.* **2005,** *6*, 11; (c) Djurovich, P. I.; Mayo, E. I.; Forrest, S. R.; Thompson, M. E. *Org. Electron.* **2009,** *10*, 515.

29. Wopschall, R. H.; Shain, I. *Anal. Chem.* **1967,** *39*, 1514.

30. Davidson, J. J.; DeMott, J. C.; Douvris, C.; Fafard, C. M.; Bhuvanesh, N.; Chen, C.-H.; Herbert, D. E.; Lee, C.-I.; McCulloch, B. J.; Foxman, B. M.; Ozerov, O. V. *Inorg. Chem.* **2015,** *54*, 2916.

31. Yan, L.; Zhao, D.; Lan, J.; Cheng, Y.; Guo, Q.; Li, X.; Wu, N.; You, J. *Org. Biomol. Chem.* **2013,** *11*, 7966.

32. Bossi, A.; Rausch, A. F.; Leitl, M. J.; Czerwieniec, R.; Whited, M. T.; Djurovich, P. I.; Yersin, H.; Thompson, M. E. *Inorg. Chem.* **2013,** *52*, 12403.

33. (a) Zhao, Y.; Truhlar, D. G. *Theor. Chem. Acc.* **2008,** *120*, 215; (b) Lee, C.; Yang, W.; Parr, R. G. *Phys. Rev. B: Condens. Matter* **1988,** *37*, 785; (c) Stephens, P. J.; Devlin, F. J.; Chabalowski, C. F.; Frisch, M. J. *J. Phys. Chem.* **1994,** *98*, 11623.

34. Rogers, J. E.; Nguyen, K. A.; Hufnagle, D. C.; McLean, D. G.; Su, W.; Gossett, K. M.; Burke, A. R.; Vinogradov, S. A.; Pachter, R.; Fleitz, P. *J. Phys. Chem. A* **2003,** *107*, 11331.

35. Lee, C.-I.; Zhou, J.; Ozerov, O. V. *J. Am. Chem. Soc.* **2013,** *135*, 3560.

36. Tsuji, J., *Palladium Reagents and Catalysts: New Perspectives for the 21st Century*. Hoboken, NJ : Wiley: Hoboken, NJ, 2004.

37. Fulmer, G. R.; Miller, A. J. M.; Sherden, N. H.; Gottlieb, H. E.; Nudelman, A.; Stoltz, B. M.; Bercaw, J. E.; Goldberg, K. I. *Organometallics* **2010,** *29*, 2176.

38. Connelly, N. G.; Geiger, W. E. *Chem. Rev.* **1996,** *96*, 877.

39. Guthrie, D. B.; Curran, D. P. *Org. Lett.* **2009,** *11*, 249.

40. Van Rossom, W.; Asby, D. J.; Tavassoli, A.; Gale, P. A. *Org. Biomol. Chem.* **2016,** *14*, 2645.

41. Frisch, M. J.; Trucks, G. W.; Schlegel, H. B.; Scuseria, G. E.; Robb, M. A.; Cheeseman, J. R.; Scalmani, G.; Barone, V.; Mennucci, B.; Petersson, G. A.; Gaussian 09, revision A. 2; Gaussian, Inc.: Wallingford, CT, 2009.

Chapter 3: Luminescent Platinum(II) Complexes of N^N^{-}^N Amido Ligands with Benzannulated N-Heterocyclic Donor Arms

3.1. Abstract:

A platform for investigating the impact of π-extension in benzannulated, anionic pincer-type *N*^*N*$^{-}$^*N*-coordinating amido ligands and their Pt(II) complexes is presented. Based on *bis*(8-quinolinyl)amine, symmetric and asymmetric proligands bearing quinoline or π-extended phenanthridine (3,4-benzoquinoline) units are reported, along with their red-emitting, phosphorescent Pt(II) complexes of the form (*N*^*N*$^{-}$^*N*)PtCl. Comparing the photophysical properties of complexes of (quinolinyl)amido ligands with those of π-extended (phenanthridinyl)amido analogs revealed a counter-intuitive impact of site-selective benzannulation. Contrary to conventional assumptions regarding π-extension, and in contrast to isoenergetic lowest energy absorption bands and a red shift in fluorescence from the organic proligands, a blue shift of nearly 40 nm in the emission wavelength is observed for Pt(II) complexes with more extended *bis*(phenanthridinyl) ligand π-systems. Comparing the ground state and triplet excited state structures optimized from DFT and TD-DFT calculations, we trace this effect to a greater rigidity of the benzannulated complexes, resulting in a higher energy emissive triplet state, rather than to a significant perturbation of orbital energies caused by π-extension.

3.2. Introduction:

The utility of phosphorescent platinum(II) complexes in chemosensing,[1-2] bioimaging,[3-5] and light-emitting diodes[6-9] is owed both to the large spin-orbit coupling (SOC) constant of the third row transition metal, which promotes the formally forbidden $T_1 \rightarrow S_0$ radiative process, and to a well-developed coordination chemistry where ligand design is used to control color and

enhance emission.[10-11] Amongst the most brightly luminescent Pt(II) complexes, cyclometallating ligands predominate, particularly those based on 2-phenylpyridine (ppy).[12-14] Tridentate derivatives[15-19] that combine *N*-heterocycles and *C*-metallated aryl rings have also been reported as shown in Figure 3.1). In such ligand sets, the synergistic combination of strong σ-donation (C–Pt bond) and the π--accepting nature of the heterocycle stabilizes charge-transfer (CT) excited states over metal-centreed (MC) ones, limiting undesirable non-radiative decay and ligand photolability through population of d orbitals with metal-ligand anti-bonding character.[20] The multidentate, chelating ligand arrangement also increases the rigidity of the complex, suppressing excited-state distortions that can contribute to non-radiative decay pathways. This may have an additional effect, too, of enhancing color purity by reducing contributions from longer-wavelength Franck-Condon vibrational components, often particularly desirable in the design of OLED emitters.[21-22] These frameworks also increase the stability of a complex, important in high temperature processing common to device fabrication by evaporation.[23]

Once a promising ligand framework has been identified, tuning the photophysical properties commonly involves either substitution of a ligand with donor/acceptor groups or expansion of a ligand's conjugated π-system. Both strategies are understood to impact absorption/emission spectra by influencing the relative energies of the frontier orbitals (HOMO/LUMO), though not always in an obvious manner. For example, despite the prevailing expectation that extending π-conjugation via benzannulation of aromatic molecules or ligands will induce bathochromic (red) shifts in absorption/emission spectra by stabilizing ligand-based π* acceptor orbitals, both red and blue shifts in absorption/emission bands have been recorded for Pt(II) complexes of benzannulated derivatives of 1,3-*bis*(2-pyridylimino)isoindoline (BPI) ligands (Figure 1b).[24-26] Using a series of benzannulated (BPI)PtCl complexes, Thompson and colleagues[27]

detailed a general theoretical framework for understanding and predicting the direction of energy shifts caused by benzannulation. In that paradigm, the site of benzannulation is critical and the shift in absorption/emission energy can be traced to a selective stabilization or destabilization of the HOMO or the LUMO.

With this background in mind, the *bis*(quinolinyl)amido (BQA) ligand attracted our attention as an alternative *N^N⁻^N*-binding ligand, potentially well-suited to the construction of Pt(II)-based emitters (Figure 1c).[28-31] First, this tridentate, pincer-like amido ligand bears two all-sp^2 quinolinyl heterocyclic donor arms and forms robust, square planar coordination compounds with Group 10 elements with 5-membered chelate rings (in contrast to the 6-membered rings of Pt(BPI)Cl).[28] Second, unlike *N^C⁻^N* cycloplatinated complexes, which often require forcing conditions to prepare and which incorporate a central carbon donor whose strong *trans* influence can labilize *trans* disposed ligands,[32] ligands that feature anionic amido donors can be installed following more accessible deprotonation of an N–H group. Third, the strong, rigid, planar binding of the tridentate ligand suggests that a triplet state populated by light absorption might exhibit only

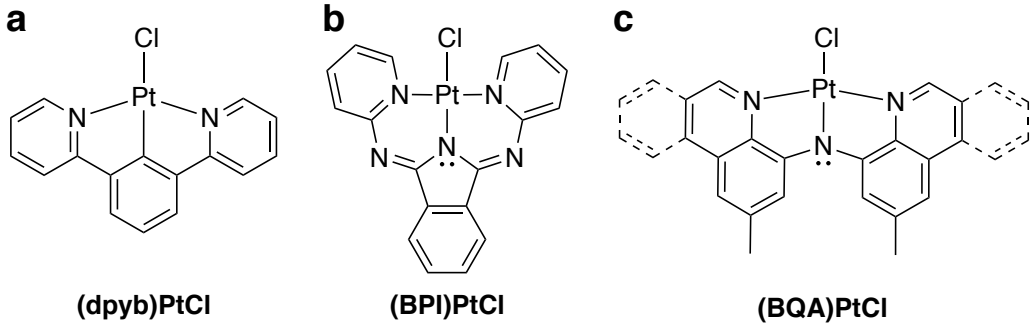

Figure 3.1. Structures of (a) (dpyb)PtCl featuring an *N^C^N*-coordinating, tridentate cyclometallated ligand, dpybH = 1,3-di(2-pyridyl)benzene; (b) (BPI)PtCl containing an *N^N⁻N*-coordinating tridentate ligand, BPI = 1,3-*bis*(2-pyridylimino)isoindoline; (c) (BQA)PtCl-derived

complexes containing benzannulated, tridentate *N*^*N*⁻*N*-coordinating ligands with either quinolinyl or phenanthridinyl donor arms, BQA = *bis*(8-quinolinyl)amine.

small structural distortions in the excited state, potentially favoring emission over non-radiative decay processes. Finally, thinking of *bis*(quinolinyl)amine as a framework, the quinolinyl arms provide a conceptual site for benzannulation to 3,4-benzoquinoline (phenanthridine) where the site-selection for π-extension should not impact the coordinating ability of the tridentate ligand; such modification contrasts with 2,3-benzannulation, for example, that converts quinoline to acridine. In this chapter I report the synthesis and luminescence properties of Pt(II) complexes of BQA pincer-type amido ligands and their benzannulated analogs. For this ligand design, neither of the prevailing predictive paradigms for understanding the impact of benzannulation on photophysical properties is appropriate: absorption and emission are not impacted in the same direction by benzannulation.

3.3. Results and Discussion:

3.3.1. Ligand Design:

Taking *bis*(8-quinolinyl)amine as the conceptual starting point, targeted synthesis of methyl-substituted *bis*(8-(6-methyl)quinolinyl)amine (**L5**) and *bis*(4-(2-methyl)phenanthridinyl)amine (**L6**) proligands, together with a "mixed" analog that incorporates one quinoline and one phenanthridine (**L3**). These compounds were prepared via Pd-catalyzed Buchwald-Hartwig coupling of methyl-substituted amino/bromoquinolines and phenanthridines as shown in Scheme 3.1. 6-(Methyl)quinolines amenable for cross-coupling were accessible via the Skraup reaction,[33] while 2-methylphenanthridine derivatives were assembled using one-pot Suzuki coupling/condensation reactions.[34] In both cases, methyl substitution improves precursor

yields over unsubstituted derivatives. Proligand synthesis proceeded efficiently and the *bis*(*N*-heterocyclic)amines **L5** and **L6** were isolated in high yields (80-90%) as yellow solids following chromatography. **L3** has been previously described.[35]

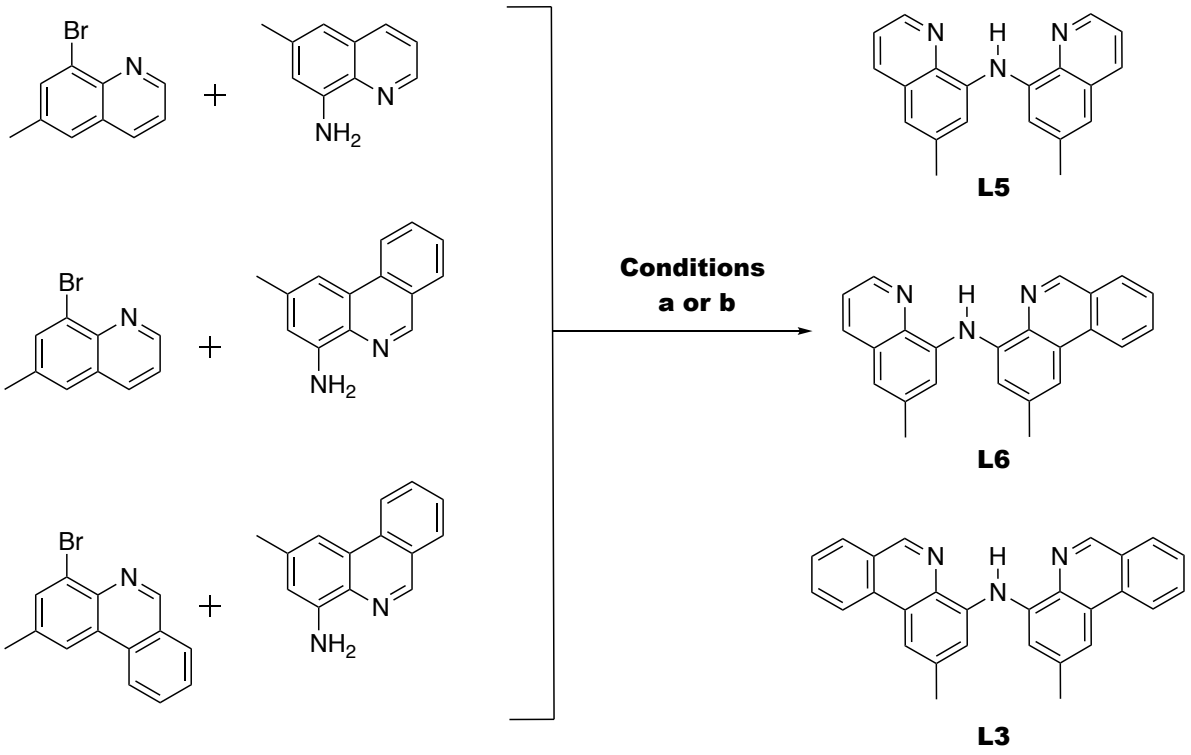

Scheme 3.1. Synthetic routes to proligands **L5**, **L6** (conditions *a*) and **L3** (conditions *b*)[35] and their corresponding Pt(II) complexes **L5-PtCl**, **L6-PtCl** and **L3-PtCl**. Conditions: *a*: $Pd_2(dba)_3$, *rac*-BINAP, NaO*t*Bu, toluene, 150 °C; *b*: $Pd(OAc)_2$, dppf, NaO(*tert*-pentoxide); toluene, 150 °C.

3.3.2: Platinum Metal Complexes of *N*^*N*⁻^*N* Ligands:

The *N*^*N*⁻^*N*-coordinated Pt(II) complexes (**L5-PtCl**, **L6-PtCl**, **L3-PtCl** from **L5**, **L6**, **L3** respectively) were prepared upon reaction of the appropriate proligands with $Pt(COD)Cl_2$ in refluxing dichloromethane, in the presence of a sodium alkoxide base as shown in Scheme 3.2.

The complexes precipitated over the course of the reaction as deep red solids. Their solubility is generally poor in standard organic solvents and benzannulation was found to further decrease the solubility. Nevertheless, ^{1}H NMR spectroscopy in solution could be used to verify ligand coordination, which was followed by the shift of the diagnostic [C*H*] resonance in the 6-position of the phenanthridinyl arms of **L6** and **L3** as shown in Table 3.1. Compound structures could thereby be confirmed by NMR spectroscopy, and their purity was established by elemental analysis.

Table 3.1. Diagnostic phenanthridinyl "imine-like" [N=C$_6$*H*] resonances for **L5**, **L6** and **L3** and **L5-PtCl**, **L6-PtCl** and **L3-PtCl**. [a] in $CDCl_3$, 295 K, 300 MHz.

Resonance[a]	**L5**	**L6**	**L3**
δ (^{1}H) C$_6$ – *H* /ppm	8.88	9.27	9.29
	L5-PtCl	**L6-PtCl**	**L3-PtCl**
δ (^{1}H) C$_6$ – *H* /ppm	9.14	9.50	9.58

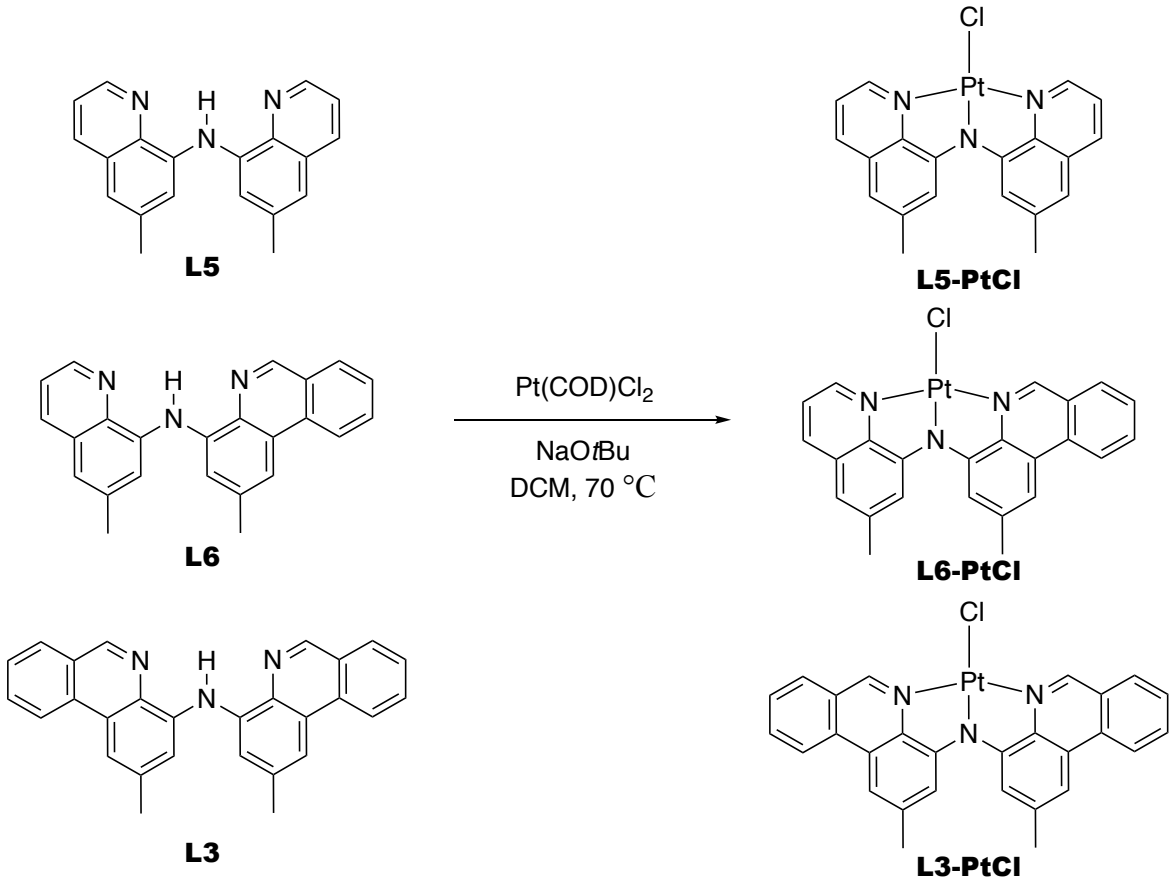

Scheme 3.2. Synthetic routes to metal complexes **L5-PtCl**, **L6-PtCl** and **L3-PtCl** using proligands **L5**, **L6** and **L3** respectively.

3.3.3: X-ray Crystallography studies:

The crystal structure of **L5-PtCl** is shown in Figure 3.2a (the structure of **L3-PtCl** was previously reported[35]). In the solid state, the ligands are rigidly planar and bind meridionally to the metal centre. The three nitrogen donor atoms of the ligands are coplanar with the coordinated metal atom, resulting in an essentially flat molecular structure. The structure of **L5-PtCl** does not include any solvent in the crystal lattice, while crystals of complex **L3-PtCl** suitable for X-ray diffraction could only be obtained with a co-crystallized molecule of chloroform[35] as shown Figure 3.2d. In the structure of **L5-PtCl**, close intermolecular π-π interactions are observed (~3.3 Å), while only

hydrogen bonding with co-crystallized $CHCl_3$ can be seen in the structure of **L3-PtCl**. The decreasing solubility in the order **L5-PtCl** > **L6-PtCl** > **L3-PtCl** is presumably attributable to similar π-π interactions as seen in the structure of **L5-PtCl**, likely enhanced by benzannulation. Crystals with sufficient long-range order for good diffraction could only be obtained if these intermolecular interactions could be disrupted, for example, through inclusion of a hydrogen bond donor solvent in the crystal lattice. As solids, all three platinum complexes show high thermal stability, which varies a little with the degree of benzannulation: 5% weight reduction was observed at temperatures of 386 °C (**L5-PtCl**), 430 °C (**L6-PtCl**) and 378 °C (**L3-PtCl**), respectively as shown in Figure 3.3.

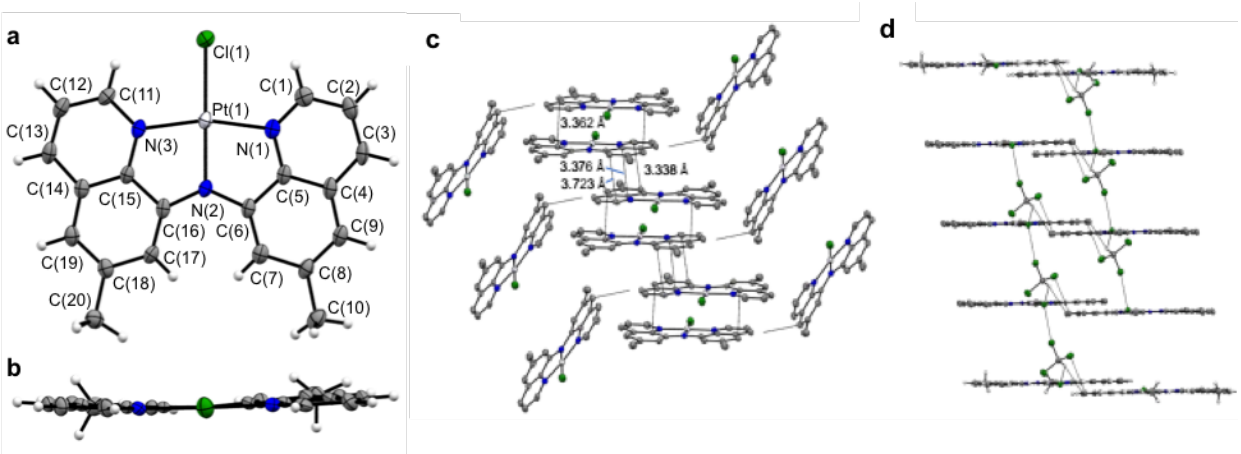

Figure 3.2. Solid-state structure of **L5-PtCl** shown (a) perpendicular to the metal square plane, and (b) along the Cl–Pt–N(2) axis. Thermal ellipsoids are shown at 50% probability and hydrogen atom labels are omitted for clarity. Packing diagrams for (c) **L5-PtCl** and (d) **L3-PtCl** with thermal ellipsoids shown at 50% probability levels. Close π-π interactions are noted for **L5-PtCl**, while hydrogen bonding interactions with co-crystallized chloroform solvent molecule are shown for **L3-PtCl**.

Selected bond distances (Å) and angles (°): Cl(1)–Pt(1) 2.339(1), N(1)–Pt(1) 1.998(4), N(2)–Pt(1) 1.971(4), N(3)–Pt(1) 2.000(4), N(1)–C(1) 1.329(6); N(1)-Pt(1)-N(3) 165.23(17), N(2)-Pt(1)-Cl(1) 179.42(11), N(1)-Pt(1)-Cl(1) 97.55(12), N(3)-Pt(1)-Cl(1) 97.10(12), N(2)-Pt(1)-N(1) 82.56(16), N(2)-Pt(1)-N(3) 82.77(16), C(6)-N(2)-C(16) 130.7(4).

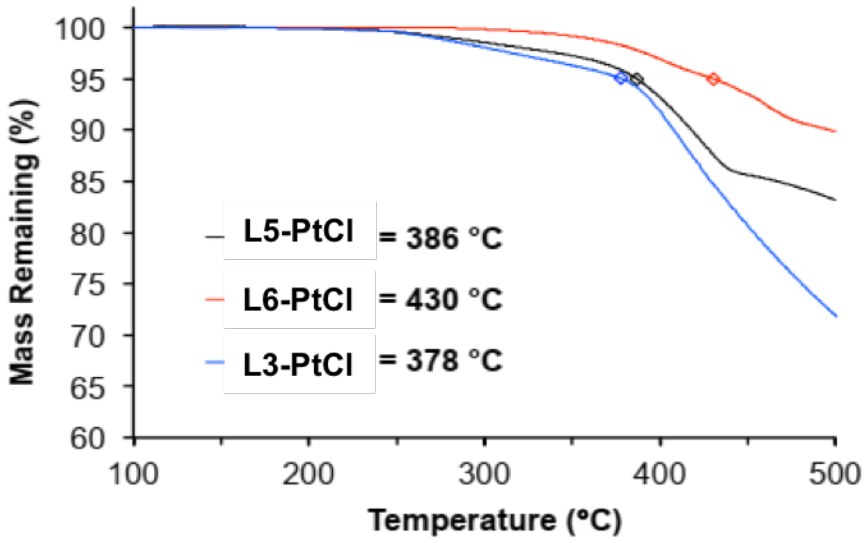

Figure 3.3. TGA traces of Platinum complexes **L5-PtCl**, **L6-PtCl** and **L3-PtCl**.

3.3.4: Photophysical Properties:

Absorption and emission spectra for the three proligands in dichloromethane solution at room temperature are shown in Figure 3.4 and associated data are compiled in Table 3.2. In its absorption spectrum, the *bis*(quinolinyl)amine proligand **L5** displays two main bands, one deep in the UV region at 270 nm and a longer wavelength band extending into the visible region, centreed at 403 nm. The *bis*(phenanthridinyl) analogue **L3** has a similar, but broader, long-wavelength band with a blue-shifted λ_{max} (388 nm), an intense band at 253 nm, and a band at 299 nm that has no counterpart in the spectrum of **L5**. The "mixed" quinoline-phenanthridine system **L6** shows

features corresponding to both **L5** and **L3**; in fact, its spectrum is nearly identical to that simulated from an average of **L5** and **L3** as shown Figure 3.5. While the peak maximum of the long wavelength band appears blue shifted in the phenanthridine-containing systems **L6** and **L3** relative to that of the *bis*(quinolinyl)amine **L5**, it should be noted that this band tails further into the visible for **L6** and **L3**, with higher absorption at $\lambda > 415$ nm, suggesting that the lowest energy transitions may indeed be lower in energy in the phenanthridine proligands with their more extended π systems. For comparison, the first-excited singlet state energies (E_S) of quinoline and phenanthridine are 31850 and 28590 cm^{-1} respectively.[36]

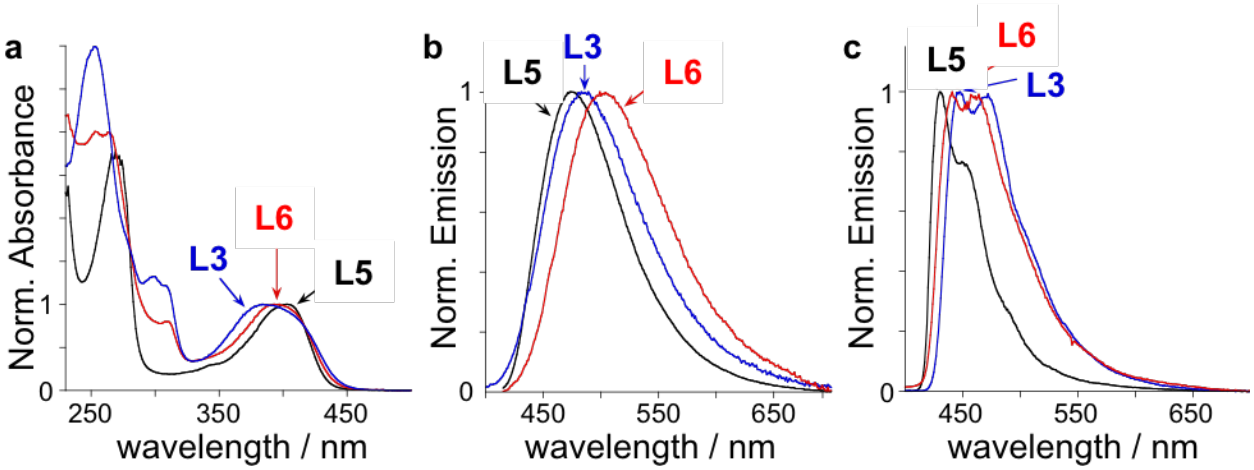

Figure 3.4. (a) UV-visible absorption spectra of proligands **L5, L6** and **L3** in CH_2Cl_2 solution at 295±1 K; Photoluminescence spectra in (b) CH_2Cl_2 solution at 295±1 K and (c) EPA at 77 K.

Table 3.2. Absorption and emission data of proligands[a] and Pt(II) complexes[b]

	Absorption λ_{max}/nm (ε / mM^{-1} cm^{-1})	**Emission** λ_{max}/nm[c]	Φ_{lum} (%)[c,d]	τ / ns[e]	k_r /10^3 s^{-1}[f]	Σk_{nr} /10^5 s^{-1}[g]	k_Q^{O2} /10^9 M^{-1} s^{-1} [h]	**Emission 77K[i]** λ_{max}/nm	**Emission 77K[i]** τ / ns
L5	269 (28.4), 344 (3.2), **403** (9.8)	474	0.55	--[i]	--	--	--	431, 451	3.5
L6	254 (26.0), 264 (27.1), 310 (7.4), **395** (9.0)	503	0.25	--[i]	--	--	--	441, 461	3.8
L3	253 (65.2), 299 (22.0), 308 (sh), **388**	485	0.20	--[i]	--	--	--	447, 471	3.2

	(15.9)								
L5-PtCl	301 (35.3), 340 (6.0), 356 (4.9), 381 (1.6), **501** (9.2)	738	0.081	1800 [230]	0.49	5.6	1.7	696, 763	2200
L6-PtCl	284 (23.7), 315 (21.8), 338 (15.3), 354 (9.8), 405 (3.0), **502** (8.5)	740	0.13	1000 [180]	1.3	10	2.1	692, 756	3000
L3-PtCl	265 (28.0), 321 (16.1), 338 (13.6), 355 (9.6), 405 (2.6), **503** (4.9)	703	0.18	2500 [190]	0.72	4.0	2.2	663, 727	18300

[a] In CH_2Cl_2 at 298±1 K and in EPA (diethyl ether/isopentane/ethanol, 2:2:1 v/v) glass at 77 K; λ_{ex} = 400 nm. [b] In degassed CH_2Cl_2 at 295±1 K, except where indicated otherwise. [c] Emission maxima and photoluminescence quantum yields Φ_{lum} determined from spectra recorded using a Synapse CCD detector. [d] Measured in deoxygenated solution (**L5-PtCl**, **L6-PtCl** and **L3-PtCl**), using $[Ru(bpy)_3]Cl_{2(aq)}$ as the standard. [e] Luminescence lifetimes in deoxygenated solution (**L5-PtCl**, **L6-PtCl** and **L3-PtCl**). Values in air-equilibrated solution are given in square parenthesis. [f] Radiative (k_r) and non-radiative (Σk_{nr}) rate constants estimated from quantum yield and lifetime, assuming unitary population of the emissive state upon light absorption: $k_r \sim \Phi / \tau$; $k_{nr} \sim (1-\Phi) / \tau$. [g] Bimolecular Stern-Volmer constant for quenching by molecular oxygen, estimated from the lifetimes in deoxygenated and air-equilibrated solution, and assuming $[O_2] = 2.2$ mmol dm^{-3} at atmospheric pressure of air. [h] In diethyl ether / isopentane / ethanol (2:2:1 v/v). [i] Emission spectra at 77 K were recorded using a Hamamatsu R928 PMT detector. [j] The lifetimes of the proligands are probably < 1 ns but the intensity is too weak to allow reliable deconvolution from the instrument response and a precise value to be obtained.

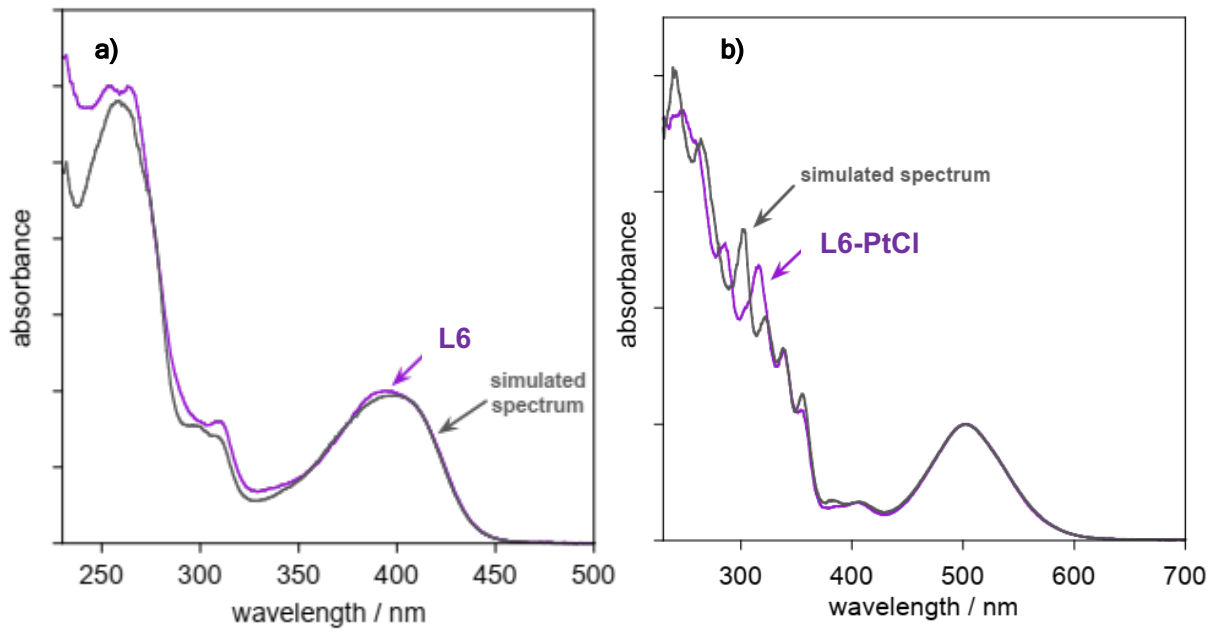

Figure 3.5 a) The UV-vis absorption spectrum in CH2Cl2 at 295 K of the quinoline- phenathridine proligand **L6** (purple) and the spectrum simulated by taking an average of the spectra of the corresponding bis-quinoline and bis-phenanthridine proligands **L5** and **L3** respectively (grey). b) The UV-visible absorption spectrum in CH_2Cl_2 at 295 K of the quinoline-phenathridine Pt(II) complex **L6-PtCl** (purple) and the spectrum simulated by taking an average of the spectra of the corresponding bis-quinoline and bis-phenanthridine complexes **L5-PtCl** and **L3-PtCl** respectively (grey).

Time-dependent density functional theory (TD-DFT) analysis assigns the lowest energy transition for all three proligands as HOMO→LUMO in nature were shown in Figure 3.6 and data is tabulated in Tables 3.3-3.5. Population analysis shows the HOMOs are comprised largely of the amino (N-H) lone pair, with contributions from the hydrocarbon portions of the heterocycle arms (shown in Figure 3.7 and Figure 3.8; Tables 3.6 – 3.8). Interestingly, for both **L6** and **L3**, the HOMO does not significantly include any orbital density located on the most distal fragments of

the benzannulated ligand moieties, *i.e.*, at the site of benzannulation. In contrast, the LUMOs of all three proligands are comprised of out-of-phase (π*) contributions from the *N*-heterocycle π systems; the LUMO of **L6** (and **L3**) are heavily influenced by benzannulation. The distinctive bands at 299 nm in the spectra of phenanthridinyl-containing **L6** and **L3**, but absent from the spectra of **L5**, arise primarily from HOMO–1→LUMO transitions. The HOMO–1 orbitals of **L6** and **L3** are higher in energy than in **L1**, and this transition is therefore likely buried deeper in the UV for the smallest ligand **L5**. The contribution from the phenanthridinyl moiety is clear here - the HOMO–1 of the asymmetric **L6** is mostly located on the phenanthridine moiety, with very little contribution from the quinolinyl arm.

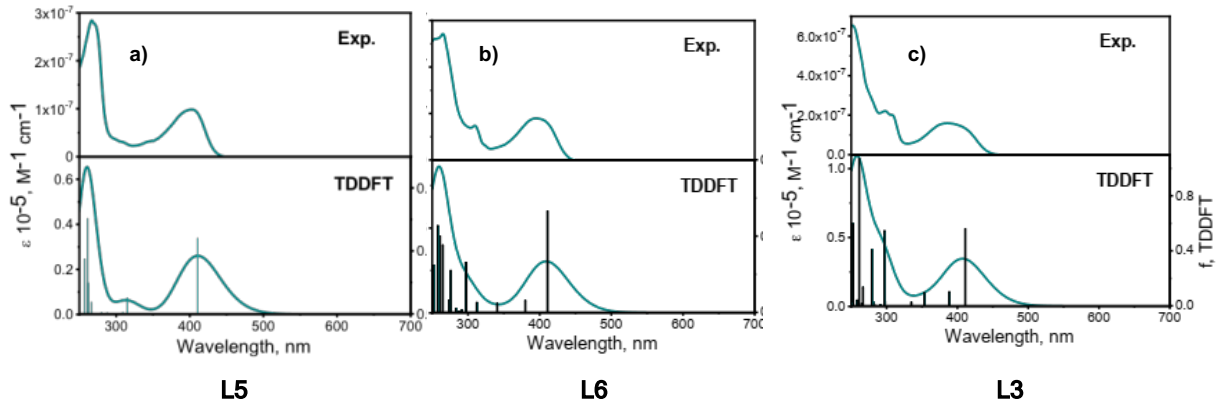

Figure 3.6. TD-DFT simulated spectrum and vertical excitation energies (bottom) with the experimental spectrum (top) of a) **L5** b) **L6** and c) **L3** in CH2Cl2 (SMD-M06/LANL2DZ/ /SMDM062x/LANL2DZ)).

Table 3.3. TD-DFT predicted vertical excitation energies, oscillator strengths (f > 0.01) and MO contributions (>10%) for **L5-PtCl**.

No.	*E*/eV	*f*	Orbital Transition	Contribution (%)
1	3.02	0.482	H--> L	98
3	3.93	0.103	H-->L+2	87
4	4.01	0.011	H-->L+3	85
7	4.42	0.010	H-5-->L	14
			H-1-->L	72
8	4.65	0.075	H-1-->L+1	62
			H-->L+4	25
9	4.72	0.197	H-3-->L+1	16
			H-2-->L	51
			H-->L+3	12
			H-3-->L	58
10	4.75	0.607	H-2-->L+1	14
			H-1-->L+3	11
			H-->L+2	11
			H-1-->L+1	29
11	4.82	0.351	H-->L+4	64
			H-5-->L	20

Table 3.4. TD-DFT predicted vertical excitation energies, oscillator strengths (f > 0.01) and MO contributions (>10%) for **L6-PtCl**.

No.	E/eV	*f*	Orbital Transition	Contribution (%)
1	3.02	0.530	H-->L	97
2	3.26	0.061	H-->L+1	96
3	3.64	0.047	H-->L+2	90
4	3.97	0.052	H-->L+3	86
5	4.17	0.261	H-1-->L	60
6	4.26	0.012	H-5-->L	39
			H-5-->L+1	11
			H-4-->L	23
8	4.38	0.018	H-5-->L	13
			H-2-->L	36
			H-1-->L	10
			H-1-->L+1	13
			H-1-->L+2	13
9	4.49	0.219	H-->L+4	81
10	4.53	0.064	H-2-->L	12
			H-2-->L+1	12
			H-1-->L+1	54
11	4.68	0.352	H-2-->L+1	59
			H-1-->L	13
			H-1-->L+1	10
12	4.75	0.400	H-3-->L	37
			H-3-->L+1	27
			H-->L+3	11
13	4.81	0.454	H-2-->L	14
			H-1-->L+2	55
14	4.92	0.246	H-2-->L+2	51
			H-->L+5	22

Table 3.5. TD-DFT predicted vertical excitation energies, oscillator strengths (f > 0.01) and MO contributions (>10%) for **L3**.

No.	E/eV	*f*	Orbital Transition	Contribution (%)
1	3.02	0.558	H-->L	97
2	3.19	0.102	H-->L+1	97
3	3.51	0.096	H-->L+2	92
4	3.70	0.025	H-->L+3	88
5	4.16	0.034	H-3-->L+1	14
			H-2-->L	53
			H-1-->L+1	11
6	4.17	0.545	H-2-->L+1	25
			H-1-->L	49
10	4.40	0.024	H-2-->L+2	15
			H-1-->L+1	46
			H-->L+4	13
11	4.44	0.405	H-->L+4	77
13	4.65	0.134	H-3-->L+1	32
			H-2-->L	39
			H-1-->L+1	18
14	4.68	0.015	H-2-->L+1	18
			H-1-->L	11
			H-->L+5	56
15	4.74	1.069	H-3-->L+1	24
			H-2-->L+2	43
			H-1-->L+3	10
16	4.79	0.041	H-3-->L	23
			H-1-->L+2	42
			H-->L+5	15
17	4.91	0.597	H-3-->L+2	60
			H-2-->L+3	17
18	4.96	0.016	H-5-->L+3	13
			H-4-->L+2	21
			H-3-->L+3	21
			H-1-->L+3	24

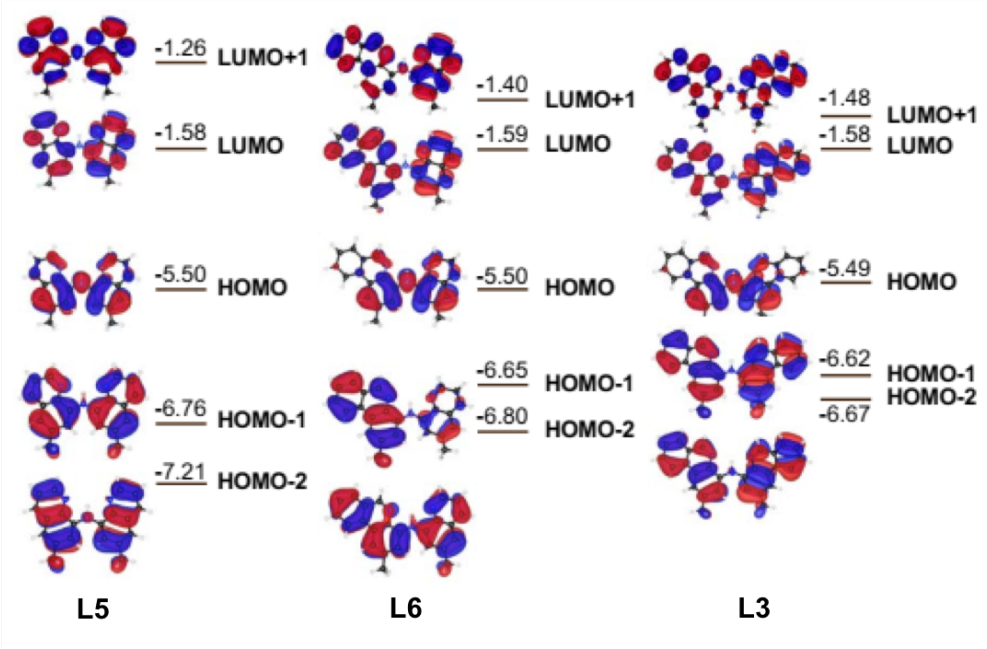

Figure 3.7. Relevant ground state MOs of **L5**, **L6**, **L3** (isosurface = 0.02; SMDM06/LANL2DZ//SMD-M062x/LANL2DZ)

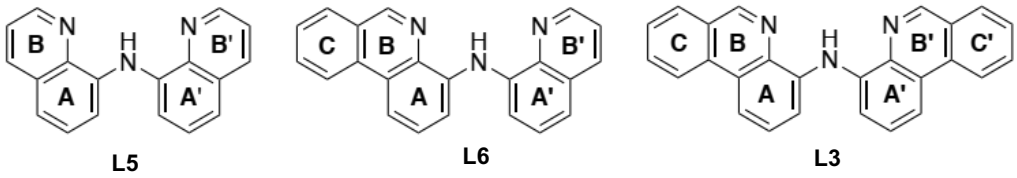

Figure 3.8. Diagram of assigned fragment contributions for **L5**, **L6** and **L3**

Table 3.6. Fragment contributions (%) to the ground state MOs of **L1** using the Hirshfeld atomic population method (SMD-M06L/6-31+G(d,p)//SMD-O3LYP/6-31+G(d,p)).

L1	*E*(eV)	NH	A	A'	B	B'
L+4	-0.29	2	33	33	15	15
L+3	-0.50	0	29	29	19	19
L+2	-0.59	0	29	29	19	19
L+1	-1.25	3	14	14	34	34
L	-1.58	1	22	22	27	27
H	-5.50	20	34	34	5	5
H-1	-6.76	2	33	33	14	14
H-2	-7.21	1	34	34	13	13
H-3	-7.23	0	32	32	16	16
H-4	-7.37	3	9	9	39	39

Table 3.7. Fragment contributions (%) to the ground state MOs of **L2** using the Hirshfeld atomic population method (SMD-M06L/6-31+G(d,p)//SMD-O3LYP/6-31+G(d,p)).

L2	*E*(eV)	NH	A	A'	B	B'	C
L+4	-0.10	1	42	6	19	5	24
L+3	-0.54	0	1	57	0	37	0
L+2	-1.04	2	32	4	21	10	31
L+1	-1.40	2	12	18	14	33	19
L	-1.59	1	17	14	32	17	17
H	-5.50	21	33	35	4	5	1
H-1	-6.65	0	42	6	17	2	29
H-2	-6.79	1	33	26	11	12	14
H-3	-7.21	1	2	63	1	27	1
H-4	-7.37	3	6	12	27	51	1

Table 3.8. Fragment contributions (%) to the ground state MOs of **L3** using the Hirshfeld atomic population method (SMD-M06L/6-31+G(d,p)//SMD-O3LYP/6-31+G(d,p)).

L3	*E*(eV)	NH	A	A'	B	B'	C	C'
L+4	-0.16	1	24	24	11	11	13	13
L+3	-0.99	2	17	17	15	15	17	17
L+2	-1.17	1	23	23	7	7	19	19
L+1	-1.48	1	10	10	21	21	18	18
L	-1.58	1	13	13	24	24	13	13
H	-5.49	21	33	33	5	5	1	1
H-1	-6.62	0	24	24	10	10	14	14
H-2	-6.67	0	23	23	8	8	18	18
H-3	-6.81	1	28	28	11	11	11	11
H-4	-7.39	2	9	9	38	38	2	2

The proligands are weakly fluorescent in solution at room temperature, each displaying a broad unstructured emission band with λ_{max} in the range 474 – 518 nm, quantum yields < 1% and lifetimes < 1 ns at room temperature (shown in Figure 3.4b, Table 3.1). Considering the impact of benzannulation, the *bis*(quinolinyl)amine proligand **L5** emits at higher energy than the phenanthridine analogues **L6** and **L3**, in line with the aforementioned differences in E_S for quinoline and phenanthridine. Comparing the room temperature and low temperature spectra, the red shift of the mixed quinoline–phenanthridine proligand **L6** relative to **L3** at ambient temperature might be explained in terms of more pronounced charge-transfer character between the different aromatic arms (quinoline→phenanthridine), evident in transitions involving the frontier orbitals in the asymmetric **L6**, which is destabilized at 77 K as shown in Figure 3.4c.

Photophysical data for the corresponding platinum complexes are compiled in Table 1. The most striking difference in the spectra of the metal complexes compared to the corresponding proligands is the appearance of an intense, broad band centered close to 500 nm. This band evidently accounts for the strong, deep red color of the complexes. The substantial displacement of the band to lower energy by some 5000 cm^{-1} relative to the lowest energy band in the proligands is intuitively consistent with the deprotonation of the amine N–H that accompanies complexation. This would be expected to increase the energy of highest occupied orbitals, while the vacant heterocycle-based π* orbitals may be conversely lowered in energy upon binding to Pt(II). The resulting decrease in the frontier orbital energy gap would produce the observed red shift, very much in line with those observed for BPI ligands (as shown in Figure 3.1) upon binding to transition metal ions.[25, 27]

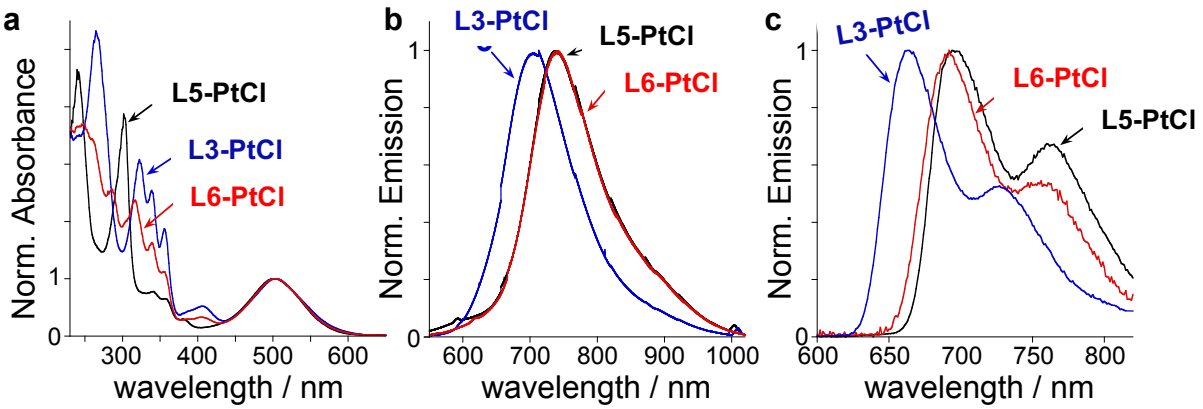

Figure 3.9. (a) UV-visible absorption spectra of Pt(II) complexes **L5-PtCl**, **L6-PtCl** and **L3-PtCl** in CH_2Cl_2 solution at 295±1 K; Photoluminescence spectra in (b) CH_2Cl_2 solution at 295±1 K and (c) EPA at 77 K.

As with the proligands, the main difference between the *bis*(quinolinyl) complex **L5-PtCl** and *bis*(phenanthridinyl) complex **L3-PtCl** is the stronger absorption of the latter in the 300–350 nm region. The "mixed" quinoline-phenanthridine system **L6-PtCl** again has an absorption spectrum that closely matches that simulated from the average of **L5-PtCl** and **L3-PtCl** as sown in Figure 3.5. All of the complexes are luminescent in deoxygenated solution at room temperature, emitting in the deep red / near-infrared region of the spectrum as shown in Figure 3.9b and Table 3.2. The emission tails into the 800–1000 nm region, a part of the spectrum where the sensitivity of conventional photomultiplier tubes falls off steeply. The recording of the emission spectra was better achieved using a CCD detector (see Experimental Section for details).

The spectra each show a single, unstructured band that is relatively narrow compared to many red/NIR-emitting transition metal-based phosphors (FWHM ~ 2300 cm^{-1}).[37-40] Interestingly, and counterintuitively, amongst the series **L5-PtCl**, **L6-PtCl** and **L3-PtCl**, the *bis*(phenanthridinyl) complex **L3-PtCl** unequivocally emits at higher energy than the quinoline-

containing complexes, despite the more extended conjugation of phenanthridine compared to quinoline and the isoenergetic absorption maxima. Furthermore, the spectrum of the mixed quinoline-phenanthridine **L6-PtCl** is essentially identical to that of *bis*(quinoline) **L5-PtCl**, suggesting that the emissive excited state in the former involves the quinoline rather than the phenanthridine. At 77 K, a vibrational 0,1 band is resolved to low energy of the main 0,0 component in each case,[41] but the trend in emission energies **L3-PtCl** > **L6-PtCl** ~ **L5-PtCl** is retained as shown in Figure 3.9c. This counterintuitive trend is reminiscent of an unexpected blue-shift, observed by Thompson and co-workers, in the phosphorescence of Pt(*N^C*-dbq)(dpm) compared to Pt(*N^C*-bzq)(dpm), where dbq and bzq are cyclometallated dibenzo[*f,h*]quinoline and benzo[*h*]quinoline respectively (dpm = *O^O*-coordinated dipivolylmethanoate),[42] and in benzannulated Pt(BPI)Cl complexes.[27] In those cases, however, the impact of benzannulation on absorption matched that on emission. We also observed a similar effect in the luminescence of dinuclear Cu(I) complexes $[(P\text{^}N)\text{Cu}]_2(\mu\text{-X})_2$ with *P^N*-coordinating phosphine-pyridine ligands based on quinolines and phenanthridines (X = halide): the luminescence of the more conjugated phenanthridine-based complexes was blue-shifted relative to the quinoline analogues.[43] Here, the absorption maxima are unchanged by benzannulation, while emission is starkly affected. We return to the likely origin of this effect in the next section. The luminescence lifetimes in deoxygenated solution are of the order of a microsecond (Table 3.2), which is quite typical of cyclometallated Pt(II) complexes and indicative of phosphorescence from a formally forbidden triplet state that is facilitated by the spin-orbit coupling associated with the metal. The lifetimes are an order of magnitude shorter in air-equilibrated solutions, indicating quenching of the triplet excited state by molecular oxygen: the bimolecular rate constants for quenching are around $2 \times 10^9\ M^{-1}\ s^{-1}$.

The luminescence quantum yields are in the range of 0.1–0.2 %. A close match of the excitation spectra with the absorption spectra suggests that the emitting triplet state forms with high efficiency, irrespective of the state to which light absorption occurs (as typically observed in most phosphorescent Pt(II) complexes thanks to efficient intersystem crossing to the triplet state). Quantum yields are then determined by the relative values of the radiative k_r and non-radiative $\sum k_{nr}$ rate constants. Assuming that the emitting state is indeed formed with unitary efficiency, they can be estimated as follows: $k_r = \Phi / \tau$ and $\sum k_{nr} = (\tau^{-1} - k_r)$. The values thus obtained are compiled in Table 3.2. From these data, it can be seen that the low quantum yields are a combined result of low k_r values in the range 500–1300 s^{-1} and high $\sum k_{nr}$ up to 10^6 s^{-1}. In contrast, the most efficient red-emitting Pt(II) complexes reported to date (albeit emitting at shorter λ_{max} ~650 nm) have k_r values almost two orders of magnitude higher and $\sum k_{nr}$ up to two orders of magnitude lower.[44] The low k_r values may reflect a relatively low degree of metal character in the triplet state, given the highly conjugated nature of the organic ligand. Indeed, the systems bear some resemblance to the units found in Pt(II) phthalocyanines and Pt(II) porphyins, where quantum yields are limited by low k_r.[41] TD-DFT calculations lend support to this interpretation in terms of limited metal character, as discussed in the next section. They also reveal substantial distortion of the excited triplet state relative to the ground state, which could account for the large $\sum k_{nr}$ values.

Amongst the three complexes, the highest $\sum k_{nr}$ value is found for that which emits at lowest energy and vice versa, qualitatively in line with intramolecular vibrational deactivation of electronic excited states and the "energy gap law".[45] There is no clear-cut trend in k_r. A smaller k_r for the highest-energy emitter **L3-PtCl** evidently limits the quantum yield, which is not significantly higher than for **L6-PtCl**, despite having the lowest $\sum k_{nr}$ value.

3.3.5. DFT Calculations:

Density functional theory (DFT) and time-dependent DFT (TD-DFT) calculations were carried out on the three complexes (**L5-PtCl**, **L6-PtCl** and **L3-PtCl**) to interpret the trends observed in the photophysical properties. Inspecting the orbital densities of the frontier orbitals and the LUMO+1 illustrates the similarities between the sets of complexes (Figure 3.10 and Figure 3.11). For example, the HOMOs of all three Pt(II) complexes are comprised of nearly even contributions from the metal centre, the amido 2p lone pair, and the C_6 ring of the *N*-heterocyclic ligand arms (for Hirshfeld populations, see Figure 3.12 and Tables 3.9 – 3.11). In comparison, the unoccupied orbitals are almost completely localized on the C_5N rings of the *N*-heterocycles, split equally in the symmetric complexes (**L5-PtCl** / **L3-PtCl**) with the LUMO weighted more heavily (64%) on the phenanthridinyl arm in the asymmetric complex (**L6-PtCl**).

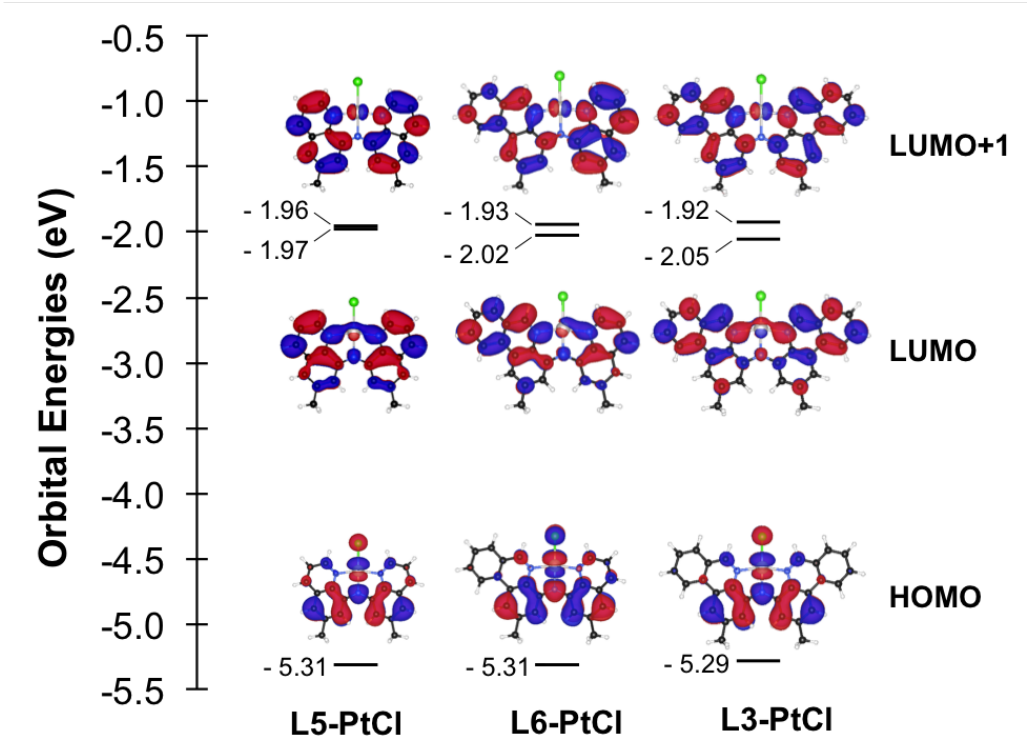

Figure 3.10. Orbital diagrams of the HOMO, LUMO and LUMO+1 of **L5-PtCl**, **L6-PtCl** and **L3-PtCl** shown with isovalues of 0.02.

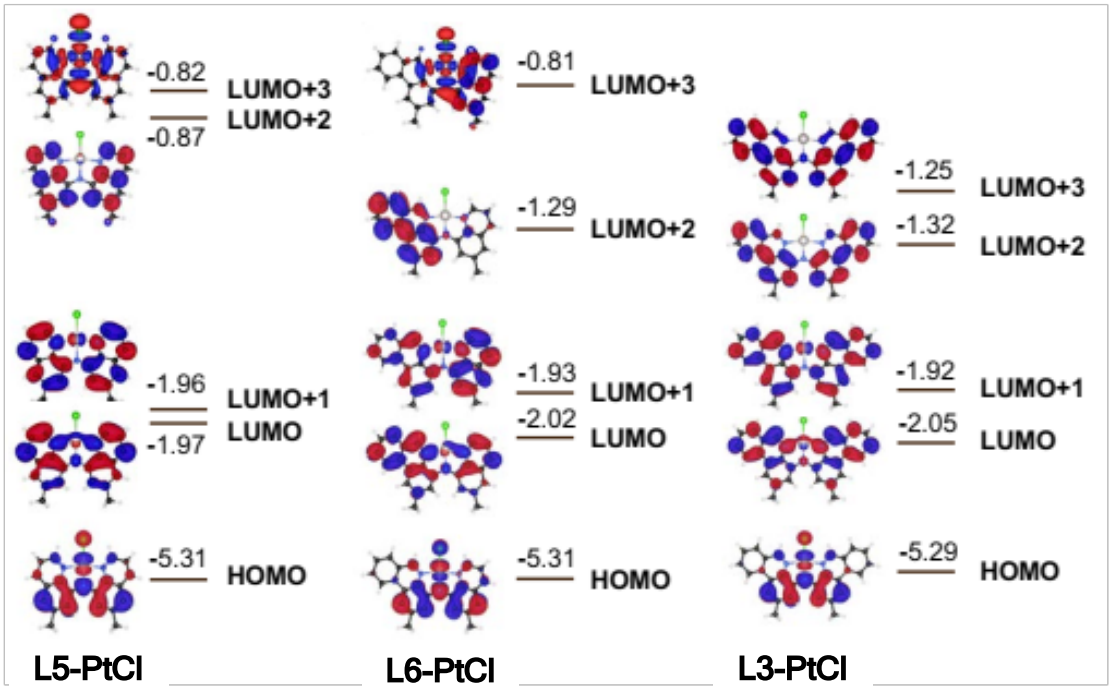

Figure 3.11. Relevant ground state MOs of **L5-PtCl**, **L6-PtCl** and **L3-PtCl** (isosurface = 0.02; SMDM06/ LANL2DZ// SMD-M062x/LANL2DZ)

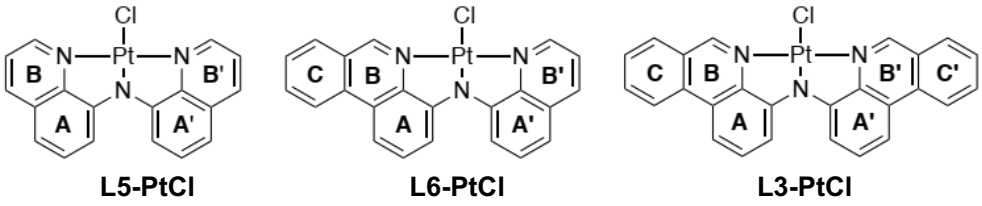

Figure 3.12. Diagram of assigned fragment contributions for **L5-PtCl**, **L6-PtCl** and **L3-PtCl**.

The major difference between the absorption spectra of the three metal complexes is the appearance of additional prominent peaks at higher energy (300-430 nm) that grow in intensity when comparing complexes of **L6-PtCl** and **L3-PtCl**, and therefore can be attributed to the phenanthridinyl arms. TD-DFT (as shown in Figure 3.13 and Tables 3.12 - 3.14) assigns these to HOMO→LUMO+2 transitions (**2**) and HOMO→LUMO+2/HOMO→LUMO+3 transitions (**L3-**

PtCl). These virtual orbitals are largely π-anti-bonding combinations on the π-extended portion of the phenanthridinyl ligand arms. The corresponding orbitals (LUMO+2) are at much higher energy for the smaller quinolinyl π-system of **L5-PtCl**, pushing these transitions further into the UV.

Table 3.9. Fragment contributions (%) to the ground state MOs of **L5-PtCl** using Hirshfeld atomic population method SMD-M06/LANL2DZ//SMD-M062x/LANL2DZ).

1	*E*(eV)	Pt	Cl	N	A	A'	B	B'
L+4	-0.74	3	1	1	27	27	19	19
L+3	-0.82	52	11	10	5	5	8	8
L+2	-0.87	1	0	0	29	29	19	19
L+1	-1.96	3	0	1	20	20	27	27
L	-1.97	5	0	2	12	12	34	34
H	-5.31	17	4	19	26	26	3	3
H-1	-6.65	40	0	1	13	13	16	16
H-2	-6.79	91	1	2	1	1	2	2
H-3	-6.81	35	35	2	12	12	1	1
H-4	-6.96	32	59	1	1	1	3	3

Table 3.10. Fragment contributions (%) to the ground state MOs of **L6-PtCl** using Hirshfeld atomic population method (SMD-M06/LANL2DZ//SMD-M062x/LANL2DZ).

2	*E*(eV)	Pt	Cl	N	A	A'	B	B'	C
L+4	-0.79	20	4	4	2	37	3	27	1
L+3	-0.81	35	7	7	3	23	5	18	0
L+2	-1.29	1	0	1	40	2	18	2	36
L+1	-1.93	4	0	1	11	24	14	39	6
L	-2.02	4	0	1	9	7	35	21	20
H	-5.31	16	4	19	26	27	3	3	1
H-1	-6.63	38	0	1	12	9	16	13	10
H-2	-6.80	91	1	2	1	1	2	2	0
H-3	-6.80	34	31	2	12	14	2	2	1
H-4	-6.94	3	5	0	41	1	12	1	35

Table 3.11. Fragment contributions (%) to the ground state MOs of **L3-PtCl** using Hirshfeld atomic population method (SMD-M06/LANL2DZ//SMD-M062x/LANL2DZ).

3	*E*(eV)	Pt	Cl	N	A	A'	B	B'	C	C'
L+4	-0.78	53	11	11	4	4	8	8	1	1
L+3	-1.25	1	0	1	20	20	11	11	18	18
L+2	-1.32	0	0	0	22	22	8	8	20	20
L+1	-1.92	4	0	1	12	12	24	24	11	11
L	-2.05	4	0	1	6	6	26	26	15	15
H	-5.29	16	4	20	26	26	3	3	1	1
H-1	-6.60	36	0	1	9	9	13	13	9	9
H-2	-6.78	32	28	1	14	14	2	2	2	2
H-3	-6.78	90	1	2	1	1	2	2	0	0
H-4	-6.93	3	0	0	23	23	7	7	17	17

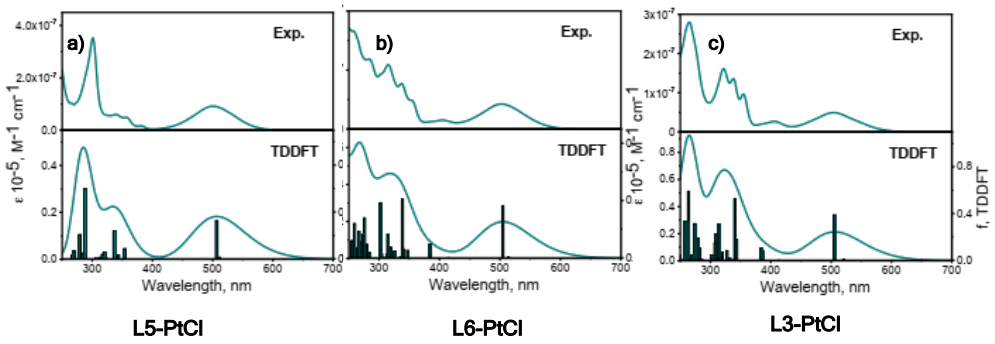

Figure 3.13. TD-DFT simulated spectrum and vertical excitation energies (bottom) with the experimental spectrum (top) of **L5-PtCl**, **L6-PtCl** and **L3-PtCl** in CH2Cl2 (SMD-M06/ LANL2DZ//SMDM062x/LANL2DZ)).

Table 3.12. TD-DFT predicted vertical excitation energies, oscillator strengths (f > 0.01) and MO contributions (>10%) for **L5-PtCl**.

No.	E/eV	*f*	Orbital Transition	Contribution (%)
3	2.43	0.012	H-->L	99
4	2.45	0.326	H-->L+1	99
13	3.50	0.086	H-->L+2	94
16	3.61	0.031	H-1-->L	25
			H-->L+4	65
17	3.64	0.014	H-2-->L	91
22	3.68	0.240	H-1-->L	66
			H-->L+4	20
28	3.87	0.053	H-3-->L+1	92
30	3.91	0.036	H-4-->L	18
			H-3-->L	24
			H-1-->L+1	51
31	3.95	0.012	H-4-->L	65
			H-1-->L+1	10
			H-1-->L+3	12
39	4.30	0.597	H-->L+5	84
41	4.36	0.047	H-3-->L+3	74
44	4.44	0.207	H-6-->L	24
			H-5-->L+1	53
			H-1-->L+4	12
46	4.59	0.065	H-7-->L	44
			H-5-->L	29
50	4.65	0.027	H-7-->L+1	38
			H-6-->L	18
			H-5-->L+1	30

Table 3.13. TD-DFT predicted vertical excitation energies, oscillator strengths (f > 0.01) and MO contributions (>10%) for **L6-PtCl**.

No.	E/eV	*f*	Orbital Transition	Contribution (%)
2	2.46	0.364	H-->L+1	98
4	3.23	0.094	H-->L+2	95
5	3.57	0.052	H-->L+3	31
			H-->L+4	57
6	3.64	0.059	H-2-->L	80
			H-1-->L	14

7	3.66	0.410	H-2-->L	15
			H-1-->L	70
10	3.81	0.045	H-3-->L	67
			H-1-->L+1	21
11	3.88	0.072	H-3-->L+1	76
14	3.94	0.161	H-4-->L	51
			H-4-->L+1	20
15	3.95	0.025	H-5-->L	34
			H-3-->L	10
			H-1-->L+1	19
			H-1-->L+3	13
17	4.07	0.025	H-5-->L+3	39
			H-5-->L+4	23
			H-->L+5	14
18	4.10	0.384	H-->L+5	70
19	4.36	0.024	H-4-->L	11
			H-4-->L+1	23
			H-3-->L+3	32
			H-3-->L+4	16
20	4.37	0.037	H-4-->L	16
			H-4-->L+1	32
			H-3-->L+3	22
			H-3-->L+4	12
21	4.43	0.092	H-6-->L	31
			H-6-->L+1	38
22	4.49	0.277	H-7-->L	17
			H-6-->L	23
			H-4-->L+1	11
			H-1-->L+2	32
23	4.55	0.161	H-7-->L	14
			H-6-->L	14
			H-1-->L+2	38
			H-->L+6	10
24	4.60	0.032	H-->L+6	38
			H-->L+7	46
25	4.61	0.110	H-7-->L+1	18
			H-6-->L+1	25
			H-->L+6	33
26	4.64	0.181	H-7-->L+1	14
			H-4-->L+2	11
			H-->L+7	31
28	4.75	0.070	H-4-->L+2	10

			H-3-->L+2	77
29	4.78	0.239	H-4-->L+2	47
30	4.87	0.119	H-7-->L	47
			H-7-->L+1	20
			H-4-->L+2	13

Table 3.14. TD-DFT predicted vertical excitation energies, oscillator strengths (f > 0.01) and MO contributions (>10%) for **L3-PtCl**.

No.	E/eV	*f*	Orbital Transition	Contribution (%)
2	2.45	0.388	H-->L+1	99
4	3.21	0.077	H-->L+2	96
5	3.23	0.101	H-->L+3	96
6	3.61	0.177	H-3-->L	64
			H-1-->L	32
7	3.64	0.524	H-3-->L	33
			H-1-->L	57
9	3.73	0.015	H-3-->L+1	51
			H-3-->L+4	29
			H-1-->L+1	11
10	3.79	0.082	H-2-->L	69
11	3.88	0.069	H-2-->L+1	81
12	3.88	0.011	H-6-->L	67
			H-1-->L+4	16
13	3.91	0.034	H-1-->L+1	46
			H-1-->L+4	21
14	3.93	0.023	H-5-->L+1	32
			H-4-->L	47
15	3.94	0.307	H-6-->L	14
			H-5-->L	30
			H-4-->L+1	28
16	3.97	0.023	H-1-->L+1	26
			H-1-->L+4	27
17	4.01	0.222	H-6-->L+1	21
			H-->L+5	62
18	4.03	0.146	H-6-->L+1	59
			H-->L+5	22
19	4.10	0.044	H-6-->L+1	11
			H-6-->L+4	61
23	4.39	0.104	H-5-->L+1	44
			H-4-->L	34

24	4.44	0.187	H-7-->L	73
25	4.52	0.313	H-4-->L+1	22
			H-1-->L+2	61
28	4.60	0.042	H-7-->L+1	33
			H-->L+7	53
30	4.66	0.018	H-3-->L+3	97
31	4.70	0.590	H-4-->L+3	15
			H-2-->L+2	49
			H-->L+8	10
32	4.73	0.332	H-5-->L+2	22
			H-4-->L+3	22
			H-2-->L+2	37
33	4.76	0.045	H-2-->L+3	82
34	4.81	0.330	H-5-->L+3	27
			H-4-->L+2	46

For the lowest energy absorption manifold, (d_{Pt}+p_N)-to-π* metal-to-ligand charge transfer character is evident from the population analyses and MO diagrams. TD-DFT calculations show that the peak with the highest oscillator strength in all three complexes is composed of a HOMO→LUMO+1 transition; the HOMO→LUMO excitation does not contribute significantly to this band. Fragment contributions calculated using the Hirshfeld atomic population method[46] reveal that for all three complexes, the HOMO/LUMO+1 pair are more co-extensive than the HOMO/LUMO pair, thanks to sizeable contributions from the C_6 rings of the heterocyclic arms. While the LUMO+1 experiences a slight destabilization with π-extension, this is offset in a small perturbation in the HOMO energy of **L3-PtCl** as shown in Table 3.15. Thus, while the LUMO is actually stabilized progressively with benzannulation (**L3-PtCl** > **L6-PtCl** > **L5-PtCl**), there is little change to the wavelengths of the lowest energy absorption manifold. Indeed, both experimental and TD-DFT predicted spectra show isoenergetic absorptions.

In their analysis of Pt(II) complexes with *bis*(2-pyridylimino)isoindole (BPI) and benzannulated ligand analogs, Hanson *et al.* noted that the HOMO of a 1,3-butadiene fragment has appropriate symmetry to act as an effective electron-donating group to the LUMO of the isoindole of BPI, and that the destabilization is due largely to this effect on the LUMO, as opposed to a significant influence on the HOMO.[27] The orbital contributions to the frontier orbitals of the Pt complexes presented here similarly reveal that the LUMO/LUMO+1 (but not the HOMO) present lobes of the appropriate symmetry at the site of benzannulation to interact with the HOMO of a 1,3-butadiene moiety. While the LUMO+1 is slightly destabilized upon benzannulation, consistent with the fused 1,3-butadiene moiety acting as an effective electron donor, benzannulation has a more conventional impact on the LUMO, which drops in energy. Our ligand design therefore can be contrasted with the experimental paradigm previously put forward as a general explanation for blue-shifted emission in benzannulated ligands.[27] In this case, the nearly 40 nm blue shift in the emission maximum cannot be solely explained by the impact of site-specific benzannulation on ligand electronics.

Table 3.15. TD-DFT Vertical Excitation Energies and HOMO, LUMO, and LUMO+1 energies for complexes **L5-PtCl**, **L6-PtCl** and **L3-PtCl**.

	Orbital Energies (eV)			λ_{calc} /nm	Assignment	Oscillator Strength	Coefficient	% Contribution
	HOMO	LUMO	LUMO+1					
L5-PtCl	-5.31	-1.97	-1.96	506.7	HOMO→LUMO+1	0.3263	0.70258	98.7
L6-PtCl	-5.31	-2.02	-1.93	504.7	HOMO→LUMO+1	0.3637	0.70136	98.4
L3-PtCl	-5.29	-2.05	-1.92	505.7	HOMO→LUMO+1	0.3884	0.70193	98.5

To investigate the origin of this curious blue shift, the complexes were optimized with triplet multiplicities to compare the energies of the lowest lying triplet states (T_1) with estimates of the first excited singlet states from TD-DFT as shown in Table 3.16 and Figure 3.14. Calculated single-point energies of the complexes at the optimized triplet geometry with singlet multiplicity ($T_1@S_0$; Figure 3.14) were used to computationally estimate emission energies. Consistent with experimentally observed phosphorescence, the T_1 state for **L3-PtCl** indeed lies higher in energy relative to its ground state (S_0; 1.88 eV) compared to the energies of the T_1 states calculated for **L5-PtCl** and **L6-PtCl**. In addition, the corresponding calculated emission energy $E(T_1)$ – $E(T_1@S_0)$ is also higher for the largest π-system (1.63 eV for **L3-PtCl** vs 1.51 (**L5-PtCl**) and 1.49 (**L6-PtCl**)), again reproducing experiment.

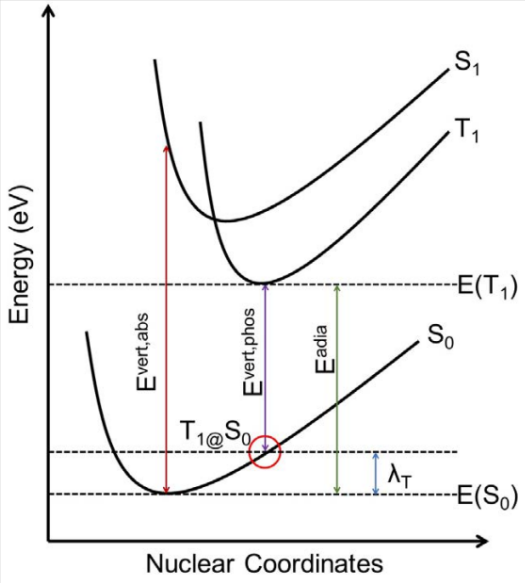

Figure 13

Figure 3.14. Diagram illustrating parameters calculated using the protocol described in computational experimental section.

Table 3.16. Calculated photophysical parameters of **L5-PtCl**, **L6-PtCl** and **L3-PtCl**.

E(eV)	L5-PtCl	L6-PtCl	L3-PtCl
$E^{vert,abs}$	2.45	2.46	2.45
$E^{vert,phos}$	1.51	1.49	1.63
E^{adia}	1.78	1.77	1.88
λ_T[9]	0.28	0.27	0.25

Comparing the optimized geometries of the ground state (S_0) and first excited state (T_1) of **L5-PtCl**, **L6-PtCl** and **L3-PtCl** reveals structural changes that accompany emission as shown in Figure 3.18 and Tables 3.17-3.18. The root-mean-squared deviations, calculated from overlaying the optimized S_0 and T_1 structures (**L5-PtCl**: 0.328 Å, **L6-PtCl**: 0.356; **L3-PtCl**: 0.295; Figure 3.15), are consistent with bigger structural differences for the smaller quinolinyl-containing systems (**L5-PtCl** and **L6-PtCl**) compared with **L3-PtCl**. In all three ground-state structures, the rigid tridentate ligand maintains a highly planar orientation. In their T_1 excited states, the two-ligand arms twist to break this plane, which likely contributes strongly to the rates of non-radiative decay.[47] In particular, a strong torsional twist of up to ~13° is observed. For example, while similar torsions are observed for the optimized T_1 geometries for **L6-PtCl** (13.2°) and **L3-PtCl** (12.76°), the deviation from the planarity of the ligand in the triplet geometry compared with the ground state is more pronounced for **L6-PtCl** (S_1 4.2, T_1 13.2; $\Delta = 9.0$) than for **L3-PtCl** (S_1 7.6, T_1 12.8; $\Delta = 5.2$).

With respect to the *N*-heterocyclic moieties themselves, the C_5N sub-unit in the quinolinyl moiety in **L5-PtCl** in the T_1 excited state is more significantly distorted compared with the benzannulated C_5N sub-unit in the phenanthridinyl moiety of the ligand in **L3-PtCl**. The largest change in the phenanthridinyl moiety is localized in the C=N sub-unit, consistent with localization of double-bond character in this position which maximizes the number of aromatic sextets in the

fused three ring system.[48] This buffers the phenanthridinyl ring system from larger overall changes compared with quinoline. Comparing all three complexes, the C_5N rings of the calculated T_1 structures are all strongly distorted in one half of the tridentate ligand only: in **L5-PtCl** and **L6-PtCl**, this is the quinolinyl arm; in **L3-PtCl**, a phenanthridinyl arm as shown in Figure 3.26. This is consistent with isoenergetic emission from **L5-PtCl** and **L6-PtCl**, as the emissive excited state in both involves the quinoline (rather than the phenanthridine).

This implies that the higher energy triplet state of **L3-PtCl** can also be attributed to inhibition of the electronically desirable distortion for **L3-PtCl** compared with **L5-PtCl**. A similar observation has been made for cyclometallated Pt complexes with extended π-systems[42] and for Cu emitters.[43] With respect to the cyclometallated Pt complexes, the extent of π-conjugation in aromatic *C^N* ligands was found to also *not* correspond with the observed trends in emission energies, and was rationalized in terms of structural distortions that occur upon cyclometalation matching distortions that stabilized the molecules' triplet states. The energy cost of geometry relaxation of the T_1 state to the S_0 state has been previously estimated by calculating the corresponding relaxation energy (λ_T).[49] For **L3-PtCl**, the λ_T (0.25 eV) is smaller than those determined for **L5-PtCl** and **L6-PtCl** (0.28, 0.27 eV respectively), though these values are close to being within error of each other. Nevertheless, the observed and measurable geometric changes are consistent with the phenanthridinyl *P^N* ligands enforcing an excited state geometry more similar to the ground state geometry in **L3-PtCl** than for the smaller quinolinyl-containing analogs **L5-PtCl** and **L6-PtCl** with a commensurately smaller resulting apparent Stokes shift.

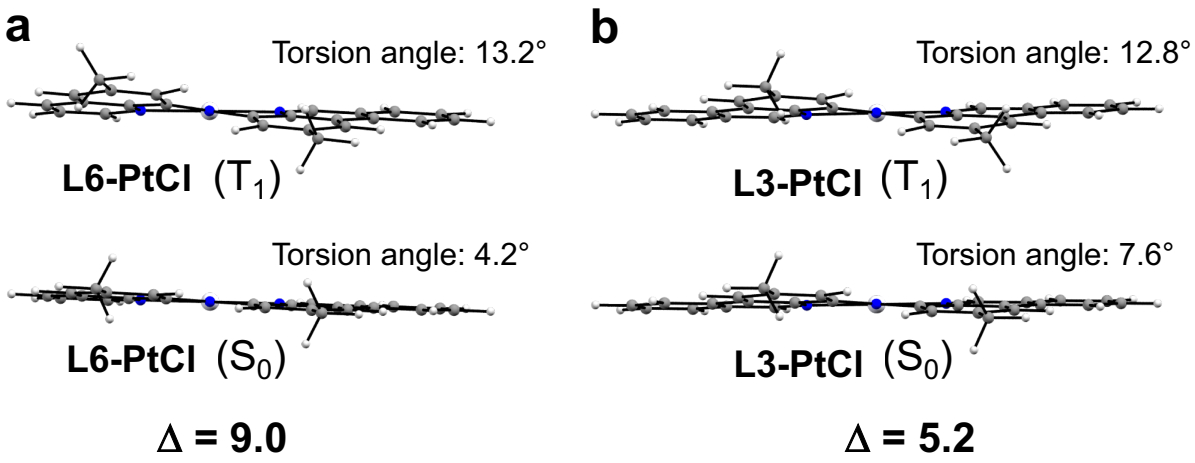

Figure 3.15. Comparison of torsion angles in DFT-optimized structures of S_0 and T_1 states of **L6-PtCl** and **L3-PtCl**.

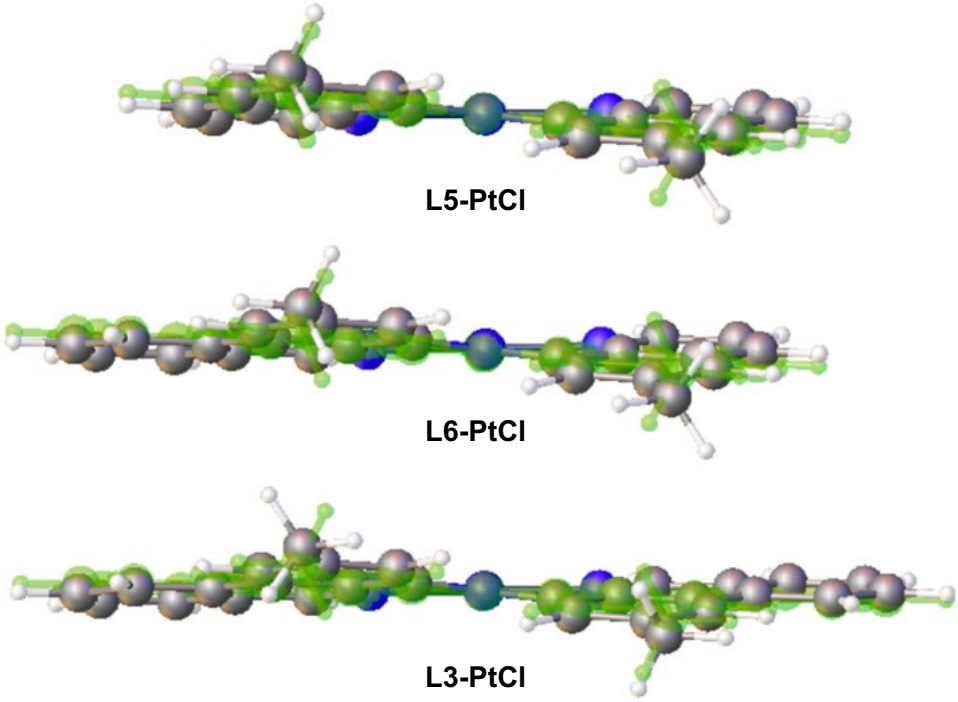

Figure 3.16. Overlay of DFT-optimized S0 (green) and T1 structures of **L5-PtCl**, **L6-PtCl** and **L3-PtCl**.

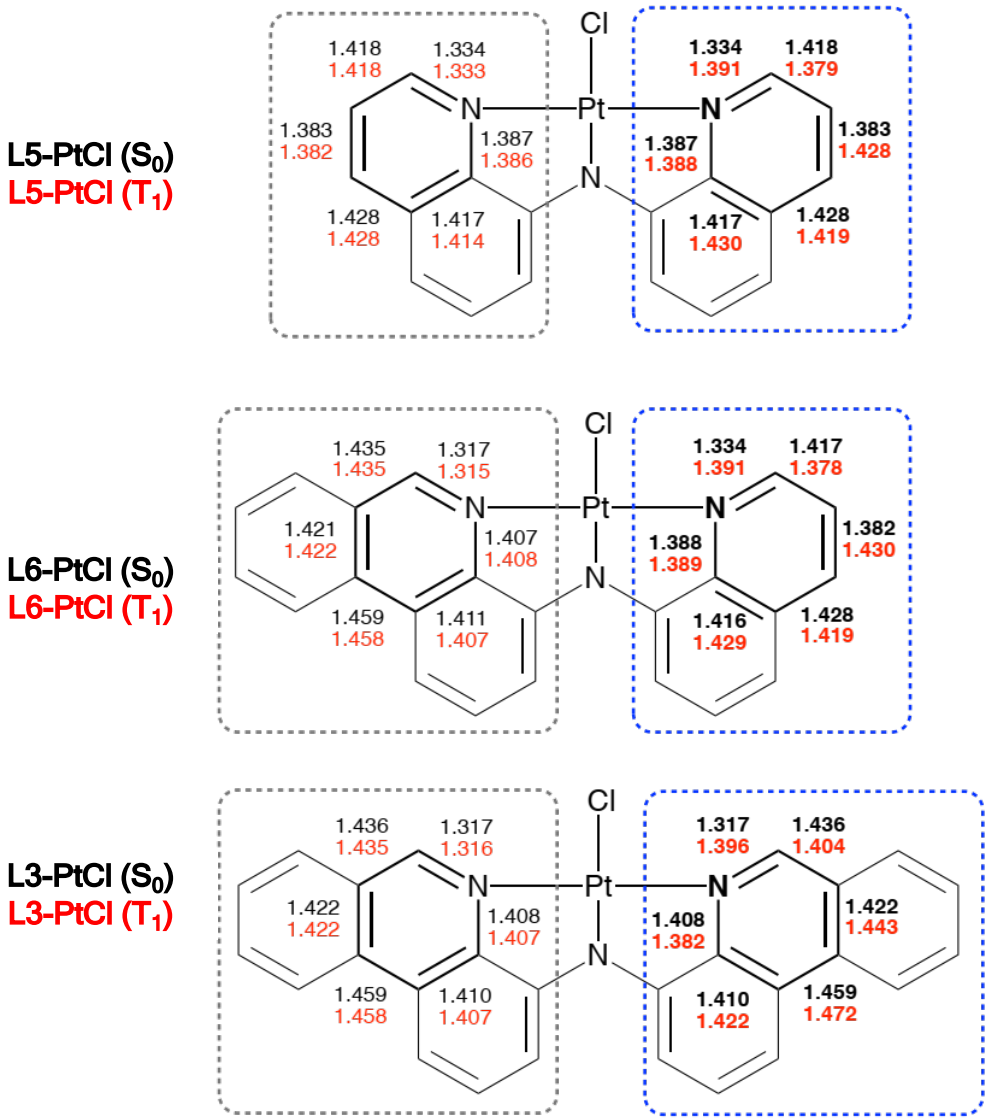

Figure 3.17. Selected bond length comparison of DFT-optimized S0 and T1 structures of **L5-PtCl**, **L6-PtCl** and **L3-PtCl**. The most impacted ligand arm is outlined in blue.

Table 3.17. Comparison of computed bond angles (°) for **L5-PtCl**, **L6-PtCl** and **L3-PtCl** (S0/T1; M062x/LANL2DZ).

Bond (Å)	1			2			3		
	S_0	T_1	$\Delta(S_0\text{-}T_1)$	S_0	T_1	$\Delta(S_0\text{-}T_1)$	S_0	T_1	$\Delta(S_0\text{-}T_1)$
1Pt-2Cl	2.475	2.459	0.016	2.479	2.457	0.022	2.479	2.452	0.027
1Pt-3N	2.031	2.013	0.020	2.029	2.013	0.016	2.029	2.048	-0.019
1Pt-4N	1.990	1.983	0.007	1.987	1.979	0.008	1.983	1.972	0.010
1Pt-5N	2.031	2.050	-0.019	2.027	2.048	-0.021	2.029	2.011	0.018

Table 1.18. Comparison of computed bond distances (Å) for **L5-PtCl**, **L6-PtCl** and **L3-PtCl** (S0/T1; M062x/LANL2DZ).

Angle (°)	1			2			3		
	S_0	T_1	$\Delta(S_0\text{-}T_1)$	S_0	T_1	$\Delta(S_0\text{-}T_1)$	S_0	T_1	$\Delta(S_0\text{-}T_1)$
2Cl-1Pt-3N	97.252	98.045	-0.793	97.148	98.053	-0.905	97.15	96.414	0.736
2Cl-1Pt-5N	97.252	96.702	0.550	97.111	96.733	0.378	97.15	98.321	-1.171
3N-2Pt-4N	82.748	82.445	0.303	82.857	82.447	0.410	82.85	82.952	-0.102
4N-1Pt-5N	82.748	82.808	-0.060	82.884	82.769	0.115	82.85	82.312	0.538

3.4. Conclusions:

The complexes discovered during this study are amongst the most red-shifted of phosphorescent Pt(II) complexes reported to date that emit from monomolecular excited states. While emission peaking around 700 nm in solution is well-established for bimolecular (aggregate or excimer) excited states of Pt(II) complexes,[50-51] complexes with sufficient conjugation to emit in this region from monomolecular states are rare and are largely limited to platinum porphyrins and phthalocyanins. Of particular interest also is the observation of the intense low-energy absorption band around 500 nm. For many applications, particularly those envisaged for use in biological media such as bio-sensing and imaging, intense absorption in the visible region is desirable.[3] The "brightness" of the phosphor – defined as the product of the emission quantum yield and the extinction coefficient at the excitation wavelength – is crucial. Similar criteria apply to the development of materials for photodynamic therapy (PDT) where low-energy excitation is sought, beyond the wavelength range where endogenous biological molecules absorb strongly.[52-53] In PDT, long-lived excited states that can sensitize the formation of singlet oxygen are desirable, and the efficient excited-state quenching by oxygen observed in this new series of complexes (Table 1) suggests that such a process is at work. The availability of molecules with intense visible

absorption in conjunction with efficient formation of triplet states having microsecond lifetimes is similarly desirable for upconversion through triplet-triplet annihilation (TTA-UC).[54]

Finally, molecular-level control over emission properties is a critical tool in designing useful light-emitting materials. Ligand benzannulation and the resultant extension of a molecule's π-system have long been successfully exploited to narrow HOMO-LUMO gaps and shift absorption/emission to the red. The work of Thompson and colleagues[27] demonstrated that a more nuanced consideration of the impact of benzannulation on frontier orbital energies can also predict 'counter-intuitive' shifts in absorption/emission energy that sometimes accompany π-extension. Here, I present a further exception, wherein combining quinolinyl and phenanthridinyl arms in ligand frameworks results in complexes where absorption and emission are not impacted in the same direction by benzannulation. The findings of this study will hopefully serve as an additional tool to materials designers. Comparative study of all proligands (**L1-L12**) and corresponding complexes is under way.

3.5. Experimental Section:

3.5.1. General Information:

All air-sensitive manipulations were carried either in a N_2-filled glove box or using standard Schlenk techniques under Ar. 2-Formylphenyl boronic acid (AK Scientific), *N*-iodosuccinimide (AK Scientific), *N*-bromosuccinimide (Alpha Aesar), $Pd(PPh_3)_4$ (Sigma Aldrich), $Pd(OAc)_2$ (Sigma Aldrich), 2-nitro-4-(trifluoromethyl)aniline (Sigma Aldrich), 2-bromo-4-(trifluoromethyl)aniline (Combi Blocks), (1,1'-diphenylphosphino)ferrocene (dppf, Sigma Aldrich), (±)-2,2′-bis(diphenylphosphino)-1,1′-binaphthalene (*rac*-BINAP), Sigma Aldrich), Na_2CO_3 (Alpha Aesar), trifluoroacetic acid (Sigma Aldrich), sodium *tert*-pentoxide (NaO*t*Pen, Sigma Aldrich), sodium *tert*-butoxide (NaO*t*Bu, Sigma Aldrich), zinc (Alpha Aesar), hydrazine

hydrate (Sigma Aldrich), formic acid (Alpha Aesar), and $PtCl_2$ (Sigma Aldrich) were purchased and used without any further purification. 8-bromo-4-methylquinoline,[33] 8-amino-4-methylquinoline,[55] $Pt(COD)Cl_2$,[56] 2-bromo-6-iodo-4-(*tert*-butyl)aniline, 2-iodo-6-nitro-4-(trifluoromethyl)aniline, **L1** and **L1-PtCl**;[28] 2-bromo-6-iodo-*p*-toluidine, **L2**, **L3**, **L2-PtCl** and **L3-PtCl**; **L4** and **L7**;[67] 4-amino-2-*tert*-butylphenanthridine, 4-nitro-2-*tert*-butylphenanthridine and 4-bromo-2-(trifluoromethyl)phenanthridine[REF-JASON Fe PAPER] were synthesized according to literature procedures. Organic solvents were dried and distilled using appropriate drying agents, and distilled water was degassed prior to use. 1- and 2D NMR spectra were recorded on Bruker Avance 300 MHz or Bruker Avance – III 500 MHz spectrometers. ^{1}H and $^{13}C\{^{1}H\}$ NMR spectra were referenced to residual solvent peaks.[57] Elemental analyses were performed by Microanalytical Service Ltd., Delta, BC (Canada), and at the University of Manitoba using a Perkin Elmer 2400 Series II CHNS/O Elemental Analyzer. Thermogravimetric analyses (TGA) were recorded on a Perkin Elmer TGA 7 instrument under an argon atmosphere.

3.5.2. General Procedure for Proligand Synthesis (L1-L12):

A thick-walled, 100 mL Teflon-stoppered flask was charged with Pd catalyst, ligand and toluene (30 mL). After stirring briefly, the appropriate quinoline or phenanthridine reagents were added, along with an additional 30 mL of toluene, followed by the alkoxide base. The sealed flask was then stirred vigorously for 72 h in an oil bath set to 150 °C. After cooling and removing the volatiles, the residue was taken up in CH_2Cl_2 (120 mL) with the resulting suspension filtered over Celite and dried.

^{Me,Quin}NN(H)N^{Quin,Me} (L5): The general procedure was followed using: $Pd_2(dba)_3$ (84.0 mg, 0.09 mmol), *rac*-BINAP (112.6 mg, 0.18 mmol); 8-bromo-4-methylquinoline (0.36 g, 2.27 mmol), 8-amino-4-methylquinoline (0.50 g, 2.26 mmol); and NaO*t*Bu (0.26 g, 2.71 mmol). Column

chromatography gave a red solid (neutral alumina; 1:5 EtOAc/hexane; R_f = 0.5). Isolated yield = 0.67 g (98%). ^{1}H NMR ($CDCl_3$, 300 MHz, 22 °C): δ 10.55 (br s, 1H; N*H*), 8.88 (dd, 2H, J_{HH} = 4.2, 1.7 Hz; $C_{Ar}H$), 8.04 (dd, 2H, J_{HH} = 8.2, 1.7 Hz; $C_{Ar}H$), 7.74 (d, 2H, J_{HH} = 1.6 Hz; $C_{Ar}H$), 7.41 (dd, 2H, J_{HH} = 8.2, 4.2 Hz; $C_{Ar}H$), 7.11 (bs, 2H, $C_{Ar}H$), 2.58 ppm (s, 6H; CH_3). $^{13}C\{^1H\}$ NMR ($CDCl_3$, 75 MHz, 22 °C): δ 147.4 (C_{Ar}), 139.0 (C_{Ar}), 138.6 (C_{Ar}), 137.1 (C_{Ar}), 135.5 (C_{Ar}), 129.1 (C_{Ar}), 121.8 (C_{Ar}), 117.0 (C_{Ar}), 112.0 (C_{Ar}), 22.7 ppm (CH_3).

^{Me,Phen}NN(H)N^{Quin,Me} (L6): The general procedure was followed using: $Pd_2(dba)_3$ (0.174 g, 0.180 mmol), *rac*-BINAP (0.275 g, 0.440 mmol); 8-bromo-4-methylquinoline (0.700 g, 3.15 mmol), 4-amino-2-methylphenanthridine (0.660 g, 3.15 mmol); and NaO*t*Bu (0.450 g, 4.73 mmol). Column chromatography gave a red solid (neutral alumina; 1:5 EtOAc/hexane; R_f = 0.3). Isolated yield = 1.01 g (92%). ^{1}H NMR ($CDCl_3$, 300 MHz, 22 °C): δ 10.60 (br s, 1H; N*H*), 9.27 (s, 1H; $C_{Ar}H$), 8.90 (d, 1H, J_{HH} = 4.1 Hz; $C_{Ar}H$), 8.60 (d, 1H, J_{HH} = 8.3 Hz; $C_{Ar}H$), 8.11-8.00 (overlapped m, 2H; $C_{Ar}H$), 7.88-7.81 (overlapped m, 3H; $C_{Ar}H$), 7.76 (s, 1H; $C_{Ar}H$), 7.69 (app t, 1H, J_{HH} = 7.4 Hz; $C_{Ar}H$), 7.40 (dd, 1H, J_{HH} = 8.2, 4.2 Hz; $C_{Ar}H$), 7.10 (s, 1H; $C_{Ar}H$), 2.67 ppm (s, 3H; $C_{Phen}H_3$), 2.58 (s, 3H; $C_{Quin}H_3$). $^{13}C\{^1H\}$ NMR ($CDCl_3$, 75 MHz, 22 °C): δ 150.2 (C_{Ar}), 147.3 (C_{Ar}), 139.5 (C_{Ar}), 139.0 (C_{Ar}), 138.8 (C_{Ar}), 137.1 (C_{Ar}), 135.5 (C_{Ar}), 133.9 (C_{Ar}), 132.7 (C_{Ar}), 130.6 (C_{Ar}), 129.2 (C_{Ar}), 128.8 (C_{Ar}), 127.3 (C_{Ar}), 127.0 (C_{Ar}), 124.8 (C_{Ar}), 122.5 (C_{Ar}), 121.7 (C_{Ar}), 116.9 (C_{Ar}), 112.8 (C_{Ar}), 112.6 (C_{Ar}), 111.9 (C_{Ar}), 23.0 ($C_{Phen}H_3$), 22.7 ppm ($C_{Quin}H_3$).

3.5.3. General Procedure for Pt(II) Complexes Synthesis:

In a thick-walled Teflon-stoppered flask, equimolar amounts of $Pt(COD)Cl_2$[56] and NaO*t*Bu were added to a solution of the appropriate ligand (L4-L12) in 10 mL of CH_2Cl_2, and the mixture stirred vigorously at 70 °C for 18 h. The resulting red suspension was allowed to cool, and the volatiles

were removed *in vacuo*. The residue was then was washed with acetonitrile (3 x 10 mL) and diethyl ether (3 x 10 mL).

^{Me,Quin}NNN^{Quin,Me}-PtCl (L5-PtCl): The general procedure was followed using: **L5** (0.15 g, 0.50 mmol), Pt(COD)Cl_2 (0.19 g, 0.51 mmol), and NaO*t*Bu (0.05 g, 0.52 mmol). Isolated yield = 0.217 g (82 %). ^{1}H NMR ($CDCl_3$, 300 MHz, 22 °C): δ 9.13 (dd, 2H, J_{HH} = 5.2, 1.4 Hz; $C_{Ar}H$), 8.17 (d, 2H, J_{HH} = 8.4 Hz; $C_{Ar}H$), 7.51 (s, 2H, $C_{Ar}H$), 7.36 (dd, 2H, $J_{H\text{-}H}$ = 8.3, 5.1 Hz; $C_{Ar}H$), 6.89 (s, 2H, $C_{Ar}H$), 2.59 ppm (s, 6H, CH_3). Anal. Calcd for $C_{20}H_{16}ClN_3Pt$: C, 45.42; H, 3.05. Found: C, 44.70; H, 3.27.

Synthesis of ^{Me,Phen}NNN^{Quin,Me}-PtCl (L6-PtCl): The general procedure was followed using: **L5** (0.20 g, 0.58 mmol), Pt(COD)Cl_2 (0.22 g, 0.59 mmol), and NaO*t*Bu (0.060 g, 0.60 mmol). Isolated yield = 0.266 g (79 %). ^{1}H NMR ($CDCl_3$, 300 MHz, 22 °C): δ 9.50 (s, 1H, $C_{Ar}H$), 9.10 (d, 1H, J_{HH} = 4.8 Hz; $C_{Ar}H$), 8.43 (d, 1H, J_{HH} = 8.4 Hz; $C_{Ar}H$), 8.11 (d, 1H, J_{HH} = 8.3 Hz; $C_{Ar}H$), 8.02 (d, 1H, J_{HH} = 7.9 Hz; $C_{Ar}H$), 7.87 (app t, 1H, J_{HH} = 7.7 Hz; $C_{Ar}H$), 7.67 (app t, 1H, J_{HH} = 7.5 Hz; $C_{Ar}H$), 7.54 (s, 1H, $C_{Ar}H$), 7.49 (s, 1H, $C_{Ar}H$), 7.45 (s, 1H, $C_{Ar}H$), 7.32 (dd, 1H, J_{HH} = 8.3, 5.0 Hz; $C_{Ar}H$), 6.78 (s, 1H, $C_{Ar}H$), 2.62 (s, 3H, CH_3), 2.55 ppm (s, 3H, CH_3). Anal. Calcd for $C_{24}H_{18}ClN_3Pt$: C, 49.79; H, 3.13. Found: C, 49.49; H, 3.20.

3.5.4. X-Ray Crystallography:

X-ray crystal structure data was using collected from a multi-faceted crystals of suitable size and quality selected from a representative sample of crystals of the same habit using an optical microscope. The crystal was mounted on MiTiGen loops with data collection carried out in a cold stream of nitrogen (150 K; Bruker D8 QUEST ECO; Mo K_α radiation). All diffractometer

manipulations were carried out using Bruker APEX3 software.[58] Structure solution and refinement was carried out using XS, XT and XL software, embedded within the Bruker SHELXTL suite.[59] For each structure, the absence of additional symmetry was confirmed using ADDSYM incorporated in the PLATON program.[60] CCDC No. 1947217 contains the supplementary crystallographic data for this paper. The data can be obtained free of charge from The Cambridge Crystallographic Data Centre via www.ccdc.cam.ac.uk/structures.

Crystal structure data for **L5-PtCl**: X-ray quality crystals were grown following diffusion of diethyl ether vapor into a $CHCl_3$ of the compound at room temperature. Crystal structure parameters: $C_{20}H_{16}Cl_1N_3Pt_1$ 528.90 g/mol, monoclinic, space group $P2_1/n$; a = 9.8984(3) Å, b = 7.6056(3) Å, c = 21.7673(7) Å, α = 90°, β = 98.1820(10)°, γ = 90°, V = 1622.03(10) Å^3; Z = 4, ρ_{calcd} = 2.166 g cm^{-3}; crystal dimensions 0.110 x 0.080 x 0.020 mm^3; θ_{max} = 27.525°; 36146 reflections, 3726 independent (R_{int} = 0.0672), direct methods; absorption coeff (μ = 8.823 mm^{-1}), absorption correction semi-empirical from equivalents (SADABS); refinement (against F_o^2) with SHELXTL V6.1, 228 parameters, 0 restraints, R_1 = 0.0287 ($I > 2\sigma$) and wR_2 = 0.0617 (all data), Goof = 1.066, residual electron density 1.285/−0.880 e Å^{-3}.

3.5.5. Thermal Gravimetric Analysis:

Thermal gravimetric analysis was performed on 2-3 mg of each complex. The temperature was started initially at 50 °C and ramped to 500 °C for the corresponding complexes at the following rates: **1**: 1 °C/min; **2**: 50 °- 200 °C at 5 °C/min; 200 °C – 500 °C at 2 °/min; **3**: 50 °- 200 °C at 5 °C/min; 200 °C – 500 °C at 2 °/min.

3.5.6. Optical Spectroscopy Measurements:

The absorption spectra of the complexes were measured in solution in CH_2Cl_2 in 1 cm quartz cuvettes using a Biotek Instruments XS UV-visible spectrometer at room temperature. The emission spectra of the proligands at 295 and 77 K, and of their Pt(II) complexes at 77 K, were recorded using a Jobin Yvon Fluoromax-2 spectrometer equipped with a red-sensitive Hamamatsu R928 photomultiplier tube. The emission spectra of the Pt(II) complexes at 295 K, which extend up to around 1000 nm, were recorded using a thermoelectrically cooled Synapse CCD detector, which offers better sensitivity in the red / NIR region compared to the R928 PMT. The samples for measurements at 295 K were contained within 1 cm pathlength quartz cuvettes modified for attachment to a vacuum line and were degassed prior to measurement by a minimum of three freeze-pump-thaw cycles; final vapor pressure at 77 K was $< 10^{-2}$ mbar. Emission spectra at 77 K were recorded in 4 mm diameter tubes held within a liquid-nitrogen-cooled quartz dewar. Luminescence lifetimes were measured by time-correlated single-photon counting (TCSPC) following excitation using a pulsed laser diode at 405 nm; the emitted light was detected at right angles to the excitation beam, using an R928 PMT thermoelectrically cooled to –20°C.

3.5.7. DFT Calculations:

DFT calculations were carried out using Gaussian09[61] with M062x/LANL2DZ[62-63] with an IEFPCM[64] solvent model with DCM. TD-DFT calculations were performed with M06/LANL2DZ[62-63]on the M062x/LANL2DZ optimized structures. Molecular orbital analyses were carried out with Hirshfeld partition method[46] available in Multiwfn software.[65] and visualized using VESTA,[66] while TD-DFT results were analyzed using Origin 2017 software package.

To calculate ground-state, excited-state and reorganization energies,[49] the following protocol was followed: (1) The S_0 geometry was optimized by restricted DFT (charge = 0, multiplicity = 1) using the crystal structure coordinates as starting input. The T_1 geometry was optimized with unrestricted DFT (charge = 0, multiplicity = 3) using the optimized S_0 geometry as starting input. Frequency calculations were then subsequently carried out to confirm that these structures are at a minimum and to derive free energies. (2) To determine the relative atomic contributions to the frontier MOs, population analyses were carried out on the optimized structures of S_0 states. The electronic energies, $E(S_0)$ and $E(T_1)$, obtained from the single point calculations of S_0 and T_1 in their respective minimum were used to estimate the adiabatic energy (E^{adia}), where, $E^{adia} = E(T_1) - E(S_0)$. (3) TD-DFT was then carried out on the following: (a) $S_n \leftarrow S_0$ singlet-singlet transitions (first 50 transitions) with the restricted formalism with charge = 0 and multiplicity = 1; (b) $T_n \leftarrow (T_1@S_0)$ singlet-triplet transitions (first 50 transitions) with the unrestricted formalism, but keeping the same charge and multiplicity as in (a). These gave $E^{vert\text{-}abs}$ and $E^{vert\text{-}phos}$ as shown in Figure S15. The reorganization energy (λ_T) after the emission of light was then calculated as $\lambda_T = E^{adia} - E^{vert\text{-}phos}$. As shown in Figure S15, "$T_1@S_0$" denotes a single point calculation on the singlet potential energy surface (*i.e.*, with singlet multiplicity) with a geometry matching that of optimized T_1 structure.

3.6. References:

1. Zhao, Q.; Li, F.; Huang, C. *Chem. Soc. Rev.* **2010**, *39*, 3007.

2. Wong, K. M.-C.; Yam, V. W.-W. *Coord. Chem. Rev.* **2007**, *251*, 2477.

3. Baggaley, E.; Weinstein, J. A.; Williams, J. A. G. *Coord. Chem. Rev.* **2012**, *256*, 1762.

4. Mauro, M.; Aliprandi, A.; Septiadi, D.; Kehr, N. S.; De Cola, L. *Chem. Soc. Rev.* **2014**, *43*, 4144.

5. Chen, Y.; Guan, R.; Zhang, C.; Huang, J.; Ji, L.; Chao, H. *Coord. Chem. Rev.* **2016**, *310*, 16.

6. *Highly Efficient OLEDs with Phosphorescent Materials*. Ed. Yersin, H.; Wiley-VCH: Weinheim, Germany, 2007.

7. Cebrian, C.; Mauro, M. *Beilstein J. Org. Chem.* **2018**, *14*, 1459.

8. Kalinowski, J.; Fattori, V.; Cocchi, M.; Williams, J. A. G. *Coord. Chem. Rev.* **2011**, *255*, 2401.

9. Wong, W.-Y.; Ho, C.-L. *Coord. Chem. Rev.* **2009**, *253*, 1709.

10. Chou, P.-T.; Chi, Y.; Chung, M.-W.; Lin, C.-C. *Coord. Chem. Rev.* **2011**, *255*, 2653.

11. Li, K.; Ming Tong, G. S.; Wan, Q.; Cheng, G.; Tong, W.-Y.; Ang, W.-H.; Kwong, W.-L.; Che, C.-M. *Chem. Sci.* **2016**, *7*, 1653.

12. Williams, J. A. G. *Top. Curr. Chem.* **2007**, *281*, 205.

13. Chou, P.-T.; Chi, Y. *Chem. Eur. J.* **2007**, *13*, 380.

14. Zhou, G.; Wong, W.-Y.; Yang, X. *Chem. Asian J.* **2011**, *6*, 1706.

15. Williams, J. A. G. *Chem. Soc. Rev.* **2009**, *38*, 1783.

16. Murphy, L.; Williams, J. A. G. *Top. Organomet. Chem.* **2010**, *28*, 75.

17. Freeman, G. R.; Williams, J. A. G. *Top. Organomet. Chem.* **2013**, *40*, 89.

18. Vezzu, D. A. K.; Ravindranathan, D.; Garner, A. W.; Bartolotti, L.; Smith, M. E.; Boyle, P. D.; Huo, S.-Q. *Inorg. Chem.* **2011**, *50*, 8261.

19. Kong, F. K.-W.; Tang, M.-C.; Wong, Y.-C.; Ng, M.; Chan, M.-Y.; Yam, V. W.-W. *J. Am. Chem. Soc.* **2017**, *139*, 6351.

20. Chow, P.-K.; Cheng, G.; Tong, G. S. M.; To, W.-P.; Kwong, W.-L.; Low, K.-H.; Kwok, C.-C.; Ma, C.; Che, C.-M. *Angew. Chem., Int. Ed.* **2015**, *54*, 2084.

21. Rausch, A. F.; Murphy, L.; Williams, J. A. G.; Yersin, H. *Inorg. Chem.* **2009**, *48*, 11407.

22. Rausch, A. F.; Murphy, L.; Williams, J. A. G.; Yersin, H. *Inorg. Chem.* **2012**, *51*, 312.

23. Zhao, D.; Tang, X.; Liu, X.-Y.; Fan, J.; Liao, L.-S. *Org. Electron.* **2017**, *50*, 473.

24. Wen, H.-M.; Wu, Y.-H.; Fan, Y.; Zhang, L.-Y.; Chen, C.-N.; Chen, Z.-N. *Inorg. Chem.* **2010**, *49*, 2210.

25. Wen, H.-M.; Wu, Y.-H.; Xu, L.-J.; Zhang, L.-Y.; Chen, C.-N.; Chen, Z.-N. *Dalton Trans.* **2011**, *40*, 6929.

26. Wen, H.-M.; Wang, J.-Y.; Li, B.; Zhang, L.-Y.; Chen, C.-N.; Chen, Z.-N. *Eur. J. Inorg. Chem.* 2013, **2013**, 4789.

27. Hanson, K.; Roskop, L.; Djurovich, P. I.; Zahariev, F.; Gordon, M. S.; Thompson, M. E. *J. Am. Chem. Soc.* **2010**, *132*, 16247.

28. Peters, J. C.; Harkins, S. B.; Brown, S. D.; Day, M. W. *Inorg. Chem.* **2001**, *40*, 5083.

29. Harkins, S. B.; Peters, J. C. *Organometallics* **2002**, *21*, 1753.

30. Maiti, D.; Paul, H.; Chanda, N.; Chakraborty, S.; Mondal, B.; Puranik, V. G.; Lahiri, G. K. *Polyhedron* **2004**, *23*, 831.

31. Betley, T. A.; Qian, B. A.; Peters, J. C. *Inorg. Chem.* **2008**, *47*, 11570.

32. Hofmann, A.; Dahlenburg, L.; van Eldik, R. *Inorg. Chem.* **2003**, *42*, 6528.

33. Lee, C.-I.; Zhou, J.; Ozerov, O. V. *J. Am. Chem. Soc.* **2013**, *135*, 3560.

34. Mondal, R.; Giesbrecht, P. K.; Herbert, D. E. *Polyhedron* **2016**, *108*, 156.

35. Mandapati, P.; Giesbrecht, P. K.; Davis, R. L.; Herbert, D. E. *Inorg. Chem.* **2017**, *56*, 3674.

36. Zander, M. *Z. Naturforsch., A* **1978**, *33A*, 998.

37. Ho, C.-L.; Li, H.; Wong, W.-Y. *J. Organomet. Chem.* **2014**, *751*, 261.

38. Tan, G.; Chen, S.; Siu, C.-H.; Langlois, A.; Qiu, Y.; Fan, H.; Ho, C.-L.; Harvey, P. D.; Lo, Y. H.; Liu, L.; Wong, W.-Y. *J. Mater. Chem. C* **2016**, *4*, 6016.

39. Tuong Ly, K.; Chen-Cheng, R.-W.; Lin, H.-W.; Shiau, Y.-J.; Liu, S.-H.; Chou, P.-T.; Tsao, C.-S.; Huang, Y.-C.; Chi, Y. *Nat. Photon.* **2017**, *11*, 63.

40. Zhang, Y.; Luo, Q.; Zheng, W.; Wang, Z.; Lin, Y.; Zhang, E.; Lu, S.; Xiang, J.; Zhao, Y.; Wang, F. *Inorg. Chem. Front.* **2018**, *5*, 413.

41. Paul-Roth, C. O.; Drouet, S.; Merhi, A.; Williams, J. A. G.; Gildea, L. F.; Pearson, C.; Petty, M. C. *Tetrahedron* **2013**, *69*, 9625.

42. Bossi, A.; Rausch, A. F.; Leitl, M. J.; Czerwieniec, R.; Whited, M. T.; Djurovich, P. I.; Yersin, H.; Thompson, M. E. *Inorg. Chem.* **2013**, *52*, 12403.

43. Mondal, R.; Lozada, I. B.; Davis, R. L.; Williams, J. A. G.; Herbert, D. E. *Inorg. Chem.* **2018**, *57*, 4966.

44. Shafikov, M. Z.; Daniels, R.; Pander, P.; Dias, F. B.; Williams, J. A. G.; Kozhevnikov, V. N. *ACS Appl. Mater. Interfaces* **2019**, *11*, 8182.

45. Englman, R.; Jortner, J. *Mol. Phys.* **1970**, *18*, 145.

46. Hirshfeld, F. L.*Theor. Chim. Acta* **1977**, *44*, 129.

47. Tong, G. S. M.; Che, C.-M. *Chem.-Eur. J.* **2009**, *15*, 7225.

48. Maksić, Z. B.; Barić, D.; Müller, T. *J. Phys. Chem. A* **2006**, *110*, 10135.

49. Uoyama, H.; Goushi, K.; Shizu, K.; Nomura, H.; Adachi, C. *Nature* **2012**, *492*, 234.

50. Lai, S.-W.; Chan, M. C.-W.; Cheung, T.-C.; Peng, S.-M.; Che, C.-M. *Inorg. Chem.* **1999**, *38*, 4046.

51. Cocchi, M.; Kalinowski, J.; Virgili, D.; Williams, J. A. G. *Appl. Phys. Lett.* **2008**, *92*, 113302/1-113302/3.

52. McKenzie, L. K.; Sazanovich, I. V.; Baggaley, E.; Bonneau, M.; Guerchais, V.; Williams, J. A. G.; Weinstein, J. A.; Bryant, H. E. *Chem. Eur. J.* **2017**, *23*, 234.

53. Colombo, A.; Fontani, M.; Dragonetti, C.; Roberto, D.; Williams, J. A. G.; Scotto di Perrotolo, R.; Casagrande, F.; Barozzi, S.; Polo, S. *Chem. Eur. J.* **2019**, *25*, 7948.

54. Wu, W.; Zhao, J.; Guo, H.; Sun, J.; Ji, S.; Wang, Z. *Chem. Eur. J.* **2012**, *18*, 1961, S1961/1-S1961/25.

55. Medina Padilla, M.; Castro Morera, A.; Sanchez-Quesada, J.; Garcia Palomero, E.; Alonso Cascon, M.; Herrero Santos, S.; Vela Ruiz, M.; Usan Egea, P.; Rodriguez Villanueva, A. L. Triple Substituted Phenanthroline Derivatives for the Treatment of Neurodegenerative or Haematological Diseases or Conditions, or Cancer. *US20110306631A1*, 2011.

56. Clark, H. C.; Manzer, L. E. *J. Organomet. Chem.* **1973**, *59*, 411.

57. Fulmer, G. R.; Miller, A. J. M.; Sherden, N. H.; Gottlieb, H. E.; Nudelman, A.; Stoltz, B. M.; Bercaw, J. E.; Goldberg, K. I. *Organometallics* **2010**, *29*, 2176.

58. Bruker-AXS *APEX3 v2016.1-0*, Madison, Wisconsin, USA, 2016.

59. Sheldrick, G. M. *Acta Cryst.* **2008**, *A64*, 112.

60. Spek, A. L. *Acta Cryst.* **2009**, *D65*, 148.

61. Frisch, M. J.; Trucks, G. W.; Schlegel, H. B.; Scuseria, G. E.; Robb, M. A.; Cheeseman, J. R.; Scalmani, G.; Barone, V.; Mennucci, B.; Petersson, G. A.; Nakatsuji, H.; Caricato, M.; Li, X.; Hratchian, H. P.; Izmaylov, A. F.; Bloino, J.; Zheng, G.; Sonnenberg, J. L.; Hada, M.; Ehara, M.; Toyota, K.; Fukuda, R.; Hasegawa, J.; Ishida, M.; Nakajima, T.; Honda, Y.; Kitao, O.; Nakai, H.; Vreven, T.; Montgomery, J. A.; Peralta, J. E.; Ogliaro, F.; Bearpark, M.; Heyd, J. J.; Brothers, E.; Kudin, K. N.; Staroverov, V. N.; Kobayashi, R.; Normand, J.; Raghavachari, K.; Rendell, A.; Burant, J. C.; Iyengar, S. S.; Tomasi, J.; Cossi, M.; Rega, N.; Millam, J. M.; Klene, M.; Knox, J. E.; Cross, J. B.; Bakken, V.; Adamo, C.; Jaramillo, J.;

Gomperts, R.; Stratmann, R. E.; Yazyev, O.; Austin, A. J.; Cammi, R.; Pomelli, C.; Ochterski, J. W.; Martin, R. L.; Morokuma, K.; Zakrzewski, V. G.; Voth, G. A.; Salvador, P.; Dannenberg, J. J.; Dapprich, S.; Daniels, A. D.; Farkas; Foresman, J. B.; Ortiz, J. V.; Cioslowski, J.; Fox, D. J., Gaussian 09, Revision B.01. In *Gaussian 09, Revision B.01, Gaussian, Inc., Wallingford CT*, Wallingford CT, 2009.

62. Zhao, Y.; Truhlar, D. G. *Theor. Chem. Acc.* **2008**, *120*, 215.

63. Dunning, T. H., Jr.; Hay, P. J., In *Modern Theoretical Chemistry*, Schaefer III, H. F., Ed. Plenum, New York, 1977; Vol. 3, pp 1-28.

64. Tomasi, J.; Mennucci, B.; Cammi, R. *Chem. Rev.* **2005**, *105*, 2999.

65. Lu, T.; Chen, F. *J. Comput. Chem.* **2012**, *33*, 580.

66. Momma, K.; Izumi, F. *J. Appl. Cryst.* **2011**, *44*, 1272.

67. Braun, J. D.; Lozada, I. B.; Kolodziej, C.; Burda, C.; Newman, K. M. E.; van Lierop, J.; Davis, R. L.; Herbert, D. E. *Nature Chem.* **2019**, *11*, 1144.

Chapter 4: Deep Red Luminescence From Platinum(II) Complexes of *N*^*N*^-*N*-Amido Ligands With Benzannulated N-Heterocyclic Donor Arms

4.1 Abstract:

A synthetic methodology for accessing narrow-band, deep-red phosphorescence from mononuclear Pt(II) complexes is presented. These charge-neutral complexes have the general structure (*N*^*N*–^*N*)PtCl, in which the Pt(II) centres are supported by benzannulated diarylamido ligand scaffolds bearing substituted quinolinyl and/or phenanthridinyl arms. Emission maxima ranging from 683 to 745 nm are observed, with lifetimes spanning from 850 to 4500 ns. In contrast to the corresponding proligands, benzannulation is found to counter-intuitively, but markedly, blue-shift emission from metal complexes with differing degrees of ligand benzannulation but similar substitution patterns. This effect can be further tuned by incorporation of electron-releasing (Me, *t*Bu) or electron-withdrawing (CF_3) substituents in either the phenanthridine 2-position or quinoline 6-position. Compared with symmetric *bis*(quinoline) and *bis*(phenanthridine) architectures, "mixed" ligands incorporating one quinoline and one phenanthridine unit present a degree of charge transfer between the *N*-heterocyclic arms that is more pronounced in the proligands than in the Pt(II) complexes. The impact of benzannulation and ring-substitution on the structure and photophysical properties of both the proligands and their deep-red emitting Pt(II) complexes is discussed.

4.2. Introduction:

Luminescent complexes that emit light in the deep red region of the electromagnetic spectrum are of interest for a variety of applications. For example, white light-emitting diode (LED) devices are commonly constructed by combining high purity red, green and blue emission

into a broad spectral output.[1] In addition, deep red and near infrared (NIR) light can penetrate biological tissue to a greater extent than shorter wavelengths and so is more compatible with bioimaging and sensing applications.[2] While fluorescent deep red and NIR emitters have found application in luminescent devices and sensors,[3] phosphorescent complexes present certain distinct advantages.[4] In biosensing/imaging applications, for example, the longer lifetime of phosphorescence can avoid signal complications due to autofluorescence from endogenous fluorophores.[5,6] In LED devices, phosphorescence can enable harvesting of excitons of both singlet and triplet multiplicity.[7]

Efficient, deep red molecular phosphors – emitting from *triplet* states – are not as common as the corresponding fluorescent emitters. Nevertheless, examples built on late transition metal ions are known for elements of Group 7 (Re[8,9]), Group 8 (Ru,[10] Os[11]), Group 9 (Ir[12,13]), Group 10 (Pt[14–17]) and Group 11 (Cu,[18] Au[19]). As a third-row transition element, Pt has a large spin-orbit coupling (SOC) constant that boosts $T_1 \rightarrow S_0$ radiative decay, the formally forbidden phosphorescence process. In addition, the coordination chemistry of Pt is well-established.[20] Taken together, this has led to the design and use of platinum(II) complexes in phosphorescence-based applications including light-emitting diodes,[21–23] bioimaging,[24–26] and chemosensing.[27] The pursuit of deep red Pt(II) emitters is therefore of significant interest. Solution-state emission within this target wavelength region (~700 nm) has been extensively described for Pt(II) complexes with bimolecular excited states (*e.g.*, aggregates or excimers).[28,29] In comparison, complexes that can emit at these wavelengths from monomolecular excited states are very rare, as the extended conjugation required typically limits the available supporting ligand platforms to porphyrins or phthalocyanines.[30–33]

In addition to engineering bathochromically shifted emission with narrow profiles, intense absorption of the chromophore in the visible region can also be desirable, particularly in biological media where emissive probes and labels are ideally excited at wavelengths longer than those at which endogenous biological molecules strongly absorb.[34,35] The "brightness" of a phosphor, defined as the product of the extinction coefficient at the excitation wavelength and the emission quantum yield, is thus a critical parameter.[24] Beyond imaging, in photodynamic therapy (PDT) too, triplet excited states with long enough lifetimes to sensitize singlet oxygen formation are advantageous.[36] Designing molecules which combine strong absorption of visible light with efficient triplet excited-state formation and microsecond lifetimes is also attractive for accessing upconversion via triplet-triplet annihilation (TTA-UC).[37]

I have reported a series of Pt(II) complexes that to date present some of the most red-shifted phosphorescence for non-porphyrinic Pt(II) complexes emitting from monomolecular excited states.[38] These complexes are based on anionic, tridentate pincer-like ligands, with the form (*N*^*N*^–^*N*)PtCl. In this work, I extend our synthetic strategy and demonstrate how ligand substitution can be used to further tune the emission properties of a rare class of mononuclear Pt(II) deep red emitters.

4.3. Results and Discussion:

4.3.1. Ligand Preparation and Scope:

To build a library of ligands, functionalized amino/bromoquinolines and phenanthridines bearing either electron-withdrawing (EWG: CF_3), electron-donating (EDG: CH_3, *t*Bu) groups, or no substituent (H) on the heterocycle were synthesized as shown in Scheme 4.1. Phenanthridine precursors were prepared using tandem Pd-catalyzed cross-coupling/condensation reactions of 2-formylphenylboronic acid and appropriately substituted anilines, following a protocol we

previously established.[39] Quinoline precursors were prepared using Skraup reaction conditions.[40] For the tricyclic systems, formation of the phenanthridine core was confirmed in each case by the appearance of a diagnostic proton resonance between 9.35 and 9.50 ppm, attributed to the N=C*H* in the 6-position of the heterocycle as hown in Table 4.1.[41] Once in hand, the amino- and bromo-substituted heterocycles were subjected to Buchwald-Hartwig amination conditions, similar to those reported for the synthesis of the *bis*(quinolinyl)amine **L1**.[42] In general, proligand synthesis proceeded efficiently with Buchwald-Hartwig C-N coupling reactions and twelve *bis*(*N*-heterocyclic)amines with a variety of substitution patterns. They are grouped into **L1^{R,R} (L1, L5)**, **L2^{R,R}** (**L2**, **L4**, **L5**, **L6**, **L7**, **L8** and **L9)** and **L3^{R,R}** (**L2**, **L10**, **L11** and **L12**). All the ligands were isolated in good yields (70-90%) as orange-red (**L8**) or yellow-green solids following chromatography. The **L1^{R,R}** and **L3^{R,R}** proligands are *bis*(quinolyl)amines and *bis*(phenanthridinyl)amines respectively; superscripts are used to denote the substituents *meta* to the amine N–H. These proligands are symmetric around the N–H, apart from **L3^{CF3,tBu}(L12)** which comprises two differently substituted phenanthridines. Within the **L2^{R,R}** group, in contrast, each proligand contains one phenanthridine and one quinoline donor.

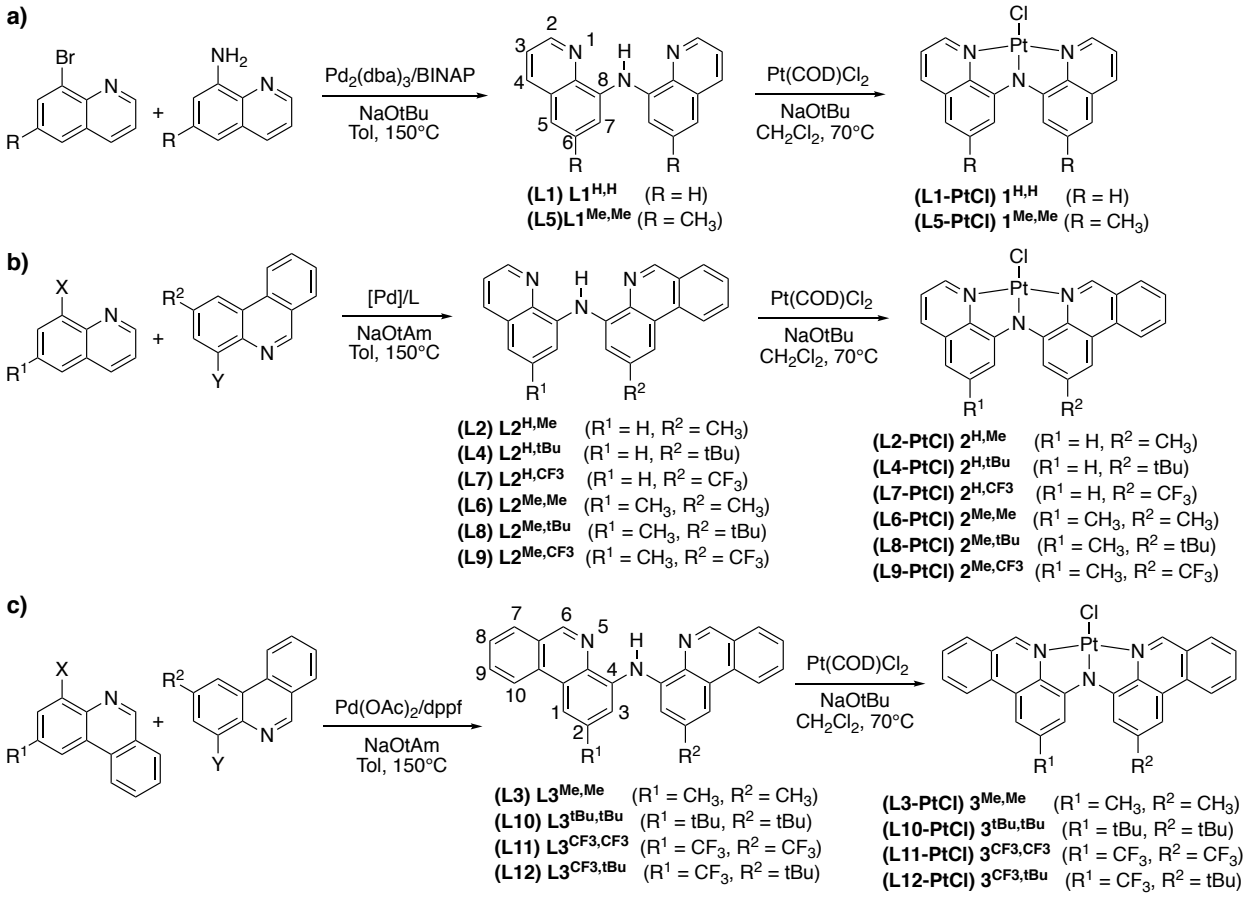

Scheme 4.1. Synthetic routes to proligands (a) $\mathbf{L1^{H,H}}$ (**L1**)[42] and $\mathbf{L1^{Me,Me}}$ (**L3**) [38]; (b) $\mathbf{L2^{H,Me}}$ (**L2**)[43], $\mathbf{L2^{H,tBu}}$ (**L4**)[44], $\mathbf{L2^{H,CF3}}$ (**L7**) [44] (R^1 = H, X = NH_2; R^2 = CF_3, Y = Br; [Pd] = $Pd_2(dba)_3$, L = *rac*-BINAP); $\mathbf{L2^{Me,Me}}$ (**L6**) [38]; $\mathbf{L2^{Me,tBu}}$ (R^1 = CH_3, X = Br; R^2 = *t*Bu, Y = NH_2; [Pd] = $Pd_2(dba)_3$, L = *rac*-BINAP), $\mathbf{L2^{Me,CF3}}$ (**L9**) (R^1 = CH_3, X = NH_2; R^2 = CF_3, Y = Br; [Pd] = $Pd(OAc)_2$, L = dppf); (c) $\mathbf{L3^{Me,Me}}$ (**L3**)[43], $\mathbf{L3^{tBu,tBu}}$ (**L10**), $\mathbf{L3^{CF3,CF3}}$(**L11**), $\mathbf{L3^{tBu,CF3}}$ (**L12**). The preparation and structures of their corresponding (*N*^*N*^*N*)PtCl complexes $\mathbf{1^{R,R}}$/$\mathbf{2^{R,R}}$/$\mathbf{3^{R,R}}$ are also shown. The IUPAC numbering system for quinolines and phenanthridines is illustrated for $\mathbf{L1^{R,R}}$ and $\mathbf{L3^{R,R}}$.

The proligands were characterized by ^{1}H, ^{13}C and ^{19}F (for the CF_3 derivatives) NMR spectroscopy in solution as shown in Table 4.1 for selected ^{1}H NMR resonances. The crystal structure of a representative proligand $\mathbf{L3^{CF3,CF3}}$ (**L11**), was obtained to verify the solution-state structure assigned by NMR as shown in Figure 4.1. Appendage of two, 2-substituted phenanthridinyl rings about the central N–H unit can be clearly seen in the solid state. The importance of the 'imine-

bridged biphenyl' resonance contributor to the ground state of phenanthridine derivatives is evident in the comparably short C1-N1 [1.301(4) Å] and C15-N3 distances [1.301(3) Å]. Unlike related diarylamine proligands, **L3^{CF3,CF3}** (**L11**) is essentially flat in the solid state, likely a result of packing effects; π-stacking is evidenced by contacts of < 3.4 Å between neighboring phenanthridine units which are staggered head-to-tail relative to one another

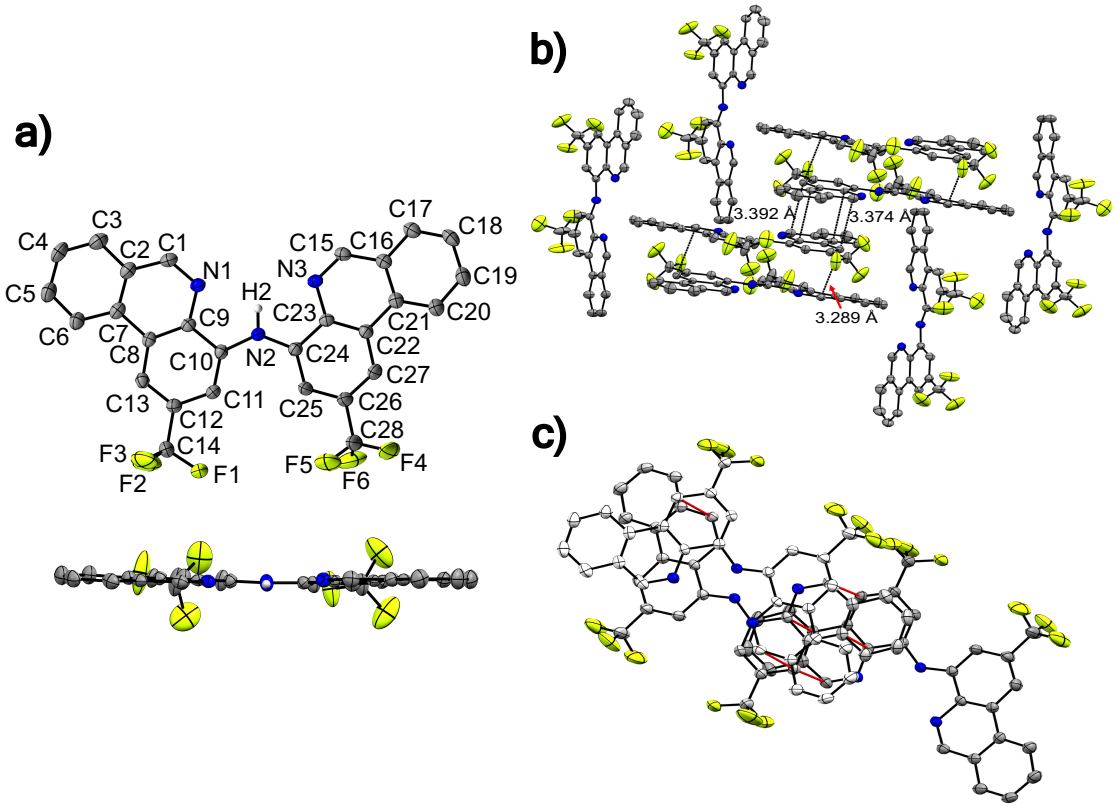

Figure 4.1. a) Solid-state structure of **L3^{CF3,CF3}**(**L11**) with thermal ellipsoids at 50% probability and hydrogen atoms omitted for clarity. Selected bond distances (Å) and angles (°): N(1)–C(1) 1.301(4), N(2)–C(10) 1.380(3), N(2)–C(24) 1.375(3), N(3)–C(15) 1.301(3); C(10)-N(2)-C(24) 132.9(2). Packing diagram showing close-contacts in the solid-state structure of **L3$^{CF3,\ CF3}$** (**L11**) from (b) side-on and (c) face-on views.

With the proligands in hand, a full library of Pt(II) complexes (series **L1^{R,R}-PtCl**, **L2^{R,R}-PtCl**, **L3^{R,R}-PtCl** from **L1^{R,R}**, **L2^{R,R}**, **L3^{R,R}**) were prepared by refluxing dichloromethane solutions of proligand and Pt(COD)Cl$_2$ (COD = 1,5-cyclooctadiene) in the presence of a base (sodium *tert*-

butoxide). Over the course of the reaction, the complexes were observed to precipitate as dark red solids. They are all poorly soluble in common organic solvents, and solubility was further diminished by benzannulation despite the introduction of substituents such as *t*Bu or CF_3 onto the *N*-heterocyclic arms of **L2^{R,R}-PtCl** and **L3^{R,R}-PtCl**. Nonetheless, solution-state ^{1}H NMR spectroscopy verified ligand binding, as the 6-positioned [C*H*] resonance of the phenanthridinyl arms of **L2^{R,R}** and **L3^{R,R}** shifted in a diagnostic fashion upon coordination as shown Table 4.1. When resolved, $^3J_{PtH}$ coupling constants of 33-39 Hz could be observed between the coordinated Pt and the hydrogen nucleus *ortho* to the donor nitrogen of the heterocyclic ligand. In this way, we were able to establish the structures of the library of compounds in solution. Compound purity in the solid-state was confirmed using combustion analysis.

Table 4.1. Diagnostic phenanthridinyl [C_6H] resonances for **L1^{R,R}-L3^{R,R}** and **L(1^{R,R}-3^{R,R})-PtCl**.

	L1^{H,H}	**L1^{Me,Me}**	**L2^{H,Me}**	**L2^{H,tBu}**	**L2^{H,CF3}**	**L2^{Me,Me}**	**L2^{Me,tBu}**	**L2^{Me,CF3}**
δ(^{1}H) C_6-*H* /ppm	8.97	8.88	9.27	9.10	9.38	9.27	9.29	9.43
	1^{H,H}	**1^{Me,Me}**	**2^{H,Me}**	**2^{H,tBu}**	**2^{H,CF3}**	**2^{Me,Me}**	**2^{Me,tBu}**	**2^{Me,CF3}**
δ(^{1}H) C_6-*H* /ppm ($^3J_{PtH}$ / Hz)	9.14 (37)	9.14 (33)	9.49 (36)	9.60 (39)	9.79 ([a])	9.50 (39)	9.60 (39)	9.76 (39)

	L3^{Me,Me}	**L3^{tBu,tBu}**	**L3^{tBu,CF3}**	**L3^{CF3,CF3}**
δ(^{1}H) C_6-*H* /ppm	9.29	9.30	9.43; 9.30	9.42
	3^{Me,Me}	**3^{tBu,tBu}**	**3^{tBu,CF3}**	**3^{CF3,CF3}**
δ(^{1}H) C_6-*H* /ppm	9.58 (39)	9.63 ([a])	9.75; 9.58 ([a])	[a,b]

[a] Not resolved.

[b] Compound is too insoluble to record a meaningful NMR spectrum.

The crystal structures of $\mathbf{2}^{\mathbf{Me,}t\mathbf{Bu}}$ (**L8-PtCl**) and $\mathbf{3}^{t\mathbf{Bu},t\mathbf{Bu}}$ (**L10-PtCl**) are shown in Figure 4.2. As with previously reported structures of $\mathbf{1}^{\mathbf{H,H}}$ (**L1-PtCl**),[42] $\mathbf{1}^{\mathbf{Me,Me}}$ (**L5-PtCl**),[38] $\mathbf{2}^{\mathbf{H,Me}}$ (**L2-PtCl**) and $\mathbf{3}^{\mathbf{Me,Me}}$ (**L3-PtCl**),[43] the coordinated ligands bind in a meridional fashion to each Pt centre and form planar structures. The structure of $\mathbf{2}^{\mathbf{Me,}t\mathbf{Bu}}$(**L8-PtCl**) does not contain any solvent molecules embedded in the crystal lattice, while that of $\mathbf{3}^{t\mathbf{Bu},t\mathbf{Bu}}$ (**L10-PtCl**) reveals a co-crystallized equivalent of CH_2Cl_2. Close intermolecular π-π interactions (3.3-3.5 Å) can be discerned in the structure of $\mathbf{2}^{\mathbf{Me,}t\mathbf{Bu}}$ (**L8-PtCl**) (Figure 4.2); in that of $\mathbf{3}^{t\mathbf{Bu},t\mathbf{Bu}}$ (**L10-PtCl**), they are replaced by non-covalent interactions with co-crystallized CH_2Cl_2 solvent (Figure 4.2). The trend of decreasing solubility within the series $\mathbf{L1}^{\mathbf{R,R}}$**-PtCl** > $\mathbf{L2}^{\mathbf{R,R}}$**-PtCl** > $\mathbf{L3}^{\mathbf{R,R}}$**-PtCl** likely arises from the presence of π-π interactions similar to those seen in structure of $\mathbf{2}^{\mathbf{Me,}t\mathbf{Bu}}$ (**L8-PtCl**), which are plausibly enhanced by benzannulation. Thus, crystals of $\mathbf{3}^{t\mathbf{Bu},t\mathbf{Bu}}$ (**L10-PtCl**) suitable for diffraction could only be grown through disruption of these interactions by inclusion of solvent in the lattice.

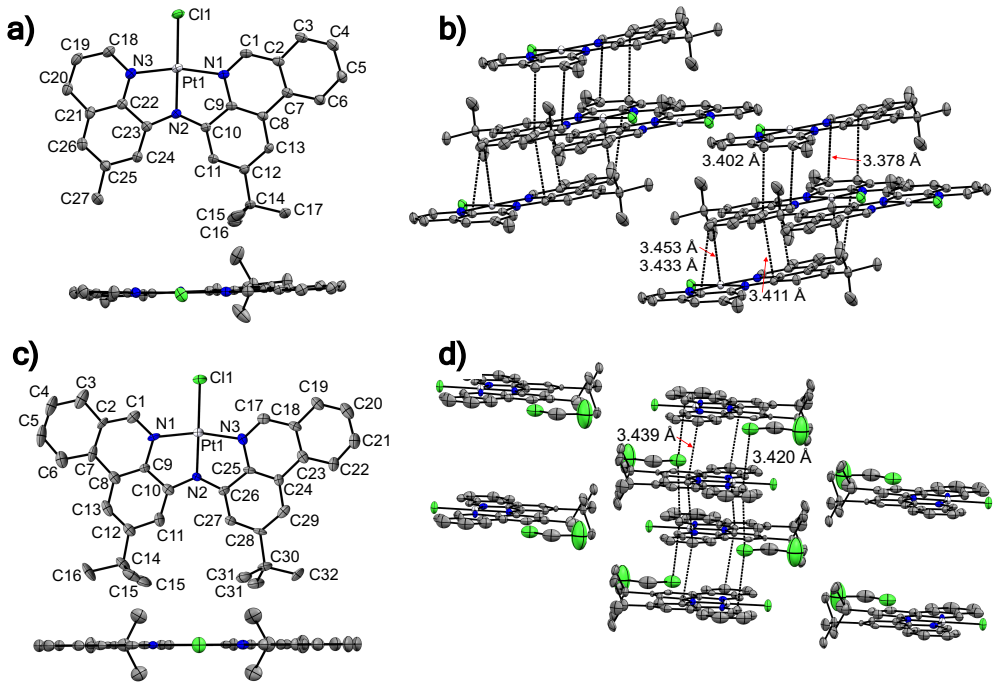

Figure 4.2. Solid-state structures of (a) & (b) **2^{Me,tBu} (L8-PtCl)**; Packing diagram showing close contacts in the solid-state structure of **2^{Me,tBu} (L8-PtCl)**. and (c) & (d) **3^{tBu,tBu} (L10-PtCl)**; Packing diagram showing close contacts in the solid-state structure of **3^{tBu,tBu} (L10-PtCl)**, with thermal ellipsoids at 50% probability and hydrogen atoms omitted for clarity. For each structure, views perpendicular to the metal square plane (top) and along the Cl–Pt–N(2) axis (bottom) are shown. Selected bond distances (Å) and angles (°) for **2^{Me,tBu}(L8-PtCl):** Cl(1)–Pt(1) 2.3307(6), N(1)–Pt(1) 1.9918(18), N(2)–Pt(1) 1.9736(18), N(3)–Pt(1) 1.9950(19), N(1)–C(1) 1.314(3), N(3)–C(18) 1.336(3); N(1)-Pt(1)-N(3)165.62(7), N(2)-Pt(1)-Cl(1) 178.55(5), N(1)-Pt(1)-Cl(1) 97.37(5), N(3)-Pt(1)-Cl(1) 97.00(6), N(2)-Pt(1)-N(1) 83.06(7), N(2)-Pt(1)-N(3) 82.60(7), C(10)-N(2)-C(23) 131.27(18). **3^{tBu,tBu} (L10-PtCl):** Cl(1)–Pt(1) 2.337(2), N(1)–Pt(1) 1.996(8), N(2)–Pt(1) 1.950(7), N(3)–Pt(1) 1.998(8), N(1)–C(1) 1.287(13), N(3)–C(17) 1.292(13); N(1)-Pt(1)-N(3) 165.9(3), N(2)-Pt(1)-Cl(1) 179.4(3), N(1)-Pt(1)-Cl(1) 96.0(3), N(3)-Pt(1)-Cl(1) 98.1(3), N(2)-Pt(1)-N(1) 83.4(4), N(2)-Pt(1)-N(3) 82.5(3), C(10)-N(2)-C(26) 130.1(8).

4.4. Photophysical Properties:

Extension of a conjugated ligand's π-system through benzannulation and introducing donor or acceptor substituents represent two common strategies for red-shifting emission from transition metal coordination complexes without introducing significant changes to the parent structure. Thompson and coworkers have shown that the structure-property relationship between benzannulation and absorption/emission, however, is more nuanced than is often supposed.[45] In that study, they demonstrated that the effect of benzannulation must be evaluated in light of the site of benzannulation and the localization of the frontier orbitals for systems in which the lowest energy spin-allowed absorption and spin-forbidden emitting state involve HOMO-LUMO transitions. This new paradigm has been verified for 1,3-*bis*(2-pyridylimino)isoindoline-supported platinum chlorides, various organic emitters,[45] and phosphorescent cyclometallated Ir(III) complexes.[46] For platinum chloride complexes supported by *bis*(8-quinolinyl)amido ligands (*e.g.*, $\mathbf{1^{Me,Me}}$ (**L5-PtCl**), *bis*(phenanthridinyl)amido ligands $\mathbf{3^{Me,Me}}$ (**L3-PtCl**) and "mixed" analogues $\mathbf{2^{Me,Me}}$(**L6-PtCl**) that incorporate one quinoline and one phenanthridine, however, we have discovered that this model does not fully hold.[38] In these compounds, absorption and emission are not affected in the same way by benzannulation; all three complexes show isoenergetic absorption maxima, but emission from the complex with the most extended ligand π-system $\mathbf{3^{Me,Me}}$ (**L3-PtCl**) is blue-shifted by nearly 40 nm. Similarly, exceptional behavior was observed for phenanthridinyl and quinolinyl derivatives of $(P\text{^}N)_2CuX_2$ dimers.[47] In that case, emission was shifted to higher energy for complexes of phenanthridinyl ligands despite a red-shift in absorption. The library of proligands presented here enables both further insight into the impact of π-extension and also how substitution patterns of benzannulated ligands affect absorption and emission.

4.4.1. Proligands L1–L3:

The photophysical properties of the proligands are considered first, followed by those of the corresponding Pt(II) complexes. Table 1 compiles room temperature absorption and emission data in dichloromethane solution for all twelve proligands, with a selection of representative spectra shown in Figure 4.3 (absorption) and Figure 4.4 (emission). In my previously published report,[38] only the dimethylated compounds $\mathbf{L1^{Me,Me}}$ (**L5**), $\mathbf{L2^{Me,Me}}$ (**L6**)and $\mathbf{L3^{Me,Me}}$ (**L3**) in order to isolate the effect of benzannulation by keeping ring substitution patterns consistent. All three proligands were found to show a strong, lowest energy absorption band centered around 400 nm. Although this band appears to be shifted slightly to higher energy in the phenanthridine-containing systems $\mathbf{L2^{R,R}}$, $\mathbf{L3^{R,R}}$ relative to the *bis*(quinoline) congener $\mathbf{L1^{Me,Me}}$ (**L5**) in terms of the λ_{max} value as shown Table 4.2 and Figure 4.3, the former tail further into the visible and absorb more intensely at wavelengths greater than 415 nm. The first spin-allowed transition may thus be lower in energy for the phenanthridine-containing molecules which present more extended π- systems, as would be anticipated based on the first singlet excited state energies of the constituent heterocycles (E_S of quinoline and phenanthridine are 31850 and 28590 cm^{-1} respectively[48]).

With the new proligand derivatives in hand, the effects of ring substitution can now be evaluated too. Considering the *bis*(phenanthridine) systems ($\mathbf{L3^{R,R}}$, Figure 4.3a), it can be seen that the replacement of the methyl substituents at the 2-position by electron-withdrawing trifluoromethyl groups leads to a blue-shift in the lowest energy absorption band, while changing to *t*Bu substituents has little effect on λ_{max} though the band is broadened slightly (Note: these shifts are best examined by referring to the spectra, rather than the λ_{max} values which do not necessarily capture the full picture; Figure 4.3c). The band of the mixed-substituent $\mathbf{L3^{CF3,tBu}}$ (**L12**) is also rather broad, but has a shorter λ_{max} similar to $\mathbf{L3^{CF3,CF3}}$ (**L11**). These observations can be

rationalized by considering the localization of the frontier orbitals. We previously demonstrated using density functional theory (DFT) and time-dependent DFT (TDDFT) calculations that the lowest energy transitions of **L1^{Me,Me}**(**L5**)-**L3^{Me,Me}**(**L3**) are HOMO→LUMO in nature.[38] The HOMOs of these systems are comprised of the amine lone pair (:NH; ~20%) and the C_6 ring of the heterocycle arms directly bonded to the amine unit (~34% from each arm). The LUMOs, in comparison, are made up of out-of-phase (π*) contributions from the π systems of the *N*-heterocycles, specifically the C_5N rings (~24% per *N*-heterocycle) and the C=N subunit in particular.[38] Ring substitution at the 2-position of the phenanthridinyl rings in **L3^{R,R}** most directly impacts the HOMO, being directly attached to the C_6 ring comprising ~70% of this frontier orbital. Substitution with a strongly electron-withdrawing CF_3 group has a stabilizing effect on the HOMO, widening the HOMO-LUMO gap, leading to the observed blue shift. CF_3 has a greater (electron-withdrawing) effect compared with the (electron-releasing) impact of *t*Bu, as evidenced by the absolute values of their respective Hammett parameters (CF_3: $\sigma_{meta} = 0.43$; *t*Bu: $\sigma_{meta} = -0.10$)[49,50] and thus the impact of substitution on the HOMO is more pronounced in **L3^{CF3,CF3}** (**L11**).

The "mixed" quinoline-phenanthridine systems **L2^{R,R}** show a similar trend on variation of the phenanthridine substituent (Figure 3b), with the lowest energy absorption in **L2^{Me,CF3}** (**L9**) blue-shifted relative to the dimethyl and *t*Bu analogues. A strong band at around 310 nm – which is a feature of the *bis*(phenanthridine) **L3^{R,R}** series but not of the *bis*(quinolines) **L1^{R,R}** – also appears in the mixed **L2^{R,R}** compounds but is proportionately weaker than in **L3^{R,R}**, consistent with the presence of one of each type of heterocycle.[38] The **L2^{H,R}** compounds (with no substituent on the quinoline) show exactly the same trend (Figure 4.3d), and there is no significant difference in their absorption spectra compared to their respective methylated quinoline analogs **L2^{Me,R}**.

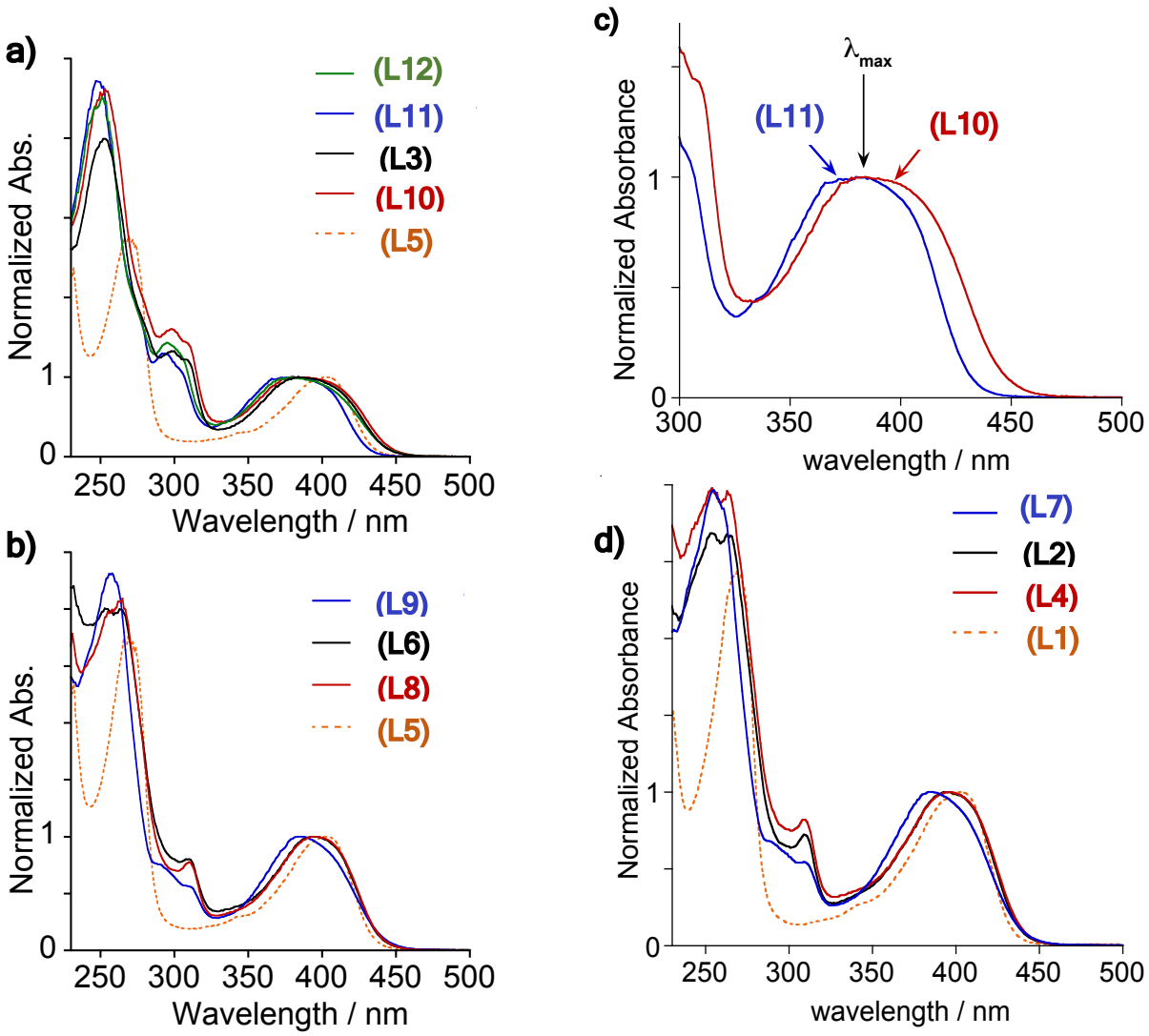

Figure 4.3. UV-visible absorption spectra in CH_2Cl_2 solution at 295 K of (a) *bis*(phenanthridine) proligands $\mathbf{L3^{R,R}}$; (b) three of the mixed quinoline-phenanthridine $\mathbf{L2^{Me,R}}$ (c) Comparison of UV-visible absorption spectra of $\mathbf{L3^{CF3,CF3}}$ (**L11**) and $\mathbf{L3^{tBu,tBu}}$ (**L10**) in CH_2Cl_2 solution at 295 K showing the noticeable blue-shifted absorption band for $\mathbf{L3^{CF3,CF3}}$, but similar λ_{max} values. (d) UV-visible absorption spectra in CH_2Cl_2 solution at 295 K of $\mathbf{L2^{H,R}}$. In both panels, the absorption spectrum of the *bis*(quinoline) proligand $\mathbf{L1^{Me,Me}}$ (**L5**) is provided for comparison.

Table 4.2. Absorption and emission data of proligands in CH_2Cl_2 at 295 K and in EPA (diethyl ether/isopentane/ethanol, 2:2:1 v/v) glass at 77 K.

Proligand	Absorption λ_{max} / nm (ε / M^{-1} cm^{-1})	Emission λ_{max} / nm	Φ_{lum} × 10^2	Emission 77 K	
				λ_{max} / nm	τ / ns
L1^{H,H}(L1)	270 (23000), 342 (sh), 403 (9520)	475	0.35	429, 449	3.7
L1^{Me,Me}(L5)	269 (28400), 344 (3200), 403 (9800)	474	0.55	431, 451	3.5
L2^{H,Me}(L2)	254 (23900), 265 (23800), 310 (6410), 395 (8910)	497	0.16	445, 468	5.0
L2^{H,tBu}(L4)	254 (27700), 264 (27900), 309 (7640), 397 (9320)	493	0.23	437, 456	3.6
L2^{H,CF3}(L7)	255 (26800), 290 (6060), 309 (4890), 386 (9050)	509	0.10	444, 467	2.2
L2^{Me,Me}(L6)	254 (26000), 264 (27100), 310 (7400), 395 (9000)	503	0.25	441, 461	3.8
L2^{Me,tBu}(L8)	255 (28200), 265 (29300), 311 (7300), 394 (9480)	505	0.19	437, 455	3.4
L2^{Me,CF3}(L9)	257 (30200), 291 (6860), 310 (5120), 386 (9140)	518	0.12	445, 467	2.0
L3^{Me,Me}(L3)	253 (65200), 299 (22000), 308 (sh), 388 (15900)	485	0.20	447, 471	3.2
L3^{tBu,tBu}(L10)	253 (76100), 299 (26400), 309 (sh), 383 (16500)	498	0.47	443, 467, 508, 551	3.9
L3^{CF3,CF3}(L11)	247 (76000), 294 (20900), 304 (sh), 382 (16100)	476	0.098	423, 447	2.0
L3^{CF3,tBu}(L12)	254 (75400), 296 (21600), 380 (16900)	518	0.21	445, 469	3.8

At room temperature, the twelve proligands all emit weakly in solution, with unstructured and broad fluorescence peaking at ~ 474–518 nm, quantum yields below 1% and lifetimes of less than 1 ns (Figure 4.4 and Table 4.2). We noted in my initial report[38] how emission from the *bis*(quinoline) **L1^{Me,Me}** (**L5**) occurs at higher energy than either of the phenanthridine-containing molecules. This trend is likewise observed in all of the new proligands reported here, consistent

with the previously mentioned trend in the first singlet excited state energy (E_s) of the parent heterocycles.

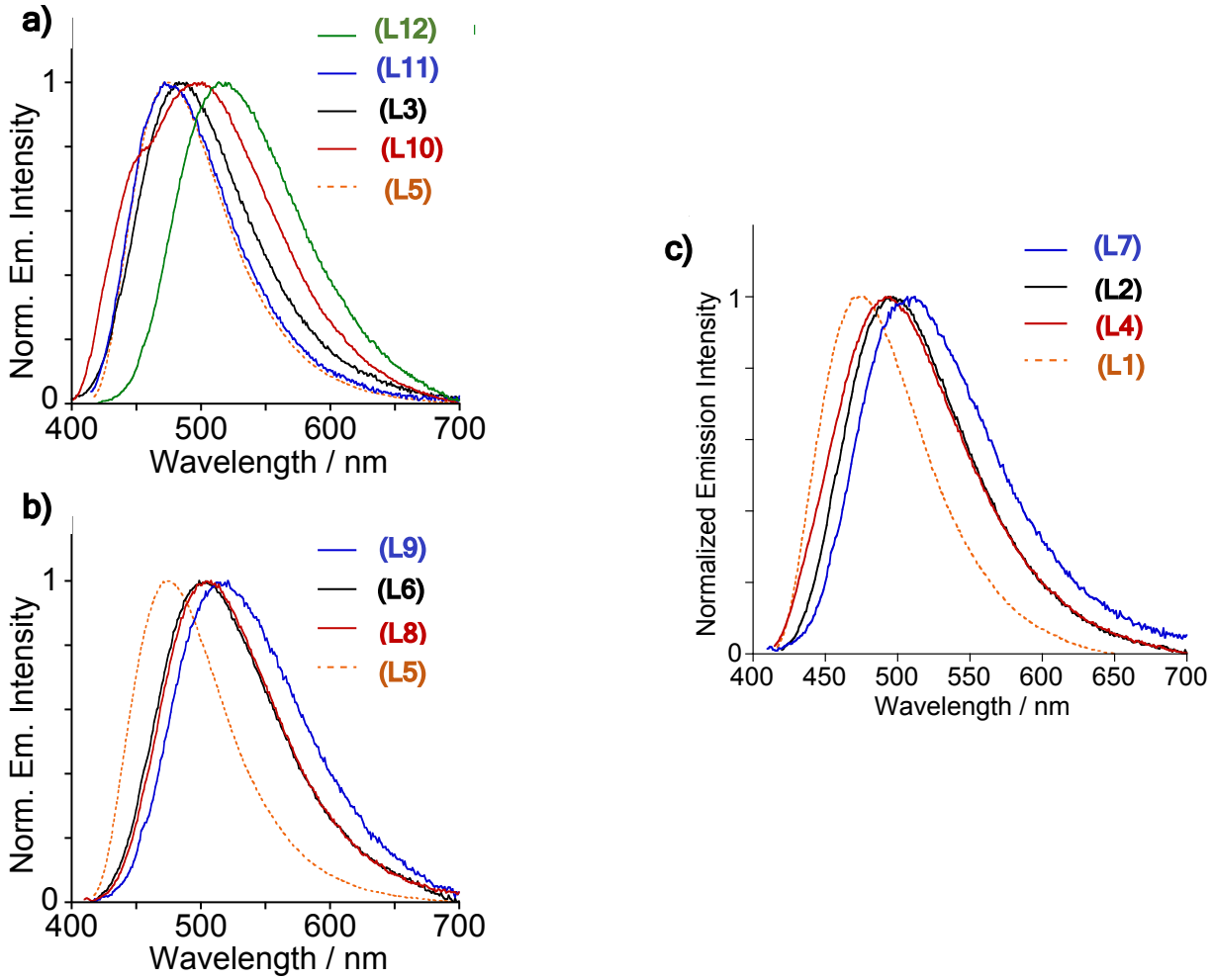

Figure 4.4. Photoluminescence spectra in CH_2Cl_2 solution at 295 K of (a) *bis*(phenanthridine) proligands $\mathbf{L3^{R,R}}$; (b) three of the mixed quinoline-phenanthridine $\mathbf{L2^{Me,R}}$ (c) three of the mixed quinoline-phenanthridine $\mathbf{L2^{H,R}}$. In both panels, the emission spectrum of the *bis*(quinoline) proligand $\mathbf{L1^{Me,Me}}$ (**L5**) is provided for comparison.

Amongst the three symmetrically substituted *bis*(phenanthridine) ligands, $\mathbf{L3^{CF3,CF3}}$ emits at highest energy and $\mathbf{L3^{tBu,tBu}}$ (**L10**) the lowest (Figure 4a). Interestingly, however, the asymmetric derivative $\mathbf{L3^{CF3,tBu}}$ (**L12**) emits at unequivocally lower energy than either of them, indicative of

an element of charge-transfer character between the differently substituted phenanthridines. A similar observation is made for the **L2**^{R,R} series: **L2**^{Me,CF3} (**L9**) emits at a lower energy than **L2**^{Me,Me} (**L6**) or **L2**^{Me,tBu} (**L8**) (Figure 4.4b), while **L2**^{H,CF3} (**L7**) emits at a lower energy compared to **L2**^{H,Me} (**L2**) and **L2**^{H,tBu} (Figure 4.4c). Across the entire library, the mixed quinoline-phenanthridine compounds **L2**^{R,R} are all red-shifted compared to their correspondingly substituted *bis*(phenanthridine) analogues **L3**^{R,R}, consistent with the quinoline and phenanthridine units acting as donor and acceptor respectively in a charge-transfer process. At 77 K (Table 4.2, Figure 4.5), this effect is largely lost which may be understood in terms of a destabilization of the charge-transfer contribution under these conditions. Underscoring this point, the three compounds incorporating a methyl substituent in the 6-position of the quinoline arm (**L2**^{Me,R}) all show a small but significant red-shift relative to those with no substituent on the quinoline (**L2**^{H,R}) at room temperature (Figure 4.6). This is consistent with the methylated quinoline being a slightly more electron-rich donor in the proposed charge-transfer process.

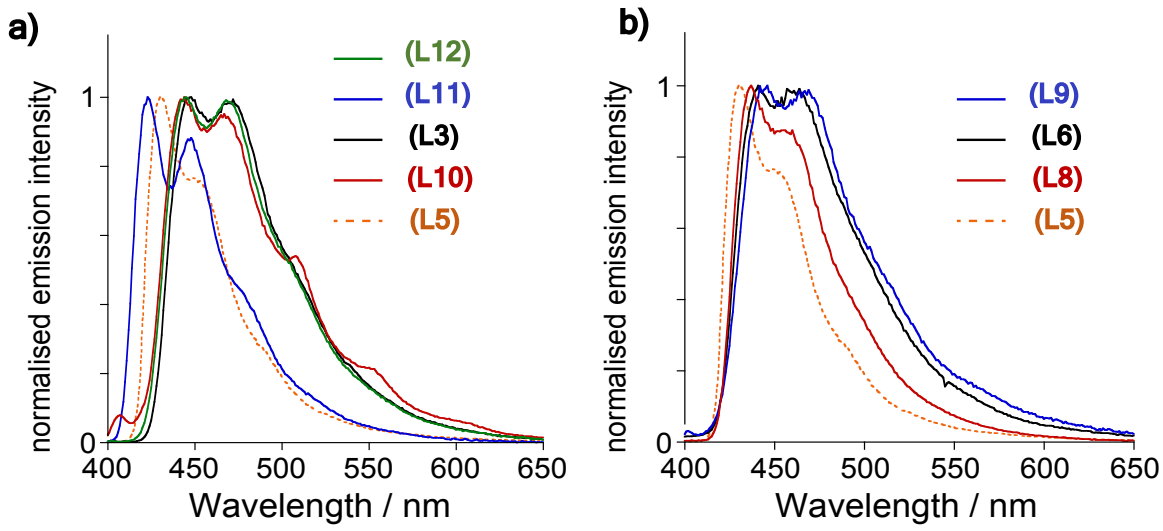

Figure 4.5. Photoluminescence spectra of proligands in EPA glass at 77 K: (a) Spectra of the **L3**^{R,R} series of bis-phenanthridine proligands; (b) Spectra of three of the mixed quinoline-phenanthridine

series $\mathbf{L2^{Me,R}}$. The emission spectrum of the bis-quinoline proligand $\mathbf{L1^{Me,Me}}$ **(L5)** is provided for comparison (dashed orange line).

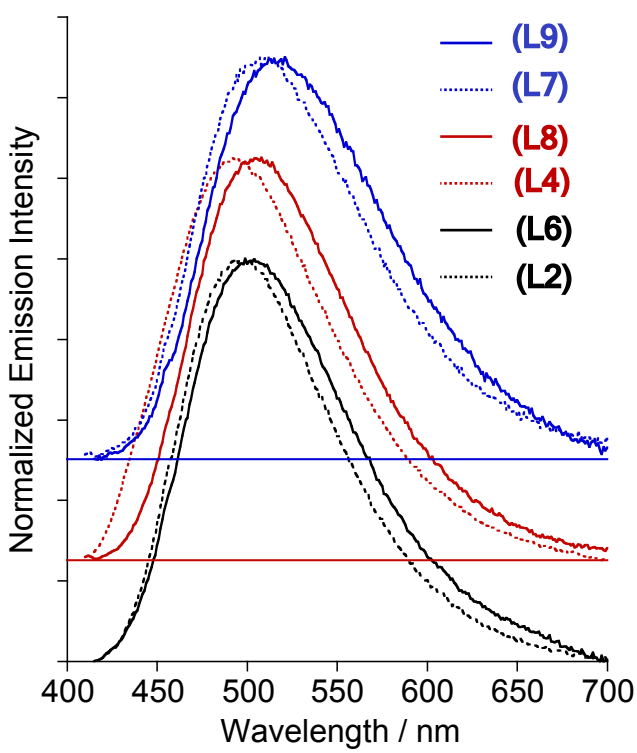

Figure 4.6. Photoluminescence spectra of all six mixed quinoline-phenanthridine proligands, showing how the $\mathbf{L2^{Me,R}}$ compounds (solid lines) display red-shifted emission relative to the corresponding $\mathbf{L2^{H,R}}$ (dashed lines) in each case (CH_2Cl_2, 295 K).

4.4.2. Platinum complexes:

Photophysical data for all twelve of the platinum complexes are reported in Table 4.3, with selected UV-visible absorption spectra shown in Figure 4.7 (additional absorption and emission spectra are shown in 4.8). The Pt complexes are all dark red in color. Accordingly, a broad and intense absorption band can be observed in each case, with a maximum at ~500 nm. Deprotonation of the amine N–H and chelation to a Lewis acidic Pt(II) centre thus increases the energy of the highest occupied orbitals and concomitantly stabilizes the heterocycle-based π* orbitals, displacing the

lowest energy absorption band by ~5000 cm^{-1} compared with the proligands. The major difference between the phenanthridine-containing complexes (**L2^{R,R}-PtCl** and **L3^{R,R}-PtCl**) and the *bis*(quinoline) analogs (**L1^{R,R}-PtCl**) is the higher absorption of the former in the 300–350 nm region, as observed for the proligands. The identity of the substituents in the 2-position of the phenanthridine (or the 6-position of the quinoline)[41] is seen to have minimal effect on the lowest-energy absorption band. As demonstrated for the methyl substituted analogs **L(1^{Me,Me}-3^{Me,Me})-PtCl**, the main contributor to the lowest energy absorption is from the HOMO→LUMO+1 transition.[38] Population analysis of both these orbitals revealed only small contributions of the carbon at the site of substitution. For example, there is no orbital density present at the carbons directly bonded to the methyl groups, nor at the methyl groups themselves, in the HOMOs of **L(1^{Me,Me}-3^{Me,Me})-PtCl**. Thus, only the *bis*-CF_3-substituted complex, bearing strongly electron-withdrawing substituents, shows some differences in relative intensities of UV and visible bands compared to the others as shown in Figure 4.7a. Nevertheless, only a small shift to lower energy is observed for the lowest energy absorption in **3^{CF3,CF3}** (**L11-PtCl**) compared with **3^{Me,Me}** (**L3-PtCl**).

Table 4.3. Absorption and emission data of Pt(II) complexes[a]

	Absorption λ_{max}/nm	Emission λ_{max}/nm[b]	Φ_{lum} × 10^2 [b,c]	τ / ns [d]	k_r / 10^3 s^{-1} [e]	Σk_{nr} / 10^5 s^{-1} [e]	k_Q^{O2} / 10^9 $M^{-1}s^{-1}$ [f]	Emission 77 K[g] λ_{max}/nm [h]	Emission 77 K[g] τ / ns
1^{H,H} (**L11-PtCl**)	239, 300, 342, 357, 381, **504**	740	0.10	1200 [170]	0.83	8.3	2.3	692, 760	3300
1^{Me,Me} (**L5-PtCl**)	240, 301, 340, 356, 381, **501**	738	0.081	1800 [230]	0.49	5.6	1.7	696, 763	2200
2^{H,Me} (**L2-PtCl**)	244, 258, 284, 315, 338, 353, 404, **504**	745	0.11	1100 [180]	1.0	9.1	2.1	692,753	5200
2^{H,tBu} (**L4-PtCl**)	245, 260, 280sh, 317, 338, 356, 403, **508**	737	0.22	1800 [190]	1.2	5.5	2.1	682,741	2900
2^{H,CF3} (**L7-PtCl**)	235, 261, 283, 325, 356, 412, **500**	712	0.31	2000 [250]	1.6	5.0	1.6	680, 726	6500
2^{Me,Me} (**L6-PtCl**)	246, 284, 315, 338, 354, 405, **502**	740	0.13	1000 [180]	1.3	10	2.1	692, 756	3000
2^{Me,tBu} (**L8-PtCl**)	243, 285, 316, 338, 355, 405, **505**	743	0.092	850 [220]	1.1	12	1.5	690, 753	5600
2^{Me,CF3} (**L9-PtCl**)	236, 261, 282, 324, 356, 415, **497**, 570sh	710	0.30	2000 [210]	1.5	5.0	1.9	711, 774	2600
3^{Me,Me} (**L3-PtCl**)	265, 321, 338, 355, 405, **503**	703	0.18	2500 [190]	0.72	4.0	2.2	663, 727	18300
3^{tBu,tBu} (**L10-PtCl**)	266, 324, 338, 356, 406, **509**	713	0.47	2000 [190]	2.4	5.0	2.2	664, 728	2600
3^{CF3,CF3} (**L11-PtCl**)	241, 263, 330, 348, 369, 404sh, **506**, 539sh	683	0.10	4500 [240]	0.22	2.2	1.8	675	1800
3^{CF3,tBu} (**L12-PtCl**)	265, 325, 337, 356, 399, **502**, 570sh	715	0.30	1300 [240]	2.3	7.7	1.5	702	2300

[a] In degassed CH_2Cl_2 at 295 K, except where indicated otherwise. [b] Emission maxima and photoluminescence quantum yields Φ_{lum} determined from spectra recorded using a Synapse CCD detector. [c] Measured in deoxygenated solution, using $[Ru(bpy)_3]Cl_{2(aq)}$ as the standard. [d] Luminescence lifetimes in deoxygenated solution. Values in air-equilibrated solution are given in square parenthesis. [e] Radiative (k_r) and non-radiative (Σk_{nr}) rate constants estimated from quantum yield and lifetime, assuming unitary population of the emissive state upon light absorption: $k_r \sim \Phi / \tau$; $k_{nr} \sim (1-\Phi) / \tau$. [f] Bimolecular Stern-Volmer constant for quenching by molecular oxygen, estimated from the lifetimes in deoxygenated and air-equilibrated solution, and assuming $[O_2]$ = 2.2 mmol dm^{-3} at atmospheric pressure of air. [g] In diethyl ether / isopentane / ethanol (2:2:1 v/v). [h] Emission spectra at 77 K were recorded using a conventional monochromator and Hamamatsu R928 PMT detector. For additional spectra, see Figure 4.6c-d and 4.7.

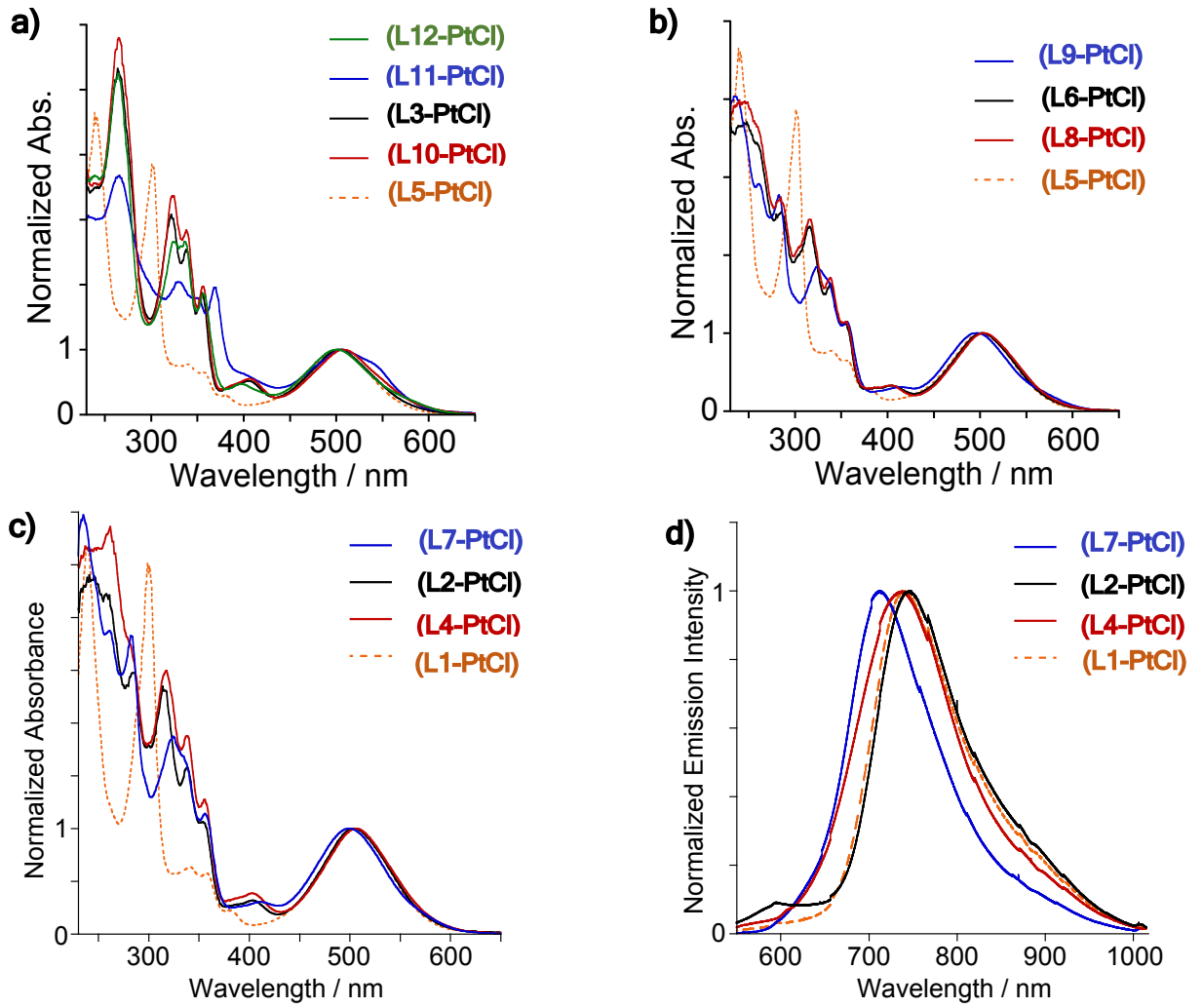

Figure 4.7. UV-visible absorption spectra in CH_2Cl_2 solution at 295 K of (a) *bis*(phenanthridine) series $\mathbf{3^{R,R}}$(**L3^{R,R}-PtCl**); (b) three of the mixed quinoline-phenanthridine series $\mathbf{2^{Me,R}}$ (**L2^{Me,R}-PtCl**) (c) three of the mixed quinoline-phenanthridine series $\mathbf{2^{H,R}}$ (**L2^{H,R}-PtCl**) (d) photoluminescence spectra in CH_2Cl_2 solution at 295 K of three of the mixed quinoline-phenanthridine series $\mathbf{2^{H,R}}$ (**L2^{H,R}-PtCl**) showing the effect of the phenanthridine substituent while the quinoline remains unsubstituted; spectra of the bis-quinoline complex $\mathbf{1^{H,H}}$ (**L1-PtCl**) are provided for comparison. In both panels (a) and (b), the absorption spectrum of the *bis*(quinoline) complex $\mathbf{1^{Me,Me}}$ (**L5-PtCl**) is provided for comparison.

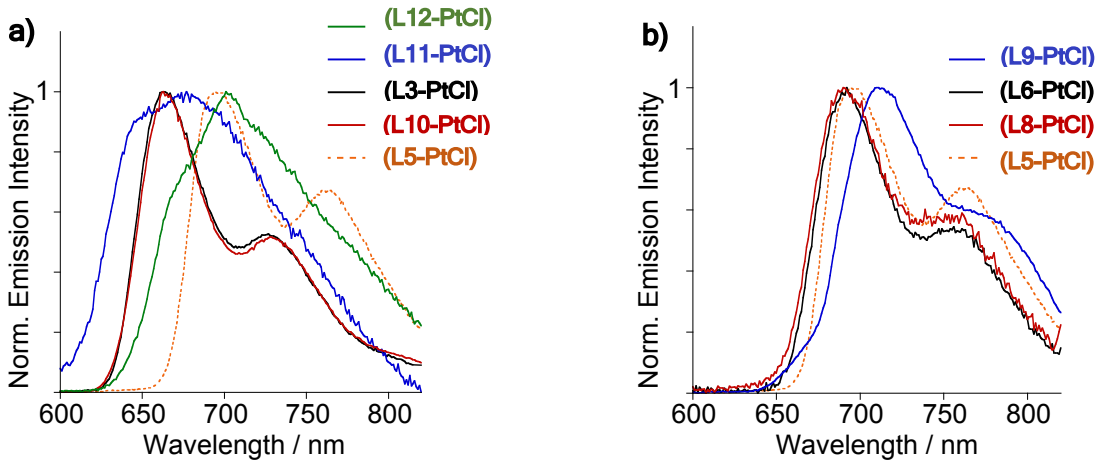

Figure 4.8. Photoluminescence spectra of Pt(II) complexes in EPA glass at 77 K: (a) Spectra of the bis-phenanthridine series $\mathbf{3^{R,R}}$ **(L3^{R,R}-PtCl)**; (b) Spectra of three of the mixed quinoline-phenanthridine $\mathbf{2^{R,R}}$ **(L2^{R,R}-PtCl)** complexes. The emission spectrum of the bis-quinoline complex $\mathbf{1^{Me,Me}}$ **(L5-PtCl)** is also provided for comparison.

DFT modeling of $\mathbf{3^{CF3,CF3}}$ **(L11-PtCl)** is consistent with this observation as shown in Figure 4.9. Namely, the introduction of strongly electron-withdrawing CF_3 groups has a stabilizing influence on both the HOMO of $\mathbf{3^{CF3,CF3}}$ **(L11-PtCl)** (E_{HOMO} = -5.74 eV) compared to $\mathbf{3^{Me,Me}}$ **(L3-PtCl)** (E_{HOMO} = -5.29 eV; ΔE_{HOMO} = -0.45 eV) and the LUMO+1 (E_{LUMO+1} = -2.40 eV, $\mathbf{3^{CF3,CF3}}$ **(L5-PtCl)**; E_{LUMO+1} = -1.92 eV, $\mathbf{3^{Me,Me}}$ **(L3-PtCl)**; ΔE_{LUMO+1} = -0.48 eV). As for $\mathbf{1^{Me,Me}}$**(L5-PtCl)** /$\mathbf{2^{Me,Me}}$**(L6-PtCl)** /$\mathbf{3^{Me,Me}}$**(L3-PtCl)**,[38] TDDFT reveals the lowest energy absorption in $\mathbf{3^{CF3,CF3}}$ **(L11-PtCl)** is dominated by the HOMO→LUMO+1 transition (Table 4.4, Figure 4.10). Interestingly, a consequence of the introduction of a strongly electron-withdrawing CF_3 substituent in $\mathbf{2^{Me,CF3}}$ **(L9-PtCl)** is to turn on the HOMO→LUMO transition, which is predicted by TDDFT to have an oscillator strength comparable to that of the HOMO→LUMO+1 transition and thus contribute to the lowest energy absorption band (Table 4.5, Figure 4.11). Indeed, it appears as a low-energy shoulder in the UV-Vis absorption spectrum as shown in Figure 4.7. Consequently, the broad, lowest energy absorption band for $\mathbf{2^{Me,CF3}}$ **(L9-PtCl)** is not significantly shifted

compared to the rest of the $\mathbf{2^{R,R}}$ (**L2^{R,R}-PtCl**) series. Despite a larger HOMO-LUMO+1 energy gap, the participation of the lower energy HOMO→LUMO transition keeps the absorption maximum relatively unchanged.

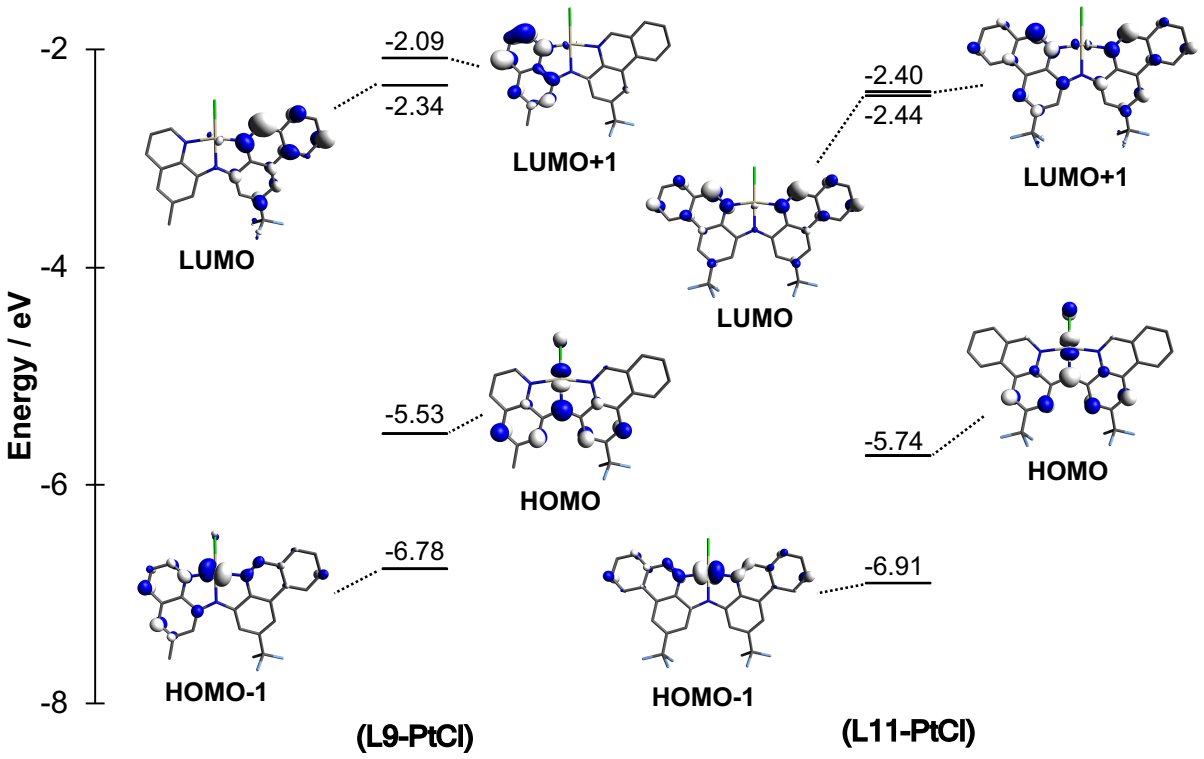

Figure 4.9. Selected MOs and energies (IEFPCM[CH_2Cl_2]-M06/LANL2DZ; isosurface = 0.05) of $\mathbf{2^{Me,CF3}}$ (**L9-PtCl**) and $\mathbf{3^{CF3,CF3}}$ (**L11-PtCl**).

The location of the CF_3 substituent on the phenanthridinyl arm in $\mathbf{2^{Me,CF3}}$ (**L9-PtCl**) has an unequal effect on the HOMO, LUMO and LUMO+1. Specifically, the electron-withdrawing effect of CF_3 results in relatively significant stabilization of both the HOMO and LUMO compared to in $\mathbf{2^{Me,Me}}$(**L6-PtCl**) but has less of an impact on the acceptor LUMO+1. The influence on the HOMO can be attributed to an inductive stabilization on the amido nitrogen *meta* to the substituent. For the mixed quin/phen systems $\mathbf{2^{R,R}}$ (**L2^{R,R}-PtCl**), the LUMO and LUMO+1 are comprised of different relative contributions from the quinolinyl and phenanthridinyl arms. In $\mathbf{2^{Me,Me}}$ (**L6-PtCl**), the quinolinyl moiety contributes more than the phenanthridinyl unit does to the LUMO+1 and

vice versa for the LUMO.[38] Introducing a CF_3 substituent exaggerates this asymmetry, such that the phenanthridinyl arm completely dominates the LUMO in $\mathbf{2^{Me,CF3}}$ (**L9-PtCl**) (see Tables 4.6 and 4.7 for population analysis). Thus, the LUMO energy is most drastically impacted by introduction of a strongly electron-withdrawing CF_3 substituent; the LUMO+1, less so. In pseudooctahedral Fe(II) complexes of $\mathbf{L2^{H,CF3}}$ (**L7-PtCl**) and $\mathbf{L2^{H,tBu}}$ (**L4-PtCl**), introduction of a strongly electron-withdrawing CF_3 at the phenanthridine was found to similarly increase the phenanthridine contributions to the LUMO over those from quinoline.[44] This contrasts with what is often observed for CF_3-containing luminescent organometallics (*e.g.*, those based on cyclometallating ligands) where, although both HOMO and LUMO are stabilized, the latter is more so, largely inducing bathochromic shifts.[51,52] Structure-property relationships accounting for the placement of substituents relative to the primary orbital density comprising the HOMO and LUMO have been previously used to explain unequal impacts on the frontier orbitals in cyclometallated Ir emitters.[49] It is notable that λ_{max} for $\mathbf{2^{Me,CF3}}$ (**L9-PtCl**) is still some 27 nm red-shifted compared to $\mathbf{3^{CF3,CF3}}$ (**L11-PtCl**), which has no quinoline unit.

All twelve platinum complexes are emissive at room temperature in deoxygenated solution, with luminescence in the deep red/NIR that tails to 800–1000 nm (Figure 4.12, Figure 4.7d; Table 4.3). Owing to the poor sensitivity of conventional photomultiplier tubes in this region, the spectra shown in Figure 4.12 were recorded using a CCD detector with superior sensitivity in the NIR (see Experimental Section for details). Each spectrum contains a relatively narrow, unstructured band (FWHM ~ 2300 cm^{-1}). In our initial study of the parent dimethyl complexes, we noted how emission from the *bis*(phenanthridine) complex $\mathbf{3^{Me,Me}}$ (**L3-PtCl**) is unequivocally higher in energy compared to that of the quinoline-containing complexes $\mathbf{1^{Me,Me}}$ (**L5-PtCl**) and $\mathbf{2^{Me,Me}}$ (**L6-PtCl**), in spite of the greater conjugation of the phenanthridinyl-containing ligands.[38] I traced this

to enhanced rigidity within the benzannulated phenanthridinyl systems, which results in a higher energy emissive triplet state. The "mixed" system **2^{Me,Me}** (**L6-PtCl**) behaves like the *bis*(quinoline) **1^{Me,Me}** (**L5-PtCl**), implying the emissive state in both primarily involves the quinoline.

Table 4.4. TDDFT calculated (IEFPCM-M06/LANL2DZ) vertical excitation energies, oscillator strengths ($f > 0.05$) for **3^{CF3,CF3} (L11-PtCl)**.

No.	λ / nm	E / eV	f_{osc}	Major Contributions
1	510	2.43	0.45	HOMO→L+1 (99%)
4	386	3.21	0.08	HOMO→L+3 (96%)
5	385	3.22	0.08	HOMO→L+2 (95%)
8	350	3.54	0.76	H-1→LUMO (89%)
12	332	3.74	0.09	H-3→L+1 (80%)
14	327	3.79	0.05	H-4→L+1 (82%), HOMO→L+5 (10%)
15	320	3.87	0.11	H-6→L+1 (11%), H-5→LUMO (23%), H-3→L+1 (11%), HOMO→L+4 (13%), HOMO→L+5 (28%)
16	318	3.90	0.07	H-1→L+4 (43%), H-1→L+5 (22%)
17	317	3.91	0.18	H-6→LUMO (31%), H-5→L+1 (32%)
23	283	4.38	0.11	H-6→L+1 (20%), H-5→LUMO (39%), H-1→L+3 (32%)
24	281	4.41	0.20	H-5→L+1 (24%), H-1→L+2 (68%)
28	268	4.63	0.15	H-3→L+3 (85%)
29	268	4.63	0.32	H-6→L+2 (12%), H-5→L+3 (24%), H-3→L+2 (44%)
30	267	4.64	0.31	H-7→LUMO (13%), H-6→L+2 (19%), H-5→L+3 (10%), H-3→L+2 (46%)
34	255	4.87	0.32	H-7→LUMO (70%), H-5→L+3 (13%)
36	252	4.92	0.09	HOMO→L+7 (77%)
37	252	4.93	0.21	H-7→L+1 (66%), H-5→L+2 (11%)

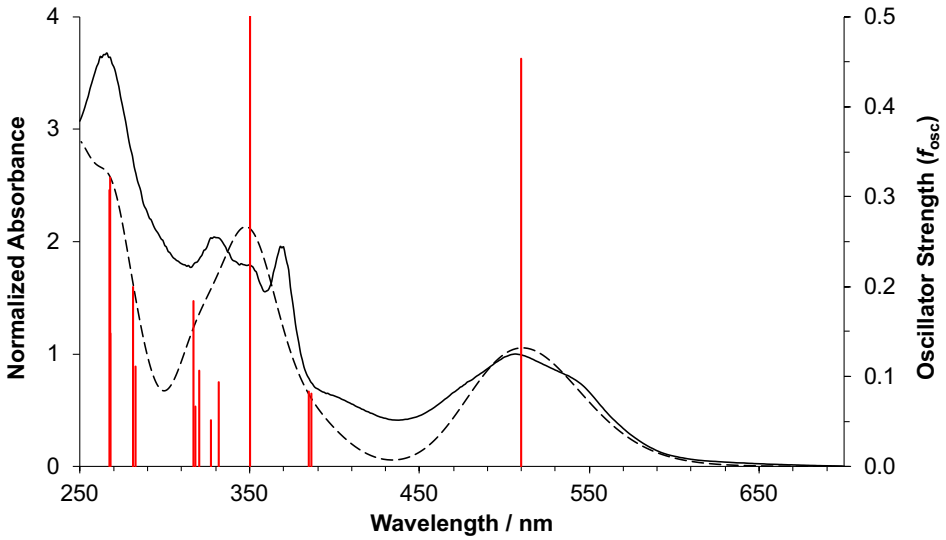

Figure 4.10. Experimental (—) and TDDFT (IEFPCM-M06/LANL2DZ) simulated absorbance spectra (---) and vertical excitations (—) of **3^{CF3,CF3} (L11-PtCl)** in CH_2Cl_2.

Table 4.5. TDDFT calculated (IEFPCM-M06/LANL2DZ) vertical excitation energies, oscillator strengths ($f > 0.05$) for **2^{Me,CF3} (L9-PtCl)**.

No.	λ / nm	E / eV	f_{osc}	Major Contributions
1	533	2.33	0.20	HOMO→LUMO (98%)
2	490	2.53	0.20	HOMO→L+1 (98%)
4	400	3.10	0.08	HOMO→L+2 (96%)
6	349	3.55	0.42	H-1→LUMO (78%), H-1→L+1 (10%)
9	337	3.68	0.09	H-3→LUMO (66%), H-2→L+1 (10%)
12	327	3.79	0.09	H-1→L+1 (69%)
13	323	3.83	0.16	H-5→LUMO (14%), HOMO→L+3 (12%), HOMO→L+4 (24%), HOMO→L+5 (30%)
16	316	3.92	0.10	H-5→LUMO (63%)
19	285	4.35	0.13	H-5→LUMO (11%), H-1→L+2 (79%)
22	278	4.46	0.12	H-6→L+1 (65%)
25	271	4.58	0.42	H-5→L+1 (19%), H-3→L+2 (20%), HOMO→L+6 (33%)
26	269	4.61	0.30	H-5→L+1 (13%), H-5→L+2 (18%), H-3→L+2 (32%), HOMO→L+6 (18%)
30	260	4.78	0.18	H-7→LUMO (39%), H-5→L+2 (33%)
31	256	4.85	0.06	H-7→L+1 (63%)

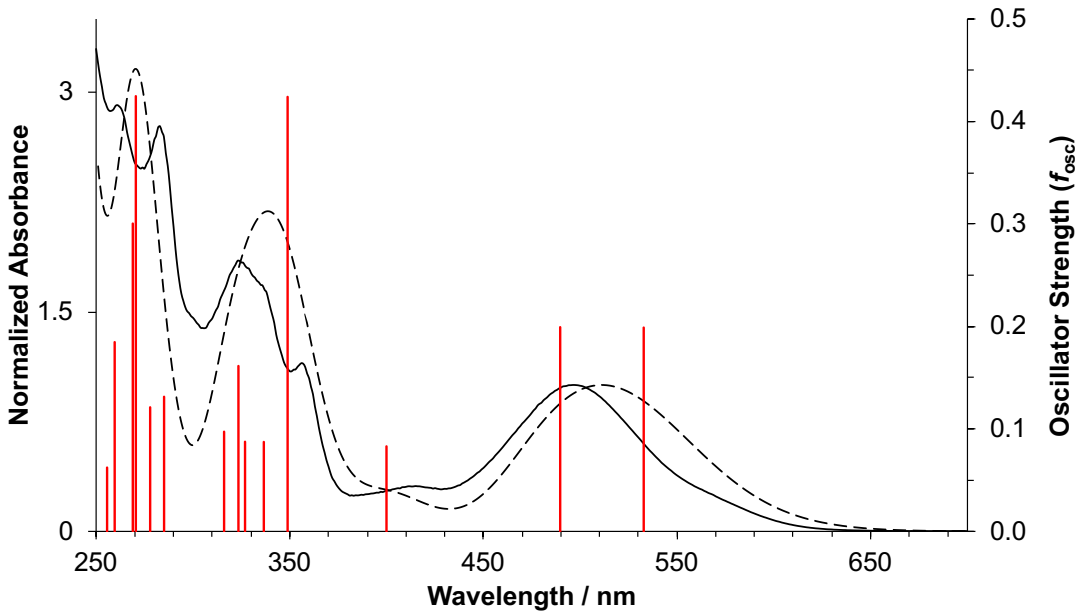

Figure 4.11. Experimental (—) and TDDFT (IEFPCM-M06/LANL2DZ) simulated absorbance spectra (---) and vertical excitations (—) of **$2^{Me,CF3}$ (L11-PtCl)** in CH_2Cl_2.

Table 4.6. Fragment contributions to the frontier molecular orbitals of **$2^{Me,CF3}$(L9-PtCl)** using Hirshfeld atomic population method[1] (IEFPCM-M06/LANL2DZ).

MO	E / eV	Pt	Cl	N^{amide}	$C{=}N^{phen}$	$C{=}N^{quin}$	Ar^{phen}	Ar^{quin}	CF_3	Me
L+2	-1.60	1	0	1	4	1	89	3	2	0
L+1	-2.09	4	0	1	0	29	7	58	0	1
LUMO	-2.34	4	0	1	35	0	54	2	3	0
HOMO	-5.53	18	5	19	2	2	25	29	0	0
H-1	-6.78	43	3	1	7	7	13	23	0	1

Table 4.7. Fragment contributions to the frontier molecular orbitals of **$3^{CF3,CF3}$ (L11-PtCl)** using Hirshfeld atomic population method[1] (IEFPCM-M06/LANL2DZ).

MO	E / eV	Pt	Cl	N^{amide}	$C{=}N^{phen}$	Ar^{phen}	CF_3
L+2	-1.71	0	0	1	4	94	2
L+1	-2.40	3	0	1	32	61	3
LUMO	-2.44	4	0	1	38	54	2
HOMO	-5.74	20	6	19	4	50	1
H-1	-6.91	48	0	1	17	34	0

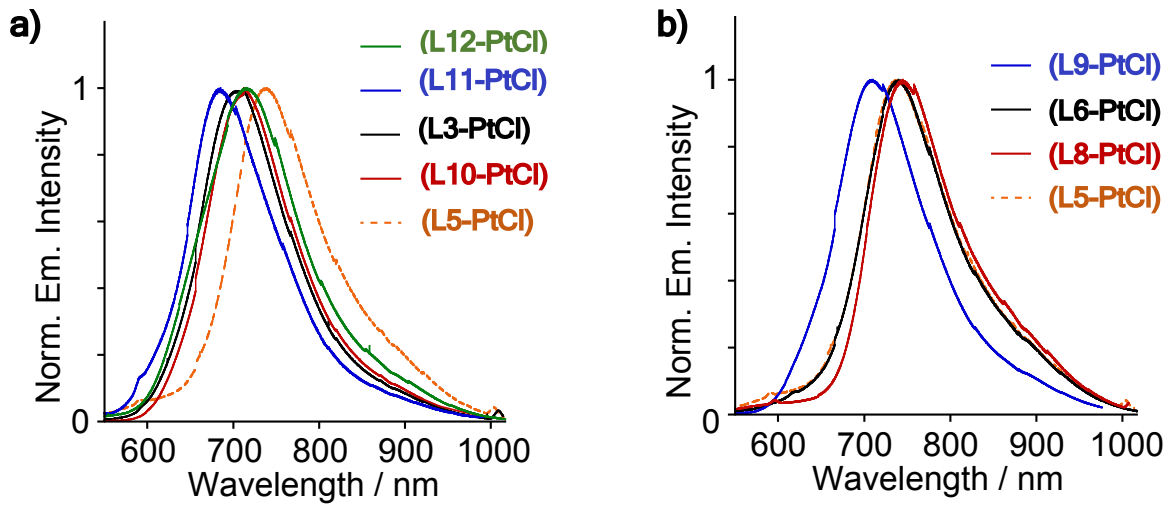

Figure 4.12. Photoluminescence spectra in CH_2Cl_2 at 295 K of (a) the *bis*(phenanthridine) series $\mathbf{3^{R,R}}$; (b) three mixed quinoline-phenanthridine $\mathbf{2^{Me,R}}$ (**L2^{Me,R}-PtCl**) complexes ($\mathbf{2^{H,R}}$ (**L2^{H,R}-PtCl**)are shown in Figure 4.6d). In both panels, the emission spectrum of the *bis*(quinoline) complex $\mathbf{1^{Me,Me}}$ (**L5-PtCl**) is provided for comparison.

These observations are largely borne out amongst the new series of complexes, with most of the quinoline-containing compounds ($\mathbf{1^{R,R}}$ (**L1^{R,R}-PtCl**) and $\mathbf{2^{R,R}}$(**L2^{R,R}-PtCl**)) emitting at lower energy than the *bis*(phenanthridines) $\mathbf{3^{R,R}}$(**L3^{R,R}-PtCl**). Within the series of substituted *bis*(phenanthridine) complexes, it can be seen that the substituents have a small but noticeable influence on λ_{max} (Figure 4.12a). The trend parallels that observed in the proligands. Namely, a blue shift is observed on going from the *bis*-CH_3 $\mathbf{3^{Me,Me}}$ (**L3-PtCl**) to *bis*-CF_3-substituted complex $\mathbf{3^{CF3,CF3}}$(**L11-PtCl**), while a red shift results from introduction of *t*Bu groups in $\mathbf{3^{CF3,tBu}}$ (**L12-PtCl**) and $\mathbf{3^{tBu,tBu}}$ (**L10-PtCl**). As noted above, the introduction of strongly electron-withdrawing CF_3 substituents in $\mathbf{3^{CF3,CF3}}$ (**L11-PtCl**) stabilizes both the HOMO and LUMO+1 by similar amounts (ΔE_{HOMO} = -0.45 eV; ΔE_{LUMO+1} = -0.48 eV). In comparison, the LUMO is stabilized by a smaller amount (ΔE_{LUMO} = -0.39 eV). This has an overall destabilizing effect on the lowest-lying emissive

state [E(T_1) = 2.03 eV; Table 4.8], which is thus less stabilized than the T_1 state of $\mathbf{3^{Me,Me}}$ (**L3-PtCl**) [E(T_1) = 1.88 eV][38] resulting in blue-shifted emission despite slightly red-shifted absorption. As for $\mathbf{3^{Me,Me}}$ (**L3-PtCl**), optimization of the T_1 structure of $\mathbf{3^{CF3,CF3}}$ (**L11-PtCl**) reveals the most significant excited state distortions in the lowest-lying T_1 state are localized in the phenanthridinyl ligand arms; the coordination environment about the Pt centre is left largely untouched (Table 4.9, Figure 4.13).

The "mixed" complexes in series $\mathbf{2^{R,R}}$ (**L2^{R,R}-PtCl**), in comparison, reveal a different picture. Those incorporating methyl or *t*Bu substituents in the phenanthridine emit at similar energy to the parent $\mathbf{2^{Me,Me}}$ (**L6-PtCl**) and $\mathbf{2^{H,Me}}$(**L2-PtCl**), consistent the emissive excited state involving the quinoline (rather than the phenanthridine). However, emission from both $\mathbf{2^{Me,CF3}}$ (**L9-PtCl**) and $\mathbf{2^{H,CF3}}$ (**L7-PtCl**) is blue-shifted by ~30 nm relative to the rest of the $\mathbf{2^{R,R}}$ (**L2^{R,R}-PtCl**) series, rendering their emission maxima similar to those of some of the *bis*(phenanthridines) and apparently counteracting the red-shifting effect of the quinoline. Comparing the optimized structures of the T_1 and ground state (S_0) of $\mathbf{2^{Me,CF3}}$(**L9-PtCl**), the most significant distortions are in fact localized in the C_5N rings of the phenanthridinyl ligand arm (Figure 4.13). Thus, unlike for $\mathbf{1^{R,R}}$ (**L1^{R,R}-PtCl**) and $\mathbf{2^{R,R}}$(**L2^{R,R}-PtCl**), inclusion of strongly electron-withdrawing substituents leads to emissive excited states in the CF_3-substituted analogs with stronger participation of the phenanthridine rather than the quinoline. A plot of the spin density in the lowest lying T_1 state (Figure 4.14) supports this assertion and confirms the ^{3}MLCT character of the lowest lying triplet excited states for both $\mathbf{2^{Me,CF3}}$ (**L9-PtCl**) and $\mathbf{3^{CF3,CF3}}$ (**L11-PtCl**). The higher energy emission from $\mathbf{2^{R,CF3}}$ (**L2^{R,CF3}-PtCl**) can be traced to a higher energy T_1 state [E(T_1, $\mathbf{2^{Me,CF3}}$(**L9**)) = 1.79 eV vs E(T_1, $\mathbf{2^{Me,Me}}$(**L6**)) = 1.77 eV[38]].

In deoxygenated solutions, the observed excited-state lifetimes are on the order of a microsecond, typical of cyclometallated Pt(II) complexes (Table 4.3). These values are consistent with formally spin-forbidden phosphorescence from a triplet excited state, expedited by the spin-orbit coupling of the heavy metal. In air-equilibrated solutions, the lifetimes are shorter by an order of magnitude. The triplet excited state is quenched by molecular oxygen with bimolecular rate constants of ~2 × 10^9 M^{-1} s^{-1}. The quantum yields are all low, in the range of 0.1–0.5%. Interestingly, the complexes that display the brightest emission do not have the longest lifetimes, suggesting that structural variation influences both radiative k_r and non-radiative k_{nr} rate constants. Assuming that the emitting state is formed with unit efficiency, these rate constants can be estimated using the expressions $k_r = \Phi / \tau$ and $k_{nr} = (\tau^{-1} - k_r)$. Considering first the k_{nr} values, it can be seen that the highest values are found for the complexes that emit at lowest energy and vice versa, as predicted by the "energy gap law". This trend is expected in the absence of deactivation processes involving higher-lying states for compounds that present a common type of excited state, as intramolecular energy transfer into vibrational modes becomes increasingly probable.[53] Previous studies of Ru(II) and Pt(II) complexes[54–56] revealed a logarithmic dependence. Here, a fairly convincing linear relationship can be seen in a plot of ln(k_{nr}) versus the excited-state energy (which we estimate from λ_{max}), when considering the twelve complexes collectively as shown in Figure 4.14. Inevitably, additional factors may be introduced when substituents are added that could also influence k_{nr} and cause some deviation from linearity.

Table 4.8. Calculated photophysical parameters for **$2^{Me,CF3}$ (L8-PtCl)** and **$3^{CF3,CF3}$(L11-PtCl)**.

E / eV	**$2^{Me,CF3}$**	**$3^{CF3,CF3}$**
E^{adia} (T_1–S_0)	1.79	2.03
$E^{vert,phos}$ (T_1–T_1@S_0)	1.57	1.89
λ_T (T_1@S_0-S_0)	0.22	0.14

Table 4.9. Selected DFT (IEFPCM-M06/LANL2DZ) optimized ground state and lowest excited triplet state bond lengths (Å) and angles (°) of **$2^{Me,CF3}$ (L8-PtCl)** and **$3^{CF3,CF3}$ (L11-PtCl)**.

	$2^{Me,CF3}$ (L8-PtCl)		**$3^{CF3,CF3}$ (L11-PtCl)**	
	S_0	**T_1**	**S_0**	**T_1**
$Pt–N^{amide}$	1.998	1.976	1.995	1.973
$Pt–N^{N\text{-het.},a}$	2.026	2.047	2.025	2.043
$Pt–N^{phen}$	2.026	2.026	2.025	2.043
Pt–Cl	2.458	2.428	2.456	2.430
$N^{amide}–Pt–Cl$	179.6	179.1	180.0	180.0
$N^{N\text{-het.}}–Pt–N^{phen}$	165.2	164.9	165.2	165.0

[a] *N*-heterocycle: **$2^{Me,CF3}$(L8-PtCl)**, *6-methylquinoline*; **$3^{CF3,CF3}$(L11-PtCl)**, *2-trifluoromethylphenanthridine*

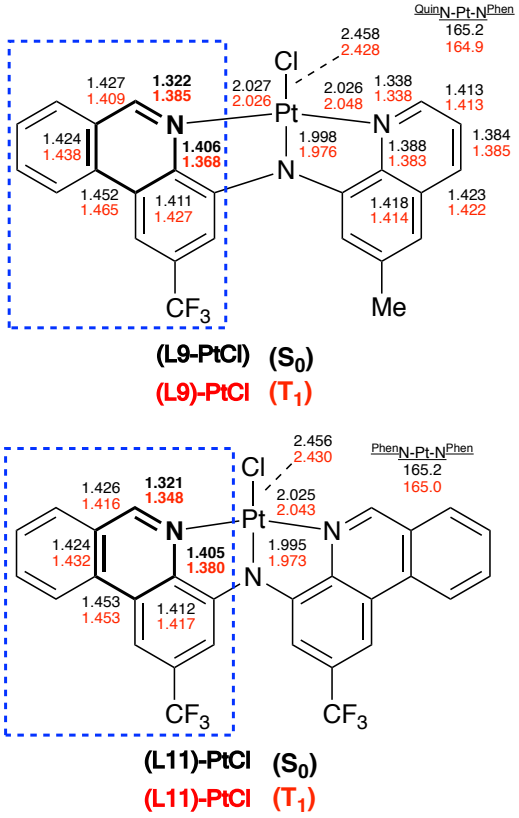

Figure 4.13. Selected bond length comparison of DFT-optimized (IEFPCM-M06/LANL2DZ) S_0 and T_1 structures of **$2^{Me,CF3}$(L9-PtCl)** and **$3^{CF3,CF3}$ (L11-PtCl)**. The most impacted moiety is outlined in blue and bolded.

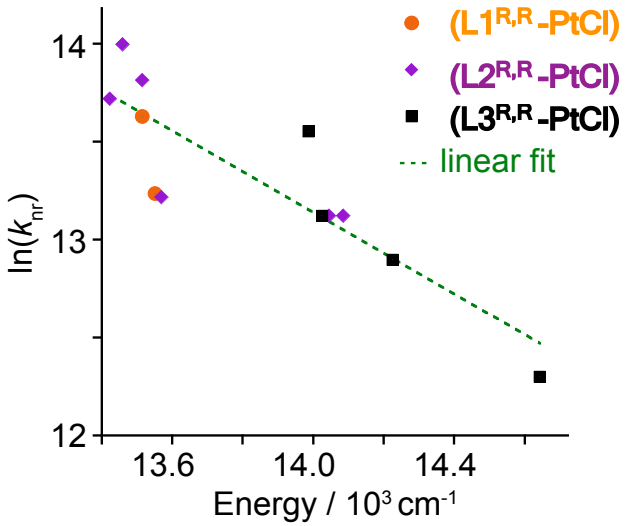

Figure 4.14. Plot of ln(k_{nr}) versus the emission energy, estimated from $\lambda_{max,em}$ in degassed CH_2Cl_2 at 295 K. Data points for the *bis*(quinoline) complexes [**1**^{R,R}(**L1**^{R,R}**-PtCl**); orange circles], *bis*(phenanthridine) series [**3**^{R,R}(**L3**^{R,R}**-PtCl**); black squares] and the mixed quinoline-phenanthridine series [**2**^{R,R}(**L2**^{R,R}**-PtCl**); purple diamonds] are shown along with the best linear fit using all data points (dashed green line).

On the other hand, there is no obvious trend in k_r. However, it can be seen that k_r is smallest for the highest-energy emitters **3**^{CF3,CF3} (**L11-PtCl**) and it is evidently for this reason that its quantum yield is not the highest amongst the series, despite having the lowest k_{nr} value. In contrast, the highest quantum yields [observed for **3**^{tBu,tBu} (**L10-PtCl**)and **3**^{CF3,tBu} (**L12-PtCl**)] reflect k_r values that are around an order of magnitude larger (*e.g.*, for **3**^{CF3,CF3}(**L11-PtCl**) and **3**^{tBu,tBu} (**L10-PtCl**), the k_r values are 220 and 2400 s^{-1} respectively). Since k_r for the formally forbidden phosphorescence process is determined by the efficiency of spin-orbit coupling, which in turn is dependent on the degree of metal character in the excited state, these observations might suggest a better matching of orbital energies of ligand and metal when electron-donating substituents are

present. The efficiency of spin-orbit coupling is also inversely dependent on the S_1–T_1 energy gap, and so it is possible that this gap is smallest in $\mathbf{3}^{t\mathbf{Bu},t\mathbf{Bu}}$ (**L10-PtCl**)and $\mathbf{3}^{\mathbf{CF3},t\mathbf{Bu}}$ (**L12-PtCl**).

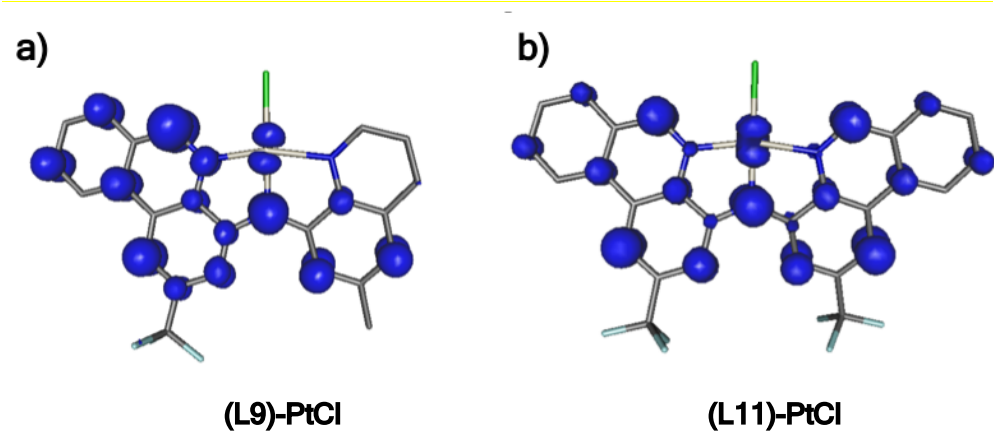

Figure 4.15. Spin density maps (isovalue = 0.005) of the lowest lying triplet excited state for (a) $\mathbf{2}^{\mathbf{Me},\mathbf{CF3}}$**(L9-PtCl)** and (b) $\mathbf{3}^{\mathbf{CF3},\mathbf{CF3}}$ **(L11-PtCl)**.

Although the quantum yields are low, such values are quite typical for NIR-phosphorescent complexes of many transition metals in solution where the combined effects of fast non-radiative decay and a low degree of metal participation in the excited state conspire to limit efficiency.[4,57] The best reported performance for Pt(II) systems is offered by complexes of highly conjugated benzoporphyrins, where quantum yields in excess of 50% have been observed,[4,58] but their synthesis is often demanding, with poor solubility and marked propensity to aggregation. In OLED devices, the use of bimolecular excited states formed through interfacial intermolecular interactions between Pt(II) complexes offers an alternative way of achieving efficient NIR emission,[23,29] but some of the best performing OLED emitters of this type are actually non-emissive in solution.[59] Notable features of the Pt(II) complexes reported here are the relatively

narrow spectra (2300 cm^{-1} compared to > 3000 cm^{-1} for some excimer-based systems[28,29]) and the sharp onset of emission on the high-energy side of the spectrum. This latter property limits or even eliminates contamination of the spectrum by visible emission, a requirement in some applications of NIR OLEDs.

4.5. Conclusions:

In conclusion, a synthetic methodology based on chelating, pincer-like benzannulated diarylamido ligand scaffolds for constructing phosphorescent Pt(II) complexes which emit in the deep red region of the electromagnetic spectrum with narrow band profiles was presented. The construction of 2-substituted phenanthridines amenable to cross-coupling conditions enables the preparation of a wide library of compounds, with varying substituents, as in the **L2^{R,R}** and **L3^{R,R}** series of proligands and platinum complexes **2^{R,R}** (**L2^{R,R}-PtCl**) and **3^{R,R}** (**L3^{R,R}-PtCl**). Benzannulation, counter-intuitively but markedly, blue-shifts emission in this series, attributable to an increase in molecular rigidity and the ability of the phenanthridine (3,4-benzoquinoline) units to buffer against substantial molecular reorganization.[38] The influence of substituents in the phenanthridine 2-position can further be used to modulate the photophysical properties dependent on the relative strength of the substituent as an electron donating/accepting group. This influence therefore is subtle for substituents with lower Hammett parameters (Me, *t*Bu) compared to those with larger ones (CF_3).[50] Overall, the impact of CF_3 substituents is most pronounced, leading to significant hypsochromic shifts to emission, to such an extent that the **2^{Me,CF3}** (**L9-PtCl**) and **2^{H,CF3}** (**L7-PtCl**) complexes emit at higher energy than the *bis*(quinolines) **1^{Me,Me}** (**L5-PtCl**) and **1^{H,H}** (**L1-PtCl**). This influence is traced to unequal impacts of the substituent on the HOMO and LUMO+1, which represent the donor and acceptor orbitals involved in formation of the lowest energy excited state. The phosphorescence radiative rate constants of the complexes are mostly in

excess of 10^3 s^{-1} but are reduced in the highest-energy emitters, possibly due to mismatching of metal and ligand orbitals and hence inefficient spin-orbit coupling. The non-radiative rate constants, meanwhile, show a trend that is in line with that expected from the energy gap law, with the lowest-energy emitters subject to the most rapid non-radiative decay. Efforts to improve deep red phosphorescence further by addressing the relative rates of radiative vs. non-radiative decay through ligand design[60] are now underway.

4.6. Experimental Section:

4.6.1. General Information:

Air-sensitive manipulations were performed in either a N_2-filled glove box or using standard Schlenk techniques in argon atmosphere. $Pd_2(dba)_3$, $Pd(PPh_3)_4$, $Pd(OAc)_2$, (±)-2,2′-*bis*(diphenylphosphino)-1,1′-binaphthalene (*rac*-BINAP), 1,1'-bis(diphenylphosphino)ferrocene (dppf), sodium *tert*-amoxide (NaO*t*Am) and sodium *tert*-butoxide (NaO*t*Bu) were purchased (Sigma Aldrich) and used without further purification. 8-Bromo-6-methylquinoline,[40] 8-amino-6-methylquinoline,[61] 4-amino-2-trifluoromethylphenanthridine,[62] $Pt(COD)Cl_2$,[63] 4-amino-2-methylphenanthridine, **L1^{Me,Me}** (**L5**), **L2^{Me,Me}** (**L6**), **1^{Me,Me}** (**L5-PtCl**) and **2^{Me,Me}** (**L5-PtCl**),[38] **L3$^{Me,Me-}$** (**L3**) and **3^{Me,Me}**(**L3-PtCl**),[43] **L2^{H,tBu}** (**L4**) and **L2^{H,CF3}** (**L7**) [44] were synthesized according to literature procedures. Organic solvents were dried and distilled using appropriate drying agents, and distilled water was degassed prior to use. 1- and 2D NMR spectra were recorded on Bruker Avance 300 MHz or Bruker Avance–III 500 MHz spectrometers. All ^1H and $^{13}C\{^1H\}$ NMR spectra were referenced to residual solvent peaks. ^{19}F NMR spectra were collected using deuterated solvents and locked to the deuterium signal. NMR spectra of all new compounds are provided in Figures S15-S39. Elemental analyses were performed by Microanalytical Service Ltd., Delta, BC

(Canada), and at the University of Manitoba using a Perkin Elmer 2400 Series II CHNS/O Elemental Analyzer.

4.6.2. Synthesis of Ligand Precursors:

4-bromo-2-*tert*-butylphenanthridine: A 500 mL Teflon-stoppered flask was charged with $Pd(PPh_3)_4$ (1.66 g, 1.43 mmol) and 50 mL of 1,2-dimethoxyethane (DME). After stirring briefly to mix, 2-bromo-6-iodo-4-*tert*-butyl-toluidine (15.02 g, 47.80 mmol), 2-formylphenylboronic acid (7.89 g, 52.58 mmol) and an additional 70 mL of DME were added, followed by Na_2CO_3 (15.20 g, 143.4 mmol) dissolved in 100 mL of degassed water. The flask was then sealed, and the mixture stirred vigorously for 6 h in an oil bath (130 °C). The flask was then allowed to cool, $HCl_{(aq)}$ (2 M, 130 mL) added, and the mixture refluxed for additional 2 h. The flask was then cooled, neutralized with NaOH, and pumped to dryness. The residue was taken up in CH_2Cl_2 (100 mL) and washed with brine (3 × 100 mL). The organic layer was separated, dried over Na_2SO_4 and volatiles removed to leave a yellow-brown solid. Column chromatography on basic alumina gave a pale-yellow solid (R_f = 0.41; 1:5 EtOAc/hexane). Isolated yield = 11.74 g (86 %). ^{1}H NMR ($CDCl_3$, 500 MHz, 22 °C): δ 9.33 (s, 1H; $C_{Ar}H$), 8.62 (d, 1H, J_{HH} = 8.4 Hz; $C_{Ar}H$), 8.52 (s, 1H; $C_{Ar}H$), 8.14 (d, 1H, J_{HH} = 1.9 Hz; $C_{Ar}H$), 8.06 (d, 1H, J_{HH} = 7.9 Hz; $C_{Ar}H$), 7.87 (t, 1H, J_{HH} = 7.6 Hz; $C_{Ar}H$), 7.71 (t, 1H, J_{HH} = 7.4 Hz; $C_{Ar}H$), 1.49 ppm (s, 9H; *t*Bu). $^{13}C\{^1H\}$ NMR ($CDCl_3$, 125 MHz, 22 °C): δ 153.8 (C_{Ar}), 150.9 (C_{Ar}), 140.0 (C_{Ar}), 132.6 (C_{Ar}), 131.3 (C_{Ar}), 131.1 (C_{Ar}), 129.1 (C_{Ar}), 128.0 (C_{Ar}), 126.6 (C_{Ar}), 125.5 (C_{Ar}), 125.3 (C_{Ar}), 122.0 (C_{Ar}), 117.8 (C_{Ar}), 35.4 (CCH$_3$)$_3$, 31.5 ppm (CH$_3$).

4.6.3. General Procedure for Proligand Synthesis ($L1^{R,R}$-$L3^{R,R}$):

A thick-walled, 100 mL Teflon-stoppered flask was charged with a Pd catalyst, ligand (*rac*-BINAP or dppf) and toluene (30 mL) in the amounts noted below. After stirring briefly, the appropriate quinoline or phenanthridine reagents were added, along with an additional 30 mL of toluene, followed by the alkoxide base. The sealed flask was then stirred vigorously for 72 h in an oil bath set to 150 °C. After cooling and removing the volatiles, the residue was taken up in CH_2Cl_2 (120 mL) with the resulting suspension filtered over Celite and dried.

$L2^{Me,tBu}$(L8): The general procedure was followed using: $Pd_2(dba)_3$ (0.110 mg, 0.120 mmol), *rac*-BINAP (0.162 g, 0.440 mmol); 8-bromo-6-methylquinoline (0.490 g, 2.20 mmol), 4-amino-2-*tert*-butylphenanthridine (0.500 g, 2.00 mmol); and NaO*t*Am (0.29 g, 3.0 mmol). Column chromatography gave an orange-red solid (neutral alumina; 1:5 EtOAc/hexane; $R_f = 0.43$). Isolated yield = 1.01 g (92%). ^{1}H NMR ($CDCl_3$, 300 MHz, 22 °C): δ 10.43 (br s, 1H; N*H*), 9.29 (s, 1H; $C_{Ar}H$), 8.91 (dd, 1H, J_{HH} = 4.2, 1.7 Hz; $C_{Ar}H$), 8.68 (d, 1H, J_{HH} = 8.2; $C_{Ar}H$), 8.19-8.02 (m, 4H; $C_{Ar}H$), 7.91-7.82 (m, 1H; $C_{Ar}H$), 7.77 (d, 1H, J_{HH} = 1.6 Hz; $C_{Ar}H$), 7.70 (dd, 1H, J_{HH} = 8.0, 7.0 Hz; $C_{Ar}H$), 7.46-7.39 (m, 1H; $C_{Ar}H$), 7.11 (br s, 1H; $C_{Ar}H$), 2.57 (s, 3H; CH_3), 1.57 (s, 9H, C(CH_3)$_3$ ppm. ^{13}C{^{1}H} NMR ($CDCl_3$, 75 MHz, 22 °C): δ 150.6 (C_{Ar}), 150.4 (C_{Ar}), 147.3 (C_{Ar}), 139.2 (C_{Ar}), 139.0 (C_{Ar}), 137.0 (C_{Ar}), 135.5 (C_{Ar}), 133.1 (C_{Ar}), 130.7 (C_{Ar}), 129.2 (C_{Ar}), 128.9 (C_{Ar}), 127.3 (C_{Ar}), 127.0 (C_{Ar}), 124.3 (C_{Ar}), 122.4 (C_{Ar}), 121.8 (C_{Ar}), 116.7 (C_{Ar}), 111.6 (C_{Ar}), 110.9 (C_{Ar}), 108.8 (C_{Ar}), 35.7(*C*(CH$_3$)$_3$), 31.7 (^{Phen}*C*H$_3$), 22.7 (^{Quin}*C*H$_3$) ppm.

$L2^{Me,CF3}$(L9): The general procedure was followed using: $Pd(OAc)_2$ (0.025 g, 0.11 mmol), dppf (0.086 g, 0.15 mmol); 4-bromo-2-trifluoromethylphenanthridine (0.710 g, 2.18 mmol), 8-amino-6-methylquinoline (0.350 g, 2.23 mmol); and NaO*t*Am (0.35 g, 3.27 mmol). Column chromatography gave a yellow-green solid (neutral alumina; 1:5 EtOAc/hexane; $R_f = 0.3$). Isolated

yield = 0.77 g (88%). ^{1}H NMR ($CDCl_3$, 300 MHz, 22 °C): δ 10.74 (br s, 1H; N*H*), 9.43 (s, 1H; C_{Ar}*H*), 8.90 (dd, 1H, J_{HH} = 4.1, 1.7 Hz; C_{Ar}*H*), 8.65 (d, 1H, J_{HH} = 8.5 Hz; C_{Ar}*H*), 8.32 (s, 1H; C_{Ar}*H*), 8.18-8.04 (overlapped m, 3H; C_{Ar}*H*), 7.93 (dd, J_{HH} = 8.4, 7.1 Hz; 1H, C_{Ar}*H*), 7.83-7.73 (overlapped m, 2H; C_{Ar}*H*), 7.45 (dd, 1H, J_{HH} = 8.3, 4.2 Hz; C_{Ar}*H*), 7.23-7.14 (br s, 1H; C_{Ar}*H*), 2.60 ppm (s, 3H; $_{Quin}C$*H*$_3$). ^{13}C{^{1}H} NMR ($CDCl_3$, 75 MHz, 22 °C): δ 153.0 (*C*$_{Ar}$), 147.6 (*C*$_{Ar}$), 140.7 (*C*$_{Ar}$), 139.1 (*C*$_{Ar}$), 137.9 (*C*$_{Ar}$), 137.2 (*C*$_{Ar}$), 136.4 (*C*$_{Ar}$), 135.6 (*C*$_{Ar}$), 132.9 (*C*$_{Ar}$), 131.6 (*C*$_{Ar}$), 131.0 (q, *C*$_{Ar}$), 129.6 (*C*$_{Ar}$), 129.20 (*C*$_{Ar}$), 129.16 (*C*$_{Ar}$), 128.3 (*C*$_{Ar}$), 127.1 (*C*$_{Ar}$), 124.5 (*C*$_{Ar}$), 122.6 (*C*$_{Ar}$),122.0 (*C*$_{Ar}$), 118.2 (*C*$_{Ar}$), 113.1 (*C*$_{Ar}$), 109.6 (q, *C*$_{Ar}$), 106.0 (q, *C*$_{Ar}$), 22.6 ppm ($_{Quin}C$H$_3$). ^{19}F{^{1}H} NMR ($CDCl_3$, 282 MHz, 22 °C): δ -62.26 ppm.

L3^{tBu,tBu}(L10): The general procedure was followed using: $Pd(OAc)_2$ (0.032 g, 0.14 mmol); dppf (0.13 g, 0.23 mmol); 4-bromo-2-*tert*-butylphenanthridine (0.90 g, 2.9 mmol); 4-amino-2-*tert*-butylphenanthridine (0.70 g, 3.2 mmol); and NaO*t*Am (0.45 g, 4.3 mmol). Column chromatography gave a yellow-green solid (neutral alumina; 1:5 EtOAc/hexane; R_f = 0.35). Isolated yield = 1.08 g (78%). ^{1}H NMR ($CDCl_3$, 300 MHz, 22 °C): δ 10.41 (br s, 1H; N*H*), 9.30 (s, 2H; C_{Ar}*H*), 8.69 (d, 2H, J_{HH} = 8.4 Hz; C_{Ar}*H*), 8.18 (s, 2H; C_{Ar}*H*), 8.14-8.05 (overlapped m, 4H; C_{Ar}*H*), 7.91-7.82 (m, 2H; C_{Ar}*H*), 7.76 (m, 2H; C_{Ar}*H*), 1.55 ppm (s, 18H; C(C*H*$_3$)$_3$). ^{13}C{^{1}H} NMR ($CDCl_3$, 75 MHz, 22 °C): δ 150.54 (*C*$_{Ar}$), 150.50 (*C*$_{Ar}$), 139.7 (*C*$_{Ar}$), 134.0 (*C*$_{Ar}$), 133.2 (*C*$_{Ar}$), 130.7 (*C*$_{Ar}$), 128.9 (*C*$_{Ar}$), 127.3 (*C*$_{Ar}$), 127.1 (*C*$_{Ar}$), 124.4 (*C*$_{Ar}$), 122.4 (*C*$_{Ar}$), 110.0 (*C*$_{Ar}$), 108.5 (*C*$_{Ar}$), 35.7 (*C*(CH$_3$)$_3$), 31.8 ppm (C(*C*H$_3$)$_3$).

L3^{CF3,CF3}(L11): The general procedure was followed using: $Pd(OAc)_2$ (21.0 mg, 0.09 mmol); dppf (72.0 mg, 0.13 mmol); 4-bromo-trifluoromethylphenanthridine (0.65 g, 1.99 mmol); 4-amino-2-trifluoromethylphenanthridine (0.53 g, 2.33 mmol); and NaO*t*Am (0.29 g, 2.78 mmol). Column chromatography gave a yellow-green solid (neutral alumina; 1:5 EtOAc/hexane; R_f = 0.2). Isolated

yield = 0.76 g (74%). ^{1}H NMR ($CDCl_3$, 500 MHz, 22 °C): δ 10.91 (br s, 1H, N-*H*), 9.42 (s, 2H, $C_{Ar}H$), 8.63 (d, 2H, J_{HH} = 8.1 Hz, $C_{Ar}H$), 8.34 (s, 2H, $C_{Ar}H$), 8.20-8.08 (overlapped m, 4H, $C_{Ar}H$), 7.94 (app t, J_{HH} = 7.4 Hz, 2H, $C_{Ar}H$), 7.83 ppm (app t, 2H, J_{HH} = 7.3 Hz, $C_{Ar}H$). ^{13}C{^{1}H} NMR ($CDCl_3$, 125 MHz, 22 °C): δ 153.3 (C_{Ar}), 140.0 (C_{Ar}), 136.5 (C_{Ar}), 132.8 (C_{Ar}), 131.8 (C_{Ar}), 129.23 (C_{Ar}), 129.19 (C_{Ar}), 128.5 (C_{Ar}), 128.4 (C_{Ar}), 127.1 (C_{Ar}), 124.7 (C_{Ar}), 122.6 (C_{Ar}), 110.7 (C_{Ar}), 106.7 ppm (C_{Ar}). ^{19}F{^{1}H} NMR ($CDCl_3$, 470 MHz): δ -62.45 ppm.

L3^{CF3,tBu}(L12): The general procedure was followed using: $Pd(OAc)_2$ (0.025 g, 0.11 mmol), dppf (0.083 g, 0.15 mmol); 4-bromo-2-trifluoromethylphenanthridine (0.70 g, 2.2 mmol); 4-amino-2-*tert*-butylphenanthridine (0.55 g, 2.2 mmol); and NaO*t*Am (0.34 g, 3.2 mmol). Column chromatography gave a yellow-green solid (neutral alumina; 1:5 EtOAc/hexane; R_f = 0.32). Isolated yield = 0.89 g (83%) ^{1}H NMR ($CDCl_3$, 300 MHz, 22 °C): δ 10.57 (br s, 1H; N*H*), 9.43 (s, 1H; $C_{Ar}H$), 9.30 (s, 1H; $C_{Ar}H$), 8.67 (dd, 2H, J_{HH} = 11.7, 8.3 Hz; $C_{Ar}H$), 8.29 (s, 1H; $C_{Ar}H$), 8.22-8.04 (m, 5H; $C_{Ar}H$), 7.97-7.85 (m, 2H; $C_{Ar}H$), 7.82-7.70 (m, 2H; $C_{Ar}H$), 1.56 ppm (s, 9H; $C(CH_3)_3$). ^{13}C{^{1}H} NMR ($CDCl_3$, 75 MHz, 22 °C): δ 152.9 (C_{Ar}), 151.0 (C_{Ar}), 150.6 (C_{Ar}), 141.2 (C_{Ar}), 138.5 (C_{Ar}), 136.3 (C_{Ar}), 134.3 (C_{Ar}), 133.1 (C_{Ar}), 132.9 (C_{Ar}), 131.6 (C_{Ar}), 130.9 (C_{Ar}), 129.6 (C_{Ar}), 129.2 (C_{Ar}), 129.2 (C_{Ar}), 129.0 (C_{Ar}), 128.3 (C_{Ar}), 127.5 (C_{Ar}), 127.1 (C_{Ar}), 127.1 (C_{Ar}), 124.7 (C_{Ar}), 124.5 (C_{Ar}), 122.6 (C_{Ar}), 122.4 (C_{Ar}), 111.7 (C_{Ar}), 110.0 (C_{Ar}), 109.2 (q, C_{Ar}), 105.8 (q, C_{Ar}), 35.7 ($C(CH_3)_3$), 31.6 ppm ($C(CH_3)_3$). ^{19}F{^{1}H} NMR ($CDCl_3$, 282 MHz, 22 °C): δ -62.52 ppm.

4.6.4. General Procedure for Pt Complex Synthesis:

In a thick-walled Teflon-stoppered flask, equimolar amounts of $Pt(COD)Cl_2$ and NaO*t*Bu were added to a solution of the appropriate ligand (**L1^{R,R}**, **L2^{R,R}** or **L3^{R,R}**) in CH_2Cl_2 (10 mL), and the mixture stirred vigorously in an oil bath set to 70 °C for 18 h. The resulting red suspension was

allowed to cool, and the volatiles were removed *in vacuo*. The residue was then washed with acetonitrile (3 × 10 mL) and diethyl ether (3 × 10 mL).

$2^{H,tBu}$(L4-PtCl): The general procedure was followed using: **$L2^{H,tBu}$** (0.20 g, 0.53 mmol), $Pt(COD)Cl_2$ (0.20 g, 0.54 mmol), and NaO*t*Bu (0.050 g, 0.54 mmol). Isolated yield = 0.279 g (87%). ^{1}H NMR ($CDCl_3$, 300 MHz, 22 °C): δ 9.60 (s, 1H, $^3J_{PtH}$ = 39 Hz, $C_{Ar}H$), 9.25 (d, 1H, J_{HH} = 5.0 Hz; $C_{Ar}H$), 8.58 (d, 1H, J_{HH} = 8.4 Hz; $C_{Ar}H$), 8.27 (d, 1H, J_{HH} = 8.2 Hz; $C_{Ar}H$), 8.09 (d, 1H, J_{HH} = 8.0 Hz; $C_{Ar}H$), 8.03-7.85 (overlapped m, 2H, $C_{Ar}H$), 7.80 (s, 1H, $C_{Ar}H$), 7.76-7.68 (overlapped m, 2H, $C_{Ar}H$), 7.53 (app t, 1H, J_{HH} = 8.0 Hz; $C_{Ar}H$), 7.41 (dd, 1H, J_{HH} = 8.3, 5.0 Hz; $C_{Ar}H$), 7.06 (d, 1H, J_{HH} = 7.9 Hz; $C_{Ar}H$), 1.57 ppm (s, 9H, CH_3). Anal. Calcd for $C_{26}H_{22}ClN_3Pt$: C, 51.45; H, 3.65. Found: C, 51.15; H, 3.74.

$2^{H,CF3}$(L7-PtCl): The general procedure was followed using: **$L2^{H,CF3}$** (0.10 g, 0.26 mmol), $Pt(COD)Cl_2$ (0.096 g, 0.26 mmol), and NaO*t*Bu (0.026 mg, 0.27 mmol). Isolated yield = 0.279 g (87%). ^{1}H NMR ($CDCl_3$, 500 MHz, 22 °C): δ 9.79 (s, 1H, $C_{Ar}H$), 9.30 (d, 1H, J_{HH} = 5.4 Hz; $C_{Ar}H$), 8.59 (d, 1H, J_{HH} = 8.6 Hz; $C_{Ar}H$), 8.36 (d, 1H, J_{HH} = 8.4 Hz; $C_{Ar}H$), 8.19 (d, 1H, J_{HH} = 7.7 Hz; $C_{Ar}H$), 8.07-7.99 (overlapped m, 2H, $C_{Ar}H$), 7.94 (s, 1H, $C_{Ar}H$), 7.86-7.78 (m, 2H, $C_{Ar}H$), 7.60 (app t, 1H, J_{HH} = 7.9 Hz; $C_{Ar}H$), 7.51-7.44 (overlapped m, 1H, $C_{Ar}H$), 7.21 ppm (d, 1H, J_{HH} = 8.0 Hz; $C_{Ar}H$). $^{19}F\{^1H\}$ NMR ($CDCl_3$, 470 MHz, 22 °C): δ -62.19 ppm. Anal. Calcd for $C_{23}H_{13}ClF_3N_3Pt$: C, 44.64; H, 2.12. Found: C, 44.57; H, 2.29.

$2^{Me,tBu}$(L8-PtCl): The general procedure was followed using: **$L2^{Me,tBu}$** (0.20 g, 0.58 mmol), $Pt(COD)Cl_2$ (0.22 g, 0.59 mmol), and NaO*t*Bu (0.06 g, 0.60 mmol). Isolated yield = 0.266 g (79%). ^{1}H NMR ($CDCl_3$, 300 MHz, 22 °C): δ 9.60 (s, 1H, $^3J_{PtH}$ = 39 Hz, $C_{Ar}H$), 9.17 (d, 1H, J_{HH} = 6.9 Hz; $C_{Ar}H$), 8.59 (d, 1H, J_{HH} = 8.2 Hz; $C_{Ar}H$), 8.17 (d, 1H, J_{HH} = 8.4 Hz; $C_{Ar}H$), 8.10 (d, 1H, J_{HH} = 7.4 Hz; $C_{Ar}H$), 7.99-7.89 (overlapped multiplet, 2H, $C_{Ar}H$), 7.80 (s, 1H, $C_{Ar}H$), 7.72 (app t, 1H,

J_{HH} = 6.6 Hz; $C_{Ar}H$), 7.56 (s, 1H, $C_{Ar}H$), 7.37 (dd, 1H, J_{HH} = 8.4, 5.2 Hz; $C_{Ar}H$), 6.88 (s, 1H, $C_{Ar}H$), 2.60 (s, 3H, CH_3), 1.57 ppm (s, 9H, $C(CH_3)_3$). Anal. Calcd for $C_{27}H_{24}ClN_3Pt$: C, 52.22; H, 3.90. Found: C, 51.91; H, 4.16.

$2^{Me,CF3}$(L9-PtCl): The general procedure was followed using: **$L2^{Me,CF3}$** (0.21 g, 0.53 mmol), Pt(COD)Cl_2 (0.20 g, 0.53 mmol), and NaO*t*Bu (0.05 g, 0.54 mmol). Isolated yield = 0.222 g (66%). ^{1}H NMR ($CDCl_3$, 300 MHz, 22 °C): δ 9.76 (s, 1H, $^3J_{PtH}$ = 39 Hz, $C_{Ar}H$), 9.18 (d, 1H, J_{HH} = 5.1 Hz; $C_{Ar}H$), 8.56 (d, 1H, J_{HH} = 8.4 Hz; $C_{Ar}H$), 8.23 (d, 1H, J_{HH} = 8.8 Hz; $C_{Ar}H$), 8.17 (d, 1H, J_{HH} = 8.0 Hz; $C_{Ar}H$), 8.08-7.95 (overlapped m, 2H, $C_{Ar}H$), 7.91 (s, 1H, $C_{Ar}H$), 7.81 (app t, 1H, J_{HH} = 7.6 Hz; $C_{Ar}H$), 7.58 (s, 1H, $C_{Ar}H$), 7.41 (dd, 1H, J_{HH} = 8.3, 5.1 Hz; $C_{Ar}H$), 7.00 (s, 1H, $C_{Ar}H$), 2.63 ppm (s, 3H, CH_3). $^{19}F\{^1H\}$ NMR ($CDCl_3$, 470 MHz, 22 °C): δ -62.49 ppm. Anal. Calcd for $C_{24}H_{15}ClF_3N_3Pt$: C, 45.54; H, 2.39. Found: C, 45.73; H, 2.41.

$3^{tBu,tBu}$(L10-PtCl): The general procedure was followed using: **$L3^{tBu,tBu}$** (0.20 g, 0.41 mmol), Pt(COD)Cl_2 (0.16 g, 0.42 mmol), and NaO*t*Bu (0.04 g, 0.43 mmol). Isolated yield = 0.228 g (78%). ^{1}H NMR ($CDCl_3$, 300 MHz, 22 °C): δ 9.63 (s, 2H, $C_{Ar}H$), 8.57 (d, 2H, J_{HH} = 8.6 Hz; $C_{Ar}H$), 8.11 (d, 2H, J_{HH} = 8.0 Hz; $C_{Ar}H$), 8.06 (s, 2H, $C_{Ar}H$), 7.99-7.88 (m, 2H, $C_{Ar}H$), 7.78 (s, 2H, $C_{Ar}H$), 7.76-7.66 (m, 2H, $C_{Ar}H$), 1.53 ppm (s, 18H, $C(CH_3)_3$). Anal. Calcd for $C_{34}H_{32}ClN_3Pt$•(4x$CHCl_3$)(0.5xEt_2O): C, 44.08; H, 4.16. Found: C, 44.05, 4.26. This compound is very insoluble and had been isolated after a series of recrystallizations from chloroform and diethyl ether.

$3^{CF3,tBu}$(L12-PtCl): The general procedure was followed using: **$L3^{CF3,tBu}$** (0.20 g, 0.40 mmol), Pt(COD)Cl_2 (0.15 g, 0.41 mmol), and NaO*t*Bu (0.04 g, 0.42 mmol). Isolated yield = 0.182 g (62%). ^{1}H NMR ($CDCl_3$, 300 MHz, 22 °C): δ 9.75 (s, 1H, $C_{Ar}H$), 9.58 (s, 1H, $C_{Ar}H$), 8.56 (d, 1H, J_{HH} = 8.4 Hz; $C_{Ar}H$), 8.47 (d, 1H, J_{HH} = 8.4 Hz; $C_{Ar}H$), 8.16 (d, 1H, J_{HH} = 7.4 Hz; $C_{Ar}H$), 8.10 (d, 1H,

J_{HH} = 8.0 Hz; $C_{Ar}H$), 8.03-7.65 (m, 8H, $C_{Ar}H$), 1.59 ppm (s, 9H, $C(CH_3)_3$). $^{19}F\{^1H\}$ NMR ($CDCl_3$, 470 MHz, 22 °C): δ -62.50 ppm. Anal. Calcd for $C_{31}H_{23}ClF_3N_3Pt$: C, 51.35; H, 3.20. Found: C, 51.43; H, 3.21.

$3^{CF3,CF3}$(L11-PtCl): The general procedure was followed using: **$L3^{CF3,CF3}$** (0.28 g, 0.54 mmol), Pt(COD)Cl_2 (0.21g, 0.55 mmol), and NaO*t*Bu (0.05 g, 0.56 mmol). Isolated yield of **$3^{CF3,CF3}$** = 0.265 g (66%). $^{19}F\{^1H\}$ NMR (DMSO, 470 MHz, 22 °C): δ -60.77 ppm. The compound appears to be too insoluble to characterize. Anal. Calcd for $C_{28}H_{14}ClF_3N_3Pt(2xCHCl_3)$: C, 36.93; H, 1.65. Found: C, 37.22; 1.88.

4.6.5. X-Ray Crystallography:

X-ray crystal structure data were collected from multi-faceted crystals of suitable size and quality selected from a representative sample of crystals of the same habit using an optical microscope. In each case, crystals were mounted on MiTiGen loops and data collection carried out in a cold stream of nitrogen (150 K; Bruker D8 QUEST ECO; Mo K_α radiation). All diffractometer manipulations were carried out using Bruker APEX3 software.[64] Structure solution and refinement was carried out using XS, XT and XL software, embedded within the Bruker SHELXTL suite.[65] For each structure, the absence of additional symmetry was confirmed using ADDSYM incorporated in the PLATON program.[66] CCDC Nos. 1992330-1992332 contain the supplementary crystallographic data for this paper. The data can be obtained free of charge from The Cambridge Crystallographic Data Centre via www.ccdc.cam.ac.uk/structures.

Crystal structure data for **$L3^{CF3,CF3}$(L11)** (CCDC 1992332): X-ray quality crystals were grown from reaction mixture in toluene. Crystal structure parameters: $C_{28}H_{15}N_3F_6$ 507.43 g/mol, monoclinic, space group $P2_1/n$; a = 13.0578(6) Å, b = 9.2399(4) Å, c = 19.4731(10) Å, α = 90°, β

= 109.319(2)°, γ = 90°, V = 2217.19(18) Å^3; Z = 4, ρ_{calcd} = 1.520 g cm^{-3}; crystal dimensions 0.22 x 0.14 x 0.06 mm^3; θ_{max} = 27.525°; 39662 reflections, 3800 independent (R_{int} = 0.0517), direct methods; absorption coeff (μ = 0.126 mm^{-1}), absorption correction semi-empirical from equivalents (SADABS); refinement (against F_o^2) with SHELXTL V6.1, 334 parameters, 0 restraints, R_1 = 0.0579 ($I > 2\sigma$) and wR_2 = 0.1518 (all data), Goof = 1.067, residual electron density 0.74/−0.55 e Å^{-3}.

Crystal structure data for **2^{Me,tBu}** (**L8-PtCl**) (CCDC 1992330): X-ray quality crystals were grown following diffusion of diethyl ether vapor into a $CHCl_3$ solution of the compound at room temperature. Crystal structure parameters: $C_{27}H_{24}Cl_1N_3Pt_1$ 621.03 g/mol, triclinic, space group *P*-1; *a* = 8.8827(6)Å, *b* = 11.5775(8) Å, *c* = 12.2098(9) Å, α = 63.521(2)°, β = 77.693(2)°, γ = 88.681(2)°, V = 1094.37(13) Å^3; Z = 2, ρ_{calcd} = 1.885 g cm^{-3}; crystal dimensions 0.330 x 0.140 x 0.040 mm^3; θ_{max} = 27.916°; 27804 reflections, 5201 independent (R_{int} = 0.0288), direct methods; absorption coeff (μ = 6.554 mm^{-1}), absorption correction semi-empirical from equivalents (SADABS); refinement (against F_o^2) with SHELXTL V6.1, 293 parameters, 0 restraints, R_1 = 0.0151 ($I > 2\sigma$) and wR_2 = 0.0357 (all data), Goof = 1.057, residual electron density 0.909/−0.692 e Å^{-3}.

Crystal structure data for **3^{tBu,tBu}** (**L10-PtCl**) (CCDC 1992331): X-ray quality crystals were grown following diffusion of diethyl ether vapor into a CH_2Cl_2 solution of the compound at room temperature. Crystal structure parameters: $C_{34}H_{26}Cl_1N_3Pt_1(CH_2Cl_2)$ 792.04 g/mol, orthorhombic, space group *Pnma*; *a* = 24.9983(13) Å, *b* = 6.7957(3) Å, *c* = 18.1591(9) Å, α = 90°, β = 90°, γ = 90°, V = 3084.9(3) Å^3; Z = 4, ρ_{calcd} = 1.705 g cm^{-3}; crystal dimensions 0.100 x 0.022 x 0.021 mm^3; θ_{max} = 24.789°; 76058 reflections, 2888 independent (R_{int} = 0.2484), direct methods; absorption coeff (μ = 4.838 mm^{-1}), absorption correction semi-empirical from equivalents (SADABS);

refinement (against F_o^2) with SHELXTL V6.1, 249 parameters, 0 restraints, $R_1 = 0.0461$ ($I > 2\sigma$) and $wR_2 = 0.0834$ (all data), Goof = 1.145, residual electron density 1.273/−0.901 e $Å^{-3}$.

4.6.6 Optical Spectroscopy Measurements:

The absorption spectra of the complexes were measured in solution in CH_2Cl_2 in 1 cm quartz cuvettes using a Biotek Instruments XS UV-Visible spectrometer at room temperature. The emission spectra of the proligands at 295 and 77 K, and of their Pt(II) complexes at 77 K, were recorded using a Jobin Yvon Fluoromax-2 spectrometer equipped with a red-sensitive Hamamatsu R928 photomuliplier tube. The emission spectra of the Pt(II) complexes at 295 K, which extend up to around 1000 nm, were recorded using a thermoelectrically cooled Synapse CCD detector, which offers better sensitivity in the red / NIR region compared to the R928 PMT. The samples for measurements at 295 K were contained within 1 cm pathlength quartz cuvettes modified for attachment to a vacuum line, and were degassed prior to measurement by a minimum of three freeze-pump-thaw cycles; final vapor pressure at 77 K was < 10^{-2} mbar. Emission spectra at 77 K were recorded in 4 mm diameter tubes held within a liquid nitrogen cooled quartz dewar. Luminescence lifetimes were measured by time-correlated single-photon counting (TCSPC) following excitation using a pulsed laser diode at 405 nm; the emitted light was detected at right angles to the excitation beam, using an R928 PMT thermoelectrically cooled to –20 °C.

4.6.7: DFT Calculations:

DFT optimizations of $\mathbf{2}^{\mathbf{Me,CF3}}$ (**L9-PtCl**) and $\mathbf{3}^{\mathbf{CF3,CF3}}$ (**L11-PtCl**) were carried out using Gaussian16, rev. C01[67] with M06/LANL2DZ[68,69] with an IEFPCM[70] solvent model with CH_2Cl_2. TD-DFT and single point calculations were performed at the same level of theory. Molecular

orbital analyses were carried out using the Hirshfeld partition method[71] available in Multiwfn software[72] and visualized using Avogadro.[73] TD-DFT results were analyzed using GaussSum.[74] Spin density maps were generated using Gabedit.[75] To calculate ground-state, excited-state and reorganization energies, the following protocol (Figure 4.16) was followed: (1) The S_0 geometry was optimized by restricted DFT (charge = 0, multiplicity = 1) using the crystal structure coordinates as starting input. The T_1 geometry was optimized with unrestricted DFT (charge = 0, multiplicity = 3) using the optimized S_0 geometry as starting input. Frequency calculations were then subsequently carried out to confirm that these structures are at a minimum. (2) To determine the relative molecular fragment contributions to the frontier MOs, population analyses were carried out on the optimized structures of S_0 states (Tables 4.8 and 4.9). The electronic energies, $E(S_0)$ and $E(T_1)$, obtained from the single point calculations of S_0 and T_1 in their respective minimum were used to estimate the adiabatic energy (E^{adia}), where, $E^{adia} = E(T_1) - E(S_0)$. (3) TD-DFT was then carried out on the first 50 $S_n \leftarrow S_0$ singlet-singlet transitions with the restricted formalism with charge = 0 and multiplicity = 1 to yield $E^{vert\text{-}abs}$. (4) $E^{vert\text{-}phos}$ ($T_1 \rightarrow T_1@S_0$) was estimated as the ΔSCF between single point energies of the T_1 (charge = 0, multiplicity = 3) and $T_1@S_0$ (charge = 0, multiplicity = 1) both at the optimized T_1 geometry.

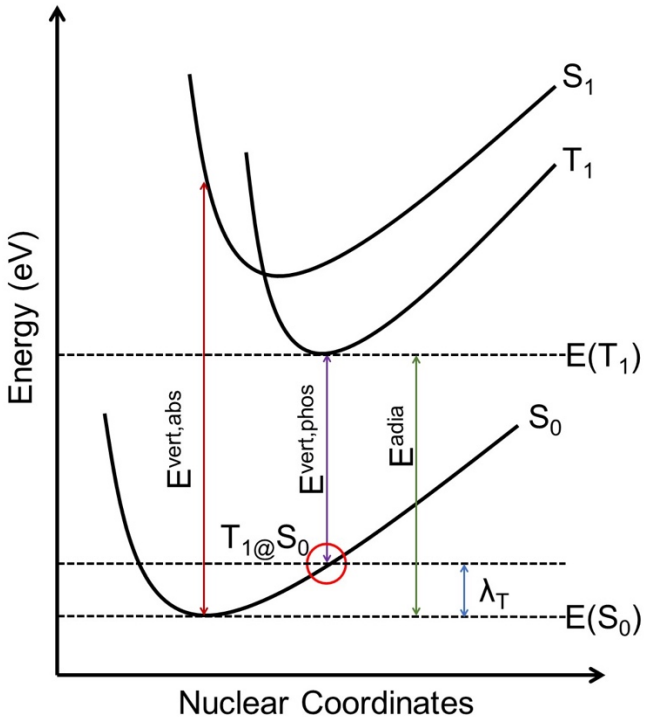

Figure 4.17. Diagram illustrating parameters calculated using the protocol described in computational experimental section.

4.7. References:

1. Li, J.; Yan, J.; Wen, D.; Khan, W. U.; Shi, J.; Wu, M.; Su, Q.; Tanner, P. A. *J. Mater. Chem. C* **2016**, *4*, 8611–8623.

2. Qian, G.; Wang, Z. Y. *Chem. - Asian J.* **2010**, *5*, 1006–1029.

3. Guo, Z.; Park, S.; Yoon, J.; Shin, I. *Chem. Soc. Rev.* **2014**, *43*, 16–29.

4. Xiang, H.; Cheng, J.; Ma, X.; Zhou, X.; Chruma, J. J. *Chem. Soc. Rev.* **2013**, *42*, 6128–6185.

5. Zhang, Y.; Luo, Q.; Zheng, W.; Wang, Z.; Lin, Y.; Zhang, E.; Lu, S.; Xiang, J.; Zhao, Y.; Wang, F. *Inorg. Chem. Front.* **2018**, *5*, 413–424.

6. Baggaley, E.; Weinstein, J. A.; Williams, J. A. G. *Struc. Bond.* **2015**, *165*, 205–256.

7. Chi, Y.; Chou, P.-T. *Chem. Soc. Rev.* **2010**, *39*, 638–655.

8. Gray, T. G.; Rudzinski, C. M.; Nocera, D. G.; Holm, R. H. *Inorg. Chem.* **1999**, *38*, 5932–5933.

9. Molard, Y.; Dorson, F.; Brylev, K. A.; Shestopalov, M. A.; Le Gal, Y.; Cordier, S.; Mironov, Y. V.; Kitamura, N.; Perrin, C. *Chem. - Eur. J.* **2010**, *16*, 5613–5619.

10. Tung, Y.-L.; Lee, S.-W.; Chi, Y.; Chen, L.-S.; Shu, C.-F.; Wu, F.-I.; Carty, A. J.; Chou, P.-T.; Peng, S.-M.; Lee, G.-H. *Adv. Mater.* **2005**, *17*, 1059–1064.

11. Carlson, B.; Phelan, G. D.; Kaminsky, W.; Dalton, L.; Jiang, X.; Liu, S.; Jen, A. K. Y. *J. Am. Chem. Soc.* **2002**, *124*, 14162–14172.

12. Lai, P.-N.; Teets, T. S. *Chem. - Eur. J.* **2019**, *25*, 6026–6037.

13. Stonelake, T. M.; Phillips, K. A.; Otaif, H. Y.; Edwardson, Z. C.; Horton, P. N.; Coles, S. J.; Beames, J. M.; Pope, S. J. A. *Inorg. Chem.* **2020**, *59*, 2266–2277.

14. Wu, W.; Guo, H.; Wu, W.; Ji, S.; Zhao, J. *Inorg. Chem.* **2011**, *50*, 11446–11460.

15. Zhang, Y.; Meng, F.; You, C.; Yang, S.; Xiong, W.; Wang, Y.; Su, S.; Zhu, W. *Dyes Pigm.* **2017**, *138*, 100–106.

16. Zhang, Y.; Yin, Z.; Meng, F.; Yu, J.; You, C.; Yang, S.; Tan, H.; Zhu, W.; Su, S. *Org. Electron.* **2017**, *50*, 317–324.

17. Xiong, W.; Meng, F.; You, C.; Wang, P.; Yu, J.; Wu, X.; Pei, Y.; Zhu, W.; Wang, Y.; Su, S. *J. Mater. Chem. C* **2019**, *7*, 630–638.

18. Gernert, M.; Balles-Wolf, L.; Kerner, F.; Mueller, U.; Schmiedel, A.; Holzapfel, M.; Marian, C. M.; Pflaum, J.; Lambert, C.; Steffen, A. *J. Am. Chem. Soc.* **2020**, *142*, 8897–8909.

19. Li, L.-K.; Tang, M.-C.; Cheung, W.-L.; Lai, S.-L.; Ng, M.; Chan, C. K.-M.; Chan, M.-Y.; Yam, V. W.-W. *Chem. Mater.* **2019**, *31*, 6706–6714.

20. Li, K.; Tong, G. S. M.; Wan, Q.; Cheng, G.; Tong, W.-Y.; Ang, W.-H.; Kwong, W.-L.; Che, C.-M. *Chem. Sci.* **2016**, *7*, 1653–1673.

21. *Highly Efficient OLEDs with Phosphorescent Materials*; Yersin, H., Series Ed.; Wiley-VCH: Weinheim, Germany, **2007**.

22. Cebrian, C.; Mauro, M. *Beilstein J. Org. Chem.* **2018**, *14*, 1459–1481.

23. Kalinowski, J.; Fattori, V.; Cocchi, M.; Williams, J. A. G. *Coord. Chem. Rev.* **2011**, *255*, 2401–2425.

24. Baggaley, E.; Weinstein, J. A.; Williams, J. A. G. *Coord. Chem. Rev.* **2012**, *256*, 1762–1785.

25. Mauro, M.; Aliprandi, A.; Septiadi, D.; Kehr, N. S.; De Cola, L. *Chem. Soc. Rev.* **2014**, *43* (12), 4144–4166.

26. Chen, Y.; Guan, R.; Zhang, C.; Huang, J.; Ji, L.; Chao, H. *Coord. Chem. Rev.* **2016**, *310*, 16–40.

27. Zhao, Q.; Li, F.; Huang, C. *Chem. Soc. Rev.* **2010**, *39*, 3007–3030.

28. Lai, S.-W.; Chan, M. C.-W.; Cheung, T.-C.; Peng, S.-M.; Che, C.-M. *Inorg. Chem.* **1999**, *38*, 4046–4055.

29. Cocchi, M.; Kalinowski, J.; Virgili, D.; Williams, J. A. G. *Appl. Phys. Lett.* **2008**, *92*, 113302/1-113302/3.

30. Baldo, M. A.; O'Brien, D. F.; You, Y.; Shoustikov, A.; Sibley, S.; Thompson, M. E.; Forrest, S. R. *Nature* **1998**, *395*, 151–154.

31. Montes, V. A.; Pérez-Bolívar, C.; Agarwal, N.; Shinar, J.; Anzenbacher, P. *J. Am. Chem. Soc.* **2006**, *128*, 12436–12438.

32. Paul-Roth, C. O.; Drouet, S.; Merhi, A.; Williams, J. A. G.; Gildea, L. F.; Pearson, C.; Petty, M. C. *Tetrahedron* **2013**, *69*, 9625–9632.

33. Zhao, D.; Huang, C.-C.; Liu, X.-Y.; Song, B.; Ding, L.; Fung, M.-K.; Fan, J. *Org. Electron.* **2018**, *62*, 542–547.

34. McKenzie, L. K.; Sazanovich, I. V.; Baggaley, E.; Bonneau, M.; Guerchais, V.; Williams, J. A. G.; Weinstein, J. A.; Bryant, H. E. *Chem. - Eur. J.* **2017**, *23*, 234–238.

35. Colombo, A.; Fontani, M.; Dragonetti, C.; Roberto, D.; Williams, J. A. G.; Scotto di Perrotolo, R.; Casagrande, F.; Barozzi, S.; Polo, S. *Chem. - Eur. J.* **2019**, *25*, 7948–7952.

36. Liu, Y.; Meng, X.; Bu, W. *Coord. Chem. Rev.* **2019**, *379*, 82–98.

37. Wu, W.; Sun, J.; Ji, S.; Wu, W.; Zhao, J.; Guo, H. *Dalton Trans.* **2011**, *40*, 11550–11561.

38. Mandapati, P.; Braun, J. D.; Killeen, C.; Davis, R. L.; Williams, J. A. G.; Herbert, D. E. *Inorg. Chem.* **2019**, *58*, 14808–14817.

39. Mondal, R.; Giesbrecht, P. K.; Herbert, D. E. *Polyhedron* **2016**, *108*, 156–162.

40. Lee, C.-I.; Zhou, J.; Ozerov, O. V. *J. Am. Chem. Soc.* **2013**, *135*, 3560–3566.

41. We adopt the IUPAC numbering system for quinolines and phenanthridines, as illustrated in Scheme 1 for $\mathbf{L1^{R,R}}$ and $\mathbf{L3^{R,R}}$.

42. Peters, J. C.; Harkins, S. B.; Brown, S. D.; Day, M. W. *Inorg. Chem.* **2001**, *40*, 5083–5091.

43. Mandapati, P.; Giesbrecht, P. K.; Davis, R. L.; Herbert, D. E. *Inorg. Chem.* **2017**, *56,* 3674–3685.

44. Braun, J. D.; Lozada, I. B.; Kolodziej, C.; Burda, C.; Newman, K. M. E.; van Lierop, J.; Davis, R. L.; Herbert, D. E. *Nat. Chem.* **2019**, *11*, 1144–1150.

45. Hanson, K.; Roskop, L.; Djurovich, P. I.; Zahariev, F.; Gordon, M. S.; Thompson, M. E. *J. Am. Chem. Soc.* **2010**, *132*, 16247–16255.

46. Liu, B.; Lystrom, L.; Brown, S. L.; Hobbie, E. K.; Kilina, S.; Sun, W. *Inorg. Chem.* **2019**, *58*, 5483–5493.

47. Mondal, R.; Lozada, I. B.; Davis, R. L.; Williams, J. A. G.; Herbert, D. E. *Inorg. Chem.* **2018**, *57*, 4966–4978.

48. Zander, M. *Z. Naturforsch. A* **1978**, *33*, 998–1000.

49. Frey, J.; Curchod, B. F. E.; Scopelliti, R.; Tavernelli, I.; Rothlisberger, U.; Nazeeruddin, M. K.; Baranoff, E. *Dalton Trans.* **2014**, *43*, 5667–5679.

50. Hansch, C.; Leo, A.; Taft, R. W. *Chem. Rev.* **1991**, *91*, 165–195.

51. Dedeian, K.; Djurovich, P. I.; Garces, F. O.; Carlson, G.; Watts, R. J. *Inorg. Chem.* **1991**, *30*, 1685–1687.

52. Brulatti, P.; Gildea, R. J.; Howard, J. A. K.; Fattori, V.; Cocchi, M.; Williams, J. A. G. *Inorg. Chem.* **2012**, *51*, 3813–3826.

53. Englman, R.; Jortner, J. *Mol. Phys.* **1970**, *18*, 145–164.

54. Caspar, J. V.; Kober, E. M.; Sullivan, B. P.; Meyer, T. J. *J. Am. Chem. Soc.* **1982**, *104*, 630–632.

55. Caspar, J. V.; Meyer, T. J. *J. Phys. Chem.* **1983**, *87*, 952–957.

56. Whittle, C. E.; Weinstein, J. A.; George, M. W.; Schanze, K. S. *Inorg. Chem.* **2001**, *40*, 4053–4062.

57. Ibrahim-Ouali, M.; Dumur, F. *Molecules* **2019**, *24*, 1412.

58. Borisov, S. M.; Nuss, G.; Haas, W.; Saf, R.; Schmuck, M.; Klimant, I. *J. Photochem. Photobiol. A* **2009**, *201*, 128–135.

59. Tuong Ly, K.; Chen-Cheng, R.-W.; Lin, H.-W.; Shiau, Y.-J.; Liu, S.-H.; Chou, P.-T.; Tsao, C.-S.; Huang, Y.-C.; Chi, Y. *Nat. Photon.* **2017**, *11*, 63–68.

60. Kabir, E.; Wu, Y.; Sittel, S.; Nguyen, B.-L.; Teets, T. S. *Inorg. Chem. Front.* **2020**, *7*, 1362–1373.

61. Medina Padilla, M.; Castro Morera, A.; Sanchez-Quesada, J.; Garcia Palomero, E.; Alonso Cascon, M.; Herrero Santos, S.; Vela Ruiz, M.; Usan Egea, P.; Rodriguez Villanueva, A. L. Triple Substituted Phenanthroline Derivatives for the Treatment of Neurodegenerative or Haematological Diseases or Conditions, or Cancer. US20110306631A1, **2011**.

62. Mandapati, P.; Braun, J. D.; Sidhu, B. K.; Wilson, G.; Herbert, D. E. *Organometallics* **2020**, *39*, 1989–1997.

63. Clark, H. C.; Manzer, L. E. *J. Organomet. Chem.* **1973**, *59*, 411–428.

64. Bruker-AXS. *APEX3 V2016.1-0*; Madison, Wisconsin, USA, **2016**.

65. Sheldrick, G. M. *Acta Cryst.* **2008**, *A64*, 112–122.

66. Spek, A. L. *Acta Cryst.* **2009**, *D65*, 148–155.

67. Frisch, M. J.; Trucks, G. W.; Schlegel, H. B.; Scuseria, G. E.; Robb, M. A.; Cheeseman, J. R.; Scalmani, G.; Barone, V.; Petersson, G. A.; Nakatsuji, H.; Li, X.; Caricato, M.; Marenich, A. V.; Bloino, J.; Janesko, B. G.; Gomperts, R.; Mennucci, B.; Hratchian, H. P.; Ortiz, J. V.; Izmaylov, A. F.; Sonnenberg, J. L.; Williams; Ding, F.; Lipparini, F.; Egidi, F.; Goings, J.; Peng, B.; Petrone, A.; Henderson, T.; Ranasinghe, D.; Zakrzewski, V. G.; Gao, J.; Rega, N.; Zheng, G.; Liang, W.; Hada, M.; Ehara, M.; Toyota, K.; Fukuda, R.; Hasegawa, J.; Ishida, M.; Nakajima, T.; Honda, Y.; Kitao, O.; Nakai, H.; Vreven, T.; Throssell, K.; Montgomery Jr., J. A.; Peralta, J. E.; Ogliaro, F.; Bearpark, M. J.; Heyd, J. J.; Brothers, E. N.; Kudin, K. N.; Staroverov, V. N.; Keith, T. A.; Kobayashi, R.; Normand, J.; Raghavachari, K.; Rendell, A. P.; Burant, J. C.; Iyengar, S. S.; Tomasi, J.; Cossi, M.; Millam, J. M.; Klene, M.; Adamo, C.; Cammi, R.; Ochterski, J. W.; Martin, R. L.; Morokuma, K.; Farkas, O.; Foresman, J. B.; Fox, D. J. *Gaussian 16 Rev. C.01*; Wallingford, CT, **2016**.

68. Zhao, Y.; Truhlar, D. G. *Theor. Chem. Acc.* **2008**, *120*, 215–241.

69. Dunning, T. H.; Hay, P. J. In *Modern Theoretical Chemistry*; Schaefer III, H. F., Ed.; Plenum, New York, **1977**; Vol. 3, pp 1–28.

70. Tomasi, J.; Mennucci, B.; Cammi, R. *Chem. Rev.* **2005**, *105*, 2999–3094.

71. Hirshfeld, F. L. *Theor. Chim. Acta* **1977**, *44*, 129–138.

72. Lu, T.; Chen, F. *J. Comput. Chem.* **2012**, *33*, 580–592.

73. Hanwell, M. D.; Curtis, D. E.; Lonie, D. C.; Vandermeersch, T.; Zurek, E.; Hutchison, G. R. *J. Cheminf.* **2012**, *4*, 17.

74. O'Boyle, N. M.; Tenderholt, A. L.; Langner, K. M. *J. Comput. Chem.* **2008**, *29*, 839–845.

75. Allouche, A.-R. *J. Comput. Chem.* **2011**, *32*, 174–182.

Chapter 5: Synthesis, Characterization and Reactivity Studies of Phenanthridine-Based *N^N-^NMe₂* Pincer Complexes of Nickel and Palladium

5.1. Abstract:

Proligands based on *bis*(2-(dimethylamino)phenyl)amido ligands (**A**) were prepared containing one quinolinyl unit (**L13**) and one benzo-fused *N*-heterocyclic phenanthridinyl (**L14**, **L15**, **L16**) unit, installed with electron donating groups (Me, *t*Bu) and electron withdrawing group (CF_3) to address the solubility issue and explore the impact of systematic π-extension conjugation in the context of tridentate pincer-like amido complexes of Group 10 metals. Divalent nickel and palladium complexes were synthesized using proligands (**L13**-**L16**) in good yields. Ni(II) complexes supported by tridentate *N^N-^N* diarylamido pincer-type ligands have been demonstrated to act as active catalysts in the carbon-carbon bond forming alkylation of azoles using unactivated alkylhalides. Here, we show that benzannulated phenanthridine-containing ligands can form homogenous Ni(II) catalysts active with both benzoxazole and benzothiazole substrates. These precatalysts have been fully characterized in solution and the solid-state, including by cyclic voltammetry.

5.2. Introduction:

The homogeneous catalytic conversion of C–H bonds to C–C bonds mediated by coordination complexes of first-row transition metals is of prime interest in the drive to increase sustainability in chemical synthesis.[1-2] First, direct functionalization of C–H bonds obviates the need for leaving groups that can limit atom economy.[3] Second, the use of first-row metal catalysts reduces reliance on less abundant precious metals for transformations that add value to organic substrates such as aromatic heterocycles.[4] With respect to these widely used synthetic building blocks, transition metal catalyzed C–H alkylation reactions using alkylhalides with ß-hydrogens

can be challenging, as ß-hydride elimination can lead to unproductive side reactions.[5] As a result, a relatively limited number of examples of such cross-couplings have been reported, with palladium,[6-7] nickel[8-11] and copper[12-14] catalysts featuring most prominently.

Well-defined complexes of nickel supported by diarylamido *N^N-^N* pincer-type ligands, in particular, have been shown to direct the alkylation of oxazoles and thiazoles using unactivated alkyl halides (Figure 5.1).[8, 10] While Ni(II) complexes of *bis*(2-(dimethylamino)phenyl)amido ligands (**A**) show excellent catalytic activity, as reported by Hu and coworkers, addition of a copper co-catalyst is necessary to achieve high yields.[8] Moreover, decomposition of **A** was observed over time under the high temperature reaction conditions, depositing nanoparticulate metal into the reaction mixture.[8] Punji and coworkers elaborated this scaffold into a more robust quinolinyl-based pincer type analog. The corresponding Ni chloride complexes supported by a (2-(dimethylamino)phenyl)(8-quinolinyl)amido donor set (**B**) exhibit greater temperature stability and do not require a co-catalyst in the catalytic alkylation of benzothiazoles.[10]

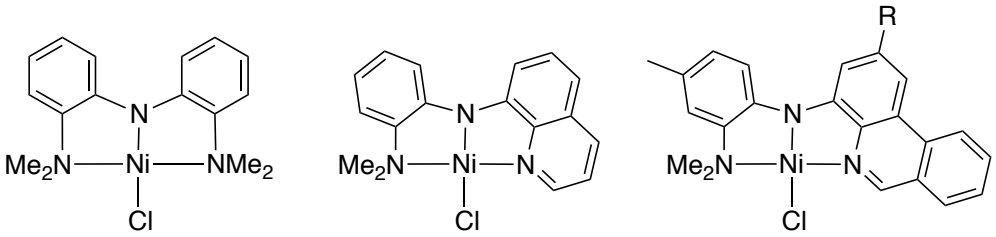

A (ref. 8) **B** (ref. 10) **C** (*this work*)

Figure 5.1. *N^N-^N* pincer-type ligand supported Ni complexes for the C-H alkylation of azoles (**A**, see ref.[8]; **B**, see ref.[10]; **C**, this work).

In previous chapters, the synthesis of tridentate, *N^N-^N* diarylamido pincer-type ligands bearing benzannulated phenanthridine (3,4-benzoquinoline) heterocyclic donor arms were

described.[15] Compared with (8-amino)quinolines, a relatively broad range of 2-substituted (4-amino)phenanthridines can be easily accessed via tandem cross-coupling/condensation reactions using various 4-substituted anilines;[16] accessing 6-substituted (8-amino)quinolines can require less tractable Skraup reaction conditions.[17] Moreover, in these benzannulated pincer-type frameworks, the phenanthridinyl donor arm can act as an efficient Lewis base with strong π-acid character thanks to the presence of low-lying vacant orbitals[18] and are sterically less encumbered than isomeric acridines.[19] As mechanistic studies of azole alkylation reactions mediated by **B** suggest involvement of a Ni(II)/Ni(III) redox couple,[20] we decided to apply our phenanthridine-containing ligand architecture in the preparation of π-extended Ni(II) analogs (**C**) to probe the impact of π-extension on the stability of higher oxidation states[21] and potentially with it, catalytic activity. We report here that complexes of the type **C** are competent in the catalytic C-H bond alkylation of azoles with unactivated alkylhalides containing *β*-hydrogens, with activity and good substrate scope comparable to **A** and **B** without the requirement of a Cu co-catalyst.

5.3. Results and Discussion:

5.3.1. N^N$^-$^NMe2 Ligand Synthesis:

To access the proligands used in this chapter, aminophenanthridines/quinolines suitable for elaboration into the target scaffolds were prepared similarly to those described in earlier chapters. First, (4-nitro)phenanthridines were assembled via tandem cross-coupling/condensation reactions[15,16] to produce **1-NO$_2$**, **2-NO$_2$** and **3-NO$_2$**, and these were then reduced to the corresponding (4-amino)phenanthridines **1-NH$_2$**, **2-NH$_2$** and **3-NH$_2$** as shown in Scheme 5.1. Having the phenathridine precursors synthesized in good yields, they were coupled with (N,N-dimethyl)(2-bromo-4-methyl)aniline using Pd-catalyzed C–N bond formation to give proligands **L14-L16** as yellow solids, which could be purified using column chromatography. For each of the

amine proligands, the hydrogen in the 6-position of the phenanthridine framework resonates significantly downfield of the remaining aromatic resonances in the 1H NMR spectrum, indicating formation of the tricyclic phenanthridine.[22] The appearance of a broad singlet assigned to an N-H signal similarly confirmed formation of the diarylamine unit. For comparison, the (6-methyl)quinolinyl analog **L13** was also prepared via Pd-catalyzed C–N coupling as shown in Scheme 4.2.

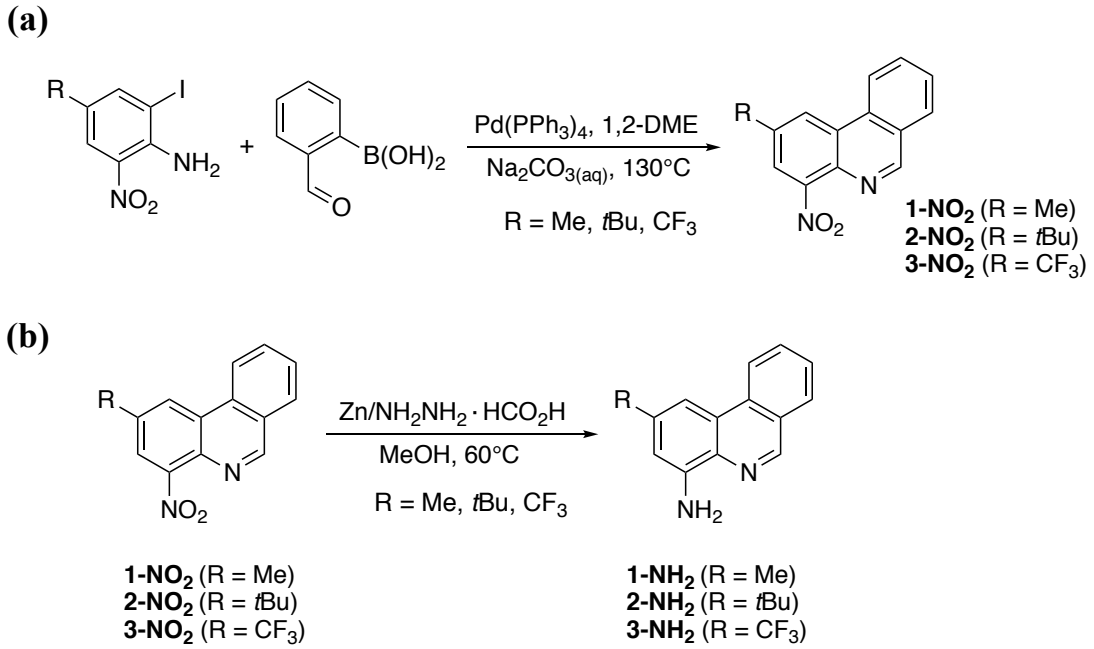

Scheme 5.1. Synthesis of (a) and (b) phenanthridine precursors, installed with EDGs (Me, *t*Bu) and EWGs (CF_3).

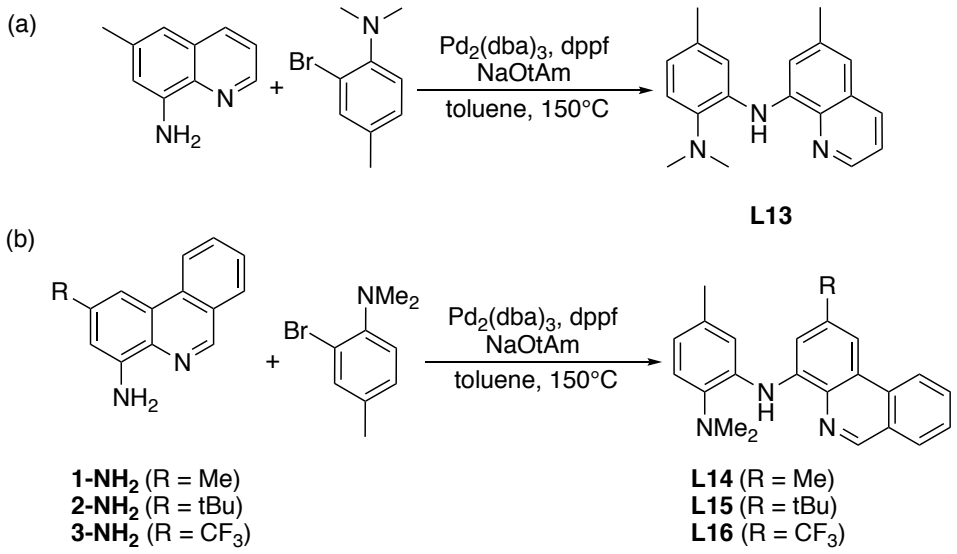

Scheme 5.2. Synthesis of (a) methyl-substituted quinolinyl analogs of **B**[10], described in this chapter (b) proligands **L14-L16** installed with EDGs (Me, *t*Bu) and EWGs (CF_3).

The solid-state structures of the phenanthridine-containing proligands L14-L16 were determined using single crystal X-ray diffraction as shown in Figure 5.2. Consistent with the general importance of 'imine-bridged biphenyl' resonance contributors to the ground-state structure of phenanthridines,[23] the C–N distance between the phenanthridinyl nitrogen and the adjacent carbon in the 6-position is quite short in all three proligands [L14: C(1)-N(1) 1.3034(11); L15: C(1)-N(1) 1.302(3); L16: C(1)-N(1) 1.291(4)] pointing to localization of imine C=N character at this site.18 The localization of imine C=N π character at this site has been shown to temper the impacts of π-extension, for example, in emissive complexes of phenanthridinyl-based ligands.[22, 24]

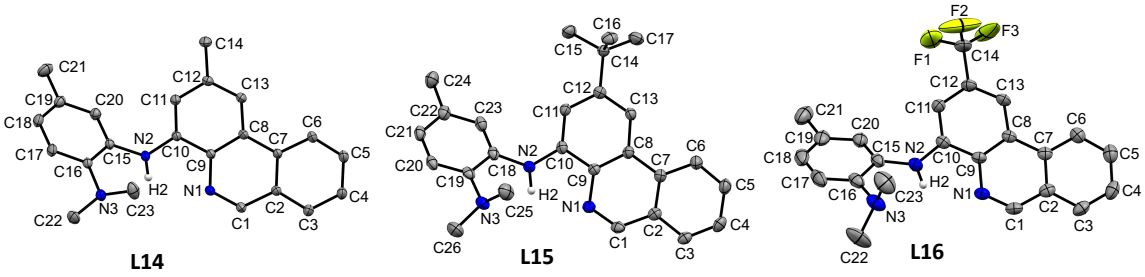

Figure 5.2. Solid-state structures of **L14-L16** shown with thermal ellipsoids at 50 % probability levels. Hydrogens other than H2 are omitted for clarity. Selected bond distances (Å) and angles (°) for **L14**: C(1)-N(1) 1.3034(11), C(10)-N(2) 1.3957(10), C(15)-N(2) 1.4124(11), C(16)-N(3) 1.4168(12); C(10)-N(2)-C(15) 122.64(7), C(9)-C(10)-N(2) 117.25(7), C(16)-C(15)-N(2) 121.17(8). **L15**: C(1)-N(1) 1.302(3), C(10)-N(2) 1.386(3), C(18)-N(2) 1.397(3), C(23)-N(3) 1.425(3); C(10)-N(2)-C(18) 128.8(2), C(9)-C(10)-N(2) 115.4(2), C(19)-C(18)-N(2) 122.4(2). **L16**: C(1)-N(1) 1.291(4), C(10)-N(2) 1.374(3), C(15)-N(2) 1.395(4), C(16)-N(3) 1.430(4); C(10)-N(2)-C(15) 129.9(2), C(9)-C(10)-N(2) 116.2(2), C(16)-C(15)-N(2) 116.6(3).

With the proligands in hand, divalent Ni(II) coordination complexes [(**L14-L16)-NiCl**] and the quinoline congener **L13-NiCl** were synthesized through metalation with $NiCl_2$•$6H_2O$ in the presence of base (sodium *tert*-butoxide) in dichloromethane at elevated temperatures, and isolated in good yields (83-93%) as dark red solids as shown in Scheme. The disappearance of the signal assigned to the N-*H* resonance in the ^{1}H NMR spectrum and shifts to the remaining signals, including the diagnostic signals for the hydrogen nucleus in the 6-position of the phenanthridinyl/quinolinyl arms, confirmed installation of the ligand frameworks on the Ni(II) ion. The geometry and structures of both the (*N*^*N*-^*N*)NiCl complexes were determined using single-crystal X-ray diffraction as shown in Figure 5.3. In keeping with analogous complexes such as **B**,[10] the nickel ions in **L14-NiCl**, **L15-NiCl** and **L13-NiCl** sit within the meridional pocket formed by the *N*^*N*-^*N* diarylamido ligand. All complexes are essentially flat (angles between planes

formed by six carbon rings (e.g., C8-C13 and C15-C20 for **L14-NiCl**) flanking the amido nitrogens: **L14-NiCl** 9.43º, **L15-NiCl** 3.49º, **L13-NiCl** 10.42º), but with distorted square-planar geometry resulting from tied-back bond angles formed by the two neutral donor arms [**L14-NiCl**: N(1)-Ni(1)-N(3) 170.83(10); **L15-NiCl**: N(1)−Ni(1)−N(3) 171.60(6); **L13-NiCl**: N(1)−Ni(1)−N(3) 170.93(10)°]. The Ni–N_{amido} distances (**L14-NiCl**: 1.848(2); **L15-NiCl**: 1.8511(14); **L13-NiCl**: 1.859(2) Å] are within range of those reported for **A**[25] and **B**[10], and shorter than between nickel and the neutral donor arms [**L14-NiCl**: Ni(1)–N(1) 1.895(2), Ni(1)–N(3) 1.951(2); **L15-NiCl**: Ni(1)–N(1) 1.8937(14), Ni(1)–N(3) 1.9512(15); **L13-NiCl** Ni(1)–N(1) 1.896(2), Ni(1)–N(3) 1.949(2) Å]. For these latter Ni–N distances, the Ni–NMe_2 distance is consistently longer than the Ni–$N_{heterocycle}$ distance. All three complexes show similar Ni–Cl distances (~2.2 Å), implying very similar *trans* influence to the amido nitrogens of the ligand frameworks.

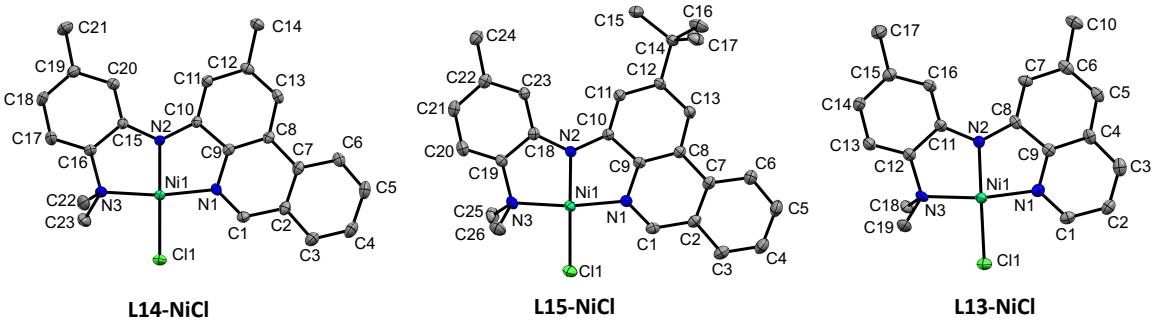

Figure 5.3. Solid-state structure of **L14-NiCl**, **L15-NiCl** and **L13-NiCl** shown with thermal ellipsoids at 50 % probability levels. Hydrogens are omitted for clarity. Selected bond distances (Å) and angles (°) for **L14-NiCl**: Ni(1)–Cl(1) 2.1919(8), Ni(1)–N(1) 1.895(2), Ni(1)–N(2) 1.848(2), Ni(1)–N(3) 1.951(2), C(1)–N(1) 1.304(4); N(1)–Ni(1)-N(3) 170.83(10), Cl(1)−Ni(1)−N(2) 179.08(8), N(1)−Ni(1)−N(2) 84.95(10), N(3)−Ni(1)−N(2) 86.35(10), N(1)−Ni(1)−Cl(1) 94.03(7), N(3)−Ni(1)−Cl(1) 93.62(7). **L15-NiCl**: Ni(1)–Cl(1) 2.1950(5),

Ni(1)–N(1) 1.8937(14), Ni(1)–N(2) 1.8511(14), Ni(1)–N(3) 1.9512(15), C(1)–N(1) 1.316(2); N(1)−Ni(1)−N(3) 171.60(6), Cl(1)−Ni(1)−N(2) 176.71(5), N(1)−Ni(1)−N(2) 85.12(6), N(3)−Ni(1)−N(2) 86.49(6), N(1)−Ni(1)−Cl(1) 94.50(5), N(3)−Ni(1)−Cl(1) 93.90(5). **L13-NiCl**: Ni(1)–Cl(1) 2.2094(9), Ni(1)–N(1) 1.896(2), Ni(1)–N(2) 1.859(2), Ni(1)–N(3) 1.949(2), C(1)-N(1) 1.326(4); N(1)−Ni(1)−N(3) 170.93(10), Cl(1)−Ni(1)−N(2) 176.84(8), N(1)−Ni(1)−N(2) 84.69(10), N(3)−Ni(1)−N(2) 86.25(10), N(1)−Ni(1)−Cl(1) 94.59(8), N(3)−Ni(1)−Cl(1) 94.42(7).

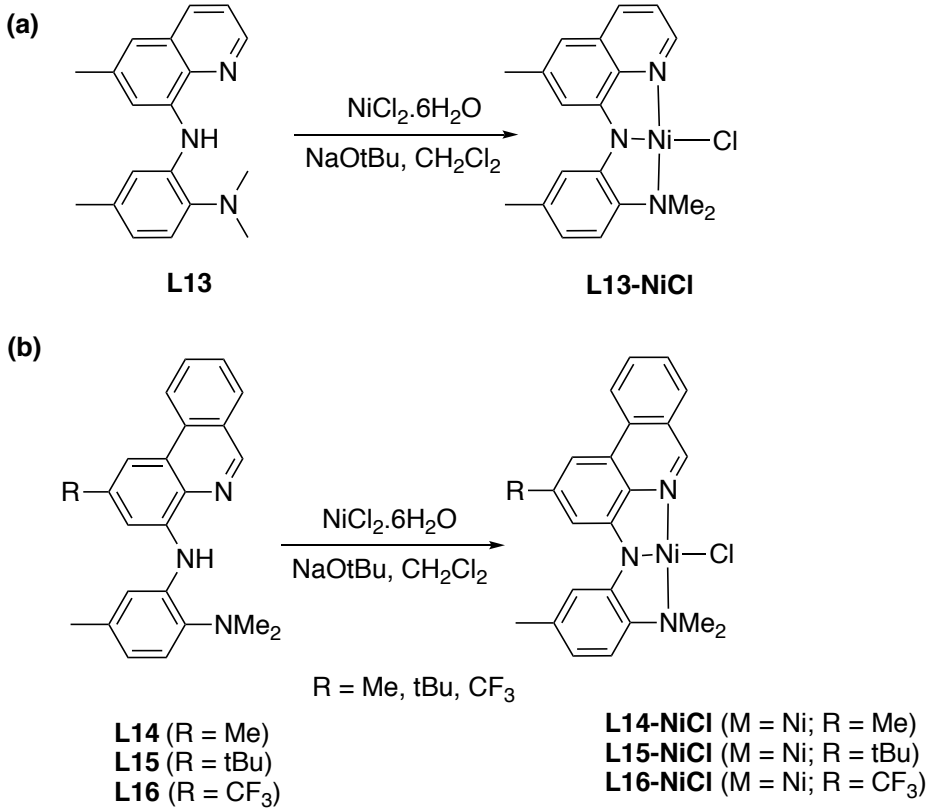

Scheme 5.3. Synthesis of (a) methyl-substituted quinolinyl based metal complexes, (b) phenanthridine-based *N^N(H)^N* nickel complexes.

5.3.2. Nickel(II) Complexes - Catalytic Activity:

I then screened the prepared coordination complexes for reactivity in the direct C-H activation of azoles using unactivated alkyl halides as shown in Table 5.1. Comparing all four precatalysts, the 6-methyl substituted quinolinyl congener **L13-NiCl**, a direct analog of **B**[10], was found to give the highest yield (61 %, run 5) in the direct alkylation of benzothiazole (**H1**) with iodooctane (**A1**) using 5 mol % catalyst loading, 1 equiv. of LiO*t*Bu, 1,4-dioxane solvent and 16h reaction time at 140 °C. As noted, complex **B** has been previously shown to be highly competent in the coupling of alkylhalides with sulfur-containing benzothiazoles.[10] Phenanthridinyl-based analogs (**L4-L16)-NiCl** were competitive but gave slightly lower yields (42-49 %; runs 1-4) under these conditions. In the coupling of alkyl halides with the oxygen-containing starting material benzoxazole (**H2**), **L16-NiCl** began to significantly outperform all other precatalysts. Yields of the coupled product were found to reach as high as 87 % using octylchloride (**A3**) in the presence of NaI.

Table 5.1. Catalyst comparison for [Ni]-Catalyzed Alkylation of Benzannulated Azoles[a]

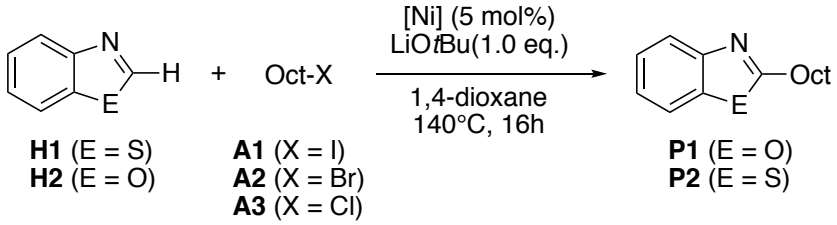

Entry	Catalyst	Heterocycle	Alkyl Halide	Yield[b]
1	**L14-NiCl**	H1	A1	49
2	**L15-NiCl**	H1	A1	49
3	**L16-NiCl**	H1	A1	42
4	**L13-NiCl**	H1	A1	61

5	**L14-NiCl**	H2	A1	46
6	**L15-NiCl**	H2	A1	39
7	**L16-NiCl**	H2	A1	73
8[c]	**L16-NiCl**	H2	A1	63
9[d]	**L16-NiCl**	H2	A1	55
10[e]	**L16-NiCl**	H2	A1	65
11[f]	**L16-NiCl**	H2	A1	0
12	**L13-NiCl**	H2	A1	39
13	**L16-NiCl**	H2	A2	35
14[g]	**L16-NiCl**	H2	A2	57
15[g]	**L16-NiCl**	H2	A3	87

[a] Conditions unless otherwise specified: heterocycle (1.006 mmol), alkyl halide (1.509 mmol), LiO*t*Bu (1.06 mmol), solvent (2.0 mL); oil bath set to 140 °C, 16 h

[b] GC yield; average of two runs

[c] In the presence of 100 equivalents of elemental Hg

[d] In the presence of 500 equivalents of elemental Hg

[e] Reaction mixture filtered after 1 h

[f] In the presence of added TEMPO

[g] With 0.2 equivalents of NaI.

Having observed promising reactivity with benzannulated coordination complex **L16-NiCl**, next a brief substrate scope for **L16-NiCl** as precatalyst was explored as shown in Table 5.2. The reaction conditions were found to be amenable to the coupling of benzoxazole with a variety of alkylhalides bearing carbazole (**P3**), ester (**P4**), aryl (**P5**), arylether (**P6**), thioether (**P7**), alkenyl (**P8**) and aliphatic (**P9**, **P10**) substituents. The catalysis mediated by **(L14-L16)-NiCl** and **L13-**

NiCl likely proceeds analogously to what has been observed by Punji and coworkers using their related quinolinyl-supported precatalyst **B**.[10,20] In support of this, participation of heterogeneous particulate nickel generated via catalyst decomposition appears to be minimal, as catalysis in the presence of added Hg as shown in Table 5.1, (runs 8-9) and following filtration (run 10) proceeded unimpeded. On the other hand, addition of the radical scavenger TEMPO (2,2,6,6-tetramethylpiperidine 1-oxyl) completely shut down reactivity (run 11). This is consistent with the homogenous radical rebound pathway proposed by Punji and coworkers, which involves on-cycle high-valent Ni(III) and Ni(IV) intermediates[20] as shown in Scheme 5.4. Accordingly, electrochemical data was collected for the precatalysts screened in this work in an attempt to correlate catalytic behavior with redox potentials.

Table 5.2. Scope for **L16-NiCl** Catalyzed Alkylations of Benzoxazole with Alkylbromides[a]

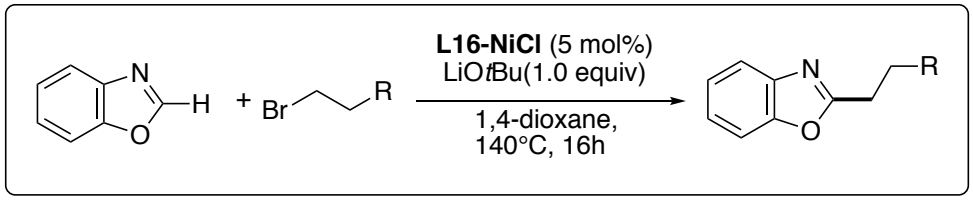

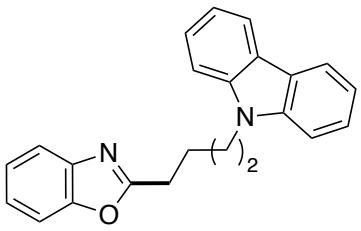

P3 (71)

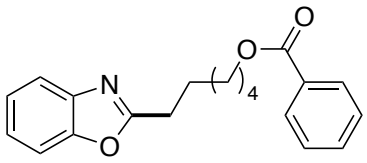

P4 (24)

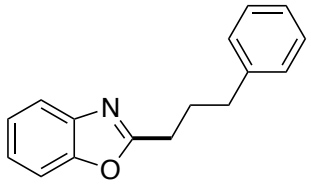

P5 (74)

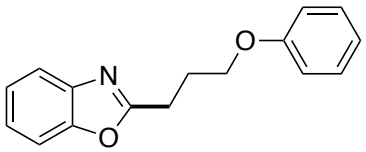

P6 (20)

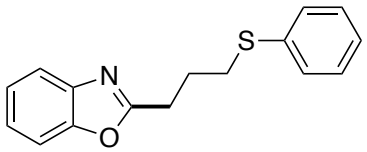

P7 (22)

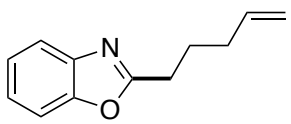

P8 (39)

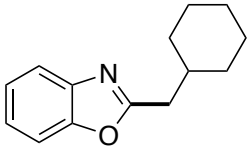

P9 (18)

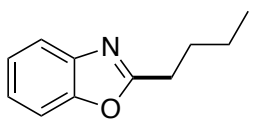

P10 (60)

[a] Conditions: heterocycle (1.006 mmol), 1-bromoalkane (1.509 mmol), LiO*t*Bu (1.060 mmol), solvent (2.0 mL); 140 °C, 16 h; GC yield in parentheses

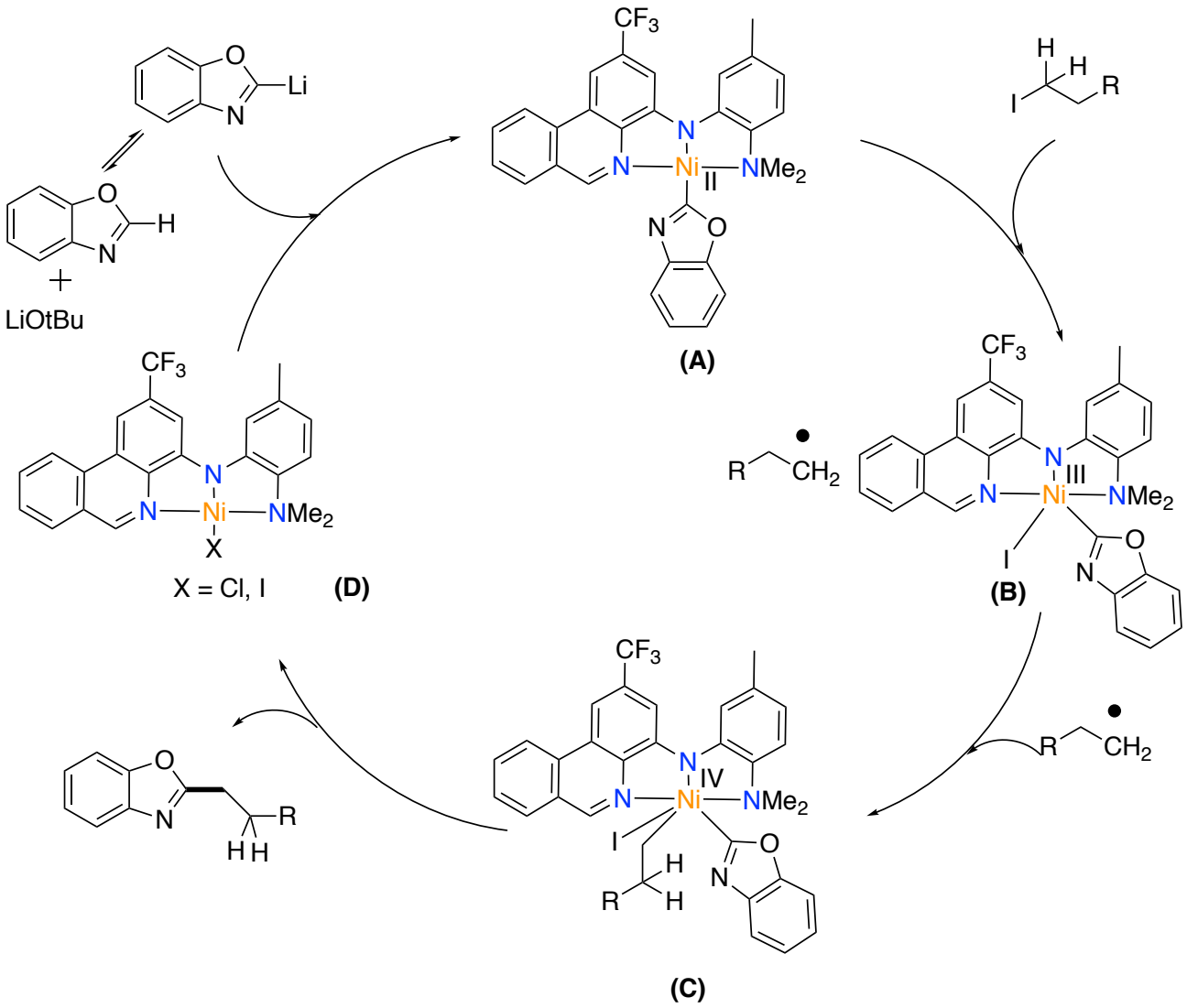

Scheme 5.4. Plausible alkylation pathway catalyzed by **L16-NiCl**.[20]

Cyclic voltammograms (CVs) and differential pulse voltammograms (DPVs) of precatalysts **(L14-L16)-NiCl** and **L13-NiCl** were taken in a dichloromethane solution with 0.1 M [*n*Bu$_4$N][PF$_6$] as the supporting electrolyte as shown in Figure 5.4. A quasi-reversible anodic wave between 0 and +0.3 V (vs $FcH^{0/+}$; FcH = ferrocene) is observed for each compound, consistent with an overall $1e^-$ oxidation. All compounds exhibit broad, irreversible reductions that overlap with the edge of the solvent window, making comparisons of these cathodic features within the series challenging. Accordingly, I focus here on the anodic electrochemical events. The oxidation potentials and peak parameters for the complexes are tabulated in Table 5.3. The electron releasing *t*Bu group of **L15-NiCl** shifts the oxidation potential to more accessible potentials compared with methyl analogs **L14-NiCl** and **L13-NiCl**. In comparison, an anodically shifted oxidation is observed for **L16-NiCl**, consistent with the presence of an electron withdrawing substituent on the ligand. The alkylation pathway catalyzed by **B** proposed by Punji and coworkers[20] invokes a one-electron Ni(II/III) pathway that occurs by oxidative addition of alkyl iodide via iodine atom transfer (IAT).[26] The lack of reactivity in the presence of the radical trap TEMPO as shown in Table 5.1, (run 11) supports a similar mechanism here. Oxidative addition by (inner-sphere) electron-transfer mechanisms are typically associated with metal centres with coordinative unsaturation to bind a substrate, and sufficiently cathodic electrochemical potentials to reduce the organic electrophile.[27] The observation of higher yields for the most electrophilic congener **L16-NiCl** with a pronounced anodic shift to its oxidation event, suggests that the elevated π-acidicity of the CF_3-substituted phenanthridine ligand framework[18] may be key in this context.

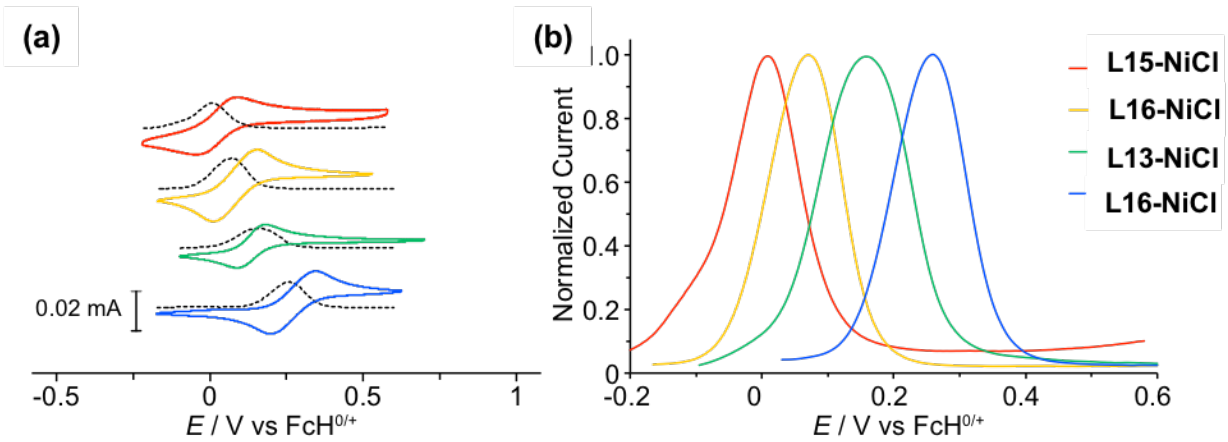

Figure 5.4. (a) Cyclic voltammograms (—) and corresponding differential pulse voltammograms (---) of **(L14-L16)-NiCl** and **L13-NiCl** in CH_2Cl_2 with 0.10 M [nBu$_4$N][PF_6] as the supporting electrolyte, glassy carbon working electrode. CV scan rates were 100 mV/s. Potentials are referenced vs. the $FcH^{0/+}$ redox couple (FcH = ferrocene); (b) Normalized DPVs of **(L14-L16)-NiCl** and **L13-NiCl**.

Table 5.3. Electrochemical parameters for Ni complexes

Compound	$E_{1/2}$/V	Δ_{ptp}[a]/mV	i_{red}/i_{ox}
L15-NiCl	0.01	133	1.17
L14-NiCl	0.07	143	1.04
L13-NiCl	0.16	91	0.87
L16-NiCl	0.26	147	0.92

[a]Δ_{ptp} = distance measured from 'peak-to-peak', showing the separation in mV between the peak maximum of the oxidation and corresponding reduction.

5.3.3. *N^N-^NMe$_2$* Complexes of Palladium:

Having shown the potential of the divalent Ni(II) metal complexes in terms of solubility, coordination chemistry, robustness at higher temperatures and reactivity towards catalysis involving C–H bond alkylation of azoles with alkyl halides to synthesize aromatic heterocycles, it is interesting to expand the scope and explore the reactivity of other group 10 metals.

With the proligands in hand, divalent Pd(II) coordination complexes **L14-PdCl**, **L16-PdCl** and the quinoline congener **L13-PdCl** were synthesized through metalation with $Pd(COD)Cl_2$ in the presence of base (sodium *tert*-butoxide) in dichloromethane at elevated temperatures, and isolated in good yields (79-88%) as dark red solids as shown in Scheme 5.5. The disappearance of the signal assigned to the N-*H* resonance in the ^1H NMR spectrum and shifts to the remaining signals, including the diagnostic signals for the hydrogen nucleus in the 6-position of the phenanthridinyl/quinolinyl arms, confirmed installation of the ligand frameworks on the Pd(II) ion, as observed in corresponding nickel complexes. The geometry and structures of the (*N*^*N*^*N*)PdCl complexes were determined using single-crystal X-ray diffraction as shown in Figure 5.5. All the palladium ions in **L14-PdCl**, **L16-PdCl** and **L13-PdCl** sit within the meridional pocket formed by the *N*^*N*^*N* diarylamido ligand. All complexes are essentially flat (angles between planes formed by six carbon rings (e.g., C8-C13 and C15-C20 for **L14-PdCl**) flanking the amido nitrogens: **L14-PdCl** 10.08º, **L16-PdCl** 11.85º, **L13-PdCl** 12.46º), but with distorted square-planar geometry resulting from tied-back bond angles formed by the two neutral donor arms [**L14-PdCl**: N(1)-Pd(1)-N(3) 167.73(6); **L16-PdCl**: N(1)−Pd(1)−N(3) 165.9(2); **L13-PdCl**: N(1)−Pd(1)−N(3) 167.41(14)°]. The Pd-N_{amido} distances (**L14-PdCl**: 1.9599(15); **L16-PdCl**: 1.959(5); **L13-PdCl**: 1.961(3) Å] are within range of those reported for *bis*(2-(dimethylamino)phenyl)amido-**PdCl**[34] , and shorter than between palladium and the neutral donor arms [**L14-PdCl**: Pd(1)-N(1) 2.0034(15), Pd(1)-N(3) 2.0627(15); **L16-PdCl**: Pd(1)-N(1) 2.003(6), Pd(1)-N(3) 2.045(5); **L13-PdCl** Pd(1)-N(1) 1.996(4), Pd(1)-N(3) 2.054(3) Å]. For these latter Pd-N distances, the Pd-NMe_2 distance is consistently longer than the Ni-$N_{heterocycle}$ distance. All three complexes show similar Pd-Cl distances (~2.2 Å), implying very similar *trans* influence to the amido nitrogens of the ligand frameworks.

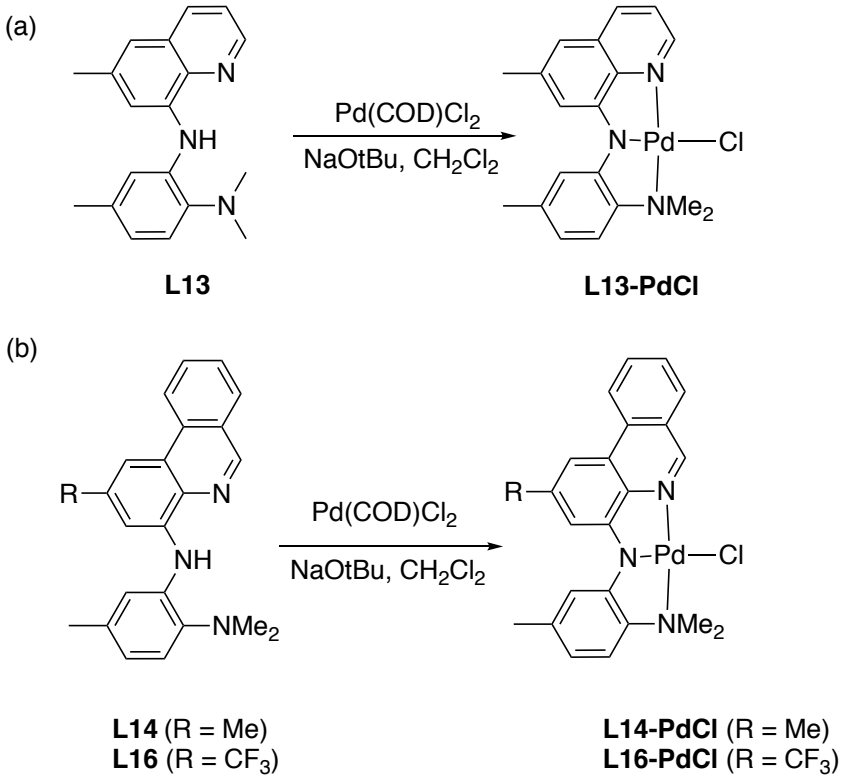

Scheme 5.5. Synthesis of (a) methyl-substituted quinolinyl based palladium complex **L13-PdCl**, (b) phenanthridine-based *N^N-^NMe2* palladium complexes.

5.3.4. UV-Vis Spectroscopy of Nickel and Palladium Complexes:

UV-Vis experiments were performed on both divalent nickel and palladium complexes in at $1x10^{-4}$M concentration using dichloromethane as solvent. Absorption spectra of L**13-NiCl**, **L14-NiCl**, **L15-NiCl** and **L16-NiCl** are marked by a broad peak at low energy, whose maximum shifts to higher wavelength (**L13-NiCl**: 515 nm; **L14-NiCl**: 520 nm; **L15-NiCl**: 531nm; **L16-NiCl**: 538nm;) with increasing conjugation. Significant red shift was observed with various substituents (Me, *t*Bu and CF_3) on the phenanthridine ring, **L16-NiCl** (CF_3) being the far red shifted complex as shown in Figure 5.4a. Similarly, UV-Vis absorption spectra of **L13-PdCl**, **L14-PdCl** are marked by a broad peak at low energy, whose maximum shifts to higher wavelength (**L13-PdCl**:

491 nm; **L14-PdCl**: 516 nm;) in dichloromethane with increasing conjugation. Although, similar red shift trend was observed divalent palladium complexes recorded absorption maxima at lower wavelengths. To study the effect for solvents on palladium complexes, the same experiment was performed for both complexes **L14-PdCl** and **L13-PdCl** in solvents with increasing polarity (toluene to DMF), initially hypsochromic (blue) shift was observed representing 'negative solvatochromism' until methanol as shown in Figure 5.6, which indicates ground state molecule is better stabilized than the exited state.[35] Later inverted solvatochromism was observed from methanol to DMF with bathochromic (red) shift as shown in Table 5.4 which could be due to coordinating ability of acetonitrile and DMF with metal complex.

Table 5.4. UV-Vis data for **L14-PdCl** and **L13-PdCl** in different solvents.

Solvent	**L14-PdCl (λ_{max}, nm)**	**L13-PdCl (λ_{max}, nm)**
Toluene	527	507
Diethyl ether	525	503
Dichloromethane	516	491
Acetone	515	492
Methanol	504	486
Acetonitrile	507	484
N,N-dimethylformamide	518	495

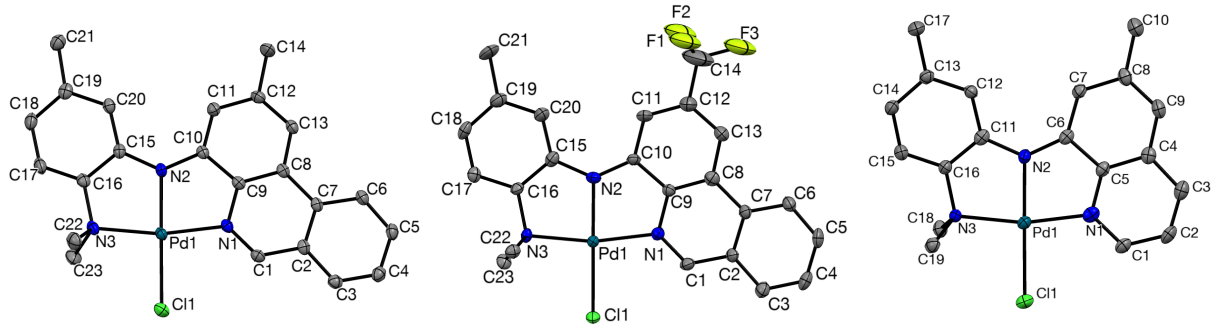

Figure 5.5. Solid-state structure of **L14-PdCl**, **L15-PdCl** and **L13-PdCl** shown with thermal ellipsoids at 50 % probability levels. Hydrogens are omitted for clarity. Selected bond distances (Å) and angles (°) for **L14-PdCl**: Pd(1)-Cl(1) 2.3358(5), Pd(1)-N(1) 2.0034(15), Pd(1)-N(2) 1.9599(15), Pd(1)-N(3) 2.0627(15), C(1)-N(1) 1.308(2); N(1)-Pd(1)-N(3) 167.73(6), Cl(1)−Pd(1)−N(2) 178.99(5), N(1)−Pd(1)−N(2) 82.77(6), N(3)−Pd(1)−N(2) 85.02(6), N(1)−Pd(1)−Cl(1) 96.81(5), N(3)−Pd(1)−Cl(1) 95.38(5). **L16-PdCl**: Pd(1)-Cl(1) 2.3332(16), Pd(1)-N(1) 2.003(6), Pd(1)-N(2) 1.959(5), Pd(1)-N(3) 2.045(5), C(1)-N(1) 1.298(8); N(1)−Pd(1)−N(3) 165.9(2), Cl(1)−Pd(1)−N(2) 178.64(18), N(1)−Pd(1)−N(2) 82.6(2), N(3)−Pd(1)−N(2) 85.2(2), N(1)−Pd(1)−Cl(1) 97.08(16), N(3)−Pd(1)−Cl(1) 95.29(16). **L13-PdCl**: Pd(1)-Cl(1) 2.3382(11), Pd(1)-N(1) 1.996(4), Pd(1)-N(2) 1.961(3), Pd(1)-N(3) 2.054(3), C(1)-N(1) 1.321(5); N(1)−Pd(1)−N(3) 167.41(14), Cl(1)−Pd(1)−N(2) 178.85(11), N(1)−Pd(1)−N(2) 82.53(14), N(3)−Pd(1)−N(2) 84.96(14), N(1)−Pd(1)−Cl(1) 97.02(11), N(3)−Pd(1)−Cl(1) 95.46(10).

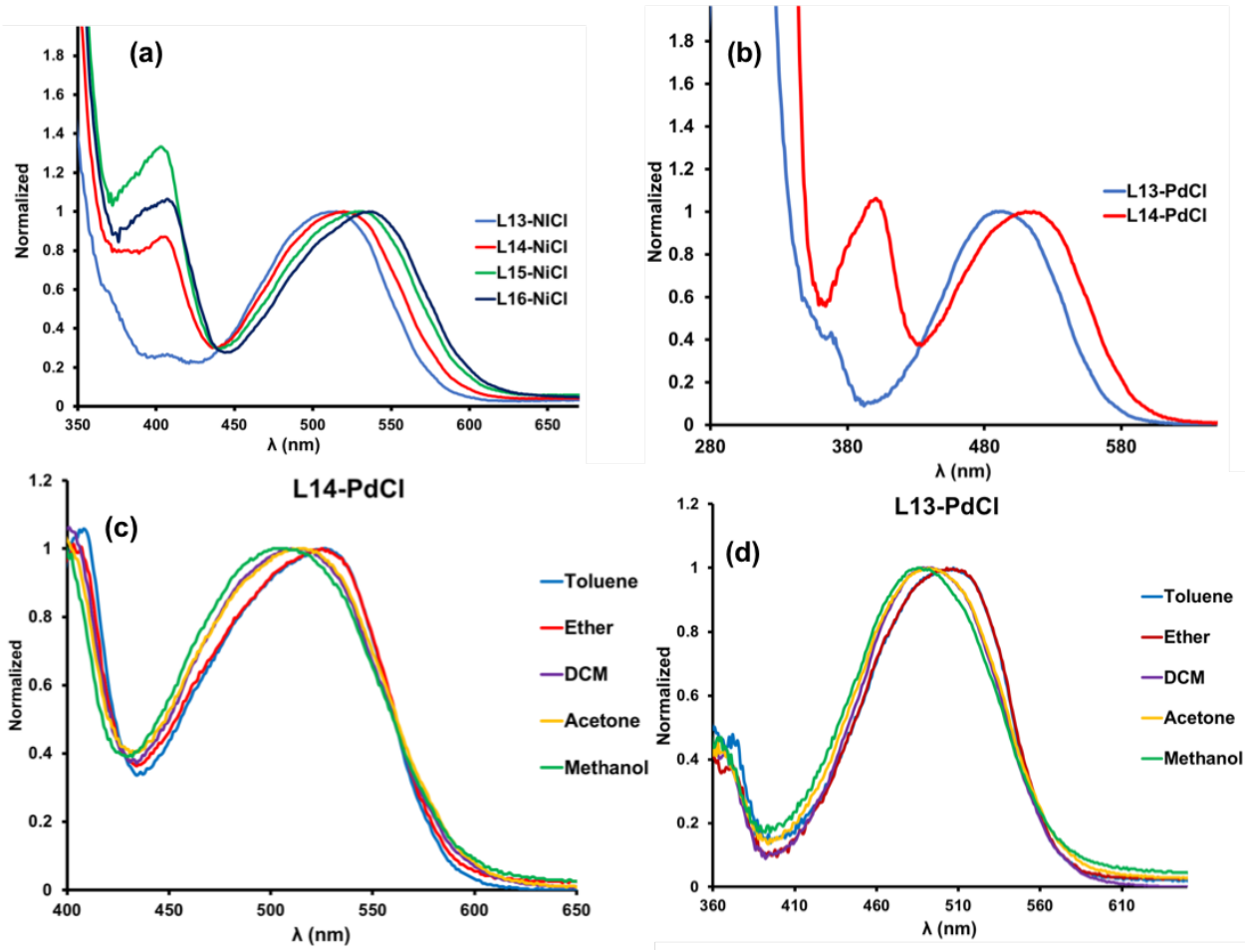

Figure 5.6. UV-Vis absorption spectra (a) for Ni(II) complexes (b) for **L13-PdCl** and **L14-PdCl** in (CH_2Cl_2, 22 °C) (b) observed bathochromic shift for **L13-PdCl** (c)&(d) negative solvatochromism observed for **L14-PdCl** and **L3-PdCl** respectively

5.3.5. Reactivity of Pd(II) complexes:

After successfully demonstrating the role divalent Ni(II) complexes in C–H bond alkylation of azoles with alkyl halides, initial attempts were made to understand and study the reactivity of Pd(II) complexes to isolate metal hydrides (nickel and palladium) with reducing agents. Reaction of **L14-PdCl** with TMSOTf/AgOTf in dichloromethane/THF at room temperature gave a red precipitate indicating the possible formation of triflate bound complex (**L14-PdOTf**) but could not be well characterized due to solubility issues in non-coordinating solvents. A broad range of

reducing agents to isolate Pd(II)hydride were used as shown in Scheme 4.6a, but none of them gave fruitful products, often, free ligand was observed suggesting demetallation of the palladium complex. When **L14-PdCl** was reacted with excess sodium isopropoxide in C_6D_6 a trace amounts of acetone were observed in preliminary ^1H NMR studies. This suggests the possible occurrence of β-hydride elimination at the palladium metal centre, leaving behind acetone. Further studies are currently underway to investigate the possibility and scope with different palladium complexes and ligand frameworks.

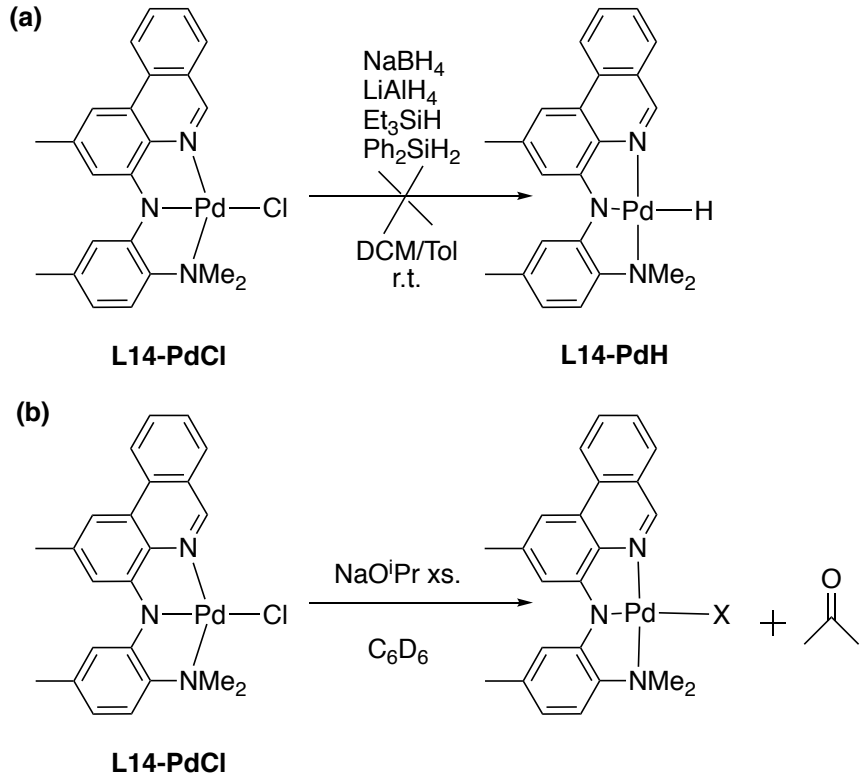

Scheme 5.6. (a) Unsuccessful attempts to isolate **L14-PdH** using different reducing agents, (b) reaction of **L14-PdCl** with NaO^iPr

5.4. Conclusions:

In conclusion, I have demonstrated that the introduction of benzannulated phenanthridine ligands supporting Ni(II) coordination complexes maintain the high activity observed in the C-H alkylation of azoles observed with quinoline congeners,[10] for both benzoxazole and benzothiazole. The synthetic route to the *N^N(H)^N* proligand frameworks **L14-L16** allows for facile incorporation of different substituents, whose electron-releasing/electron-withdrawing properties can be quantified in terms of the redox properties of their Ni complexes in solution. Comprehensive mechanistic studies, including investigating correlation of catalytic activity to the π-acidity of the benzannulated phenanthridine ligand frameworks,[18] and expansion of the scope of C-C bond forming reactions to other substrate classes is presently underway. **L13-PdCl** and **L14-PdCl** show inverted solvatochromism trend with increasing solvent polarity. The reactivity studies to further investigate β-hydride elimination at the palladium metal centre is currently underway.

5.5. Experimental Section:

Unless otherwise specified, air sensitive manipulations were carried either in an N2-filled glove box or using standard Schlenk techniques under Ar. (N,N-dimethyl)-para-toluidine (Sigma Aldrich), 2-formylphenyl boronic acid (AK Scientific), N-iodosuccinimide (AK Scientific), N-bromosuccinimide (Alpha Aesar), $Pd(PPh_3)_4$ (Sigma Aldrich), $Pd_2(dba)_3$ (Sigma Aldrich), 2-nitro-4-(trifluoromethyl)aniline (Sigma Aldrich), (1,1'-diphenylphosphino)ferrocene (dppf, Sigma Aldrich), (±)-2,2'-bis(diphenylphosphino)-1,1'-binapthalene (*rac*-BINAP, Sigma Aldrich), Na_2CO_3 (Alpha Aesar), trifluoroacetic acid (Sigma Aldrich), sodium tert-pentoxide (NaO*t*pen, Sigma Aldrich), sodium tert-butoxide (NaO*t*Bu, Sigma Aldrich), zinc (Alpha Aesar), hydrazine hydrate (Sigma Aldrich), formic acid (Alpha Aesar), $NiCl_2•6H_2O$ (Alfa Aesar) and all reagents used in precursor synthesis and catalytic trials were purchased and used without any further

purification. (2-bromo-4,N,N-trimethyl)aniline,[28] (8-amino-4-methyl)quinoline,[29] (4-amino-2-methyl)phenanthridine (1-NH2),[15] (4-amino-2-tert-butyl)phenanthridine (**2-NH$_2$**),[18] and 2-iodo-6-nitro-4-trifluoromethylaniline[30] were synthesized according to published procedures. Organic solvents were dried and distilled using appropriate drying agents, while distilled water was degassed prior to use. Multinuclear 1- and 2D NMR spectra were recorded on Bruker Avance 300 MHz or Bruker Avance – III 500 MHz spectrometers. ^{1}H and ^{13}C{^{1}H} NMR spectra were referenced to residual solvent peaks. Elemental analyses were performed by Microanalytical Service Ltd., Delta, BC, Canada, and at the University of Manitoba using a Perkin Elmer 2400 Series II CHNS/O Elemental Analyzer. High-resolution mass spectra were recorded using a Bruker microOTOF-QIII.

Synthesis of 4-nitro-2-trifluoromethylphenanthridine (3-NO$_2$): A 500 mL Teflon-stoppered flask was charged with Pd(PPh$_3$)$_4$ (1.04 g, 0.90 mmol), and 50 mL of 1,2-dimethoxyethane (DME). After stirring briefly to mix, 2-iodo-6-nitro-4-trifluoromethylaniline (10.0 g, 30.1 mmol), 2-formylphenylboronic acid (4.97 g, 33.1 mmol) and an additional 70 mL of DME were added, followed by Na_2CO_3 (9.6 g, 90.4 mmol) dissolved in 100 mL of degassed water. The flask was then sealed and the mixture stirred vigorously for 6 h in an oil bath set to 130 °C. The flask was then allowed to cool, charged with 130 mL of 2M HCl, and refluxed for additional 2 h. The reaction mixture was cooled, neutralized with NaOH, and pumped to dryness. The residue was then taken up in dichloromethane (100 mL) and washed with brine (3 x 100 mL). The organic layer was separated, dried over Na_2SO_4 and volatiles removed. Column chromatography on neutral alumina gave a pale yellow solid (R_f = 0.41; 1:5 EtOAc/hexanes). Isolated yield = 7.86 g (89 %). ^{1}H NMR ($CDCl_3$, 300 MHz, 22 °C): δ 9.48 (s, 1H; $C_{Ar}H$), 9.01 (s, 1H; $C_{Ar}H$), 8.67 (d, 1H, J_{HH} = 8.0 Hz; $C_{Ar}H$), 8.18 (overlapped m, 2H; $C_{Ar}H$), 8.05 (ddd, 1H, J_{HH} = 8.4, 7.2, 1.4 Hz; $C_{Ar}H$), 7.92 ppm (m,

1H; $C_{Ar}H$). $^{13}C\{^1H\}$ NMR ($CDCl_3$, 125 MHz, 22 °C): δ 158.0 (C_{Ar}), 149.8 (C_{Ar}), 137.5 (C_{Ar}), 133.1 (C_{Ar}), 131.2 (q, C_{Ar}), 130.0 (C_{Ar}), 129.8 (C_{Ar}), 128.4 (C_{Ar}), 126.9 (C_{Ar}), 126.0 (C_{Ar}), 124.3 (C_{Ar}), 123.2 (q, CF_3), 122.3 (C_{Ar}), 118.7 ppm (q, C_{Ar}). $^{19}F\{^1H\}$ NMR ($CDCl_3$, 282 MHz, 22 °C): δ -62.03 ppm.

4-amino-2-trifluoromethylphenanthridine (4-NH$_2$): To a stirred solution of **1c** (6.02 g, 20.5 mmol) in methanol (100 mL), Zn dust (2.68 g, 41.1 mmol), and hydrazinium monoformate solution (54 mL; prepared by slowly neutralizing equal molar amounts of hydrazine hydrate (50 mL) with 85% formic acid (4 mL) in an ice-water bath) were added and stirred vigorously at 60 °C. The resulting green suspension was cooled and filtered over Celite. The filtrate was pumped dry, the residue dissolved in dichloromethane (100 mL), and washed with brine (3 x 60 mL). The organic layer was separated, dried over Na_2SO_4 and dried to leave a brown solid. Column chromatography on neutral alumina gave a pale-yellow solid (R_f = 0.43; 1:5 EtOAc/hexane). Isolated yield = 3.74 g (86 %). ^1H NMR ($CDCl_3$, 300 MHz, 22 °C): δ 9.15 (s, 1H; $C_{Ar}H$), 8.50 (d, 1H, J_{HH} = 8.3; $C_{Ar}H$), 8.07 (s, 1H; $C_{Ar}H$), 8.01 (dd, 1H, J_{HH} = 8.0, 1.3 Hz; $C_{Ar}H$), 7.83 (app t, 1H, J_{HH} = 8.4, 7.0 Hz; $C_{Ar}H$), 7.70 (app t, 1H, J_{HH} = 8.1, 7.0; $C_{Ar}H$), 7.13 (d, 1H, J_{HH} = 1.8 Hz; $C_{Ar}H$), 5.22 ppm (br s, 2H; NH). $^{13}C\{^1H\}$ NMR ($CDCl_3$, 75 MHz, 22 °C): δ 152.2 (C_{Ar}), 145.6 (C_{Ar}), 134.5 (C_{Ar}), 132.7 (C_{Ar}), 131.3 (q, C_{Ar}), 128.9 (C_{Ar}), 128.1 (C_{Ar}), 126.9 (C_{Ar}), 124.3 (C_{Ar}), 122.5 (C_{Ar}), 107.9 (q, CF_3), 106.7 ppm (q, C_{Ar}). $^{19}F\{^1H\}$ NMR ($CDCl_3$, 282 MHz, 22 °C): δ -62.28 ppm.

Synthesis of ^{Me,Quin}NN(H)NMe$_2$ (L13): A 350 mL Teflon-stoppered flask was charged with $Pd_2(dba)_3$ (1.91 g, 2.09 mmol), dppf (2.69 g, 4.69 mmol), and toluene (30 mL). After stirring briefly, (8-amino-4-methyl)quinoline[29] (4.15 g, 26.1 mmol), (2-bromo-4,*N*,*N*-trimethyl)aniline[28] (6.70 g, 31.3 mmol) were combined with an additional 90 mL of toluene, followed by NaO*t*Am (4.30 g, 39.1

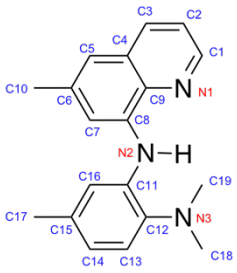

mmol). The mixture was then stirred vigorously for 72 h in an oil bath set to 130 °C. After cooling the flask and removing the volatiles, the residue was taken up in dichloromethane (120 mL), and the resulting suspension filtered over Celite and dried. Column chromatography gave a yellow oil which solidified on standing (neutral alumina; 1:10 EtOAc/hexane; $R_f = 0.5$). Isolated yield = 8.23 g (74%). ^{1}H NMR ($CDCl_3$, 500 MHz, 22 °C): δ 8.76 (dd, 1H; J_{HH} = 4.2, 1.7 Hz, C_1H), 8.65 (brs, 1H; N*H*), 8.01 (dd, 1H, J_{HH} = 8.3, 1.7 Hz; C_3H), 7.50 (d, 1H, J_{HH} = 1.9 Hz; $C_{16}H$), 7.46 (d, 1H, J_{HH} = 1.7 Hz; C_7H), 7.38 (dd, 1H, J_{HH} = 8.2, 4.2 Hz; C_2H), 7.06 (d, 1H, J_{HH} = 8.0 Hz; $C_{13}H$), 7.00 (s, 1H, C_5H), 6.81 (m, 1H, J_{HH} = 8.0, 2.0 Hz; $C_{14}H$), 2.72 (s, 6H; N($C_{(18,19)}H_3$)$_2$), 2.51 (s, 3H; $C_{10}H_3$), 2.38 (s, 3H, $C_{17}H_3$). ^{13}C{^{1}H} NMR ($CDCl_3$, 125 MHz, 22 °C): δ 146.7 (C_1), 142.7 (C_{12}), 139.7 (C_8), 138.1 (C_9), 137.3 (C_6), 136.0 (C_{11}), 136.0 (C_3), 132.7 (C_{15}), 129.1 (C_4), 122.1 (C_{14}), 121.6 (C_2), 119.2 (C_{13}), 118.5 (C_{16}), 115.5 (C_5), 109.6 (C_7), 44.1 (N($C_{18,19}$)$_2$), 22.5 (C_{10}), 21.4 ppm (C_{17}).

Synthesis of ^{Me}PhenNN(H)NMe$_2$ (L14): An identical procedure to the synthesis of **5** was employed, using $Pd_2(dba)_3$ (0.51 g, 0.55 mmol), dppf (0.67 g, 1.21 mmol), **2a** (2.30 g, 11.0 mmol), (2-bromo-4,*N*,*N*-trimethyl)aniline[28] (2.83 g, 13.3 mmol) and NaO*t*Am (1.82 g, 16.6 mmol). Column chromatography on neutral alumina gave a yellow solid

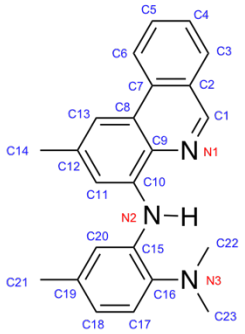

(1:10 EtOAc/hexane; $R_f = 0.5$). Isolated yield = 1.34 g (97%). ^{1}H NMR ($CDCl_3$, 500 MHz, 22 °C): δ 9.18 (s, 1H; C_1H), 8.72 (br s, 1H; N*H*), 8.61 (d, 1H, J_{HH} = 8.2 Hz; C_6H), 8.06 (d , 1H, J_{HH} = 7.7 Hz; C_3H), 7.84 (dd, 1H, J_{HH} = 8.4, 7.0 Hz; C_5H), 7.78 (s, 1H; $C_{20}H$), 7.71 (dd, 1H, J_{HH} = 8.0, 7.0 Hz; C_4H), 7.55 (s, 1H; $C_{13}H$), 7.51(s, 1H; $C_{11}H$), 7.07 (d, 1H, J_{HH} = 8.0 Hz; $C_{17}H$), 6.82 (dd, 1H, J_{HH} = 8.0, 1.9 Hz; $C_{18}H$), 2.74 (s, 6H; N($C_{22,23}H_3$)$_2$), 2.60 (s, 3H; $C_{14}H_3$), 2.38 ppm (s, 3H; $C_{21}H_3$). ^{13}C{^{1}H} NMR ($CDCl_3$, 75 MHz, 22 °C): δ 149.5 (C_1), 142.7 (C_{16}), 140.7 (C_{10}), 137.7 (C_{12}), 136.1

(C_{15}), 132.8 (C_9), 132.7 (C_{19}), 132.6 (C_2), 130.5 (C_5), 128.6 (C_3), 127.3 (C_4), 127.1 (C_8), 124.7 (C_7), 122.4 (C_6), 122.0 (C_{18}), 119.1 (C_{17}), 118.7 (C_{11}), 111.0 (C_{20}), 110.5 (C_{13}), 44.1 (N($C_{22,23}$)$_2$), 22.8 (C_{14}), 21.3 ppm (C_{21}).

Synthesis of $^{t\text{Bu}}$PhenNN(H)NMe$_2$ (L15): An identical procedure to the synthesis of **5** was employed, using $Pd_2(dba)_3$ (0.55 g, 0.60 mmol), dppf (0.73 g, 1.32 mmol), **2b** (3.0 g, 11.9 mmol), (2-bromo-4,*N*,*N*-trimethyl)aniline[28] (2.87 g, 13.4 mmol) and NaO*t*Am (1.98 g, 17.9 mmol). Column chromatography on neutral alumina gave a yellow solid

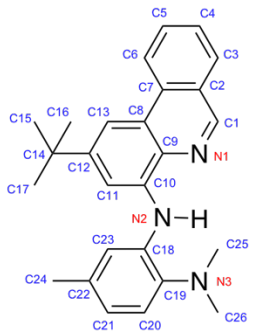

(1:10 EtOAc/hexane; R_f = 0.5). Isolated yield = 4.18 g (91%) ^{1}H NMR ($CDCl_3$, 300 MHz, 22 °C): δ 9.18 (s, 1H; C_1H), 8.73 (brs, 1H; N*H*), 8.65 (d, 1H, J_{HH} = 8.4 Hz; C_6H), 8.11-7.97 (m, 2H; C_3H, $C_{23}H$), 7.96-7.80 (m, 2H; C_5H, $C_{13}H$), 7.69 (m, 1H; C_4H), 7.54 (s, 1H; $C_{11}H$), 7.08 (dd, 1H, J_{HH} = 8.0, 2.5 Hz; $C_{20}H$), 6.80 (dd, 1H, J_{HH} = 8.1, 2.2 Hz; $C_{21}H$), 2.78 (s, 6H; N($C_{25,26}H_3$)$_2$), 2.37 (s, 3H; $C_{24}H_3$), 1.52 ppm (s, 9H; ($C_{15,16,17}H_3$)$_3$). ^{13}C{^{1}H} NMR ($CDCl_3$, 75 MHz, 22 °C): δ 150.6 (C_{12}), 150.0 (C_1), 142.3 (C_{19}), 140.1 (C_{10}), 136.6 (C_{18}), 133.2 (C_9), 133.1 (C_2), 132.9 (C_{22}), 130.6 (C_5), 128.8 (C_3), 127.2 (C_4), 127.0 (C_8), 124.3 (C_7), 122.4 (C_6), 121.5 (C_{21}), 119.3 (C_{20}), 117.4 (C_{11}), 108.9 (C_{23}), 107.4 (C_{13}), 44.2 (N($C_{25,26}$)$_2$), 35.7 (C_{14}), 31.7 ($C_{15,16,17}$), 21.5 ppm (C_{24}).

Synthesis of ^{CF3}PhenNN(H)NMe$_2$ (L16): An identical procedure to the synthesis of **5** was employed, using $Pd_2(dba)_3$ (0.20 g, 0.22 mmol), dppf (0.27 g, 0.49 mmol), **2c** (1.16 g, 4.42 mmol), (2-bromo-4,*N*,*N*-trimethyl)aniline[28] (1.14 g, 5.30 mmol) and NaO*t*Am (0.73 g, 6.63 mmol). Column chromatography on neutral alumina gave a yellow solid

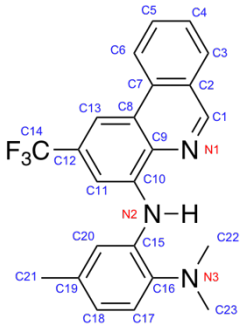

(1:10 EtOAc/hexane; R_f = 0.5). Isolated yield = 1.50 g (85%) ^{1}H NMR ($CDCl_3$, 300 MHz, 22 °C): δ 9.30 (s, 1H; C_1H), 8.89 (brs, 1H; N*H*), 8.63 (d, 1H, J_{HH} = 8.3 Hz; C_6H), 8.18 (s, 1H; $C_{13}H$), 8.11

(d, 1H, J_{HH} = 8.0 Hz; C_3H), 7.92 (t, 1H, J_{HH} = 8.3, 6.9 Hz; C_5H), 7.83-7.73 (m, 2H; C_4H, $C_{11}H$), 7.46 (s, 1H, $C_{20}H$) 7.07 (d, 1H, J_{HH} = 8.0, Hz; $C_{17}H$), 6.87 (d, 1H, J_{HH} = 8.2; $C_{18}H$), 2.72 (s, 6H; $N(C_{22,\ 23}H_3)_2$), 2.37 ppm (s, 3H; $C_{21}H_3$). $^{13}C\{^1H\}$ NMR ($CDCl_3$, 125 MHz, 22 °C): δ 152.3 (C_1), 143.2 (C_{10}), 141.9 (C_{16}), 135.2 (C_{15}), 135.1 (C_9), 133.1 (C_2), 133.0 (C_{19}), 131.5 (C_5), 129.6 (C_{14}, quartet), 129.0 (C_3), 128.2 (C_4), 127.1 (C_{12}), 125.8 (C_8), 123.7 (C_7), 123.3 (C_{18}), 122.6 (C_6), 119.5 (C_{17}), 119.4 (C_{20}), 108.0 (C_{13}), 104.2 (C_{11}), 44.14 ($N(C_{22,\ 23})_2$), 21.4 ppm (C_{21}). $^{19}F\{^1H\}$ NMR ($CDCl_3$, 282 MHz, 22 °C): δ -62.37 ppm (s, 3F; CF_3).

Synthesis of ^{Me}QuinNNNMe$_2$-NiCl (L13-NiCl): To a stirred solution of compound **5** (1.01 g, 3.43 mmol) in 30 mL of dichloromethane, $NiCl_2$•$6H_2O$ (0.86g, 3.60 mmol), and NaO*t*Bu (0.35 g, 3.60 mmol) were added, and the mixture stirred vigorously at 65 °C for 18 h. The resulting red suspension was allowed to cool, and the volatiles removed *in vacuo*. The residue was then washed with diethyl ether (3 x 15 mL) to isolate red solid. The compound is further purified by redissolving in DCM and passed through Celite. Isolated yield = 1.17 g (89%). ^1H NMR ($CDCl_3$, 500 MHz, 22 °C): δ 8.46 (d, 1H, J_{HH} = 5.0 Hz; C_1H), 7.98 (dd, 1H, J_{HH} = 8.2, 1.5 Hz; C_3H), 7.34 (s, 1H; $C_{16}H$), 7.24 (s, 1H; $C_{7/5}H$), 7.17 (dd, 1H, J_{HH} = 8.2, 5.3 Hz; C_2H), 6.96 (d, 1H, J_{HH} = 8.1; $C_{13}H$), 6.67 (s, 1H; $C_{5/7}H$), 6.47-6.40 (m, 1H; $C_{14}H$), 3.02 (s, 6H; $N(C_{19,18}H_3)_2$), 2.48 (s, 3H; $C_{10}H_3$), 2.36 ppm (s, 3H; $C_{17}H_3$). $^{13}C\{^1H\}$ NMR ($CDCl_3$, 125 MHz, 22 °C): δ 149.5 (C_1), 147.9 (C_8), 147.2 (C_{11}), 146.1 (C_9), 145.2 (C_{12}), 139.6 (C_6), 138.5 (C_{15}), 137.7 (C_3), 129.5 (C_4), 120.9 (C_2), 119.9 (C_{13}), 117.9 (C_{14}), 115.5 (C_{16}), 112.5 ($C_{5/7}$), 112.3 ($C_{5/7}$), 51.9 ($N(C_{18,\ 19})_2$), 22.6 (C_{10}), 21.7 ppm (C_{17}). Anal. Calcd for $C_{19}H_{20}ClN_3Ni$: C, 59.35; H, 5.24. Found: C, 59.07; H, 5.25.

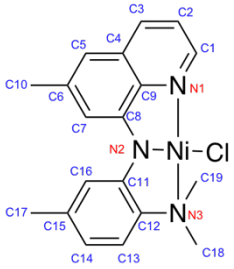

Synthesis of ^{Me}PhenNNNMe$_2$-NiCl (L14-NiCl): An identical procedure to the synthesis of **6** was employed, using **3a** (1.14 g, 3.33 mmol), $NiCl_2$•$6H_2O$ (0.81 g, 3.42 mmol), and NaO*t*Bu (0.34 g, 3.50 mmol) in 15 mL of dichloromethane. Isolated yield = 1.32 g (91 %). ^{1}H NMR ($CDCl_3$, 300 MHz, 22 °C): δ 8.88 (s, 1H; C_1H), 8.39 (d, 1H, J_{HH} = 8.4 Hz; C_6H), 7.88 (d, 1H, J_{HH} = 8.1 Hz; C_3H), 7.83 (t, 1H, J_{HH} = 7.8 Hz; C_5H), 7.61 (t, 1H, J_{HH} = 7.6 Hz; C_4H), 7.37 (s, 1H; $C_{20}H$), 7.31 (s, 1H; $C_{11}H$), 7.28 (s, 1H; $C_{13}H$), 6.96 (d, 1H, J_{HH} = 8.1 Hz; $C_{17}H$), 6.43 (d, 1H, J_{HH} = 7.8 Hz; $C_{18}H$), 3.05 (s, 6H; N($C_{22,\,23}H_3$)$_2$), 2.57 (s, 3H; $C_{14}H_3$), 2.36 ppm (s, 3H; $C_{21}H_3$). ^{13}C{^{1}H} NMR ($CDCl_3$, 125 MHz, 22 °C): δ 153.9 (C_1), 148.5 (C_{10}), 147.3 (C_{15}), 145.0 (C_{16}), 140.0 (C_9), 139.6 (C_{12}), 138.3 (C_{19}), 132.7 (C_2), 132.4 (C_5), 129.6 (C_3), 127.5 (C_4), 126.0 (C_8), 125.2 (C_7), 122.2 (C_6), 119.8 (C_{17}), 117.6 (C_{18}), 115.4 (C_{20}), 112.2 (C_{11}), 108.3 (C_{13}), 51.8 (N($C_{22,\,23}$)$_2$), 22.8 (C_{14}) and 21.6 (C_{21}). Anal. Calcd for $C_{23}H_{22}ClN_3Ni$: C, 63.57; H, 5.10. Found: C, 63.60; H, 5.21.

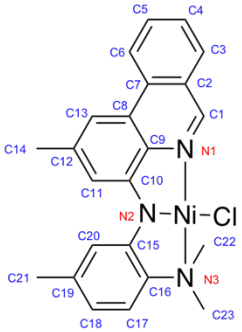

Synthesis of ^{tBu}PhenNNNMe$_2$-Ni (L15-NiCl): An identical procedure to the synthesis of **6** was employed, using **3b** (1.01 g, 2.60 mmol), $NiCl_2$•$6H_2O$ (0.65 g, 2.74 mmol), and NaO*t*Bu (0.26 g, 2.74 mmol) in 15 mL of dichloromethane. Isolated yield = 1.17 g (93 %). ^{1}H NMR ($CDCl_3$, 500 MHz, 22 °C): δ 8.93 (s, 1H; C_1H), 8.51 (d, 1H, J_{HH} = 8.3 Hz; C_6H), 7.94 (d, 1H, J_{HH} = 8.1 Hz; C_3H), 7.88 (t, 1H, J_{HH} = 8.1 Hz; C_5H), 7.64 (m, 2H; $C_{4,\,11/13}H$), 7.55 (s, 1H; $C_{11/13}H$), 7.40 (s, 1H; $C_{23}H$), 6.98 (d, 1H, J_{HH} = 8.2 Hz; $C_{20}H$), 6.43 (d, 1H, J_{HH} = 8.2 Hz; $C_{21}H$), 3.05 (s, 6H; N($C_{25,\,26}H_3$)$_2$), 2.36 (s, 3H; $C_{24}H_3$) and 1.49 ppm (s, 9H; ($C_{15,\,16,\,17}H_3$)$_3$). ^{13}C{^{1}H} NMR ($CDCl_3$, 125 MHz, 22 °C): δ 154.4 (C_1), 152.9 (C_{12}), 148.4 (C_{10}), 147.5 (C_{18}), 145.2 (C_{19}), 140.1 (C_9), 138.5 (C_{22}), 133.4 (C_2), 132.6 (C_5), 129.9 (C_3), 127.7 (C_4), 126.3 (C_8), 125.0 (C_7), 122.3 (C_6), 120.0 (C_{20}), 117.5 (C_{21}), 115.4 (C_{23}), 109.4 ($C_{11/13}$), 104.7 ($C_{11/13}$), 51.9 (N($C_{25,\,26}$)$_2$), 35.7 ($C_{15,\,16,\,17}$)$_3$),

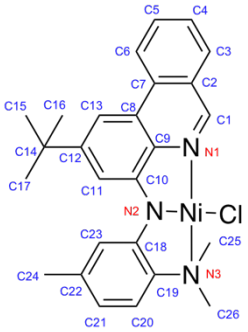

31.8 (C_{14}), 21.9 ppm (C_{24}). Anal. Calcd for $C_{26}H_{28}ClN_3Ni$: C, 65.51; H, 5.92. Found: C, 65.35; H, 6.03.

Synthesis of ^{CF3}PhenNNNMe$_2$-Ni (L16-NiCl): An identical procedure to the synthesis of **6** was employed, using **3c** (1.80 g, 4.56 mmol), $NiCl_2$•$6H_2O$ (1.14 g, 4.77 mmol), and NaO*t*Bu (0.46 g, 4.79 mmol) in 15 mL of dichloromethane. Isolated yield = 1.86 g (83 %). ^{1}H NMR ($CDCl_3$, 500 MHz, 22 °C): δ 9.10 (s, 1H; C_1H), 8.48 (d, 1H, J_{HH} = 8.3 Hz; C_6H), 8.10-7.90 (m, 2H; $C_{3,5}H$), 7.84-7.56 (m, 3H; $C_{4,11,13}H$), 7.36 (s, 1H; $C_{20}H$), 7.01 (d, 1H, J_{HH} = 8.2 Hz; $C_{17}H$), 6.52 (d, 1H, J_{HH} = 8.2 Hz; $C_{18}H$), 3.06 (s, 6H; N($C_{22,23}H_3$)$_2$), and 2.37 (s, 3H; $C_{21}H_3$). ^{13}C{^{1}H} NMR ($CDCl_3$, 125 MHz, 22 °C): δ 156.1 (C_1), 149.0 (C_{10}), 146.5 (C_{15}), 145.3 (C_{16}), 142.6 (C_9), 138.8 (C_{19}), 133.4 (C_5), 132.9 (C_2), 131.1 (C_{14}, quartet), 130.1 (C_3), 128.5 (C_4), 126.1 (C_{12}), 125.5 (C_8), 123.4 (C_7), 122.4 (C_6), 120.1 (C_{17}), 119.0 (C_{18}), 115.8 (C_{20}), 105.9 (C_{13}), 105.1 (C_{11}), 52.0 (N($C_{22,\ 23}$)$_2$), 21.7 ppm (C_{21}). ^{19}F{^{1}H} NMR ($CDCl_3$, 470 MHz, 22 °C): δ -62.27 ppm (s, 3F; CF_3). Anal. Calcd for $C_{23}H_{19}ClF_3N_3Ni$: C, 56.54; H, 3.92. Found: C, 56.33; H, 3.63.

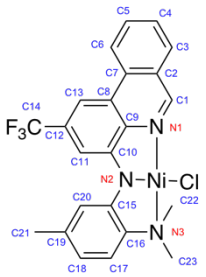

Synthesis of ^{Me}QuinNNNMe$_2$-PdCl (L13-PdCl): To a stirred solution of compound **L13** (0.20 g, 0.69 mmol) in 30 mL of THF, Pd(COD)Cl_2 (0.33 g, 0.69 mmol), and NaO*t*Bu (0.070 g, 0.72 mmol) were added, and the mixture stirred vigorously at 65 °C for 18 h. The resulting red suspension was allowed to cool, and the volatiles removed *in vacuo*. The residue was then washed with diethyl ether (3 x 15 mL) to isolate a red solid. The compound was redissolved in CH_2Cl_2 and passed through a short plug (1 cm) of Celite. Isolated yield of **L13-PdCl** = 0.24 g (83%). ^{1}H NMR ($CDCl_3$, 500 MHz, 22 °C): δ 8.78 (d, 1H, J_{HH} = 5.0 Hz; C_1H), 8.03 (dd, 1H, J_{HH} = 8.3 Hz; C_3H), 7.42 (s, 1H; $C_{16}H$), 7.34 (s, 1H; C_7H), 7.29-7.23 (m, 1H, C_2H), 7.06 (d, 1H, J_{HH} = 8.1 Hz; $C_{13}H$),

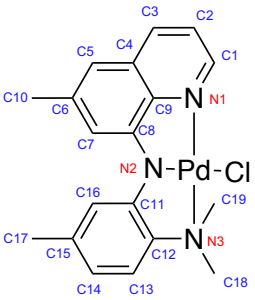

6.76 (s, 1H; C_5H), 6.54 (d, 1H, J_{HH} = 8.1 Hz; $C_{14}H$), 3.27 (s, 6H; N($C_{19,18}H_3$)$_2$), 2.49 (s, 3H; $C_{10}H_3$), 2.38 ppm (s, 3H; $C_{17}H_3$). $^{13}C\{^1H\}$ NMR ($CDCl_3$, 125 MHz, 22 °C): δ 149.3(C_7), 148.6 (C_{11}), 148.0 (C_1), 146.8 (C_6), 145.7 (C_{12}), 139.8 (C_9), 139.1 (C_{15}), 137.9 (C_3), 130.9 (C_5), 121.1 (C_2), 121.1 (C_{13}), 118.8 (C_{14}), 115.9 (C_{16}), 113.6 (C_{10}), 113.1 (C_8), 53.9 (N($C_{18,\ 19}$)$_2$), 22.5 (C_{10}), 21.7 ppm (C_{17}). Anal. Calcd for $C_{19}H_{20}ClN_3Pd$: C, 52.79; H, 4.66. Found: C, 52.99; H, 4.69.

Synthesis of ^{Me}PhenNNNMe$_2$-PdCl (L14-PdCl): To a stirred solution of compound **L14** (0.20 g, 0.59 mmol) in 30 mL of THF, Pd(COD)Cl_2 (0.17 g, 0.59 mmol), and NaO*t*Bu (0.060 g, 0.62 mmol) were added, and the mixture stirred vigorously at 65 °C for 18 h. The resulting red suspension was allowed to cool, and the volatiles removed *in vacuo*. The residue was then washed with diethyl ether (3 x 15 mL) to isolate a red solid. The compound was redissolved in CH_2Cl_2 and passed through a short plug (1 cm) of Celite. Isolated yield of **L14-PdCl** = 0.23 g (79%). ^1H NMR ($CDCl_3$, 500 MHz, 22 °C): δ 9.26 (s, 1H; C_1H), 8.50 (d, 1H, J_{HH} = 8.3 Hz; C_6H), 8.02 (d, 1H, J_{HH} = 8.0 Hz; C_3H), 7.88 (t, 1H, J_{HH} = 7.7 Hz; C_5H), 7.69 (t, 1H, J_{HH} = 7.5 Hz; C_4H), 7.51 (s, 1H; $C_{20}H$), 7.48 (s, 1H; $C_{11}H$), 7.47(s, 1H; $C_{13}H$), 7.09 (d, 1H, J_{HH} = 8.2 Hz; $C_{17}H$), 6.56 (d, 1H, J_{HH} = 8.1 Hz; $C_{18}H$), 3.31 (s, 6H; N($C_{22,\ 23}H_3$)$_2$), 2.60 (s, 3H; $C_{14}H_3$), 2.41 ppm (s, 3H; $C_{21}H_3$). $^{13}C\{^1H\}$ NMR ($CDCl_3$, 125 MHz, 22 °C): δ 151.9 (C_1), 150.2 (C_{10}), 148.9 (C_{15}), 145.6 (C_{16}), 140.7 (C_9), 140.1 (C_{12}), 139.1 (C_{19}), 132.9 (C_5), 132.7 (C_7), 129.8 (C_3), 128.1 (C_4), 127.0 (C_8), 126.2 (C_2), 122.6 (C_6), 121.1 (C_{17}), 118.7 (C_{18}), 115.9 (C_{20}), 112.8 (C_{11}), 109.5 (C_{13}), 54.0 (N($C_{22,\ 23}$)$_2$), 22.9 (C_{14}) and 21.7 (C_{21}). Anal. Calcd for $C_{23}H_{22}ClN_3Pd$: C, 57.28; H, 4.60. Found: C, 56.90; H, 4.63.

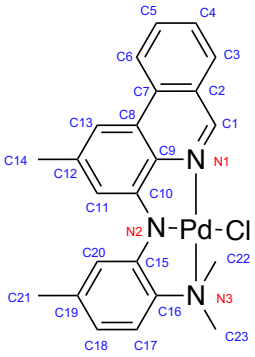

Synthesis of ^{CF3}PhenNNNMe$_2$-PdCl (L16-PdCl): To a stirred solution of compound **L16** (0.20 g, 0.51 mmol) in 30 mL of THF, Pd(COD)Cl$_2$ (0.15 g, 0.51 mmol), and NaO*t*Bu (0.051 g, 0.54 mmol) were added, and the mixture stirred vigorously at 65 °C for 18 h. The resulting red suspension was allowed to cool, and the volatiles removed *in vacuo*. The residue was then washed with diethyl ether (3 x 15 mL) to isolate a red solid. The compound was redissolved in CH_2Cl_2 and passed through a short plug (1 cm) of Celite. Isolated yield of **L16-PdCl** = 0.24 g (88%). ^{1}H NMR ($CDCl_3$, 500 MHz, 22 °C): δ 9.32 (s, 1H), 8.46 (d, 1H; *J* = 8.4 Hz), 8.03 (d, 1H; *J* = 7.9 Hz), 7.95 (t, 1H; *J* = 7.7 Hz), 7.77 (d, 2H; *J* = 11.6 Hz), 7.68 (s, 1H), 7.39 (s, 1H), 7.12 (d, 1H; *J* = 8.2 Hz,), 6.63 (d, 1H; *J* = 8.4 Hz,), 3.31 (s, 6H), 2.39 (s, 3H). ^{13}C{^{1}H} NMR ($CDCl_3$, 125 MHz, 22 °C): 154.5 (C_{Ar}), 150.3 (C_{Ar}), 147.8 (C_{Ar}), 143.1 (C_{Ar}), 139.3 (C_{Ar}), 133.4 (C_{Ar}), 132.8 (C_{Ar}), 131.2 (CF_3, quartet), 130.1 (C_{Ar}), 128.8 (C_{Ar}), 126.7 (C_{Ar}), 126.0 (C_{Ar}), 122.5 (C_{Ar}), 121.1 (C_{Ar}), 119.9 (C_{Ar}), 116.1 (C_{Ar}), 106.2 (C_{Ar}), 105.8 (C_{Ar}), 54.0 (C_{NMe2}), 21.55 (C_{Me}). ^{19}F{^{1}H} NMR ($CDCl_3$, 470 MHz, 22 °C): δ -62.25 ppm (s, 3F; C*F*$_3$).

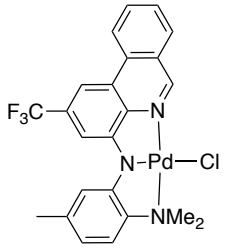

5.5.1. X-Ray Crystallography:

X-ray crystal structure data was using collected from multi-faceted crystals of suitable size and quality selected from a representative sample of crystals of the same habit using an optical microscope. In each case, crystals were mounted on MiTiGen loops with data collection carried out in a cold stream of nitrogen (150 K; Bruker D8 QUEST ECO; Mo K$_\alpha$ radiation). All diffractometer manipulations were carried out using Bruker APEX3 software.[31] Structure solution and refinement was carried out using XS, XT and XL software, embedded within the Bruker SHELXTL suite.[32] For each structure, the absence of additional symmetry was confirmed using ADDSYM incorporated in the PLATON program.[33] CCDC Nos. 1985563-1985568 contain the

supplementary crystallographic data for this chapter. The data can be obtained free of charge from The Cambridge Crystallographic Data Centre via www.ccdc.cam.ac.uk/structures.

Crystal structure data for **L14** (CCDC No. 1985568): X-ray quality crystals were grown following diffusion of diethyl ether vapor into a saturated $CHCl_3$ solution of the compound at room temperature. Crystal structure parameters: $C_{23}H_{23}N_3$ 341.44 g/mol, monoclinic, space group $P2_1/c$; a = 17.2243(11) Å, b = 14.7273(9) Å, c = 7.1219(5) Å, α = 90°, β = 99.910(3)°, γ = 90°, V = 1779.6(2) Å^3; Z = 4, ρ_{calcd} = 1.274 g cm^{-3}; crystal dimensions 0.266 x 0.200 x 0.150 mm^3; θ_{max} = 39.509°; 114196 reflections, 10645 independent (R_{int} = 0.0597), intrinsic phasing; absorption coeff (μ = 0.076 mm^{-1}), absorption correction semi-empirical from equivalents (SADABS); refinement (against F_o^2) with SHELXTL V6.1, 239 parameters, 0 restraints, R_1 = 0.0553 ($I > 2\sigma$) and wR_2 = 0.1722 (all data), Goof = 1.046, residual electron density 0.620/−0.610 e Å^{-3}.

Crystal structure data for **L15** (CCDC No. 1985565): X-ray quality crystals were grown following diffusion of diethyl ether vapor into a saturated $CHCl_3$ solution of the compound at room temperature. Crystal structure parameters: $C_{26}H_{29}N_3$ 383.52 g/mol, trigonal, space group $P3_2$; a = 10.2023(3) Å, b = 10.2023(3) Å, c = 17.7612(6) Å, α = 90°, β = 90°, γ = 120°, V = 1061.03(11) Å^3; Z = 3, ρ_{calcd} = 1.193 g cm^{-3}; crystal dimensions 0.100 x 0.050 x 0.050 mm^3; θ_{max} = 30.499°; 37488 reflections, 6534 independent (R_{int} = 0.0833), intrinsic phasing; absorption coeff (μ = 0.070 mm^{-1}), absorption correction semi-empirical from equivalents (SADABS); refinement (against F_o^2) with SHELXTL V6.1, 269 parameters, 1 restraints, R_1 = 0.0533 ($I > 2\sigma$) and wR_2 = 0.1243 (all data), Goof = 1.032, residual electron density 0.294/−0.245 e Å^{-3}.

Crystal structure data for **L16** (CCDC No. 1985563): X-ray quality crystals were grown following diffusion of diethyl ether vapor into a $CHCl_3$ solution of the compound at room temperature. Crystal structure parameters: $C_{23}H_{20}F_3N_3$ 395.42 g/mol, triclinic, space group P-1; a

= 7.8443(4) Å, b = 9.5831(4) Å, c = 13.4612(6) Å, α = 89.4932(18)°, β = 78.5285(18)°, γ = 87.8849(19)°, V = 991.02(8) Å^3; Z = 2, ρ_{calcd} = 1.325 g cm^{-3}; crystal dimensions 0.280 x 0.150 x 0.040 mm^3; θ_{max} = 27.721°; 23306 reflections, 4645 independent (R_{int} = 0.0560), intrinsic phasing; absorption coeff (μ = 0.099 mm^{-1}), absorption correction semi-empirical from equivalents (SADABS); refinement (against F_o^2) with SHELXTL V6.1, 265 parameters, 0 restraints, R_1 = 0.0793 ($I > 2\sigma$) and wR_2 = 0.2179 (all data), Goof = 1.050, residual electron density 1.031/−0.771 e Å^{-3}.

Crystal structure data for **L13-NiCl** (CCDC No. 1985567): X-ray quality crystals were grown following diffusion of diethyl ether vapor into a $CHCl_3$ solution of the compound at room temperature. Crystal structure parameters: $C_{19}H_{20}Cl_1N_3Ni_1$ 384.54 g/mol, triclinic, space group *P*-1; a = 9.8825(13) Å, b = 14.352(3) Å, c = 24.736(4) Å, α = 90.844(12)°, β = 94.338(10)°, γ = 102.995(13)°, V = 3406.9(10) Å^3; Z = 8, ρ_{calcd} = 1.499 g cm^{-3}; crystal dimensions 0.300 x 0.200 x 0.050 mm^3; θ_{max} = 30.679°; 97358 reflections, 20976 independent (R_{int} = 0.1012), intrinsic phasing; absorption coeff (μ = 1.300 mm^{-1}), absorption correction semi-empirical from equivalents (SADABS); refinement (against F_o^2) with SHELXTL V6.1, 881 parameters, 0 restraints, R_1 = 0.0601 ($I > 2\sigma$) and wR_2 = 0.1253 (all data), Goof = 1.021, residual electron density 0.770/−0.722 e Å^{-3}.

Crystal structure data for **L14-NiCl** (CCDC No. 1985564): X-ray quality crystals were grown following diffusion of diethyl ether vapor into a $CHCl_3$ solution of the compound at room temperature. Crystal structure parameters: $C_{23}H_{22}Cl_1N_3Ni_1$ 434.59 g/mol, triclinic, space group *P*-1; a = 6.9170(4) Å, b = 11.9707(8) Å, c = 12.3017(11) Å, α = 72.668(3)°, β = 82.739(3)°, γ = 89.465(3)°, V = 964.12(11) Å^3; Z = 2, ρ_{calcd} = 1.497 g cm^{-3}; crystal dimensions 0.200 x 0.100 x 0.030 mm^3; θ_{max} = 27.979°; 39487 reflections, 4613 independent (R_{int} = 0.0453), intrinsic phasing;

absorption coeff (μ = 1.159 mm^{-1}), absorption correction semi-empirical from equivalents (SADABS); refinement (against F_o^2) with SHELXTL V6.1, 257 parameters, 0 restraints, R_1 = 0.0424 ($I > 2\sigma$) and wR_2 = 0.1011 (all data), Goof = 1.137, residual electron density 0.806/−0.637 e $Å^{-3}$.

Crystal structure data for **L15-NiCl** (CCDC No. 1985566): X-ray quality crystals were grown following diffusion of diethyl ether vapor into a $CHCl_3$ solution of the compound at room temperature. Crystal structure parameters: $C_{26}H_{28}Cl_1N_3Ni_1$ 476.67 g/mol, monoclinic, space group $P2_1/c$; a = 14.9402(10) Å, b = 16.7884(11) Å, c = 8.9308(6) Å, α = 90°, β = 98.074(3)°, γ = 90°, V = 2217.8(3) $Å^3$; Z = 4, ρ_{calcd} = 1.428 g cm^{-3}; crystal dimensions 0.200 x 0.150 x 0.050 mm^3; θ_{max} = 33.129°; 68772 reflections, 7415 independent (R_{int} = 0.0419), intrinsic phasing; absorption coeff (μ = 1.014 mm^{-1}), absorption correction semi-empirical from equivalents (SADABS); refinement (against F_o^2) with SHELXTL V6.1, 286 parameters, 0 restraints, R_1 = 0.0453 ($I > 2\sigma$) and wR_2 = 0.0915 (all data), Goof = 1.054, residual electron density 0.647/−0.642 e $Å^{-3}$.

Crystal structure data for **L13-PdCl**: X-ray quality crystals were grown following diffusion of diethyl ether vapor into a $CHCl_3$ solution of the compound at room temperature. Crystal structure parameters: $C_{19}H_{20}Cl_1N_3Pd_1$ 432.26 g/mol, triclinic, space group P-1; a = 9.8508(5) Å, b = 14.02447(7) Å, c = 14.9899(8) Å, α = 75.218(2)°, β = 75.159(2)°, γ = 88.144(2)°, V = 1934(17) $Å^3$; Z = 4, ρ_{calcd} = 1.689 g cm^{-3}; crystal dimensions 0.160 x 0.080 x 0.050 mm^3; θ_{max} = 29.255°; 46843 reflections, 10522 independent (R_{int} = 0.1273), intrinsic phasing; absorption coeff (μ = 1.313 mm^{-1}), absorption correction semi-empirical from equivalents (SADABS); refinement (against F_o^2) with SHELXTL V6.1, 477 parameters, 0 restraints, R_1 = 0.0497 ($I > 2\sigma$) and wR_2 = 0.1052 (all data), Goof = 0.997, residual electron density 1.157/−1.449 e $Å^{-3}$.

Crystal structure data for **L14-PdCl**: X-ray quality crystals were grown following diffusion of diethyl ether vapor into a $CHCl_3$ solution of the compound at room temperature. Crystal structure parameters: $C_{23}H_{22}Cl_1N_3Pd_1$ 482.32 g/mol, triclinic, space group *P*-1; a = 9.3568(8) Å, b = 10.1501(8) Å, c = 22.0543(17) Å, α = 85.973(4)°, β = 87.953(4)°, γ = 68.173(4)°, V = 1939(3) Å^3; Z = 4, ρ_{calcd} = 1.652 g cm^{-3}; crystal dimensions 0.160 x 0.080 x 0.060 mm^3; θ_{max} = 30.592°; 127149 reflections, 11912 independent (R_{int} = 0.0416), intrinsic phasing; absorption coeff (μ = 1.109 mm^{-1}), absorption correction semi-empirical from equivalents (SADABS); refinement (against F_o^2) with SHELXTL V6.1, 513 parameters, 0 restraints, R_1 = 0.0286 ($I > 2\sigma$) and wR_2 = 0.0564 (all data), Goof = 1.076, residual electron density 0.501/−0.676 e Å^{-3}.

Crystal structure data for **L16-PdCl**: X-ray quality crystals were grown following diffusion of diethyl ether vapor into a $CHCl_3$ solution of the compound at room temperature. Crystal structure parameters: $C_{23}H_{19}Cl_1F_3N_3Pd1$ 536.29 g/mol, monoclinic, space group $P2_1/c$; a = 37.836(2) Å, b = 5.4885(3) Å, c = 20.5895(14) Å, α = 90°, β = 104.145(3)°, γ = 90°, V = 4146(4) Å^3; Z = 4, ρ_{calcd} = 1.718 g cm^{-3}; crystal dimensions 0.210 x 0.080 x 0.007 mm^3; θ_{max} = 27.468°; 119759 reflections, 9469 independent (R_{int} = 0.0548), intrinsic phasing; absorption coeff (μ = 1.067 mm^{-1}), absorption correction semi-empirical from equivalents (SADABS); refinement (against F_o^2) with SHELXTL V6.1, 529 parameters, 0 restraints, R_1 = 0.0713 ($I > 2\sigma$) and wR_2 = 0.1534 (all data), Goof = 1.210, residual electron density 0.188/−2.187 e Å^{-3}.

5.6. Catalysis Procedure:

5.6.1. Representative Procedure for Catalytic Trials:

To a 50 mL teflon stoppered flask containing catalyst **L16-NiCl** (0.012 g, 0.05 mmol), LiO*t*Bu (0.081 g, 1.01 mmol), benzoxazole (**H2**; 0.12 g, 1.01 mmol), and 1-iodooctane (**A1**; 0.291 g, 0.75

mmol), added 1,4-dioxane (2.0 mL) inside an N_2-filled glovebox. The resulting reaction mixture was stirred in a preheated oil bath set to 140 °C for 16 h. An aliquot (10 μL) of the reaction mixture diluted with 1 mL acetone was injected to GC instrument to analyze the products. GC yields of the products were obtained from the calibration curves plotted for pure reactants and products, with biphenyl as an internal standard, and are reported as an average of two runs.

5.6.2. GC Method:

Gas chromatographic analysis was performed using a Varian Cp-3800 GC gas chromatograph equipped with an autosampler and a Chrompak Cp Sil 8CB capillary column (50 mm x 0.2 mm x 0.33 μm). The instrument was set to an injection volume of 1 μL, an inlet split ratio of 10:1, and inlet and detector temperatures of 250 and 320 °C, respectively. UHP-grade argon was used as carrier gas with a flow rate of 30 mL/min. The temperature program used for all the analyses is as follows: 80 °C, 1 min; 30 °C/min to 200 °C, 2 min; 30 °C/min to 260 °C, 3 min; 30 °C/min to 300 °C, 3 min. Response factor for all the necessary compounds with respect to standard biphenyl was calculated from the average of two independent GC runs.

5.6.3. Hg Suppression Experiment:

Inside an N_2-filled glovebox, a flame-dried screw-cap tube was equipped with a magnetic stir bar, **L16-NiCl** (0.024 g, 0.050 mmol), LiO*t*Bu (0.085 g, 1.012 mmol), benzoxazole (0.120 g, 1.006 mmol), 1-iodooctane (0.291 g, 1.509 mmol) and Hg (1.0 g, or 5.0 mmol). This mixture was then dissolved/suspended in 1,4-dioxane (1.0 mL) and stirred in a preheated oil bath (oil bath temperature set to 140 °C) for 16 h. An aliquot (10 μL) of the reaction mixture was taken, diluted with 1 mL acetone and injected into the GC instrument to analyze the products. GC yields of the products were obtained from calibration curves plotted for pure reactants and products, with

biphenyl as an internal standard. The yield of the alkylated product **P1** measured was 63 % and 55 % for reactions conducted in the presence of 100 and 500 equivalents of Hg, respectively.

5.6.4. TEMPO Experiment:

Inside an N_2-filled glovebox, a flame-dried Teflon-stoppered flask was equipped with a magnetic stir bar, **L16-NiCl** (0.024 g, 0.050 mmol), LiO*t*Bu (0.085 g, 1.012 mmol), benzoxazole (0.120 g, 1.006 mmol), 1-iodooctane (0.291 g, 1.509 mmol) and TEMPO (0.236 g, 1.509 mmol), and 2 mL of 1,4-dioxane. The reaction mixture was stirred in a preheated oil bath (oil bath temperature set to 140 °C) for 16 h. An aliquot (10 μL) of the reaction mixture was taken, diluted with 1 mL acetone and injected into the GC instrument to analyze the products. GC Yields of the products were obtained from the calibration curves plotted for pure reactants and products, with biphenyl as an internal standard.

5.6.5. Filtration Experiment:

To an oven dried, 10 mL Teflon stoppered flask equipped with magnetic stir bar, catalyst **4c** (0.024 g, 0.050 mmol), LiO*t*Bu (0.085 g, 1.012 mmol), benzoxazole (0.120 g, 1.006 mmol), 1-iodooctane (0.291 g, 1.509 mmol) and 2 mL of dioxane was added inside an N_2-filled glove box. The resultant reaction mixture was stirred at 140 °C in a preheated oil bath for 1h. The reaction mixture was then cooled to room temperature and filtered into a second, oven-dried 10 mL Teflon stoppered flask, and charged with additional LiO*t*Bu (0.085 g, 1.012 mmol). The reaction mixture was once again stirred at 140 °C in a preheated oil bath for 16 h. An aliquot (10 μL) of the reaction mixture diluted with 1mL acetone was injected to GC instrument to analyze the products. GC Yields of the

products were obtained from the calibration curves plotted for pure reactants and products, with biphenyl as an internal standard.

5.6.7. Characterization Data of Coupling Products:

2-octylbenzo[d]oxazole (P1):[1] ^{1}H NMR ($CDCl_3$, 300 MHz, 22 °C): δ

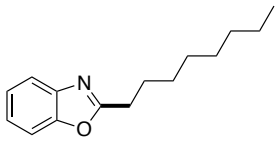

7.65-7.68 (m, 1H), 7.45-7.48 (m, 1H; Ar*H*), 7.27-7.30 (overlapped m, 2H; Ar*H*), 2.92 (t, J_{HH} = 7.6 Hz, 2H; (N=C)CH_2), 1.88 (tt, J_{HH} = 7.3, 7.6 Hz, 2H; CH_2), 1.27-1.44 (overlapped m, 10H; CH_2), 0.88 ppm (t, J = 6.9 Hz, 3H; CH_3).

2-octylbenzo[d]thiazole (P2):[2] ^{1}H NMR ($CDCl_3$, 300 MHz, 22 °C): δ

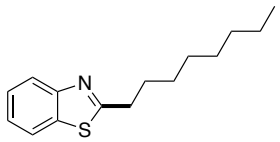

7.98 (d, J_{HH} = 8.2 Hz, 1H; Ar*H*), 7.84 (dd, J_{HH} = 8.2, 1.4 Hz, 1H; Ar*H*), 7.43 (td, J_{HH} = 7.8, 1.1 Hz, 1H; Ar*H*), 7.33 (td, J_{HH} = 7.6, 0.9 Hz, 1H; Ar*H*), 3.10 (t, J_{HH} = 7.8 Hz, 2H; (N=C)CH_2), 1.91–1.84 (m, 2H; CH_2), 1.47–1.27 (overlapped m, 10H; CH_2), 0.89 ppm (t, J = 6.9 Hz, 3H; CH_3).

2-(3-(9H-carbazol-9-yl)butyl)benzo[d]oxazole (P3): ^{1}H NMR

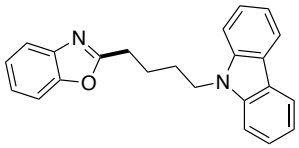

($CDCl_3$, 300 MHz, 22 °C): δ 8.10 (dd, J_{HH} = 7.7, 0.8 Hz, 2H; Ar*H*), 7.74-7.63 (m, 1H; Ar*H*), 7.51-7.38 (overlapped m, 5H; Ar*H*), 7.33-7.18 (overlapped m, 4H; Ar*H*), 4.39 (t, J_{HH} = 6.6 Hz, 2H; CH_2), 2.96 (t, J_{HH} = 6.9 Hz, 2H; CH_2), 2.02 ppm (overlapped d, J_{HH} = 5.9 Hz, 4H; CH_2). ^{13}C{^{1}H} NMR ($CDCl_3$, 125 MHz, 22 °C): δ 166.54 (N=*C*-O), 150.90 (C_{Ar}), 141.42 (C_{Ar}), 140.46 (C_{Ar}), 125.81 (C_{Ar}), 124.70 (C_{Ar}), 124.29 (C_{Ar}), 123.02 (C_{Ar}), 120.52 (C_{Ar}), 119.71 (C_{Ar}), 119.01 (C_{Ar}), 110.46 (C_{Ar}), 108.71 (C_{Ar}), 42.70 (*C*H_2), 28.51 (*C*H_2), 28.40 (*C*H_2), 24.57 ppm (*C*H_2). HRMS (APCI-TOF) m/z: $[M + H]^+$ Calc'd for $[C_{23}H_{20}N_2O+H^+]$ 341.1648; Found 341.1664.

6-(benzo[d]oxazol-2-yl)hexyl benzoate (P4):[3] ^{1}H NMR ($CDCl_3$, 300 MHz, 22 °C): δ 8.03 (d, J_{HH} = 7.6 Hz, 2H; Ar*H*), 7.67 (m, 1H; Ar*H*), 7.54 (t, J_{HH} = 6.7 Hz, 1H; Ar*H*), 7.44 (overlapped m, 3H; Ar*H*), 7.29 (overlapped m, 2H; Ar*H*), 4.32 (t, J_{HH} = 6.5 Hz, 2H; OCH_2), 2.94 (t, J_{HH} = 7.3 Hz, 2H; CH_2), 1.93 (m, 2H; CH_2), 1.79 (m, 2H; CH_2), 1.54 ppm (overlapped m, 4H; CH_2).

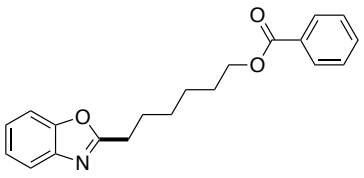

2-(3-phenylpropyl)benzo[d]oxazole (P5):[3] ^{1}H NMR ($CDCl_3$, 300 MHz, 22 °C): δ 7.70 (m, 1H; Ar*H*), 7.49 (m, 1H; Ar*H*), 7.26 (overlapped m, 7H; Ar*H*), 2.96 (t, J_{HH} = 7.6 Hz, 2H; CH_2), 2.78 (t, J_{HH} = 7.3 Hz, 2H; CH_2), 2.24 ppm (m, 2H; CH_2).

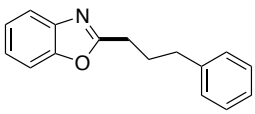

2-(3-phenoxypropyl)benzo[d]oxazole (P6):[3] ^{1}H NMR ($CDCl_3$, 300 MHz, 22 °C): δ 7.70 (m, 1H; Ar*H*), 7.50 (m, 1H; Ar*H*), 7.28 (overlapped m, 4H; Ar*H*), 6.92 (overlapped m, 3H; Ar*H*), 4.12 (t, J_{HH} = 5.9 Hz, 2H; OCH_2), 3.17 (t, J_{HH} = 7.3 Hz, 2H; CH_2), 2.40 ppm (m, 2H; CH_2).

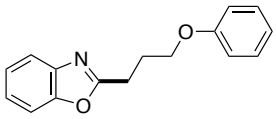

2-(3-(phenylthio)propyl)benzo[d]oxazole (P7):[3] ^{1}H NMR ($CDCl_3$, 300 MHz, 22 °C): δ 7.68 (m, 1H; Ar*H*), 7.48 (m, 1H; Ar*H*), 7.31 (overlapped m, 6H; Ar*H*), 7.18 (m, 1H; Ar*H*), 3.08 (overlapped m, apparent J_{HH} = 7.3 Hz, 4H; CH_2), 2.23 ppm (m, J_{HH} = 7.0 Hz, 2H).

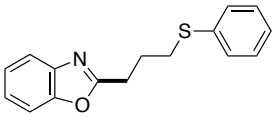

2-(pent-4-enyl)benzo[d]oxazole (P8):[3] ^{1}H NMR ($CDCl_3$, 300 MHz, 22 °C): δ 7.67 (m, 1H; Ar*H*), 7.47 (m, 1H; Ar*H*), 7.28 (overlapped m, 2H; Ar*H*), 5.82 (m, 1H; =C*H*), 5.04 (m, 2H; =CH_2), 2.93 (t, J_{HH} = 7.6 Hz, 2H; CH_2), 2.20 (m, apparent J_{HH} = 7.0 Hz, 2H; CH_2), 1.99 ppm (m, 2H; CH_2).

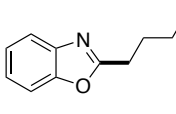

2-(cyclohexylmethyl)benzo[d]oxazole (P9):[3] ^{1}H NMR ($CDCl_3$, 300 MHz, 22 °C): δ 7.67 (m, 1H; Ar*H*), 7.47 (m, 1H; Ar*H*), 7.29 (m, 2H; Ar*H*), 2.81 (d,

J_{HH} = 7.0 Hz, 2H; CH_2), 1.97 (m, 1H; CH), 1.72 (overlapped m, 5H; CH_2), 1.15 ppm (overlapped m, 5H; CH_2).

2-butylbenzo[d]oxazole (P10):[3] ^{1}H NMR ($CDCl_3$, 300 MHz, 22 °C): δ 7.67 (m, 1H; ArH), 7.47 (m, 1H; ArH), 7.29 (overlapped m, 2H; ArH), 2.93 (t, J_{HH} = 7.6 Hz, 2H; CH_2), 1.87 (m, 2H; CH_2), 1.46 (m, 2H; CH_2), 0.97 ppm (t, J_{HH} = 7.3 Hz, 3H; CH_3).

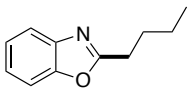

5.7. References:

1. Kulkarni, A. A.; Daugulis, O. *Synthesis* **2009**, 4087.
2. Ackermann, L. *Chem. Commun.* **2010**, *46*, 4866.
3. Ping, L.; Chung, D. S.; Bouffard, J.; Lee, S.-G. *Chem. Soc. Rev.* **2017**, *46*, 4299.
4. Qin, Y.; Zhu, L.; Luo, S. *Chem. Rev.* **2017**, *117*, 9433.
5. Hu, X. *Chem. Sci.* **2011**, *2*, 1867.
6. Verrier, C.; Hoarau, C.; Marsais, F. *Org. Biomol. Chem.* **2009**, *7*, 647.
7. Yao, T.; Hirano, K.; Satoh, T.; Miura, M. *Chem. - Eur. J.* **2010**, *16*, 12307.
8. Vechorkin, O.; Proust, V.; Hu, X. *Angew. Chem., Int. Ed.* **2010**, *49*, 3061.
9. Ackermann, L.; Punji, B.; Song, W. *Adv. Synth. Catal.* **2011**, *353*, 3325.
10. Patel, U. N.; Pandey, D. K.; Gonnade, R. G.; Punji, B. *Organometallics* **2016**, *35*, 1785.
11. Yao, T.; Hirano, K.; Satoh, T.; Miura, M. *Angew. Chem., Int. Ed.* **2012**, *51*, 775.
12. Theunissen, C.; Wang, J.; Evano, G. *Chem. Sci.* **2017**, *8*, 3465.
13. Zhao, X.; Wu, G.; Zhang, Y.; Wang, J. *J. Am. Chem. Soc.* **2011**, *133*, 3296.
14. Ren, P.; Salihu, I.; Scopelliti, R.; Hu, X. *Org. Lett.* **2012**, *14*, 1748.
15. Mandapati, P.; Giesbrecht, P. K.; Davis, R. L.; Herbert, D. E. *Inorg. Chem.* **2017**, *56*, 3674.
16. Mondal, R.; Giesbrecht, P. K.; Herbert, D. E. *Polyhedron* **2016**, *108*, 156.
17. Nainwal, L. M.; Tasneem, S.; Akhtar, W.; Verma, G.; Khan, M. F.; Parvez, S.; Shaquiquzzaman, M.; Akhter, M.; Alam, M. M. *Eur. J. Med. Chem.* **2019**, *164*, 121.
18. Braun, J. D.; Lozada, I. B.; Kolodziej, C.; Burda, C.; Newman, K. M. E.; van Lierop, J.; Davis, R. L.; Herbert, D. E. *Nat. Chem.* **2019**, *11*, 1144.
19. Gunanathan, C.; Gnanaprakasam, B.; Iron, M. A.; Shimon, L. J. W.; Milstein, D. *J. Am. Chem. Soc.* **2010**, *132*, 14763.

20. Patel, U. N.; Jain, S.; Pandey, D. K.; Gonnade, R. G.; Vanka, K.; Punji, B. *Organometallics* **2018**, *37*, 1017.

21. Lozada, I. B.; Murray, T.; Herbert, D. E. *Polyhedron* **2019**, *161*, 261.

22. Mandapati, P.; Braun, J. D.; Killeen, C.; Davis, R. L.; Williams, J. A. G.; Herbert, D. E. *Inorg. Chem.* **2019**, *58*, 14808.

23. Giesbrecht, P. K.; Nemez, D. B.; Herbert, D. E. *Chem. Commun.* **2018**, *54*, 338.

24. Mondal, R.; Lozada, I. B.; Davis, R. L.; Williams, J. A. G.; Herbert, D. E. *Inorg. Chem.* **2018**, *57*, 4966.

25. Csok, Z.; Vechorkin, O.; Harkins, S. B.; Scopelliti, R.; Hu, X. *J. Am. Chem. Soc.* **2008**, *130*, 8156.

26. Omer, H. M.; Liu, P. *J. Am. Chem. Soc.* **2017**, *139*, 9909.

27. Hill, R. H.; Puddephatt, R. J. *J. Am. Chem. Soc.* **1985**, *107*, 1218.

28. Torigoe, T.; Ohmura, T.; Suginome, M. *Angew. Chem., Int. Ed.* **2017**, *56*, 14272.

29. Medina Padilla, M.; Castro Morera, A.; Sanchez-Quesada, J.; Garcia Palomero, E.; Alonso Cascon, M.; Herrero Santos, S.; Vela Ruiz, M.; Usan Egea, P.; Rodriguez Villanueva, A. L. Triple Substituted Phenanthroline Derivatives for the Treatment of Neurodegenerative or Haematological Diseases or Conditions, or Cancer. Patent Number: US20110306631A12011.

30. Koradin, C.; Dohle, W.; Rodriguez, A. L.; Schmid, B.; Knochel, P. *Tetrahedron* **2003**, *59*, 1571.

31. Bruker-AXS *APEX3 v2016.1-0*, Madison, Wisconsin, USA, **2016**.

32. Sheldrick, G. M. *Acta Cryst.* **2008**, *A64*, 112.

33. Spek, A. L. *Acta Cryst.* **2009**, *D65*, 148.

34. Ren, Y.; Vechorkin, O.; Csok, Z.; Salihu, I.; Scopelliti, R.; Hu, X. *Dalton Trans.,* **2011**, *40*, 8906.

35. Reichardt, C. *Chem. Rev.,* **1994**, *94*, 2319-2358.

Chapter 6: Conclusions and Outlook

6.1. Conclusions:

In this thesis, I have reported the design, construction and synthesis of monoanionic, palindromic and non-palindromic, tridentate (*N*^*N*-^*N*) pincer-type ligand motifs containing phenanthridinyl and/or quinolinyl arms. I furthermore described their coordination chemistry with nickel, palladium and platinum. Applications in emissive molecule design and catalysis were also presented.

Specifically, to obtain my target proligands, I first optimized the synthesis of functionalized phenanthridines using a one-pot Pd-catalyzed C-C Suzuki coupling/condensation protocol, leading to isolated yields of various functionalized phenanthridines of greater than 85%. Reflecting on these efforts, the one-pot nature of the reaction is appealing compared with multi-step syntheses of the sort described in Chapter 1. In general, yields of phenanthridines prepared in this way were high and tolerant of both electron-releasing (Me, *t*Bu) and electron-withdrawing (CF_3, NO_2, Br) substituents. To access amino-substituted variants, use of an ortho-diamine aniline precursor was less effective for direct synthesis of (4-amino)phenanthridines in high yields. Instead, a two-step process in which the 4-nitro variant was first isolated, then reduced to the (amino)phenanthridine was found to give greater overall yields. The lower conversion using the ortho-diamine aniline likely results from chelation of the Pd catalyst, hampering turnover. These phenanthridine precursors were then used in Buchwald-Hartwig C-N coupling reactions to form the desired proligands.

As a series, metal(II) chloride complexes of Group 10 metals (nickel, palladium, and platinum) were constructed in high yields using three intial ligands. The ligands **L1**, **L2** and **L3**, and their corresponding metal complexes **(L)MCl** (M = Ni, Pd, Cl; n = **1**, **2**, **3**), were used to study the

impact of systematic π-extension on electronic and photophysical properties. To do so, the ligands and complexes were characterized using both solution (1D & 2D NMR spectroscopy, UV-Vis spectroscopy and cyclic voltammetry) and solid-state (X-ray diffraction, EA) techniques, as well as DFT studies. Metal complexes **L2-MCl** and **L3-MCl** are sparingly soluble due to the planar structure and presence of π-π stacking interactions. Attempts were made to improve the solubility by introducing *t*Bu groups into phenanthridinyl arms, but the outcome was not very significant.

Having found that platinum(II) chloride complexes of **L1**, **L2** and **L3** could be prepared, I then explored their luminescence in solution. In that work, I discovered these molecules can be used to test two different but equally common ways to control the absorption and or photophysical properties of the molecules or metal complexes. In the first way, site-specific benzannulation is typically thought to have a conventional impact on a complex's electronic properties in that it destabilizes the highest occupied molecular orbital (HOMO) and stabilizes the lowest unoccupied molecular orbital (LUMO); this will yield a red-shifted spectrum. In the second way, the introduction of electron-donating groups (Me, *t*Bu) or electron-withdrawing groups (CF_3) usually induce either hypsochromic (blue) shift to bathochromic (red) shifts in the absorption or emission spectra. This substitution will impact the HOMO and LUMO energies relative to unsubstituted molecules.[1]

To explore the impact of these potentially complimentary tools, a larger library of ligands **L1-L12** was prepared starting from bis(quinolinyl)amines (BQA) and then moving towards asymmetric and symmetric bis(phenanthridinyl)amines, with a range of different substituents in the 2-position of the phenanthridinyl rings and corresponding 6-position of the quinolinyl arms. To do so, in addition to preparing functionalized phenanthridines, 6-functionalized quinolines were also prepared using the Skraup reaction.[2] A notable finding from these investigations is that the

preparation of functionalized phenanthridines in general proceeds in higher yields and with more facile workup that the Skraup preparation of 2,6-functionalized quinolines.

Once assembled, these ligands were reacted with $Pt(COD)Cl_2$ to isolate the corresponding library of Pt(II) complexes. As the benzannulation increased, the solubility of the prepared complexes decreased significantly, which is attributable to the presence of strong π-π stacking interactions. Nevertheless, the complexes were found to be soluble enough for study by various spectroscopies. Comparing the photophysical properties of complexes of (quinolinyl)amido ligands with those of π-extended (phenanthridinyl)amido analogues revealed a counterintuitive impact of site-selective benzannulation. A blue shift of nearly 40 nm in the emission wavelength is observed for bis(phenanthridinyl)amino Pt(II) complexes, despite nearly isoenergetic absorption manifolds.

Even the presence of two bulky *t*Bu groups on bis(phenanthridinyl)amine could not improve the solubility issues, which further decreased upon coordination with the metal centre, again likely due to π-π stacking interactions. To address the solubility issues and prevent metal complexes from π-π stacking interactions, and to explore the reactivity of metal complexes in common organic solvents, a new ligand design was then pursued (*N^N-^NMe2)* bearing pyramidal NMe_2 donor groups. Proligands **L13-L14** based on *bis*(2-(dimethylamino)phenyl)amido ligands were accordingly prepared containing a second donor based on one quinolinyl unit (**L13**), or one benzo-fused *N*-heterocyclic phenanthridinyl (**L14**, **L15**, **L16**) unit bearing either electron-donating (Me, *t*Bu) or electron withdrawing (CF_3) groups. Divalent nickel(II) and palladium(II) complexes of these ligands were then prepared in good yields. The nickel(II) complexes were then evaluated in C-C bond forming catalysis, and were found to be active catalysts for C_{sp2} -C_{sp3} coupling of azoles and alkyl halides. Of the series, **L14-NiCl** containing a phenanthridinyl donor bearing an electron

withdrawing group (CF_3) outperformed the other complexes. In terms of substrates, alkyl chlorides were found to give higher yields when compared to corresponding alkyl bromides and alkyl iodides as shown in Table 5.1, further boosted by addition of NaI. This finding is important, as alkyl chlorides are typically more difficult to activate than the those containing the heavier halogens. It is accordingly potentially worth investigating the reactivity of these complexes with alkyl fluorides to pursue C-F activation. Similarly, divalent palladium (II) complexes were synthesized from the proligands **L13-14** and $Pd(COD)Cl_2$, and the coordination complexes **L13-PdCl** and **L14-PdCl** were found to show inverted solvatochromism trends, whereby the lowest energy absorption shifted to higher energy with increasing solvent polarity. Attempts to make platinum (II) complexes were unsuccessful.

6.2. Outlook:

In general, to be able to probe the reactivity of metal complexes in small molecule activation reactions and as catalysts for organic transformations, the complexes should be readily soluble in common organic solvents. Unfortunately, the metal complexes synthesized with ligands containing extended π-conjugated systems discussed in **Chapter 2**, **Chapter 3** and **Chapter 4** suffer from low solubility due to the presence of π-π stacking interactions. Protonation of these complexes with strong acids (e.g., HCl, CF_3COOH etc.) should disrupt the planarity of the complexes by pyramidalizing the amido nitrogen and break π-π stacking interactions through this effect and also through introduction of a counterion. This is anticipated to improve solubility as shown in Scheme 6.1. Preliminary investigations indeed showed that when sparingly soluble metal complexes were treated with HCl or trifluoromethanesulfonic acid (CF_3SO_3H), protonation took place at the amido nitrogen, corroborated by ^1H NMR spectroscopy. Replacing the chloride ligand

in the resulting complexes with a hydride would then produce a species that is the ostensible product of activation of H_2 by addition across a metal-amido bond. In initial investigations, however, treating protonated divalent Ni(II) or Pd(II) chloride complexes with reducing agents such as $NaBH_4$, $LiAlH_4$, NaH led to demetalation and recovery of dissociated ligand.

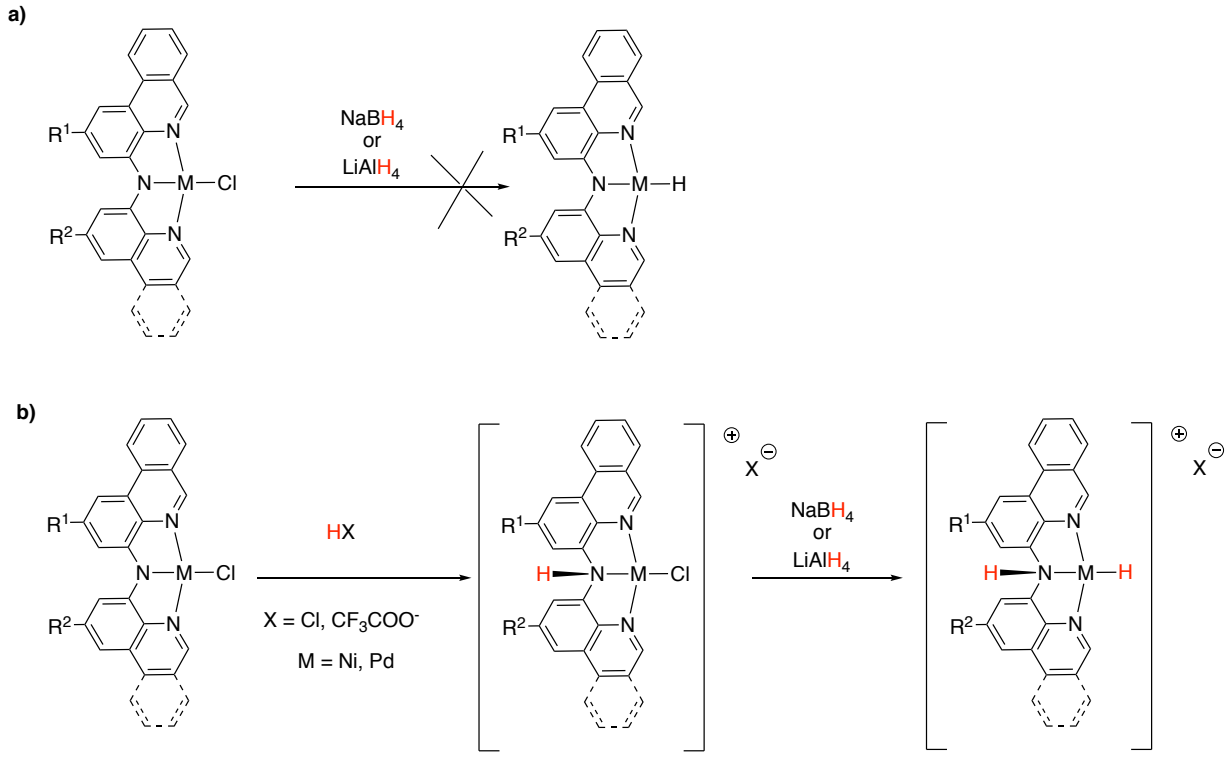

Scheme 6.1. a) Attempted reduction reaction to isolate metal hydride, b) protonation of metal complex to isolate metal hydride.

Platinum (II) metal complexes of benzannulated π-extended conjugated system have shown impressive photophysical absorption and emission properties. Previously, our group reported phenanthridine containing (*N^N-^O*) have shown shown superior *in vitro* therapeutic index compared with phenanthriplatin and cisplatin.[3] Testing complexes coordinated (*N^N-^NMe₂*) would be interesting in terms of both these potential research directions, but attempts to make platinum(II) chloride complexes of (*N^N-^NMe₂*) ligands have so far been unsuccessful. A new

tridentate hybrid (*N^P^N(H)*^{R}) ligand containing neutral phosphorous (soft donor, stronger σ donation) as central donor and X-type nitrogen donor may instead help further stabilize the metal complex. The alkynyl derivatives of these (*N^P^N(H)*^{R})PtCl complexes could then be used to enhance photophysical properties or activity as anticancer agents (Scheme 6.2).[4]

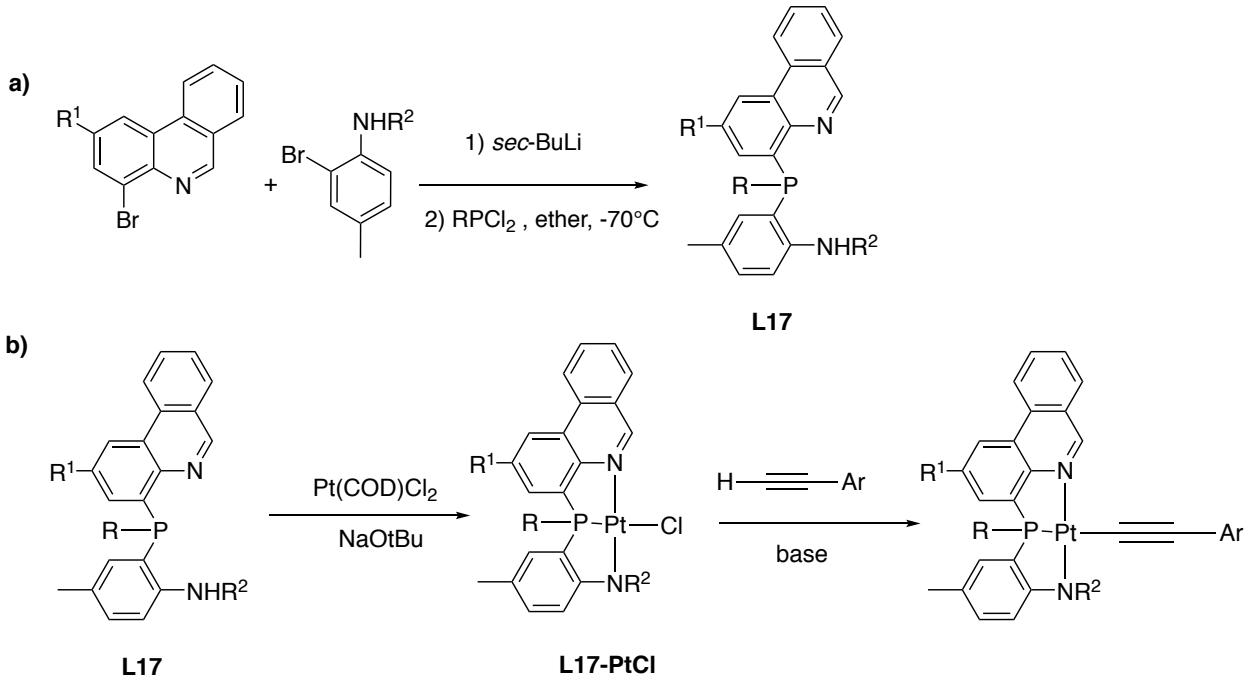

Scheme 6.2. a) Ligand design to synthesize (*N^P^N(H)*^{R}) ligand b) synthesis of corresponding platinum (II) chloride and alkynyl complexes.

Small molecule activation and heterolytic splitting of H-X bonds (X = H, alkynyl, NH_2, SPh) plays important role in 1,2-addition reactions and catalysis.[5] In Chapter **4**, I mentioned that among the Ni(II) complexes tested, the complex with a CF_3 (**L16**) outperformed in C-C bond forming catalysis. This gives us the opportunity to explore the reactivity of palladium(II) chloride complex and their corresponding palladium(II)triflate complexes ([Pd]OTf) for small molecule activation and H-X bond activation chemistry with ligands **L16** and **L17** as shown in Scheme 6.3.

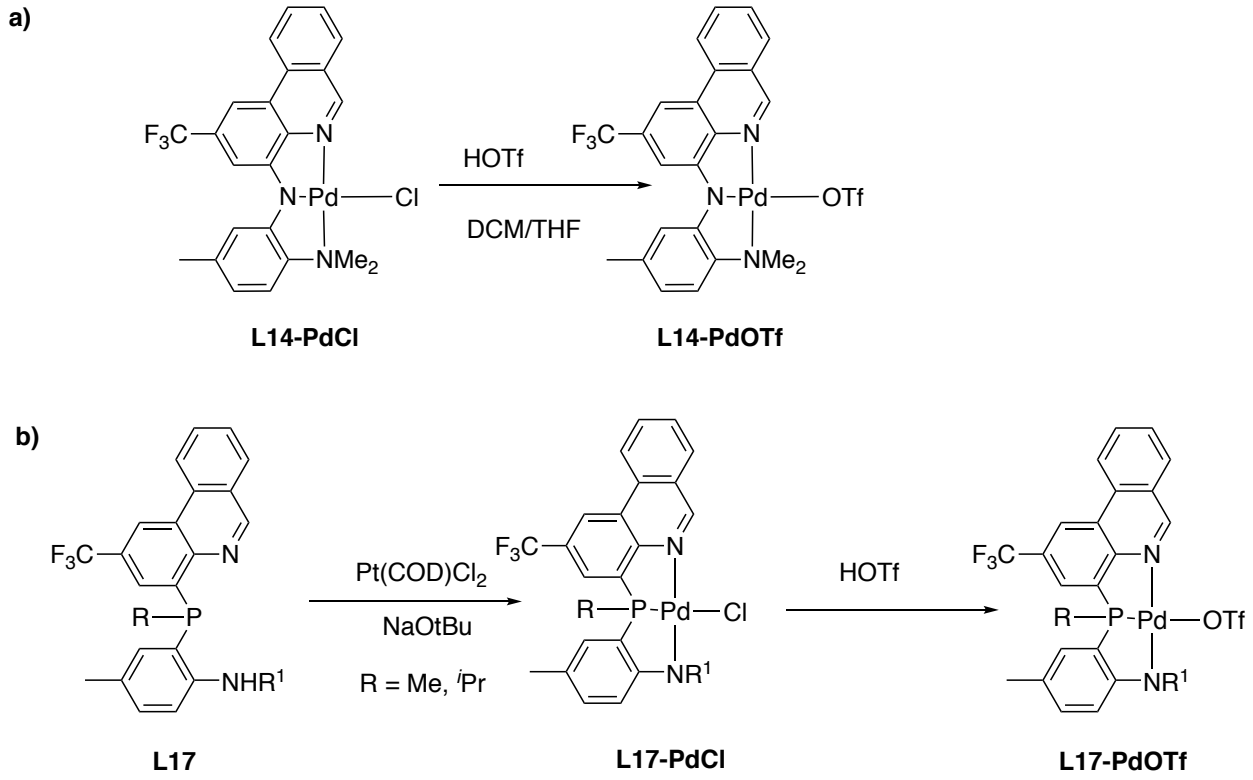

Scheme 6.3. Synthesis of **L14-PdOTf** and **L17-PdOTf** which can be potential catalysts for small molecule activation.

As a graduate student I have studied extensively phenanthridines starting from synthesis to complete characterization and introduced them into tridentate 'pincer' motifs as ancillary ligands and their coordination complexes with group 10 metals (Ni, Pd and Pt). From my previous chapters it is clear that functionalized phenanthridines are easier to synthesize compared to quinoline analogs, and can present altered photophysical properties (luminescence) and improved catalytic activity in C-C coupling reactions between azoles and alkyl halides. There may be many other interesting applications yet to be discovered. For example, as discussed in earlier chapters, phenanthridine mimic NADH/NAD(P)H model and has the potential to act a nature's hydride shuttle in chemical transformations that involves hydride transfers for sustainable chemistry. Yang-Gui Zhou and Matthias Beller research groups have used commercially available

phenanthridine for asymmetric hydrogenation[6] and reduction of α-keto/α-imino esters[7] in the presence of expensive ruthenium and cheap earth abundant iron catalysts respectively. They have demonstrated that phenanthridine can be hydrogenated/dehydrogenated under mild conditions and can be used for transfer hydrogenation, also involves aromatization and dearomatization of phenanthridine. Applying these concepts to a single metal-ligand complex may enabling intriguing new reactions.

In this work, I have explored how phenanthridine-containing ligands can be used to adjust electronic properties in photophysical applications or reactivity in organic catalysis mediated by transition metal complexes. In these applications, the phenanthridine moieties served as spectator ligands, participating in charge-transfer and/or stabilizing the metal through enhanced π-acidity. A further avenue to explore is the potential for chemical non-innocence of phenanthridines when bound to the metal centre. Acridine, a structural isomer to phenanthridine, can act as a hydride shuttle for organic transformations via reduction (hydride addition) at the C9 carbon as shown by Milstein and co-workers who incorporated acridine into pincer ligand frameworks and have reported its chemical non-innocence in catalysis.[8] Using these ligands, a number of applications in catalysis were possible including conversion of alcohols to acetals,[9] catalytic transformation of lactams from amines,[10] production of biofuel from ethanol,[11] synthesis of amides,[12] and oxidation of alkenes.[13] Phenanthridine-containing ligands accordingly provide an opportunity to access similar reactivity.

Another outlook emerging from this work is the idea of constructing phenanthridine-containing ligands with hemi-labile donor arms (Figure 6.1) and their earlier transition metal complexes (e.g., manganese, iron and cobalt) which can access higher oxidation states. As transition metal hydrides play an important role in many catalytic reactions, these might be

pursued.[14] Iron[15] and cobalt[16] hydrides would be key targets. Synthesis and isolation of such metal hydrides along with reduced phenanthridine bound to a metal centre would be an exciting area of research to explore applications in catalysis that involve transfer hydrogenation reactions,[17] and also promote short-range 'ligand-metal cooperation' (Scheme 6.4).

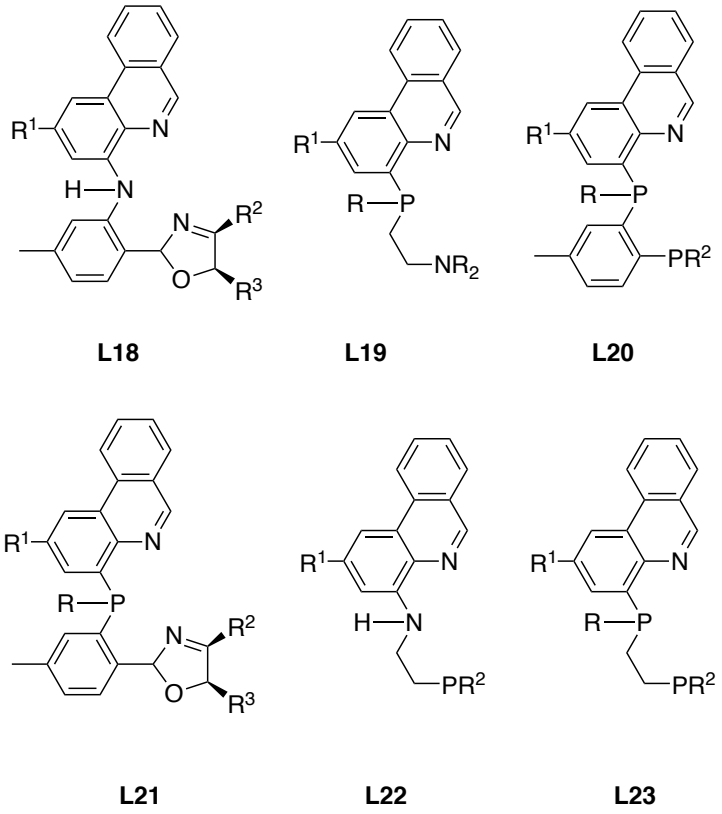

Figure 6.1. New set of proligands designed for early transition metals.

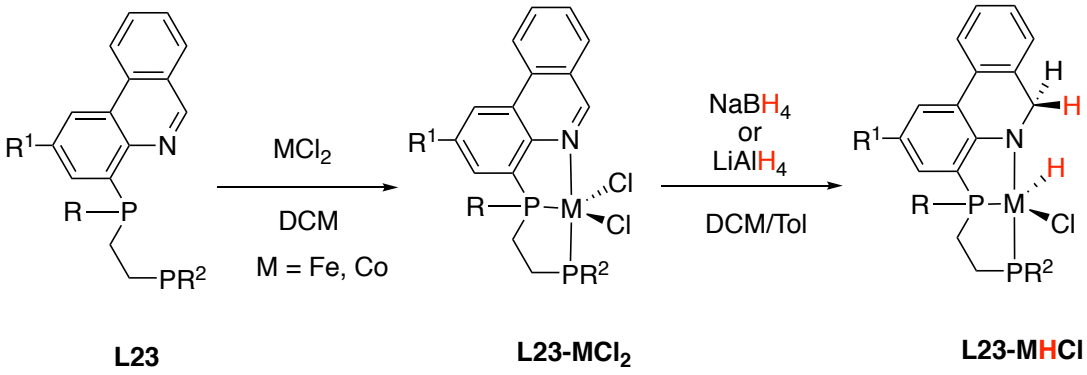

Scheme 6.4. Synthesis of Fe and Co metal hydrides using new ligand design approach

In conclusion, I have successfully incorporated phenanthridines into *N^N(H)^N* pincer frameworks and built a library of compounds and metal complexes. In this thesis, I furthermore report the coordination chemistry of these ligands, along with a study of the photophysical properties of their Group 10 metal complexes. In addition, I describe the use of Ni-complexes of related, more soluble ligands as active catalysts for catalytic C-C coupling. I anticipate this work will open many avenues for future scientists to discover the properties of these phenanthridine containing pincers with wide range of transition metals and many more applications in various fields of chemistry.

6.3. References:

1. Hanson, K.; Roskop, L.; Djurovich, P. I.; Zahariev, F.; Gordon, M. S.; Thompson, M. E. *J. Am. Chem. Soc.* **2010**, *132*, 16247.
2. Lee, C.-I.; Zhou, J.; Ozerov, O. V. *J. Am. Chem. Soc.* **2013**, *135*, 3560.
3. Lozada I. B.; Huang, B.; Stilgenbauer, M.; Beach, T.; Qiu, Z.; Zheng, Y.; Herbert, D. E. *Dalton Trans.,* **2020**, *49*, 6557.
4. Wen, H-M.; W, Y-H, Fan, Y.; Zhang, L-Y.; Chen, C-N.; Chen, Z-N. *Inorg. Chem.* **2010**, *49*, 2210.
5. Gregor, L. C.; Chen, C-H.; Fafard, C. M.; Fan, L.; Guo, C.; Foxman, B. M.; Gusev, D. G.; Ozerov, O. V. *Dalton Trans.,* **2010**, 39, 3195.
6. Chen, Q-A.; Gao, K.; Duan, Y.; Ye, Z-S.; Shi, L.; Yang, Y.; Zhou, Y-G. *J. Am. Chem. Soc.* **2012,** *134,* 2442.
7. Lu, L-Q.; Li, Y.; Junge, K.; Beller, M. *Angew. Chem. Int. Ed.* **2013,** *52,* 8382.
8. Gunanathan, C.; Gnanaprakasam, B.; Iron, M. A.; Shimon, L. J. W.; Milstein, D. *J. Am. Chem. Soc.* **2010,** *132,* 14763.
9. Gunanathan, C.; Shimon, L. J. W.; Milstein, D. *J. Am. Chem. Soc.* **2009,** *131,* 3146.
10. Gellrich, U.; Khusnutdinova, J. R.; Leitus, G. M.; Milstein, D. *J. Am. Chem. Soc.* **2015,** *137,* 4851.
11. Xie, Y.; Ben-David, Y.; Shimon, L. J. W.; Milstein, D. *J. Am. Chem. Soc.* **2016,** *136,* 9077.
12. Daw, P.; Kumar, A.; Espinosa-Jalapa, N. A.; Ben-David, Y.; Milstein, D. *J. Am. Chem. Soc.* **2019,** *141,* 12202.
13. Tang, S.; Ben-David, Y.; Milstein, D. *J. Am. Chem. Soc.* **2020,** *142,* 5980.
14. Eberhardt, N. A.; Guan, H. *Chem. Rev.* **2016**, *116*, 8373.

15. Nakazawa, H.; Itazaki, M. *Top. Organomet. Chem.* **2011**, *33*, 27.

16. Ai, W.; Zhong, R.; Liu, X.; Liu, Q. *Chem.* **2019**, *119*, 2876.

17. Balaraman, E.; Nandakumar, A.; Jaiswal, G.; Sahoo, M. K. *Catal. Sci. Technol.,* **2017**, *7*, 3177.